

GALACTIC RADIO ASTRONOMY

Yoshiaki SOFUE

Lecture Note Graduate and Undergraduate Courses at
University of Tokyo, Kagoshima University, Meisei University
and others

Contents

1	INTRODUCTION	1
1.1	Radio Astronomy	1
1.1.1	Radio window through the Galactic Disk	1
1.1.2	A History of Radio Astronomy	2
1.2	The Radio Emission	3
1.2.1	Plane waves	3
1.2.2	Acceleration of a charged particle and radiation	5
1.2.3	Radiation from an electron in a magnetic field	7
1.3	Thermal Emission	9
1.3.1	Thermal Bremsstrahlung	9
1.3.2	Thermal emission and absorption coefficient	11
1.4	Synchrotron Radiation - Non-thermal Radiation	12
1.4.1	Emissivity and spectrum	12
1.4.2	Energy equipartition	14
1.5	Recombination Lines	15
1.5.1	Frequency	15
1.5.2	Line width	17
1.5.3	Line intensity	19
1.5.4	Line to continuum intensity ratio and temperature determination	21
1.6	Molecular Lines	22
1.6.1	Frequency	23
1.6.2	Intensity	24

1.6.3	Two masses estimated from the CO intensity	26
1.6.4	Other molecules	27
1.7	HI Line	28
1.7.1	Frequency	28
1.7.2	Intensity	29
1.8	Radiations from various species	31
1.8.1	Molecular Lines	31
1.8.2	HI Line Emission	31
1.8.3	Recombination Lines	32
1.8.4	Free-Free Emission	32
1.8.5	Synchrotron Radiation	32
1.8.6	Black-Body Radiation	33
1.9	Radiative Transfer	33
2	INTERSTELLAR MATTER	39
2.1	ISM and Radio Emission	39
2.1.1	ISM at various temperatures	39
2.1.2	Population in the Galaxy	39
2.2	Energy Balance in ISM	41
2.2.1	Energy-density and Pressure balance	41
2.2.2	‘Activity’ in ISM	44
2.3	Molecular Clouds	45
2.3.1	Mass, size and intensity	45
2.3.2	The Distribution of MC and GMC	47
2.3.3	Giant Molecular Clouds (GMC)	48
2.3.4	GMC and Star-forming sites	49
2.4	HI Gas and Clouds	50
2.4.1	Mass, size, and intensity of HI clouds	50
2.4.2	The Distribution of HI gas	52
2.5	HI vs H ₂ in the ISM	52
2.5.1	The HI to H ₂ Transition	52
2.5.2	The Molecular Fraction	55

2.5.3	Molecular Fraction and the ISM Evolution	55
2.6	HII Gas	55
3	STAR FORMATION AND DEATH	57
3.1	Mechanisms of Star Formation	57
3.1.1	Sites of Star Formation	57
3.1.2	Schmidt's Law	58
3.1.3	The Virial Theorem	59
3.1.4	Gravitational Contraction – Jeans Instability – .	61
3.1.5	Gravitational Instability	63
3.1.6	The Birth of Stars	67
3.1.7	Other Instabilities	68
3.1.8	. Thermal Instability	68
3.1.9	. Rayleigh-Taylor Instability	68
3.1.10	. Kelvin-Helmholtz Instability	68
3.1.11	. Parker Instability (Magnetic Inflation)	68
3.2	The Environment of Star Formation	68
3.2.1	Triggering of Cloud Compression	68
3.2.2	Shock Wave	69
3.2.3	Formation of Molecular Clouds	72
3.2.4	Why spiral arms are bright	73
3.3	HII Regions	77
3.3.1	Ionization sphere – Strömgren sphere –	77
3.3.2	Expanding Ionization Front	79
3.3.3	Shock Compression of Ambient gas	82
3.4	Sequential Star Formation	85
3.4.1	Propagation of Shock Compression by an HII region	85
3.4.2	The Orion region	88
3.4.3	M16 - M17 Region	88
3.4.4	Sgr B2	89
3.5	Supernova Remnants	89

3.5.1	Supernovae (SN) and Supernova remnants (SNR)	89
3.5.2	Classification of SNR	91
3.5.3	The $\Sigma - D$ Relation and the Distribution of SNR	94
3.5.4	Evolution of a SNR	96
3.5.5	Interaction with the ISM	102
3.5.6	Implications of SNRs for the Galaxy Evolution	103
4	GALACTIC STRUCTURE	109
4.1	The Distance to the Galactic Center	109
4.1.1	Using Globular Clusters	109
4.1.2	Using Maser Sources	110
4.1.3	Using X-ray Bursters	111
4.2	The Galactic Rotation	112
4.2.1	Oort's Constants	112
4.2.2	The Solar Rotation Velocity	115
4.2.3	Rotation Curve within the Solar Circle	116
4.2.4	Rotation Curve beyond the Solar Circle	117
4.2.5	The Rotation Curve	119
4.2.6	The Mass of the Galaxy	119
4.3	Distributions of Interstellar Gas in the Galaxy	120
4.3.1	Velocity-to-Space Transformation using a Radial-Velocity Diagram	120
4.3.2	(l, v_r) and (b, v_r) Diagrams	123
4.3.3	'Face-on View' of the Galaxy	123
4.3.4	'Edge-on View' of the Galaxy	125
4.3.5	Radial Distributions of HI and CO and the Molecular Front	125
4.4	Mass Distribution in the Galaxy	133
4.4.1	Radial Mass Distribution for a Flat Rotation Curve	133
4.4.2	Mass Distribution perpendicular to the Disk	135
4.4.3	A Mass Distribution Law of the Whole Galaxy	137

4.4.4	Massive Halo and the Missing Mass Problem . . .	138
4.4.5	Dynamical Masses of Galaxies and of Cluster of Galaxies	141
4.5	Spiral Structure	143
4.5.1	Hubble Types and the Type of the Galaxy . . .	143
4.5.2	Origin of Spiral Arms	143
4.5.3	Density Waves	147
4.5.4	Galactic Shock Waves	152
5	THE GALACTIC CENTER AND ACTIVITY	159
5.1	The Galactic Center in Radio	159
5.1.1	Radio Continuum Emission	159
5.1.2	Flat Radio Spectra	160
5.1.3	Linear Polarization	162
5.1.4	Infrared-to-Radio Ratio	164
5.2	Thermal Emission in the Galactic Center	165
5.2.1	The Thermal Disk and Star Formation	165
5.2.2	Molecular Clouds and Star Forming Regions . .	167
5.3	Galactic Nucleus and its Surrounding Magnetic Structures	175
5.3.1	Sgr A: The Nucleus	175
5.3.2	Thermal Filaments	175
5.3.3	Vertical Magnetic Tubes: Radio Arc and Threads	178
5.4	Ejection: Lobes and Jets	179
5.4.1	The Galactic Center Lobe	179
5.4.2	The 4-kpc Jet	182
5.4.3	Giant Shock Wave in the Halo: the North Polar Spur	183
5.4.4	Extragalactic Radio Bubbles	183
5.5	Origin of Vertical Structures	186
5.5.1	Poloidal fields	186
5.5.2	Explosion	187
5.5.3	The 200-pc Expanding Molecular Cylinder . . .	188
5.5.4	Infalling-Clouds and “Galactic Sprays”	189

6	NONTHERMAL EMISSION AND MAGNETIC FIELDS	191
6.1	Synchrotron Emission and Polarization	191
6.1.1	Synchrotron intensity and magnetic field strength	191
6.1.2	Linearly Polarized Emission	194
6.1.3	Faraday Rotation	195
6.1.4	Determination of Magnetic Field Orientation . .	196
6.2	Magnetic Fields in Disk Galaxies	197
6.2.1	RM in Disk Magnetic Field	197
6.2.2	BSS Magnetic Fields and the Primordial Origin Hypothesis	198
6.2.3	Vertical Fields in spiral Galaxies	198
6.2.4	Magnetic Fields in the Galactic Halo	201
6.3	Evolution of Magnetic Fields in Spiral Galaxies	202
6.3.1	Primordial Origin of Galactic Magnetic Fields . .	202
6.3.2	Loss of Angular Momentum by the Vertical Fields	204
6.4	Nuclear Activities and the Vertical Fields	204
6.4.1	Jets from the Nuclei	204
7	HI and CO IN GALAXIES	205
7.1	HI in Galaxies	206
7.1.1	HI Gas Distributions	206
7.1.2	Rotation and Velocity Fields of HI Gas	206
7.2	CO and Molecular Gas in Galaxies	209
7.2.1	Distribution of Molecular Gas	209
7.2.2	Inner CO Kinematics	213
7.2.3	The CO-to-H ₂ Conversion Factor in Galaxies . .	213
7.3	CO vs HI in Galaxies	218
7.3.1	CO vs HI in the Position-Velocity Diagram for Edge-on Galaxies	218
7.4	Radial Variations of HI and H ₂ Densities	221
7.4.1	Deriving the Density Distribution from a PV di- agram	221

7.5	The Molecular Front	224
7.5.1	Radial Variation of Molecular Fraction	224
7.5.2	Molecular Front	225
7.5.3	Phase Transition between HI and H ₂	226
7.6	Rotation Curves of Galaxies	227
7.6.1	Rotation of Galaxies	227
7.6.2	. Definition of Rotation Curves	228
7.6.3	Rotation Curves for Nearby Galaxies	230
7.6.4	Comparison of Rotation Curves	238
7.6.5	Fitting by Miyamoto-Nagai Potential	239
7.6.6	The Four-Mass Component Model	244
7.7	The HI and CO Tully-Fisher Relation and mm-wave Cosmology	246
7.7.1	HI Tully-Fisher Relation	246
7.7.2	CO instead of HI	247
7.7.3	CO vs HI Line Profiles Correlation	248
7.7.4	The CO Tully-Fisher Relation: mm-wave Cos- mology	252
8	STARBURST	255
8.1	Starburst Galaxy M82	255
8.1.1	What is a starburst galaxy?	256
8.1.2	How a Starburst Galaxy Looks Like?	256
8.1.3	Implication of Starburst	259
8.1.4	Starburst History in M82	261
8.1.5	CO Observations of M82	263
8.2	High-Resolution CO Observations of M82	264
8.2.1	Interferometer Observations	266
8.2.2	NRO 45-m Observations	267
8.2.3	IRAM 30-m Telescope Observations of the CO($J =$ $2 - 1$) Line	269
8.2.4	Comparison with Other Observations	274

8.3	Model of M62 Starburst	277
8.3.1	Ring-and-Outflowing Cylinder Model	277
8.3.2	Numerical Models of the Ring+Cylinder Structure	279
8.3.3	Accretion of Gas and Formation of Dense Nu- clear Disk	285
8.3.4	Trigger of Starburst	286
8.3.5	Unified Scenario of Starburst	288

List of Figures

1.1	Emission from a spiraling electron in a magnetic field . .	13
1.2	Thermal emission and synchrotron emission spectra . .	16
1.3	Emission mechanism of recombination line	16
1.4	Recombination line emission of H atom	18
1.5	Thermal radio continuum emission and the recombina- tion lines	22
1.6	CO molecule: the rotation and emission	24
1.7	Molecular cloud and its eddies, emitting CO line radiation	27
1.8	Emission mechanism of HI 21-cm line radiation	30
1.9	Spectrum of the black-body radiation	34
1.10	Radiation transfer through a cloud	37
2.1	Pressure balance in the ISM	44
2.2	Most of the gaseous objects lying on the line of pressure constant	45
2.3	Molecular cloud mass and intensity	48
2.4	Density distribution of the H ₂ and HI gas	49
2.5	Cloud structure in HI to H ₂ phase transition zone . . .	54
2.6	Molecule fraction in HI to H ₂ phase transition zone . . .	54
3.1	Schmidt's law	60
3.2	Gravitational contraction of a spherical gas cloud	64
3.3	Jeans instability	67
3.4	Star formation in molecular clouds	69

3.5	Shock wave due to supersonic collision of two gases . . .	72
3.6	Gas compression by galactic shock wave	73
3.7	Formation of molecular clouds in a spiral arm	74
3.8	Mass function and luminosity function	76
3.9	Why spiral arms shine	76
3.10	Expansion of ionization sphere around an OB-star cluster	79
3.11	Expansion of a spherical HII region	82
3.12	Expansion of an HII region into a small-density ISM . .	83
3.13	Shock compression of a molecular gas cloud	84
3.14	HII regions and compressed molecular gas at the edge of GMCs: M17 and W3 and GMCs	85
3.15	Ring of HII regions in the Scutum arm	86
3.16	Ring of HII regions in the Scutum arm (continued) . . .	87
3.17	Maps of Sgr B2 HII region	90
3.18	Supernova remnants in optical	92
3.19	Supernova remnants in radio	93
3.20	Surface brightness-Diameter relation for SNRs	95
3.21	Distribution of SNRs projected on the plane of the Galaxy	97
3.22	Distribution of SNRs in the z direction as a function of the galactocentric distance	98
3.23	Spherical shocked shell produced by SN	99
3.24	Time variation of adiabatic shell of spherical shock wave	100
3.25	Evolution of a SNR	102
3.26	Interaction of a SNR shell with ISM	104
3.27	Interaction of a SNR shell with ISM (continued)	105
3.28	Shock wave due to an SN exploded at high z expands into the halo	107
4.1	Period-luminosity relation for RR Lyr stars and distri- bution of globular clusters around the Galaxy	111
4.2	Distance determination from radial velocity dispersion and dispersion of proper motions in a spherical cloud . .	112

4.3	The Sun and a galactic object rotating around the Galactic Center on circular orbits	113
4.4	The terminal velocity simply related to the rotation velocity of the disk within the solar circle	117
4.5	Rotation curve for the outer Galaxy obtained from radial velocities of sources with known distance	118
4.6	The rotation curve of the Galaxy	119
4.7	Radial-velocity diagram of the Galaxy at $b \sim 0$	122
4.8	(l, v_r) diagram for HI gas along the galactic plane(a) . .	124
4.9	(l, v_r) diagram for HI gas along the galactic plane(b) . .	124
4.10	(l, v_r) diagram for CO (molecular) gas along the galactic plane	125
4.11	(b, v_r) diagram for HI (thin contours) and CO (thick contours) gases	126
4.12	Distribution of HI gas density in the galactic plane from 21-cm line emission spectra	127
4.13	The newest HI view of the Galaxy (Nakanishi and Sofue 2003, 2006). [Top] Distribution of projected HI gas column density of the Galaxy. [Bottom] Cross section of the gas disk.	128
4.14	‘Edge-on views’ of the Galaxy in the radio, FIR, optical emission and X-ray sources	129
4.15	Edge-on view of the Galaxy in HI by integrated 21-cm line intensity	129
4.16	Edge-on view of the Galaxy in CO integrated 2.6-mm line intensity (molecular gas), and in FIR at $100 \mu\text{m}$ (dust)	130
4.17	Edge-on view of the Galaxy in CO integrated 2.6-mm line intensity and in FIR at $100 \mu\text{m}$ (continued)	131
4.18	Edge-on view of the Galaxy in radio continuum at 408 MHz	132

4.19	Radial distributions of the HI and H ₂ densities in the Galaxy	134
4.20	Radial variation of the molecular fraction f_{mol} for the Galaxy (dashed line) and edge-on galaxies	134
4.21	Distribution of mass density in the Galaxy	139
4.22	Rotation curves for spiral galaxies	141
4.23	Hubble classification of galaxies	144
4.24	Origin of spiral arms	145
4.25	Gravitational instability in a plane and rotating disk of stars	149
4.26	Rosette orbits of stars in a disk	150
4.27	Many rosette orbits as seen in a rotating frame at ω_p	151
4.28	Galactic shock waves	154
4.29	Non-circular motion in the gas disk	155
4.30	Non-circular motion in the gas disk (continued)	156
5.1	Various features around the Galactic Center	160
5.2	Whole-sky 408 MHz and 10 GHz map of the central 4° region of the Galaxy	161
5.3	Spectral index distribution for the radio Arc and Sgr A region	162
5.4	Radio spectrum distribution at 10 and 2.7 GHz in the central 3° region of the Galaxy	163
5.5	Linearly polarized radio intensity distribution at 10 GHz of the Galactic Center region	165
5.6	Radio continuum (2.7 GHz), IR 60 μm , and radio-to-FIR intensity ratio in the Galactic Center region	166
5.7	Superposition of radio continuum features on the CO line map	168
5.8	CO clouds around Sgr B2	170
5.9	Molecular clouds and continuum sources in the Galactic Center region	170

5.10	^{13}CO line intensity distribution in the galactic center . .	172
5.11	(l, V) diagram of the ^{13}CO line emission of the galactic center	172
5.12	Sgr A* and the three-armed mini spirals	176
5.13	Sgr A with the halo and the radio arc	176
5.14	Thermal filaments as observed with the VLA	177
5.15	Radio Arc	180
5.16	The Galactic Center Lobe	181
5.17	The 4-kpc Galactic Center Jet	182
5.18	The North Polar Spur in radio and X-rays	184
5.19	NGC 3079 at 1420 MHz	185
5.20	The 200-pc expanding ring in a CO line PV diagram . .	190
6.1	Radio continuum emission in galaxies (M51 and NGC 891)	193
6.2	Linear polarization and Faraday rotation	196
6.3	Transverse component of magnetic fields in a spiral galaxy	197
6.4	Variation of RM with Θ	199
6.5	Primordial origin of the BSS and ring fields in galaxies .	200
7.1	HI gas distributions and velocity fields in spiral galaxies	207
7.2	HI gas distributions and velocity fields in spiral galaxies (continued)	208
7.3	Velocity fields for galaxies (Bosma 1980)	210
7.4	Warping of galactic disk and disturbed velocity field . .	211
7.5	HI and CO intensity distributions in the face-on galaxy M51	212
7.6	Conversion factor (C^*) vs oxygen abundance relation for eight disk galaxies	215
7.7	Radial distribution of conversion factor (C^*) for the Milky Way Galaxy, M31, and M51	217
7.8	Composite PV diagrams for CO and HI emissions for edge-on galaxies (NGC 891)	219

7.9	Composite PV diagrams for CO and HI emissions for edge-on galaxies (NGC 3079, NGC 4565, NGC 5907) . . .	220
7.10	Radial density distributions for edge-on galaxies	223
7.11	Radial variations of the molecular fraction in galaxies . . .	225
7.12	Radial variation of the molecular fraction for a galaxy . . .	227
7.13	CO + HI composite position-velocity diagram for NGC 891	229
7.14	Most accurate rotation curves for nearby galaxies derived from CO + HI composite position-velocity	230
7.15	Most accurate rotation curves for nearby galaxies derived from CO + HI composite position-velocity (continued)	232
7.16	Longitude- V_{LSR} ($l - V_{\text{LSR}}$) diagram across Sgr A and Averaged $l - V_{\text{LSR}}$ diagram at $-17' < b < +12'$ for the inner 1°	238
7.17	Inner rotation curve at $-1^\circ < l < +1^\circ$ and total rotation curve of the Galaxy	239
7.18	Rotation curves of galaxies	240
7.19	Rotation curve of our Galaxy as calculated for the Miyamoto-Nagai potential (a)	242
7.20	Galactic rotation curve as calculated for the Miyamoto-Nagai potential (for NGC 6946)	243
7.21	Galactic rotation curve as calculated for the Miyamoto-Nagai potential (for NGC 253)	243
7.22	Galactic rotation curve as calculated for the Miyamoto-Nagai potential (for IC 342)	244
7.23	Total line profiles of the $^{12}\text{CO}(J = 1 - 0)$ line emission and HI for edge-on galaxies	249
7.24	Radial distributions of the H_2 and HI gas densities	249
7.25	CO vs HI line width correlation	250
7.26	CO vs HI TF distances	250

7.27	CO line profile for very distant galaxies	252
8.1	Diagram illustrating how a starburst galaxy looks like	258
8.2	FIR and radio spectrum of M82 compared with the galactic star-forming regions W3 and W51	258
8.3	Interferometer map of intergrated CO intenisty of M82	264
8.4	$^{12}\text{CO}(J = 1 - 0)$ line profiles of the central region of M82	265
8.5	CO intensity map of M82 taken with the NRO 45-m telescope	265
8.6	Distribution of the mean velocity of the CO emission in M82	266
8.7	CO ($J = 2 - 1$) intensity map of M82	270
8.8	Line profiles of ^{12}CO $J = 2 - 1$ and $1 - 0$ transitions toward the outer region and the 200-pc ring of M82	271
8.9	Warm, small-size and low-mass molecular clouds in M82	271
8.10	Comparison of maps of M82 in various emission	272
8.11	Possible evolution of M82 and formation of ring + cylin- der structure	280
8.12	Explosion model of other ring + cylinder (lobe) structure	281
8.13	Vertical outflow model of M82 driven by continuous en- ergy supply at the center	281
8.14	Shock propagation in M82 under the existence of a ver- tical magnetic field	282
8.15	HI gas in the M81-M82 system	290
8.16	Tidal encounter by another galaxy causes a self-sustaining bar	290
8.17	Strong shock of gas rotating across a barred potential results in a rapid accretion of gas toward the center	291
8.18	Schematic diagram summarizing a possible starburst mechanism	292

List of Tables

2.1	ISM and radiations	40
2.2	Population types of ISM and stars	42
2.3	Molecular Clouds and SF regions	50
2.4	HI-to-H ₂ and H ₂ -to-HI transition in the ISM	53
3.1	Jeans wavelength, mass and time	63
3.2	Typical SNRs and classification	94
4.1	Velocity dispersion in the z direction and scale thickness of the disk.	136
4.2	Parameters determining the Miyamoto-Nagai Potential of the Galaxy. See section VII for a more detailed model.	138
5.1	Molecular clouds and continuum sources in the Galactic Center region	170
7.1	Parameters for galaxies and references for PV diagrams and rotation curves	231
8.1	Comparison of the ISM in the central 1 kpc of M82 and the Milky Way	259
8.2	Parameters for M82 CO observations	268
8.3	Summarized masses of the various contents in M82	269
8.4	Observed parameters for the outflowing molecular gas	269

Chapter 1

INTRODUCTION

1.1 Radio Astronomy

1.1.1 Radio window through the Galactic Disk

The Milky Way Galaxy, in which we live, is a giant disk of 20 kpc diameter. The center of the Galaxy lies about 8.5 kpc away from the Sun. The interstellar matter (ISM) contains a significant amount of dust which hides most of the optical objects from us. The absorption in the solar vicinity is about 1 mag/kpc, and the galactic extinction amounts to ~ 30 mag. for the light from the Galactic Center (GC), or the light should be almost $100^{-(1/5)20\sim 30} = 10^{-8\sim -12}$ times the original strength. Namely, the GC cannot be observed in the visible light, even if we used the world largest telescopes. The GC and the regions beyond are the hidden world from our eyes.

However, such a deepest part of the Galaxy can be easily visible if we observe it through the radio window: The radio waves are transparent against the interstellar dust for the much longer wavelengths than the dust size, which avoids the scattering due to dust particles. This situation mimics that we can receive radio and TV waves even it is quite a foggy and rainy day. Therefore, the radio Galaxy appears quite different when we look at it in the optical light. The different

appearance is not only due to the difference in the opacity, but also due to the different locations and matter that emit the radiation at a certain wavelength as well as due to the emission mechanisms: The knowledge about the emission mechanisms can be therefore in turn used to investigate the origin and physics of the emitting regions.

1.1.2 A History of Radio Astronomy

The history of astronomy is since a few thousands of years ago, and the human being has watched the universe in the optical light, because our eyes are sensitive only in the optical light. The new window in wavelength was opened only a half century ago, when C. Jansky detected for the first time the radio signal from the Galactic Center. This young radio engineer was watching noise from the sky, and found a radio source that did not follow the rotation of the earth relative to the Sun, but followed the celestial rotation. The source is well known today as one of the brightest radio source in the sky, Sgr. A, the center of the Galaxy.

Since we opened the radio window toward the universe, we have obtained an almost revolutionary progress in getting knowledge of the radio world mainly thanks to the technical development of radio receivers, telescopes and data reduction powers. Some of the biggest findings in astronomy in the decades (particularly in 1960' and 1970') are due to radio astronomy; the discovery of the HI 21-cm line emission from the interstellar neutral hydrogen and the study of the galactic structure (1950-1970'), the discovery of the cosmic background blackbody radiation (1960'), the discovery of a pulsar and neutron stars (1960'), the discovery rush of interstellar molecules (1960-1970'), and the high-resolution interferometric techniques to reveal the cosmic rad

Today, radio observations give us huge amount of data both in imaging as well as in spectroscopy, that require highly advanced data processing. After the processing, astronomers obtain high-quality images

which can be “visible” and are stimulated by these images to get the knowledge about “unseen” objects.

1.2 The Radio Emission

1.2.1 Plane waves

The basic equations describing electro-magnetic waves in the vacuum are written as the following:

$$\operatorname{rot} E = -c \frac{dH}{dt}, \quad (1.1)$$

$$\operatorname{div} H = 0, \quad (1.2)$$

$$\operatorname{rot} H = \frac{1}{c} \frac{dE}{dt}, \quad (1.3)$$

$$\operatorname{div} E = 0, \quad (1.4)$$

where E , H , and c are the electric and magnetic vectors and the light speed, respectively. Introducing the vector potential A as defined by

$$H = \operatorname{rot} A, \quad (1.5)$$

the Maxwell’s equations can be reduced to the wave equation

$$\Delta A - \frac{\partial^2 A}{c^2 \partial t^2} = 0. \quad (1.6)$$

The electric vector can be related to the magnetic vector as

$$E = H \times n, \quad (1.7)$$

and the vectors can be related to the vector potential as

$$H = \frac{1}{c}A \times n, \quad (1.8)$$

and

$$E = \frac{1}{c}(A \times n) \times n. \quad (1.9)$$

A special solution of the wave equation is given by

$$A = ae^{i(k.r-ft)} \quad (1.10)$$

which represent a wave of wavenumber k and frequency f . For a wave in the vacuum we have $k/f = c$, and E and H can be written as

$$E_x = E_{x0}\cos(ft - k.r + g), \quad (1.11)$$

and

$$E_y = E_{y0}\sin(ft - k.r + g). \quad (1.12)$$

A wave with $E_{x0} = E_{y0}$ is called to have a circular polarization; a wave with $E_{x0} \neq E_{y0}$ is called to have an elliptical polarization; and a wave with $E_{x0} = 0$ or $E_{y0} = 0$ is called to have linear polarization.

The energy carried by an electro-magnetic wave whose speed is c is expressed by a Poynting vector

$$S = \frac{c}{4\pi}E \times H = \frac{c}{4\pi}H^2 \times n. \quad (1.13)$$

The Poynting vector can be used to calculate the energy flow per small steradian $d\Omega$ at a distance of r from the source of radiation, which is called the flux density;

$$dI = \frac{c}{4\pi}H^2r^2d\Omega. \quad (1.14)$$

1.2.2 Acceleration of a charged particle and radiation

Consider a charged particle, for example an electron. If the particle is at rest, the electric field surround this particle does not change. If the particle is moving straightly at a constant speed, we can translate the coordinate so that the particle appears to be at rest, and the electric field can be also reduced to a stationary one. Suppose that the particle is moving with acceleration: The simplest case may be a particle oscillating at a frequency f . Then the electric field oscillates at the same frequency, and the oscillation is transferred through the vacuum at a speed c . Since the amplitude of the motion of the particle is maximum when the oscillation is looked at perpendicularly to the orbit, the electromagnetic waves radiated attains the maximum toward the perpendicular direction. On the other hand the motion appears be at rest when looked at from the line of the oscillation, and hence the radiation along the line of oscillation becomes minimum, as the wave is a transverse wave. This kind of radiation of electromagnetic waves is called dipole emission. This situation can be easily understandable if one imagines a straight antenna along which electrons are oscillating: the radiation strength is maximum in the direction perpendicular to the antenna, while minimum in the direction along it. Suppose an electron whose charge is e and the position vector r , the dipole moment is defined by $d = er$. The vector potential is then written as

$$A = \frac{er'}{cR} = \frac{d'}{cR}, \quad (1.15)$$

where R is the distance of a point concerned from the coordinate origin. If the point is far enough from the origin, the waves can be approximated by plane waves. Then E and H of the plane wave is expressed as

$$H = \frac{1}{c^2 R} d'' \times n, \quad (1.16)$$

and

$$E = \frac{1}{c^2 R} (d'' \times n) \times n. \quad (1.17)$$

Let the angle between the wave direction n and the direction of the oscillation (the direction of the vector d) be θ , then the flux density of the radiation from this particle is written as

$$dI = \frac{(d \times n)^2}{4\pi c^3} d\Omega = \frac{\dot{d}^2}{4\pi c^3} \sin^2 \theta^2 d\Omega. \quad (1.18)$$

The radiation attains the maximum toward the direction perpendicular to d or to the antenna, while it attains the minimum along the direction of oscillation. By integrating the intensity over the steradian, we can obtain the total intensity I of the radiation from the particle as

$$I = \int dI = \frac{2\dot{d}^2}{3c^3} = \frac{2e^2 \dot{r}^2}{3c^3}. \quad (1.19)$$

For an oscillation with a frequency f we have $r = r_0 \cos(ft - ft_0)$ or $\dot{d} = \dot{d}_0 \cos(ft - ft_0)$, yielding the total intensity as

$$I = \frac{2\dot{d}_0^2 f^4}{3c^3}. \quad (1.20)$$

The above expression is for a single electron under a simple oscillation. In the nature, however, it is rare that electrons are moving back and forth in a perfect alignment, but are more or less randomly moving. The acceleration of electrons are due to the orbital motion within an atom, due to collisions with ions in a plasma, or due to the curved motion during the Lorenz interaction with the interstellar magnetic field.

1.2.3 Radiation from an electron in a magnetic field

The simplest acceleration motion of an electron in the nature would be a circular motion. For instance, an electron moving through the interstellar space suffers from Lorentz force by the interstellar magnetic field, resulting in a circular (helical) rotation. The Lorentz force acting on an electron moving at a velocity v in a magnetic field of strength B is given by

$$F = eBv/c. \quad (1.21)$$

This force is in a balance with the centrifugal force

$$F = mr\omega^2, \quad (1.22)$$

where m and ω are the mass of the electron and the angular frequency, respectively. Since $v = r\omega$ we have

$$\omega = \frac{eB}{mc}. \quad (1.23)$$

The frequency ω is called the gyro frequency, and the radius of the circular orbit r the Larmor radius:

$$r = \frac{cmv}{eB} = \frac{v}{\omega}. \quad (1.24)$$

The dipole moment of an electron circularly rotating in a uniform magnetic field can be written as

$$d = er_0 \cos \omega t \quad (1.25)$$

and the intensity of the electromagnetic wave emitted by this electron can be expressed as

$$dI = \frac{e^2 r_0^2 \omega^4}{4\pi c^3} \sin^2 \theta d\Omega. \quad (1.26)$$

The total intensity is obtained by integrating the above equation by Ω :

$$I = \frac{2e^2 r_0^2 \omega^4}{3c^3} = \frac{2e^4 B^2 (v/c)^2}{3m^2 c^3}. \quad (1.27)$$

By using the kinetic energy $E = \frac{1}{2}mv^2$ we obtain

$$I = \frac{4e^4 B^2}{3m^3 c^5} E = c_1 E, \quad (1.28)$$

where $c_1 = 4e^4 B^2 / 3m^3 c^5$ is a constant.

Due to the radiation the kinetic energy is lost at a rate of

$$dE/dt = -I = -c_1 E. \quad (1.29)$$

Therefore the energy changes as a function of time as

$$E = E_0 \exp(-c_1 t). \quad (1.30)$$

Here E_0 is the initial kinetic energy of the electron. The decay time of the energy is given by

$$t = 1/c_1 = \frac{3m^3 c^5}{4e^4 B^2}. \quad (1.31)$$

The above expressions are valid for the case in which the velocity of the electron is small enough compared to the light speed ($v \ll c$).

If the velocity is close to the light speed, or the electron is relativistic, we obtain

$$I = \frac{2e^4 B^2 \gamma^2}{3m^2 c^3} = \frac{2e^4 B^2}{3m^4 c^7} E^2 = c_2 E^2, \quad (1.32)$$

with $\gamma = E/mc^2$. The energy changes as

$$dE/dt = -c_2 E^2. \quad (1.33)$$

This gives a solution

$$E = \frac{1}{c_1[t + (1/c_2)E_0]}, \quad (1.34)$$

and the decay time of an electron as

$$t = \frac{1}{c_2 E_0} = \frac{3m^4 c^7}{2e^4 B^2 E_0}. \quad (1.35)$$

The radiation expressed by equations (1.26)-(1.31) for a non-relativistic case is called the cyclotron radiation. The gradation expressed by the relativistic case, equation (1.32)-(1.35), is called the synchrotron radiation. The emission radiated by high-energy (cosmic-ray) electrons in the galactic disk interacting with the interstellar magnetic field is the synchrotron radiation.

1.3 Thermal Emission

1.3.1 Thermal Bremsstrahlung

We have shown that an electron which is oscillating at a frequency ω emits radiation of intensity

$$I = \frac{2d^2\omega^4}{3c^3}. \quad (1.36)$$

The electron emits the radiation at the frequency $\omega = 2\pi\nu$ with ν the frequency of radiation. The emissivity by the particle between the frequency ν and $\nu + d\nu$ is given by

$$dI_\nu = Id\nu = \frac{2d^2 16\pi^4 \nu^4}{3c^3} d\nu = \frac{32\pi^4 e^2 r_\nu^2 \nu^4}{3c^3} d\nu. \quad (1.37)$$

Suppose that the electron is encountering with an ion at an impact parameter ρ . Then the total radiation by an electron during the encounter can be expressed as

$$d\chi_\nu = \int dI_\nu 2\pi\rho d\rho = \text{const} \frac{e^4}{v^2 c^3 m^2} \ln \frac{2mv^3}{\gamma\omega e} d\omega, \quad (1.38)$$

where $\gamma = 1.78$.

In a plasma of temperature T , the free electrons have the Maxwell distribution in the velocity space;

$$f(v)dv = 4\pi \left(\frac{m}{2\pi kT}\right)^{3/2} \exp\left(-\frac{mv^2}{2kT}\right) v^2 dv, \quad (1.39)$$

where k is the Boltzmann constant. The radiation from the plasma can be calculated by integrating the emissivity of individual electrons in the velocity;

$$\begin{aligned} \varepsilon_\nu d\nu &= \int n_i n_e v d\chi_\nu f(v) dv \\ &= \text{const} \frac{e^6 n_i n_e}{\sqrt{kT} m^{3/2} c^3} \ln \frac{(2kt)^{3/2}}{\pi \gamma^{3/2} m^{1/2} \nu} d\nu \\ &= \frac{16e^6 n_e^2}{3\sqrt{2\pi} \sqrt{kT} m^{3/2} c^3} \ln \frac{0.21(kT)^{3/2}}{e^2 \sqrt{m\nu}} \\ &= 3 \times 10^{-39} \frac{n_e^2}{\sqrt{T}} \left(17.7 + \ln \frac{T^{3/2}}{\nu}\right). \end{aligned} \quad (1.40)$$

It is shown that in the radio frequencies, $h\nu \ll kT$, we have

$$\varepsilon_\nu \propto \nu^{-0.1} \quad (1.41)$$

However, if the emitting region is opaque, or the optical depth is large enough, the emission becomes close to a black-body radiation obeying the Wean's law;

$$\varepsilon_\nu \propto \nu^2. \quad (1.42)$$

1.3.2 Thermal emission and absorption coefficient

The emissivity can be related to the Einstein coefficient as

$$\varepsilon_\nu d\nu = \frac{N_2}{4\pi} A_{21} h\nu. \quad (1.43)$$

The absorption coefficient can be related to the Einstein B coefficient as

$$\kappa_\nu d\nu = \frac{1}{4\pi} (N_1 B_{12} - N_2 B_{21}) h\nu. \quad (1.44)$$

In thermal equilibrium the A and B coefficients can be related to each other as

$$A_{21} = -\frac{2h\nu^3}{c^2} B_{21}. \quad (1.45)$$

We have then

$$\frac{\kappa_\nu}{\varepsilon_\nu} = \frac{\frac{N_2}{4\pi} B_{21} (\frac{h\nu}{kT}) h\nu}{\frac{N_2}{4\pi} A_{21} h\nu} = \frac{B_{21}}{A_{21}} \frac{h\nu}{kT} = \frac{c^2}{2h\nu^3} \frac{h\nu}{kT} = \frac{c^2}{2\nu^2 kT}. \quad (1.46)$$

This yields the absorption coefficient

$$\kappa_\nu = \frac{c^2}{2\nu^2 kT} \varepsilon_\nu = 9.77 \times 10^{-3} \frac{n_e^2}{T^{3/2} 2\nu^2} (17.7 + \ln \frac{T^{3/2}}{\nu}) \text{ [cm}^{-1}\text{]} \quad (1.47)$$

with T being measured in [K], n_e in [cm^{-3}], and ν in [Hz]. The optical depth is then defined by

$$\tau_\nu = \int \kappa_\nu dx \sim L \kappa_\nu \propto L n_e^2. \quad (1.48)$$

Or more practically,

$$\tau_\nu \simeq 0.082 T^{-1.35} \nu^{-2.1} EM, \quad (1.49)$$

where

$$EM = \int n_e^2 dx \sim Ln_e^2 \quad (1.50)$$

in [pc cm^{-6}] is the emission measure of the plasma, T and ν are measured in K and GHz, respectively, and L is the geometrical depth of the emission region.

1.4 Synchrotron Radiation - Non-thermal Radiation

1.4.1 Emissivity and spectrum

We know that a single relativistic electron of energy E emits at

$$I_E = \frac{2e^4 B^2 E^2}{m^2 c^7} = c_3 B^2 E^2. \quad (1.51)$$

The energy distribution function of cosmic-ray electrons can be expressed as

$$f(E)dE = N(E)dE \propto E^{-\beta}dE, \quad (1.52)$$

or

$$N(E)dE = N_0 \left(\frac{E}{E_0}\right)^{-\beta}. \quad (1.53)$$

For an optically thin case, the emissivity can be expressed as

$$dI_E = I_E f(E)dE = c_3 B^2 E^{2-\beta} dE. \quad (1.54)$$

Since the frequency of the emission is related to the energy through

$$\nu = \frac{eB}{mc} \gamma^2 = \frac{ecBE^2}{(mc^2)^3} \propto BE^2 \quad (1.55)$$

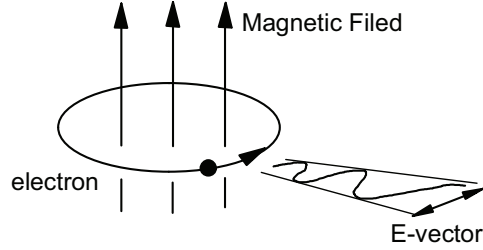


Figure 1.1: Emission from an electron spiraling around magnetic lines of force.

and

$$d\nu \propto BEdE, \quad (1.56)$$

we obtain the volume emissivity of the synchrotron radiation as

$$\varepsilon_\nu d\nu = \text{const} \nu^{\frac{2-\beta}{2}} \nu^{-1/2} d\nu = c_4 \nu^{\frac{1-\beta}{2}} d\nu. \quad (1.57)$$

It is known that observed cosmic-ray electrons have the power law spectrum with $\beta \sim 2 - 3$, which yields a spectral index of the synchrotron emission as $\varepsilon_\nu \propto \nu^{-0.5 \sim -1}$.

On the other hand if the emission region is opaque (with sufficiently large optical depth), the radiation can be expressed by a black-body radiation with the temperature related to energy as $kT = E$, and the emissivity is expressed as

$$\varepsilon_\nu d\nu = E\nu^2 d\nu \propto \nu^{5/2} d\nu. \quad (1.58)$$

1.4.2 Energy equipartition

If we adopt a simple assumption that the energy density (pressure) of the cosmic ray electrons is in a balance with the magnetic energy density (pressure), the synchrotron emissivity can be related to the magnetic field strength, averaged number density of high-energy electrons, and mean energy of the electrons. Hereby we assume that, under normal interstellar condition, the synchrotron emission source is optically thin. The cosmic-ray electron energy density is given by

$$u_{\text{CR}} = \int N(E)E dE \sim \langle NE \rangle, \quad (1.59)$$

and the magnetic energy density by

$$u_{\text{B}} = \frac{B^2}{8\pi}. \quad (1.60)$$

The condition of the equi-partition of the energy densities is expressed by

$$u_{\text{CR}} \sim u_{\text{B}}, \quad (1.61)$$

which yields

$$\frac{B^2}{8\pi} \sim \langle N \rangle \langle E \rangle \sim NE. \quad (1.62)$$

Let us also remind of the expressions

$$\nu = \frac{ec}{(mc^2)^3} BE^2 \quad (1.63)$$

and

$$\varepsilon_{\nu} \sim \frac{e^4}{m^2 c^7} B^2 E^2 N \quad (1.64)$$

or the volume emissivity defined by

$$\varepsilon = L/V \sim \frac{e^4}{m^2 c^7} B^2 E^2 N. \quad (1.65)$$

Here L in $\text{erg s}^{-1} \text{cm}^{-3}$ and V are the total luminosity and volume of the source, respectively.

Equations (1.62)–(1.65) can be then used to obtain the following relations:

$$B \sim 3.29 \times 10^2 \nu_{\text{GHz}}^{-1/7} \varepsilon^{2/7} [\text{Gauss}], \quad (1.66)$$

$$\langle N \rangle \sim 4.78 \times 10^9 \nu_{\text{GHz}}^{-6/7} \varepsilon^{5/7} [\text{cm}^{-3}], \quad (1.67)$$

and

$$\langle E \rangle \sim 9.02 \times 10^{-7} \nu_{\text{GHz}}^{4/7} \varepsilon^{-1/7} [\text{erg}], \quad (1.68)$$

where $\varepsilon = L/v$ is the emissivity measured in $[\text{erg s}^{-1} \text{cm}^{-3}]$ and ν_{GHz} is the frequency measured in $[\text{GHz}]$. The above equations can be used to obtain approximate quantities for B , $\langle N \rangle$ and $\langle E \rangle$ of cosmic ray electrons using the observed quantity $\varepsilon = L/V$. The emissivity may be also roughly calculated by dividing the observed intensity by an assumed depth of the emitting region; $\varepsilon \sim \int \varepsilon_\nu d\nu \sim \nu I/L$.

1.5 Recombination Lines

The most frequently observed line spectra in astrophysics are the recombination line emission, the molecular line emission, and the 21-cm neutral hydrogen (HI) line emission.

1.5.1 Frequency

The interstellar hydrogen gas is ionized by UV photons from massive stars of O and B types. Such ionized gas surrounding OB stars is

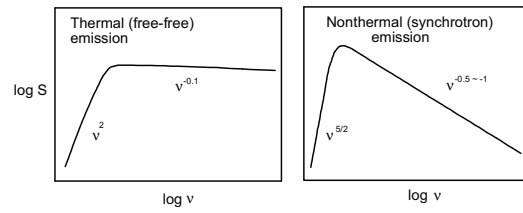


Figure 1.2: Schematic spectra of the thermal emission from ionized gas (left) and the synchrotron emission (right).

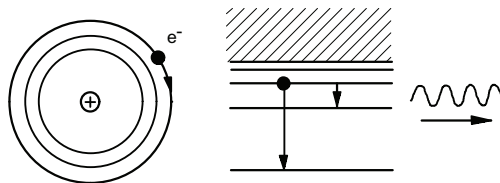


Figure 1.3: Recombination line by transition of an upper-level electron to a lower-level of hydrogen atom.

called the HII region, which comprises ionized hydrogen gas of temperature 7,000 – 10,000 K. Free electrons emit thermal Bremsstrahlung by free-free interaction with ions, and are recombined with the ions by emitting free-bound emission. The recombined hydrogen is often at high transition state, and emits bound-bound emission during its transition to the lower state. The emission is called the recombination line emission.

The energy difference between the upper and lower transition levels for a hydrogen atom is expressed by

$$h\nu = E_0\left(\frac{1}{n_1^2} - \frac{1}{n_2^2}\right) \simeq 2E_0\frac{\Delta n}{n^3}, \quad (1.69)$$

where $E_0 = h\nu_0 = hRcZ^2$ with R , Z and n being the Rydberg constant, electric charge number, and the principal quantum number, respectively. For the hydrogen $Z = 1$ and $E_0 = 13.6$ eV ($\nu_0 = 912$ Å), $n_i \simeq n$ is the quantum number of the i -th state, and $\Delta n (\ll n)$ is the level difference between the two states. We therefore obtain the frequency by

$$\nu \simeq 2RcZ^2\frac{\Delta n}{n^3}. \quad (1.70)$$

For hydrogen, $Rc = 3.288051 \times 10^{15}$ Hz. The hydrogen recombination line for $\Delta n = 1$ is called the α lines, and denoted as $Hn\alpha$ line. For small n the line is observed in the optical wave lengths, while for larger n the lines are observed at the radio frequencies. In the microwave range we often observe $Hn\alpha$ line for n around 100; for example the $H110\alpha$ line has the frequency of 4874.174 MHz.

1.5.2 Line width

Since line-emitting particles in a gas cloud of temperature T_k are moving due to the thermal motion, the distribution function of the particles

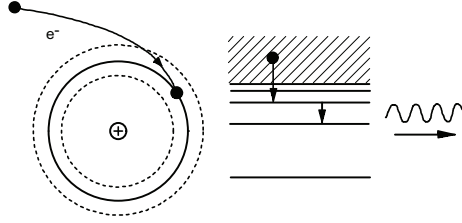


Figure 1.4: Recombination line emission of H atom.

is expressed as

$$dN(v) = N \sqrt{\frac{M}{2\pi k T_k}} \exp\left(\frac{-mv^2}{2kT_k}\right) dv. \quad (1.71)$$

The Doppler effect of a line emission at ν_0 by the motion of a particle at velocity v is expressed as

$$\nu = \nu_0 \left(1 - \frac{v}{c}\right), \quad (1.72)$$

and the thermal velocity can be related to the frequency as

$$dv = -c \frac{d\nu}{\nu}. \quad (1.73)$$

The intensity of the line emission at ν is proportional to the number of particles at the velocity corresponding to this frequency;

$$dI(\nu) = I f(\nu) d\nu = I \sqrt{\frac{4\ln 2}{\pi}} \frac{1}{\Delta\nu} \exp\left\{-4\ln 2 \left(\frac{\nu - \nu_0}{\Delta\nu}\right)^2\right\} d\nu, \quad (1.74)$$

where $f(\nu)$ is the line shape function, and $\Delta\nu$ is the half power width of the line;

$$\Delta\nu = \nu_0 \sqrt{4 \ln 2 \frac{2kT_k}{mc^2}}. \quad (1.75)$$

At $\nu = \nu_0$ we have $f(\nu_0) = 0.94 \frac{1}{\Delta\nu} \simeq \frac{1}{\Delta\nu}$. For a hydrogen cloud, observed line width of the line is expressed as

$$\Delta\nu \simeq 7.1 \times 10^{-7} \nu_0 \sqrt{T_k[\text{K}]} \text{ [Hz]}. \quad (1.76)$$

1.5.3 Line intensity

Using the Einstein's coefficients, we can write the emissivity and absorption coefficient of the line emission due to the transition from/to n_1 to/from n_2 generally as

$$\varepsilon_\nu d\nu = \frac{N_2}{4\pi} A_{21} h\nu \quad (1.77)$$

$$\kappa_\nu d\nu = \frac{1}{4\pi} (N_1 B_{12} - N_2 B_{21}) h\nu. \quad (1.78)$$

For a thermal equilibrium, we have

$$N_1 B_{12} = \exp\left\{\frac{h\nu}{kT}\right\} N_2 B_{21}, \quad A_{21} = \frac{2h\nu^3}{c^2} B_{21}. \quad (1.79)$$

For the recombination line, the absorption coefficient can be written as

$$\kappa_\nu = \frac{h\nu N_{n_1}}{4\pi \Delta\nu} \left\{1 - \exp\left(\frac{-h\nu}{kT_e}\right)\right\} B_{n_1 n_2}. \quad (1.80)$$

We make use of the formula to give the density of partially-ionized gas at n_1 -th level (Saha's formula)

$$N_{n_1} = \frac{N_e N_i h^3}{(2\pi m_e k T_e)^{3/2}} n_1^2 \exp\left\{\frac{-hcRZ^2}{n_1^2 k T_e}\right\}, \quad (1.81)$$

or

$$N_{n_1} \simeq 4.1 \times 10^{-16} n_1^2 \frac{N_e N_i}{T_e^{3/2}}. \quad (1.82)$$

Then we obtain

$$\kappa_\nu = \frac{\pi h e^2 N_{n_1} \nu}{m c k T_e \Delta \nu} f_{n_1 n_2} = 1.04 \times 10^{-27} \frac{R c Z^2 \Delta n N_e N_i}{\Delta \nu T_e^{3/2}} \frac{f_{n_1 n_2}}{n_1}, \quad (1.83)$$

where

$$f_{n_1 n_2} = B_{n_1 n_2} \left(\frac{m c h \nu}{4 \pi^2 e^2} \right) \quad (1.84)$$

is called the oscillator strength. For $\Delta n = 1$ (H α line) the oscillator strength has the value

$$\frac{f_{n_1 n_2}}{n_1} = 0.194, \quad (1.85)$$

and the above expression reduces to

$$\kappa_\nu = 6.7 \times 10^{-13} \frac{N_e N_i}{\Delta \nu T_e^{3/2}}, \quad (1.86)$$

and the optical depth is given by

$$\tau_{\text{H}\alpha} = \int_0^L \kappa_\nu dl = 2.0 \times 10^6 \int_0^L \frac{N_e N_i dx}{\Delta \nu T_e^{3/2}} \simeq 2.0 \times 10^6 \frac{EM}{\Delta \nu T_e^{3/2}}. \quad (1.87)$$

Since the electron temperature T_e of HII regions is about 10^4 K, the optical depth is expressed as

$$\tau_{\text{H}\alpha} \simeq 2.0 \times 10^{-4} \frac{EM}{\Delta \nu}. \quad (1.88)$$

Here, $EM = \int_0^L N_e N_i dl \sim N_e N_i L$ is the emission measure.

1.5.4 Line to continuum intensity ratio and temperature determination

The brightness temperature T_B of a radio emitting region is defined by the relation to the intensity by the Planck's law

$$I_\nu = \frac{2h\nu^3}{c^2} \frac{1}{\exp(h\nu/kT_B) - 1} \simeq \frac{2kT\nu^2}{c^2} = \frac{2kT_B}{\lambda^2} \quad (1.89)$$

for the Rayleigh-Jeans approximation when $h\nu \ll kT$. If the optical depth is small enough, the brightness temperature is related to the electron temperature of the gas through

$$T_B = T_e(1 - e^{-\tau}). \quad (1.90)$$

The brightness temperature of the recombination line emission is given by

$$T_{B: \text{Line}} \simeq T_e(1 - e^{-\tau_{H\alpha}}) \simeq T_e \tau_{H\alpha} \simeq 2 \times 10^6 \frac{EM}{\Delta\nu T_e^{3/2}}. \quad (1.91)$$

Recalling that the line width $\Delta\nu$ is related to the frequency and temperature by

$$\Delta\nu = 7.1 \times 10^{-7} \nu \sqrt{T(\text{K})} \quad (1.92)$$

we obtain

$$T_{B: \text{Line}} \simeq 3 \times 10^3 \frac{EM(\text{cm}^{-6}\text{pc})}{\nu_{\text{GHz}} T_e(\text{K})^2}. \quad (1.93)$$

On the other hand, the brightness temperature due to the free-free transition emission (thermal Bremsstrahlung) can be written as

$$T_{B: \text{Conti}} \sim T_e \tau_\nu \simeq 0.03 EM T_e^{-1/2} \nu_{\text{GHz}}^{-2.1}. \quad (1.94)$$

Here, EM is in unit of $\text{cm}^{-6} \text{pc}$ and T in K. Hence, the intensity

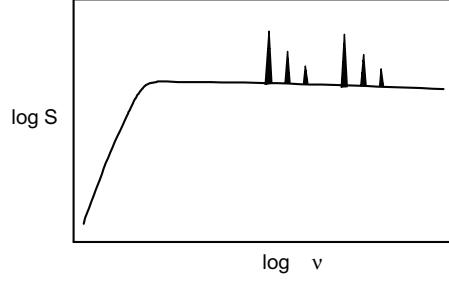


Figure 1.5: Thermal radio continuum emission and the recombination lines.

ratio of the recombination line to the continuum can be obtained by

$$\frac{T_{\text{B:Line}}}{T_{\text{B:Conti}}} \simeq 1 \times 10^5 \nu_{\text{GHz}}^{1.1} T_e^{-3/2}. \quad (1.95)$$

This equation shows that the electron temperature of an HII region can be obtained simply from the line-to-continuum intensity ratio:

$$T_e(\text{K}) \simeq 2.1 \times 10^3 \nu_{\text{GHz}}^{0.73} \left(\frac{T_{\text{B:Conti}}}{T_{\text{B:Line}}} \right)^{2/3}. \quad (1.96)$$

1.6 Molecular Lines

Interstellar molecules comprising different kind of elements, such as CO, are asymmetric with respect to their rotation axes. Molecules are asymmetrically charged due to the friction during collisions with other molecules such as H₂. Such a molecule mimics a rotating charged particle which has an electric dipole moment, and emits radiation in mm-wave range. The dipole moment for a CO molecule is $\mu = 0.112$ Debye = 1.12×10^{-19} (esu).

1.6.1 Frequency

The most abundant molecule in the interstellar space is the carbon monoxide CO. A rotating molecule of CO, for example, emits dipole emission at its rotation frequency given by

$$\nu \sim \frac{v_r}{2\pi a}, \quad (1.97)$$

where v and a are the rotation velocity of the molecule and its length (interval of C and O atoms). Since the rotation is excited by collisions with H_2 atoms in thermal motion, the rotation velocity can be approximately related to the thermal velocity v of H_2 atoms as

$$m_{\text{CO}}v_r \sim m_{\text{H}_2}v, \quad (1.98)$$

where m_i are the masses of CO and H_2 molecules. We have therefore

$$v_r \sim v \frac{m_{\text{H}_2}}{m_{\text{CO}}} \sim 0.1v. \quad (1.99)$$

The thermal velocity v in a typical molecular cloud, approximately corresponding to the first-excited state of the CO molecule, is about 1 km s^{-1} . The frequency of the dipole emission from this CO molecule with $a \sim 1.5 \text{ \AA}$ is then estimated to be

$$\nu \sim \frac{0.1 \text{ km s}^{-1}}{2\pi a} \sim 1 \times 10^2 \text{ GHz}. \quad (1.100)$$

The energy level for a rotation quantum number J of a CO molecule is given by

$$E_{\text{rot}} = hBJ(J+1), \quad (1.101)$$

where h is the Planck constant, and B is related to the moment of inertia I as

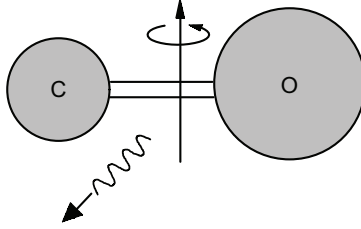


Figure 1.6: CO molecule: the rotation and emission.

$$B = \frac{h}{8\pi I}. \quad (1.102)$$

The frequency of a photon emitted by a transition from $J + 1$ to J -th rotational state is given by

$$h\nu = \Delta E_{\text{rot}} = 2(J + 1)hB. \quad (1.103)$$

The frequency of the rotational transition from $J = 1$ to $J = 0$ of a CO molecule is

$$\nu_{J=1-0} = 115.271204 \text{ GHz}, \quad (1.104)$$

or $\lambda = 2.6 \text{ mm}$.

1.6.2 Intensity

Recalling that the emission and absorption coefficients can be written by the Einstein coefficients as

$$\varepsilon_\nu d\nu = \frac{N_2}{4\pi} A_{21} h\nu, \quad (1.105)$$

$$\kappa_\nu d\nu = \frac{1}{4\pi} (N_1 B_{12} - N_2 B_{21}) h\nu, \quad (1.106)$$

we obtain the absorption coefficient for the molecular line radiation as

$$\kappa_\nu = \frac{c^2}{8\pi\nu^2} \left(\frac{g_{J+1}}{g_J} N_J - N_{J+1} \right) A_{J+1} \frac{1}{\Delta\nu} = \frac{c^2}{8\pi\nu^2} \{1 - \exp(\frac{-h\nu}{kT_{J+1,J}})\} \frac{g_{J+1}}{g_J} A_{J+1} \frac{1}{\Delta\nu}. \quad (1.107)$$

Here, g are the degenerated level number, $g_J = 2J + 1$, and $g_{J+1} = 2J + 3$, and

$$\frac{N_{J+1}}{N_J} = \frac{g_{J+1}}{g_J} \exp\left\{\frac{-h\nu}{kT_e J + 1, J}\right\}. \quad (1.108)$$

The A coefficient can be related to the dipole moment as

$$A_{J+1,J} = \frac{64\pi^4}{3hc^3} |\mu_{J+1,J}|^2 = \frac{64\pi^4}{3hc^3} \mu^2 \frac{J+1}{2J+3}. \quad (1.109)$$

Here, let us recall that the intensity of dipole emission from an electric dipole rotating at frequency ν is given by $I_\nu = 2\mu^2(2\pi\nu)^4/(3c^3)$.

If the molecule is in thermal equilibrium of temperature T , we have $T_{J+1,J} = T$, and the Boltzmann distribution of N_J can be expressed by as

$$N_J = \frac{ng_J}{Q} \exp\left\{\frac{-hBJ(J+1)}{kT}\right\}, \quad (1.110)$$

where n is the number density of the molecule, and Q is the partition function;

$$Q = \sum_{J=0}^{\infty} (2J+1) \exp\left\{\frac{-J(J+1)hB}{kT}\right\} \simeq \int_0^{\infty} (2x+1) \exp\left\{-x(J+1)\frac{hB}{kT}\right\} dx = \frac{kT}{hB}. \quad (1.111)$$

When J is small enough, we obtain finally

$$\kappa_\nu \simeq \frac{4\pi^3 h}{3c(kT)^2} \frac{2J+3}{2J+1} \frac{\nu^3 \mu^2 n}{\Delta\nu} \simeq \frac{4\pi^3 h}{3c(kT)^2} \frac{\nu^3 \mu^2 N}{\Delta\nu}. \quad (1.112)$$

1.6.3 Two mass estimated from the CO intensity

The brightness temperature is related to the temperature by $T_B = \tau T \simeq \kappa_\nu T L$ when $\tau \ll 1$, and is given by

$$T_B \simeq 9.3 \times 10^{-9} \frac{n_{\text{CO}} L}{\Delta \nu T}. \quad (1.113)$$

Using the Doppler relation we have

$$N_{\text{CO}} = \int n_{\text{CO}} dx \simeq n_{\text{CO}} L \quad (1.114)$$

$$\simeq 4.1 \times 10^{13} T \int T_B dv \simeq 4.1 \times 10^{13} T T_B \Delta v = 4.1 \times 10^{13} T I_{\text{CO}}. \quad (1.115)$$

Here, N_{CO} is the column density of CO molecules in $[\text{cm}^{-2}]$, and I_{CO} is called the CO line intensity. The temperature and velocity are measured in K and km s^{-1} , respectively. If the cloud observed is optically thin, the column density of H_2 molecules can be estimated by assuming the abundance of CO molecule, which is approximately $[\text{CO}]/[\text{H}_2] \sim 10^{-5}$ and yields

$$N_{\text{H}_2} \sim 4 \times 10^{18} I_{\text{CO}}. \quad (1.116)$$

However, usual interstellar molecular clouds are opaque against the CO line. An interstellar cloud comprises numerous turbulent eddies, each of which is also optically thick for CO line. Since the eddies have different velocities and therefore different absorbing frequencies, the cloud can be seen through because of its velocity (frequency) gradient along the line of sight. This assumption is called the large-velocity-gradient (LVG) condition. The mass of a molecular cloud can be estimated by the velocity gradient (velocity width) and its radius by the Virial relation. Observations have shown that the Virial mass (total mass) of a molecular cloud is proportional to its CO luminosity (integrated intensity over the extent). We have an empirical relation which

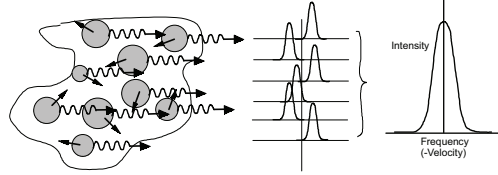


Figure 1.7: Molecular cloud and its eddies, emitting CO line radiation.

relates the CO intensity to the molecular hydrogen column density as

$$N_{\text{H}_2} \sim 2.8 \times 10^{20} I_{\text{CO}}, \quad (1.117)$$

where N_{H_2} and I_{CO} are measured in H_2 [cm^{-2}] and K km s^{-1} , respectively.

1.6.4 Other molecules

Numerous kind of interstellar molecules have been observed so far, such as ^{12}RCO (CO), ^{13}CO , H_2CO , HCN, HC_{2n+1}N ($n = 0, 1, 2, \dots, 5$), CS at various different transition states. They can be used not only to obtain the chemistry of the interstellar matter but also to obtain information about the kinematics (dynamics) and density distribution of a cloud. Each species of the molecules is representative of a certain interstellar condition, and has its characteristic distribution and kinematics in a cloud: The CO gas is distributed widely in any molecular clouds of various sizes, from core to envelope, and is most abundant; therefore, the most easily observed line among the interstellar molecular lines. Such molecules as H_2CO , HCN, HC_{2n+1}N are found in high-gas density regions, and therefore, are used as the probes to observe the cores and regions more directly related to the star-formation in molecular clouds.

1.7 HI Line

The most abundant species of the interstellar matter is the molecular hydrogen (H_2) and the neutral hydrogen (HI). The H_2 gas is usually found in low-temperature molecular clouds ($\sim 5 - 50$ K) of sizes around a few to 30 pc, and is distributed in the inner region of the Galaxy at radius < 10 kpc from the center. The HI gas is found in clouds of larger sizes, 10 to 100 pc, at temperatures of around 100 K, and is also distributed diffusely in the interstellar space and in the Galaxy for a radius up to 20 - 30 kpc. The neutral hydrogen emits the 21-cm HI line.

1.7.1 Frequency

An H atom comprises a proton and an electron. The proton has the positive charge $+e$ and is rotating (spinning) to yields a magnetic dipole moment μ_p . The electron is also rotating with the charge $-e$ to have the magnetic dipole moment μ_e . When the two magnetic dipoles are anti-parallel, the state is stable. If the spins are parallel, the atom emits the line radiation at 21 cm wavelength through the transition from the parallel to anti-parallel spin state. The parallel state is realized when the atom is excited such as due to collisions with other atoms. The energy of a photon emitted by this transition is given by

$$h\nu = \Delta E = \frac{\mu_e \mu_p}{a^3}, \quad (1.118)$$

where a is the Bohr radius:

$$a = \frac{h}{2\pi m_e c \alpha}, \quad (1.119)$$

$$\mu_e = \frac{eh}{4\pi m_e c}, \quad (1.120)$$

$$\mu_{\text{p}} = \frac{g\alpha h}{4\pi m_{\text{p}} c}, \quad (1.121)$$

where $\alpha = 1/137$ is the fine-structure constant and g is the Landé factor of order unity.

The energy level can be expressed in terms of the principal quantum number n , the total angular momentum F of the atom, $F = J + I = L + S + I$, where L is the orbital angular momentum of the electron, I the nucleus spin angular momentum, S the electron spin angular momentum, and J is the total angular momentum of the electron, respectively;

$$E = \frac{h\nu_0}{n^3} \frac{F(F+1) - I(I+1) - J(J+1)}{J(J+1)(2L+1)}, \quad (1.122)$$

with $\nu_0 = g\alpha^2 cR(m_{\text{e}}/m_{\text{p}})$ and $R = 2\pi^2 m_{\text{e}} e^4 / (ch^3)$ is the Rydberg constant. The transition energy from $F = 1$ (parallel spin) to $F = 0$ (anti-parallel) state is then written as

$$\Delta E = E(F = 1) - E(F = 0). \quad (1.123)$$

The frequency of the HI line emission is given as

$$\nu = 1420.405751786 \text{ MHz}, \quad (1.124)$$

or

$$\lambda = 21.106114 \text{ cm}. \quad (1.125)$$

1.7.2 Intensity

The absorption coefficient of the HI line radiation is expressed in terms of the Einstein A coefficient

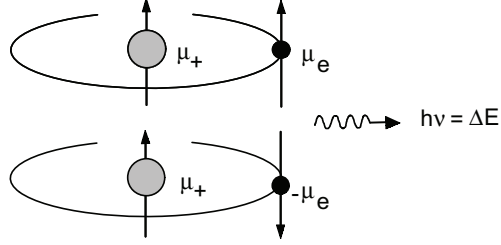


Figure 1.8: An HI atom comprises two spins (magnetic dipoles) of the proton and electron, and their transition emits the HI 21-cm line radiation.

$$\kappa_\nu = \frac{c^2 A_{10}}{8\pi\nu^2} n_0 \frac{g_1}{g_0} \{1 - \exp(\frac{-h\nu_{10}}{kT})\} f(\nu) \simeq \frac{c^2 A_{10}}{8\pi\nu_{10}} \frac{3hm_{\text{H}}}{4kT} f(\nu) \simeq 2.6 \times 10^{-15} \frac{n_{\text{H}}}{T} \frac{1}{\Delta\nu}. \quad (1.126)$$

For an optically thin gas the brightness temperature and the optical depth can be related by

$$T_{\text{B}} = T(1 - e^{-\tau_\nu}) = T \int \kappa_\nu dx \simeq TL\kappa_\nu. \quad (1.127)$$

This relation can be used to relate the observed quantities T_{B} , L , and ν (ν) as

$$N_{\text{H}} = \int n_{\text{H}} dx \simeq n_{\text{H}} L = 3.8 \times 10^{14} T_{\text{B}} d\nu = 1.82 \times 10^{18} \int T_{\text{B}} d\nu, \quad (1.128)$$

with N , T and ν being measured in H cm^{-2} , K, and km s^{-1} , respectively.

1.8 Radiations from various species

We summarize the kinds of radiations from various interstellar matters in the order of their temperature (energy) from low to high.

1.8.1 Molecular Lines

Molecular lines are emitted by the low-temperature (5 - 50 K) and high density ($10^3 \sim 10^6 \text{ H}_2 \text{ cm}^{-3}$) interstellar molecular clouds. Numerous species have been observed and can be used also to probe the chemistry of clouds. The lines can be used to probe the internal kinematics and density distribution of the individual clouds, particular the regions around the star-formation and dense galactic arms and rings. The molecular gas, mainly mapped in the CO line emission, is concentrated in the inner region of the Galaxy within radius $\sim 10 \text{ kpc}$, particularly in the 4-kpc molecular ring and the nuclear disk of a few hundred pc radius.

1.8.2 HI Line Emission

The HI line is emitted by neutral hydrogen gas of temperature around $\sim 100 - 1000 \text{ K}$ and density of $\sim 1 - 100 \text{ H cm}^{-3}$. The HI gas is distributed all over the Galaxy, forming a broad ring of radius 10 kpc . The 21-cm line used to obtain kinematical structure of the Galaxy such as the galactic rotation curve. The velocity information along the galactic plane can be used also to obtain the face-on distribution of the interstellar gas, and of the spiral arms. The majority of the HI gas forms HI clouds of sizes 10-100 pc of density $10-100 \text{ dH cm}^{-3}$, while a part is diffusely distributed in the galactic disk of thickness 100 - 200 pc.

1.8.3 Recombination Lines

Recombination lines are emitted by partially ionized gas in HII regions of temperature $\sim 6000 - 10^4$ K and density $\sim 100 - 10^4$ H cm $^{-3}$. Spectroscopic data can be used to study kinematics of HII regions. The line intensity, combined with the thermal free-free transition emission, is used to obtain the density and temperature of the HII region. HII regions are associated with and excited by young massive stars (OB stars) which emit strong UV radiation.

1.8.4 Free-Free Emission

Free-free emission (thermal Bremsstrahlung) is a continuum radiation from plasma (ionized gas) of temperature $10^4 \sim 10^7$ K. The intensity is directly related to the emission measure $\int n_e^2 dx \sim n_e^2 L$ [cm $^{-6}$ pc], and is used to obtain the ionized gas density of HII regions.

1.8.5 Synchrotron Radiation

The synchrotron (non-thermal) emission is a continuum radiation due to the interaction of relativistic electrons (cosmic-ray electrons) with the interstellar magnetic field. The volume emissivity $\sim I/L$ [ergs s $^{-1}$ cm $^{-3}$] of the emission is used to measure the strength of the magnetic field and the cosmic-ray electron energy as well as the number density of high-energy electrons, under the assumption of the energy equipartition between magnetic and cosmic-ray pressures (energy densities). The radiation is usually polarized perpendicularly to the magnetic lines of force. This fact can be used to obtain information about the orientation of interstellar magnetic fields. The synchrotron radiation is emitted by the Galactic disk, the nucleus (Sgr A), supernova remnants, pulsars, and the magnetic regions surrounding the galactic

center. Radio galaxies, quasars, and usually spiral galaxies, are also strong sources of the synchrotron radiation.

1.8.6 Black-Body Radiation

Finally, black body radiation is observed for objects in which the optical depth is large enough (optically thick). For a non-relativistic case the black-body radiation is expressed by the Planck's law:

$$I_\nu(T)d\nu = \frac{2h\nu^3}{c^2} \frac{1}{\exp(h\nu/kT) - 1} d\nu \quad (1.129)$$

in [ergs s⁻¹ cm⁻² str⁻¹], or in terms of wavelengths,

$$I_\lambda(T)d\lambda = \frac{2hc^2}{\lambda^5} \frac{1}{\exp(hc/\lambda kT) - 1} d\lambda. \quad (1.130)$$

In the radio frequency range ($h\nu \ll kT$), the Rayleigh-Jeans law is applied;

$$I_\nu = \frac{2kT}{c^2} \nu^2 \propto \nu^2. \quad (1.131)$$

For a relativistic gas with an equivalent temperature of $kT \sim E$ with E being the energy of a high-energy particle, we obtain an optically thick synchrotron spectrum;

$$I_\nu \propto \nu^{5/2}. \quad (1.132)$$

1.9 Radiative Transfer

Radiation is absorbed during its propagation through the interstellar matter. If a source with intensity I lies behind an interstellar cloud of absorption coefficient κ , a small fraction of the intensity

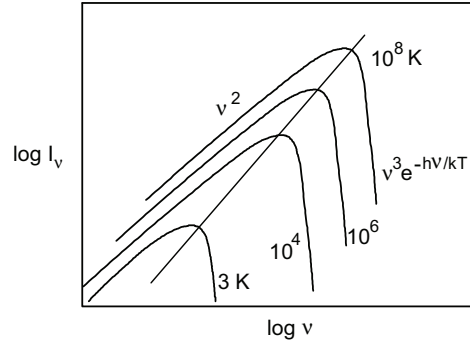


Figure 1.9: Spectrum of the black-body radiation.

$$dI = -\kappa I dx \quad (1.133)$$

is absorbed during its penetration for a small path length dx , or

$$\frac{dI}{dx} = -\kappa I. \quad (1.134)$$

This is solved to give

$$I = I_0 e^{-\int \kappa dx}. \quad (1.135)$$

By introducing an optical depth

$$\tau = \int \kappa dx \quad (1.136)$$

we have

$$I = I_0 e^{-\tau}. \quad (1.137)$$

If there is a radio-emitting cloud with the emissivity ε on the path,

we have the source term in addition to the absorption term in the above expression;

$$dI = -\kappa I + \varepsilon, \quad (1.138)$$

or

$$\frac{dI}{dx} + \kappa I = \varepsilon. \quad (1.139)$$

When $\kappa = \text{constant}$, the solution of this differential equation is

$$I = I_0 e^{-\int \kappa dx} + \frac{\varepsilon}{\kappa} (1 - e^{-\int \kappa dx}), \quad (1.140)$$

or

$$I = I_0 e^{-\tau} + \frac{\varepsilon}{\kappa} (1 - e^{-\tau}). \quad (1.141)$$

For an optically thin cloud, $\tau \ll 1$, we have

$$I = I_0 + \frac{\varepsilon}{\kappa} \tau. \quad (1.142)$$

If there is no background emitting source, $I_0 = 0$, we obtain

$$I = \frac{\varepsilon}{\kappa} \tau = S\tau. \quad (1.143)$$

The term

$$S = \frac{\varepsilon}{\kappa} \quad (1.144)$$

is called the source function. If the cloud is optically thick, $\tau \gg 1$, equation(6) yields

$$I = \frac{\varepsilon}{\kappa}, \quad (1.145)$$

or $I = S$.

[In solving eq. (1.139) we assumed that κ is a constant. However, more generally, the absorption coefficient and the emissivity are functions of the depth along the line of sight. A differential equation of the type

$$\frac{dB}{dx} + f(x)B = g(x) \quad (1.146)$$

is called the Leibnitz equation. The general solution of this equation is given by

$$B = Ae^{-\int f(x)dx} + e^{-\int f(x)dx} \int e^{\int f(x)dx} g dx, \quad (1.147)$$

where A is a constant of integration.]

A useful expression often used in radio astronomy is, for example for a plasma emitting free-free thermal radiation, as follows:

$$T_B = T_e(1 - e^{-\tau}) \quad (1.148)$$

or

$$T_B \simeq T_e \tau \quad (\text{for optically thin case, } \tau \ll 1), \quad (1.149)$$

and

$$T_B \simeq T_e \quad (\text{for optically thick case, } \tau \gg 1), \quad (1.150)$$

where T_B and T_e are the (observed) brightness temperature and the electron temperature of the cloud, respectively.

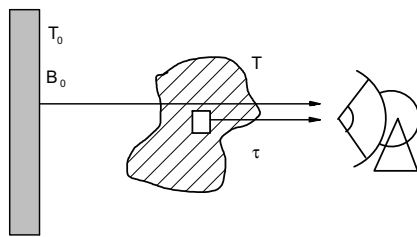


Figure 1.10: Radiation transfer through a cloud.

Chapter 2

INTERSTELLAR MATTER

The interstellar matter (ISM) comprises various kinds of gases (molecular, HI, HII and high-temperature), cosmic rays, and magnetic fields. Interstellar matter makes up approximately 10% of the mass of the Galaxy; and the majority of the IMS is HI and H₂. The rest 90% is shared by stars, which determines the dynamical properties of the Galaxy. On the other hand, the IMS is more deeply coupled with such actives as the star formation near the galactic plane, and therefore, IMS is categorized as population I.

2.1 ISM and Radio Emission

2.1.1 ISM at various temperatures

We summarize the radio continuum and line emissions from the various species of the ISM in 2.1.

2.1.2 Population in the Galaxy

The population is the basic concept to classify the interstellar matter as well as the various objects in the Galaxy. The ISM is categorized

$T(K), E$	Object	Line	Continuum	Observ.
3K	Cosmic BBR		mm, submm	Radio COBE, WMAP
10 – 50 K . . .	Mol. cl. H ₂ gas Dust	Mol. lines mm - submm		Radio FIR, IRAS
100 - 1000 K	HI clouds Diffuse HI Dust (cir. stel)	HI 21-cm 21-cm		Radio IR, IRAS
10 ⁴ K	HII regions	Recom. lines H α , etc. H α line	IR	Radio Optical
10 ^{5~7} K	SNR Diffuse HII (Inter-cloud) Halo		Thermal (ff) Nonth (Synch) X-rays	Radio Radio X-rays
High-energy . (Cosmic Ray + Mag. field)	Mag. fi, CR SNR, Pulsars Gal. Center AGN, QSO, Jets Radio Galaxies		Nonth (Synch)	Radio Polari.
γ rays	CR + MC, HI		Compton Sca.	γ ray

Table 2.1: ISM and radiations.

as the younger-population type, or Pop. I, mainly because of its contribution to the starformation and related activity. We summarize the population types of objects in the Galaxy in the following table.

2.2 Energy Balance in ISM

2.2.1 Energy-density and Pressure balance

Although ionized gas, dust, and cosmic rays are negligible concerning their mass, their energetic contribution is comparable to the other more massive species like molecular clouds. Let us estimate the energy density or the pressure of each species.

Energy density, which has the same dimension as the pressure, of molecular gas is given approximately

$$u_{\text{mol}} \sim n_{\text{H}_2} kT \sim 10^{-12} \text{ erg cm}^{-3}, \quad (2.1)$$

with $n_{\text{H}_2} \sim 10^3 \text{ H}_2 \text{ cm}^{-3}$ and $T \sim 10 - 100 \text{ K}$. The HI gas (clouds) have the amount of

$$u_{\text{HI}} \sim n_{\text{H}} kT \sim 10^{-12} \text{ erg cm}^{-3}, \quad (2.2)$$

with $n_{\text{HI}} \sim 10 \text{ H cm}^{-3}$ and $T \sim 100 - 1000 \text{ K}$. The diffuse ionized gas in the intercloud regions have the energy density of

$$u_{\text{Diff.HII}} \sim n_{\text{H}} kT \sim 10^{-12} \text{ erg cm}^{-3}, \quad (2.3)$$

for $n_{\text{HII}} \sim 10^{-2} \text{ H cm}^{-3}$ and $T \sim 10^4 \text{ K}$. Therefore, the thermal components have the energy density of around $10^{12} \text{ erg cm}^{-3} \sim 1 \text{ eV cm}^{-3}$, or

$$u_{\text{gas}} \sim 10^{-12} \text{ erg cm}^{-3} \sim 1 \text{ eV cm}^{-3}. \quad (2.4)$$

Here, n_i is the number density of the i -th gas species.

	Pop. I		Pop. II		
	Extr.Pop I	Older Pop I	Old disk	Interm.	Halo
	Young systems		Old systems		
G. str.	Young s. disk		Old s. disk		Halo Glo. cl.
	Gas disk				
	Bright arms				
Thickn. (pc) ..	$z \sim 100$	200	300 - 500	1 kpc	2 - 10 kpc
Velo. (km s ⁻¹)	$v_\sigma \sim 5 - 10$		50 - 100		100 -200
$M(10^{11} M_\odot) ..$	0.05	0.05	1	1	~ 10
Age (Gy)	< 0.1	0.1 - 1.5	1.5 - 5	5 - 6	6 - 15
Metallicity	$[Z/H] = 0.04$	0.02	0.01	0.004	0.001
ISM (Gas) ...	H ₂				
	Dust				
	Inner disk HI		Outer HI		
	Diffuse HII				
Nebulae	Dark clouds				
	Emiss. neb.				
	HII regions		Pla. neb.		
	SNR Type II		SNR Type I		
	Cirrus				
Stars	Sup. Giants	Sun			Glob. cl.
		Nearby st.		High vel.	
		Main seq.			
	Metal rich		Metal poor		Extr. poor
		Lines		weak lines	
	T Tau				
	Cepheids		RR Lyr		RR Lyr

Table 2.2: Population types of ISM and stars.

These energy densities are also approximately equal to the kinetic energy;

$$u_{\text{gas:kin}} \sim \frac{1}{2} \rho_{\text{gas}} v_{\sigma} \sim 10^{-12} \text{erg cm}^{-3}, \quad (2.5)$$

where $\rho \sim 1 - 10 \text{ H cm}^{-3}$ and $v_{\sigma} \sim 5 - 10 \text{ km s}^{-1}$ are the gas density and velocity dispersion, respectively.

The high-energy components, cosmic rays and magnetic fields, have energy densities as follows: The magnetic field energy density is

$$u_{\text{mag}} = \frac{B^2}{8\pi} \sim (3 \times 10^6 \text{ G})^2 / 8\pi \sim 10^{-12} \text{erg cm}^{-3}. \quad (2.6)$$

This is in balance with the cosmic-ray energy density which is

$$u_{\text{CR}} \sim 10^{-12} \text{ erg cm}^{-3}. \quad (2.7)$$

It must be also noted that the energy density of the starlight in the interstellar space can be estimated as

$$u_{\text{starlight}} \sim \frac{L}{\pi R^2} \frac{1}{c} \sim 10^{-12} \text{ erg cm}^{-3}, \quad (2.8)$$

where $L \sim 10^{11} L_{\odot} \sim 10^{44} \text{ ergs s}^{-1}$ is the luminosity of the Galaxy, and $R \sim 10 \text{ kpc}$ is the typical radius of the galactic disk. By the way, the cosmic background radiation of 3K has about the same amount of energy density;

$$u_{\text{3K}} \sim \frac{\sigma T^4}{c} \sim 10^{-13} \text{ erg cm}^{-3}, \quad (2.9)$$

where $\sigma = 5.670 \times 10^{-5} \text{ erg cm}^{-2} \text{ deg}^{-4} \text{ s}^{-1}$ is the Stephan-Boltzmann constant and $T = 2.7 \text{ K}$.

Thus, we have a general balance in the interstellar matters as

$$u_{\text{gas}} \sim u_{\text{mag}} \sim u_{\text{CR}} \sim u_{\text{starlight}} \sim u_{\text{3K}} \sim 1 \text{ eV cm}^{-3}. \quad (2.10)$$

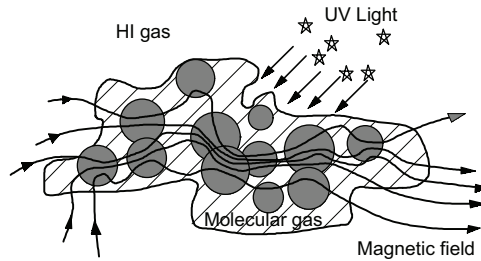


Figure 2.1: The pressure balance (energy equipartition) in the ISM for an equilibrium and steady state.

Since the energy density of gas is equivalent to the pressure, we may say that the interstellar gases of various phases, magnetic fields, cosmic rays, and starlight pressure (on dust) are in a pressure balance with each other.

2.2.2 ‘Activity’ in ISM

Gaseous objects like molecular clouds and HI clouds that composes the ISM are generally in a thermal equilibrium and are balanced with each other in pressure, as shown above; if the energy/pressure balance works, the clouds are stable and can exist in a steady state. However, such a balanced (steady) state is often broken by an injection of extra energy: An explosion of a supernova, resulting in a rapidly expanding shell of supernova remnant (SNR); injection of jets and fast outflow from the nucleus; and strong UV radiation from newly born stars, leading to expansion of ionized gas as an expanding HII region. The balance is also broken by the radiative cooling of gas, resulting in a gravitational collapse of condensations to dense cores and sometimes leading to starformation. Supersonic collisions of clouds would also act to break the balance by sudden compression of gas, often forming

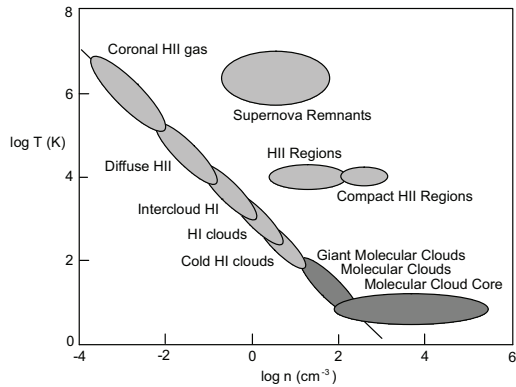


Figure 2.2: Most of the gaseous objects lie on the line of pressure constant. Objects that are significantly displaced from the balance line are in an ‘activity’.

new stars.

If an object is in such a non-equilibrium condition that the energy/pressure balance is broken, we may regard the object to be in an ‘activity’. Active regions in the Galaxy are the nucleus and its surroundings (galactic center region), star-forming regions, jets, supernovae and supernova remnants, inflating magnetic fluxes over the galactic disk, etc..

2.3 Molecular Clouds

2.3.1 Mass, size and intensity

Molecular gas is observed by spectral line observations in the mm-wave range, especially with the use of the molecular line of CO. The virial (dynamical) mass of a molecular cloud of radius r and velocity dispersion v_σ is given by

$$M_{\text{cloud}} \sim \frac{rv_{\sigma}^2}{G}. \quad (2.11)$$

The CO luminosity L_{CO} is related to the CO intensity I_{CO} as

$$L_{\text{CO}} = 4\pi D^2 \int I_{\text{CO}} d\Omega, \quad (2.12)$$

where D is the distance to the cloud and is related to r as $r \sim D\theta$ with θ the angular radius of the cloud. The distance can be obtained from the radial velocity of the cloud by using the galactic rotation law for an assumed rotation curve of the Galaxy. The velocity dispersion v_{σ} can be obtained from the line width of the cloud's CO line profile. The mass can be related to the column mass as

$$M_{\text{cloud}} = 2m_{\text{H}} \int N_{\text{H}_2} dx dy = 2m_{\text{H}} \int N_{\text{H}_2} D^2 d\Omega. \quad (2.13)$$

From observations of many molecular clouds we have an empirical relation

$$M_{\text{cloud}} \simeq AL_{\text{CO}} \quad (2.14)$$

with A being a constant, although the CO line is optically thick. This gives us an empirical relation between the CO intensity and the column mass as

$$N_{\text{H}_2} \simeq CI_{\text{CO}} = C \int T_{\text{mb}} dv, \quad (2.15)$$

where C is called the conversion factor, and has the value of

$$C = 2.8 \times 10^{20} [\text{H}_2 \text{ cm}^{-2}/\text{K km s}^{-1}]. \quad (2.16)$$

Here, T_{mb} is called the main-beam temperature when we observe, and is approximately equal to the brightness temperature of the cloud.

The conversion factor C is, of course, not a universal constant at all, and a value of $C = 3.6 \times 10^{20}$ [$\text{H}_2 \text{ cm}^{-2}/\text{K km s}^{-1}$] is used sometimes. Although there is no definite observational evidence, the conversion factor must be larger in the central region of galaxies, where the metal abundance is higher than in the outer disk. The factor also changes from galaxy to galaxy: In such a metal poor galaxy as the Large Magellanic Cloud the value is about 5 times larger. A higher value has been also observed in the central 2 kpc region of M31, where some inflow of metal-poor gas from the companion may have occurred. Although of the uncertainty, however, we use to assume the value quoted above for various circumstances, in the Galaxy and in extra galaxies, when we need to obtain the mass of molecular gas.

The mass distribution of molecular clouds is known to have a form

$$f(M)dM \propto M^{-1.5}dM \quad (2.17)$$

with a lower and upper cut off of about $\sim 10^2$ and $\sim 10^6 M_\odot$. Clouds of mass around $10^3 - 10^5$ are called normal molecular clouds, while those with $10^5 - 10^6$ are called giant molecular clouds (GMC). Sizes of molecular clouds are 10 – 30 pc, and GMC 30 – 50 pc. The mean density of clouds are typically $10^3 - 10^4 \text{ H}_2 \text{ cm}^{-3}$. The density of cores in clouds is sometimes $10^5 - 10^6 \text{ H}_2 \text{ cm}^{-3}$, from which stars would form.

2.3.2 The Distribution of MC and GMC

In Sb and Sc galaxies, the density distribution of molecular gas (H_2) is roughly approximated by an exponentially decreasing function of scale radius of about 3-4 kpc. In addition to this general distribution, molecular clouds are found to be more concentrated in the central region, making up the dense ‘nuclear gas disk’. They are again have a density peak at a galactocentric distance of 4 kpc, forming the ‘4-kpc molecular ring’. They, particularly GMCs, also show enhancing along

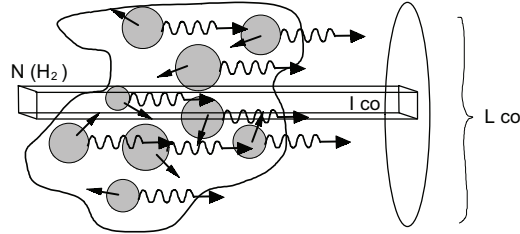


Figure 2.3: Molecular cloud mass and intensity.

the spiral arms, and the major inner arms can be traced as well as in the HI line emission.

2.3.3 Giant Molecular Clouds (GMC)

The largest (most massive) molecular clouds observed in the solar neighborhood (within a few kpc) have an extent of about ~ 50 pc and velocity dispersion $v_\sigma \sim 5 - 10.5 \text{ km s}^{-1}$. The virial (dynamical) mass of a cloud can be estimated as $M \sim rv_\sigma^2/G \sim 1.6 - 6 \times 10^5 M_\odot$ with $r \sim 1/2 \times \text{extent}$. Molecular clouds with a mass of several $10^5 \sim 10^6 M_\odot$ are called Giant Molecular Clouds (GMC). GMCs are the most massive objects in the Galaxy that are supposed to be gravitationally bound. In the Galaxy, several 10^3 GMCs (\sim a few $10^9 M_\odot$ in total mass) are distributed in the thin galactic disk within a galactocentric distance of $R \sim 10$ kpc. They are found in the nuclear disk, the 4-kpc ring, and in the major inner ($R < 10$ kpc) spiral arms. They compose the molecular gas disk of a scale thickness of about $z \sim 60$ pc near the galactic plane.

The rest of the molecular gas (of total $\sim 10^9 M_\odot$) is in the form of normal molecular clouds (MC) which are less massive than GMCs, and is also in the form of diffuse interstellar gas. They are more diffusely distributed than GMCs, even in the inter-arm regions. They

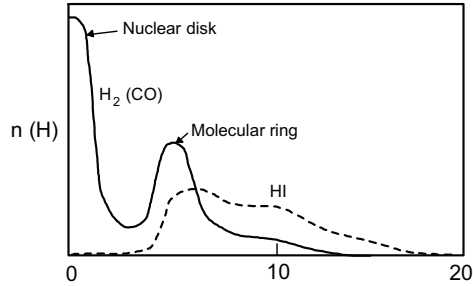


Figure 2.4: Density distribution of the H_2 and HI gas in the galactic plane for a typical Sb type galaxy.

are sometimes observed at a height several 100 pc above the galactic plane (high z molecular clouds). In some edge-on galaxies like NGC 891, molecular clouds are distributed with a scale thickness of about 1 kpc. The distribution of MC in the Galaxy away from the galactic plane (or in the halo) is still an open question, while a significant amount of MC is supposed to make up a thick molecular disk, like as in NGC 891.

2.3.4 GMC and Star-forming sites

Stars are born through gravitational contraction of dense and cool interstellar gas. Cores of molecular clouds, particularly GMC, are, therefore, the places of star formation. GMCs are often associated with young massive stars (OB stars) and HII regions that developed due to UV radiation from these high-temperature stars.

Typical examples of the association of a star-forming region (OB star cluster and HII region) and a GMC are found in Ori GMC and the Ori Great Nebula etc..

Cloud	SF region	RA	Dec	l	b
Tau MC (cold)		04h 38.6m	+25°36'	172°	-13°
Ori GMC	Ori Neb, M42	05h 32.8m	-05 25	209	-19
Sgr B2 GMC	HII+Comp. HII	17 44.2	-28 23	1	-0
M17 GMC	SF HII	18 17.5	-16 15	15	-1
M16 GMC	HII & shell	18 17.5	-16 15	15	+0
Mon GMC	Ros. N & Mon. Lp	6 29.3	+04 57	206	-2
W49 MC	W49A HII	19 07.9	+09 01	43	-0
G24 MC + HI Ring	G24 HII Ring			24 30	+0

Table 2.3: Molecular Clouds and SF regions.

2.4 HI Gas and Clouds

2.4.1 Mass, size, and intensity of HI clouds

For an optically thin case ($\tau \ll 1$), the column density of HI gas is estimated from observed intensity of the 21-cm line emission as

$$N_{\text{H}} [\text{H cm}^{-2}] = 1.82 \times 10^{18} \int T_{\text{B}} dv = 1.82 \times 10^{18} I_{\text{HI}} [\text{K km s}^{-1}]. \quad (2.18)$$

If the optical depth is close to unity or greater ($T_{\text{B}} \sim T_{\text{ex}}$) we have

$$T_{\text{B}} = T_{\text{ex}}(1 - e^{-\tau}), \quad (2.19)$$

with

$$\tau = N_{\text{H}} 1.6 \times 10^{-15} \frac{1}{\Delta\nu T_{\text{ex}}} = 5.5 \times 10^{-19} \frac{N_{\text{H}}}{T_{\text{ex}} \Delta\nu}, \quad (2.20)$$

or

$$N_{\text{H}} [\text{H cm}^{-2}] = 1.82 \times 10^{18} \tau T_{\text{ex}} \Delta v = 1.82 \times 10^{18} \tau \int T_{\text{ex}} dv [\text{K km s}^{-1}]. \quad (2.21)$$

For example, a typical HI cloud has such parameters as the excitation temperature $T_{\text{ex}} \sim 100$ K and $\tau \sim 0.1$, or a peak brightness temperature of about $T_{\text{B}} \sim 10$ K, and a velocity dispersion $v_{\sigma} \sim 10 - 20$ km s⁻¹. These gives the column density of a typical HI cloud as

$$N_{\text{H}} \sim 2 \times 10^{20} [\text{H cm}^{-2}]$$

Given the distance and size of a cloud, the mass can be obtained by

$$M_{\text{HI}} = m_{\text{H}} \int N_{\text{H}} D^2 d\Omega \sim m_{\text{H}} N_{\text{H}} S, \quad (2.22)$$

where $S \sim \pi r^2 = \pi(\theta D/2)^2$ is the projected area of the cloud with θ being the apparent angular size (diameter). The excitation temperature of HI is typically 100 K for clouds, and 100 – 1000 K for the diffuse HI gas in the inter-arm regions and in the halo (thick disk). Typical HI clouds have a size (diameter) of about 10 – 100 pc, mean density of 10 – 100 H cm⁻³, and a mass of about $10^2 \sim 10^5 M_{\odot}$.

The total amount of HI gas in the Galaxy can be approximately estimated from the intensity of the 21-cm line emission in the galactic plane. Although individual HI clouds have a velocity dispersion of $\sim 10 - 20$ km s⁻¹, the line-of-sight integration of many clouds toward a certain direction of the galactic plane yields a much larger velocity width of about $v_{\sigma} \sim 200$ km s⁻¹ because of the galactic rotation of the HI disk. Suppose that a brightness temperature at the galactic plane of about $T_{\text{B}} \sim 500$ K and a line width of $v_{\sigma} \sim 200$ km s⁻¹ have been observed, then the column density along the line of sight is given as

$$N_{\text{H}} \sim 10^{22} \text{ H cm}^{-2}.$$

This yields a mean hydrogen density on the line of sight to be ~ 0.2 H cm⁻³. Let us assume that this value is a typical column density when

the Galaxy is seen edge-on, then we obtain the total mass of HI disk in the Galaxy as

$$M_{\text{HI}} \sim m_{\text{H}} N_{\text{H}} S \sim N_{\text{H}}(2R)(2z) \sim 10^9 M_{\odot}, \quad (2.23)$$

where $R \sim 15$ kpc and $2z \sim 400$ pc are the radius and full scale thickness of the HI disk.

2.4.2 The Distribution of HI gas

The HI gas clouds are distributed in a disk of thickness $2z \sim 200$ pc, and more diffuse HI gas is distributed in a thicker disk of $2z \sim 400$ pc. The radial distribution is much broader than the H_2 gas: it is distributed from galactocentric distance of $R \sim 3$ to 30 kpc, peaking at around $R \sim 10$ pc. However, the HI gas is almost lacking in the central 2 kpc region, where the molecular (H_2) gas dominates. Namely, the gas disk of the Galaxy comprises two major gas component: the outer HI broad and thick disk with a hole at the center; and the inner thin and dense H_2 disk.

The HI gas most clearly traces spiral arms, and the spiral structure of the Galaxy have been mapped by HI observations most intensively. Since the Galaxy is seen edge-on, we used the velocity-to-space transformation with which radial velocity profiles are decoded to depths along the line of sights by using the rotation law (rotation curve) of the disk.

2.5 HI vs H_2 in the ISM

2.5.1 The HI to H_2 Transition

Concerning the mass, the HI and H_2 gases are the two major components of the ISM. We here define the molecular fraction by

$$f_{\text{mol}} = \frac{2n_{\text{H}_2}}{n_{\text{H}} + 2n_{\text{H}_2}} = \frac{\rho_{\text{H}_2}}{\rho_{\text{H}} + \rho_{\text{H}_2}}, \quad (2.24)$$

where n_i and ρ_i are the number and mass densities of the species i .

In the central few kpc region of the Galaxy (near the Galactic Center) the H_2 gas dominates ($f_{\text{mol}} \sim 1$), while in the outer region at $R > 10$ kpc the HI gas dominates ($f_{\text{mol}} \sim 0$). A large-scale phase transition from HI to H_2 , and vice versa, is clearly seen from their radial distributions.

Locally, the two gas components also avoid each other, and are pressure-balancing: The lower-density and higher-temperature HI gas is distributed more diffusely than the H_2 gas which is concentrated in higher-density and lower-temperature molecular clouds. The phase transition between HI and H_2 occurs depending on the pressure, metal abundance, the star-light field and the size/mass of a cloud. Here, we assume that H_2 molecules are formed from H atoms through catalytic action on surfaces of interstellar grains. The higher are the pressure (number densities of H and grains) and metal abundance (more grains), the higher is the formation rate of H_2 from HI. On the other hand, H_2 molecules are dissociated by UV radiation from stars, forming HI gas, and therefore, the stronger is the UV radiation (starlight), the lower is the formation rate of H_2 . Finally, the larger is the mass (radius) of the cloud, the more is the obscuration of dissociative UV photons, leading to a higher fraction of the molecular gas.

ISM condition	f_{mol} (Molecular Fraction)	
Pressure (density), P	↑	↑
Metal abundance, Z	↑	↑
UV photon density, U	↑	↓
MC Mass (size), $M(r)$	↑	↑

Table 2.4: HI-to- H_2 and H_2 -to-HI transition in the ISM.

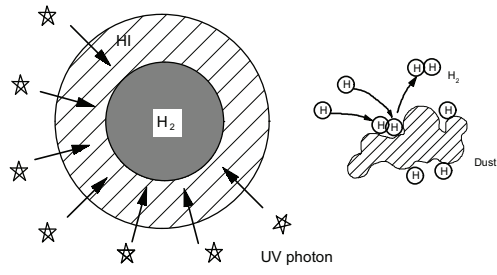


Figure 2.5: Cloud structure in HI to H₂ phase transition zone.

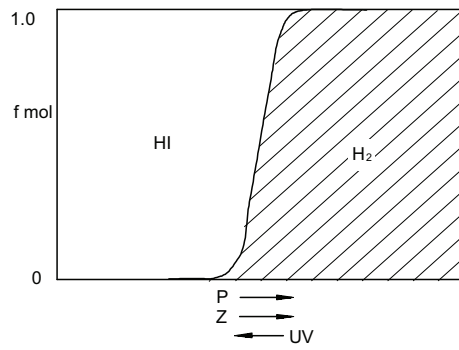


Figure 2.6: Molecule fraction in HI to H₂ phase transition zone.

2.5.2 The Molecular Fraction

Given the mass M of a spherical cloud, which comprises two zones (= central molecular core + HI envelope), then we can calculate the molecular fraction in the cloud for an ISM condition with P, Z, U : $f_{\text{mol}}(M : P, Z, U)$. By assuming that molecular masses are distributed with a power-law distribution function as

$$f(M)dM \propto M^{-1.5}dM \quad (2.25)$$

with the upper and lower cut off masses M_{max} and M_{min} , we can further calculate the mass fraction f_{mol} for a given volume of the interstellar space by

$$f_{\text{mol}}(P, Z, U) = \int f_{\text{mol}}(M : P, Z, U)f(M)dM. \quad (2.26)$$

2.5.3 Molecular Fraction and the ISM Evolution

In the solar neighborhood, the molecular fraction is known to be $f_{\text{mol}} \sim 0.2$. The molecular fraction varies with the interstellar condition, and therefore, with the location in the Galaxy. The radial variation of f_{mol} has the implication to probe the evolution of interstellar gas in the galaxy scale, which is deeply coupled with the evolution of star formation in the disk: Star formation rate is known to be a function of the molecular gas density; Massive stars among the newly born are the intense source of UV photons; The mass loss and SN explosions from the born stars contribute to supply heavy elements to increase Z . Thus, the evolution of the ISM and its chemical structure are determined through this cyclic interaction among the $\text{HI} \rightleftharpoons \text{H}_2$ transition, star formation and heavy element pollution.

2.6 HII Gas

Chapter 3

STAR FORMATION AND DEATH

3.1 Mechanisms of Star Formation

3.1.1 Sites of Star Formation

Stars are born from interstellar gas by gravitational contraction of molecular cloud cores. Therefore, star forming sites are where molecular clouds (dark clouds) are crowded. Spiral arms are the major sites of star formation, where the galactic shock wave of gas induced by the density wave compresses the interstellar gas. Particularly, the 4-kpc ring of molecular gas, which is the densest gaseous region of the Galaxy, is the most intense star forming region in the Galaxy. The central region of the Galaxy, where the nuclear molecular disk is found, is also the place of intense star formation.

Among newly born stars, massive stars (OB stars) evolve rapidly, and explode as type II supernovae when they die. (Type I SN are for stars less massive, but greater than the solar mass.) Through the SN explosion, the stars supply kinetic energy to the ISM as well as pollute it by heavy elements. The life time of OB stars are $10^6 \sim 10^7$ years, so that the type II SN explosion occurs relatively close to the places

where they were born.

The time scale of star formation is approximately given by the contraction time (free fall time $\sim 10^6$ years) of the cloud core, which is short enough compared to the galactic rotation period (10^8 years). The life time of OB stars is also short, and the luminosity of OB stars much exceed the B and V band luminosity of the rest newly born stars. Due to these facts, the spiral arms shine most intensely compared to the inter-arm region. This gives rise to the high contrast between the optical spiral arms and other regions on B and V band photographs of galaxies, impressing one with the spiral structure.

3.1.2 Schmidt's Law

The star formation rate (SFR) is defined by

$$SFR = \frac{d\rho_{\text{stars}}}{dt}, \quad (3.1)$$

and the star formation efficiency (SFE) by

$$SFE = \frac{d\rho_{\text{stars}}}{\rho_{\text{gas}}dt}, \quad (3.2)$$

where ρ_{stars} and ρ_{gas} are the densities of stars and gas in the interstellar space of a certain volume, say within 100 pc to 1 kpc square region.

The SFR can be determined from observations by counting OB associations and HII regions by dividing them by their assumed life time:

$$SFR(\text{OB}) \sim \frac{n_{\text{OB}}}{\tau_{\text{OB}}}, \quad (3.3)$$

with $\tau_{\text{OB}} \sim 10^7$ yrs, or

$$SFR(\text{HII}) \sim \frac{n_{\text{HII}}}{\tau_{\text{HII}}}, \quad (3.4)$$

with $\tau_{\text{HII}} \sim 10^6$ yrs. The SFR can be also obtained from the H_α intensity, and from the UV photon density which can be estimated from thermal radio emissivity.

The SFR is higher where gas density is higher, and vice versa. Hence, the SFR can be reasonably related to the gas density by the Schmidt's law:

$$SFR \propto \rho_{\text{gas}}^\alpha, \quad (3.5)$$

or

$$SFE \propto \rho_{\text{gas}}^{\alpha-1}. \quad (3.6)$$

If the star formation is stochastic, the power-law index would be around $\alpha \sim 1$. On the other hand, if it is related to a collisional process of gas clouds, the power would be $\alpha \sim 2$.

The star formation law can be obtained by counting the number of HII regions and OB associations, etc., as eq. (3.3) and (3.4) averaged in a certain volume of the interstellar space. On the other hand, the gas density can be measured from HI line emission or from CO line observations. The power index α is then estimated by plotting $\rho_{\text{OB}}(\rho_{\text{HII}}$ against the gas density ρ_{gas} .

3.1.3 The Virial Theorem

The gravitational equilibrium, expansion, or contraction can be expressed in terms of the Virial theorem: The moment of inertia of a system with density ρ is given by

$$I = \int \rho \mathbf{r}^2 dx dy dz. \quad (3.7)$$

The system is in an equilibrium when

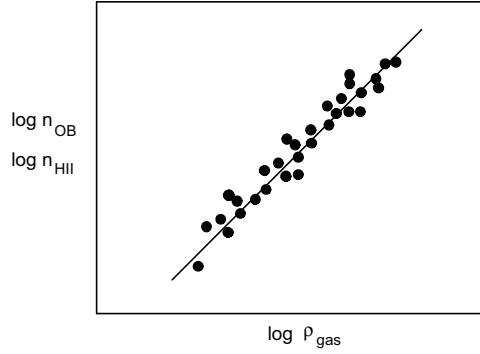


Figure 3.1: Schmidt's law: plot of the star formation rate (\propto number density of star forming regions / an assumed life time) against the interstellar gas density.

$$\frac{d^2 I}{dt^2} = 2K + \Phi_G + E_M + 3(\gamma - 1)U_T = 0, \quad (3.8)$$

where

$$K = \frac{1}{2} \int \rho v^2 dx dy dz \quad (3.9)$$

is the kinetic energy;

$$\Phi_G = -\frac{1}{2} \int \frac{\rho \rho'}{|\mathbf{r} - \mathbf{r}'|} dx' dy' dz' \quad (3.10)$$

is the potential energy;

$$E_M = \frac{1}{8\pi} \int B^2 dx dy dz \quad (3.11)$$

is the magnetic energy density; and

$$U_T = \frac{1}{\gamma - 1} \int p dx dy dz \quad (3.12)$$

is the internal (thermal) energy with p being the pressure.

For example, if a cloud is in an equilibrium with its kinetic energy due to its internal velocity dispersion (turbulence) being balancing the gravitational energy, we have

$$\frac{d^2 I}{dt^2} = 2K + \Phi_G = 0. \quad (3.13)$$

If

$$\frac{d^2 I}{dt^2} > 0 \quad (3.14)$$

the system expands, while if

$$\frac{d^2 I}{dt^2} < 0 \quad (3.15)$$

it gravitationally collapses.

3.1.4 Gravitational Contraction – Jeans Instability –

Suppose a gas cloud of density ρ , radius r , and an internal velocity dispersion v_σ which is approximately equal to the sound velocity $v_\sigma \sim c_s$. The mass is given by $M = \frac{4\pi}{3}r^3\rho$, and the gravitational energy

$$\Phi = \frac{GM^2}{r}. \quad (3.16)$$

The kinetic energy is given by

$$K = \frac{1}{2}Mc_s^2. \quad (3.17)$$

If the cloud is in a Virial equilibrium, it is stable:

$$\frac{GM^2}{r} \sim Mc_s^2, \quad (3.18)$$

or

$$r \sim \frac{c_s}{\sqrt{4\pi G\rho}}. \quad (3.19)$$

(See the next subsection for a more accurate treatment of instability for the factor 4π .) However, the cloud is gravitationally unstable and collapses, if the gravity dominates:

$$\frac{GM^2}{r} > Mc_s^2, \quad (3.20)$$

or if

$$r > \frac{c_s}{\sqrt{4\pi G\rho}}. \quad (3.21)$$

The time scale of gravitational contraction is given by the free-fall time:

$$\frac{d^2r}{dt^2} \sim \frac{r}{t^2} \sim \frac{GM}{r^2}, \quad (3.22)$$

or

$$t \sim \sqrt{\frac{r^3}{GM}} \sim \frac{\sqrt{3}}{\sqrt{4\pi G\rho}} = \frac{4.6 \times 10^7}{\sqrt{n} \text{ [H cm}^{-3}\text{]}} \text{ [years]}. \quad (3.23)$$

This is also given by the time scale that is necessary for an information to transfer and cross the cloud at the sound velocity:

$$t \sim \frac{r}{c_s} \sim \frac{1}{\sqrt{4\pi G\rho}}. \quad (3.24)$$

The scale length

$$\lambda_J \sim c_s t \sim \frac{c_s}{\sqrt{4\pi G\rho}} \quad (3.25)$$

is called the Jeans wavelength. Since the sound velocity is related to the temperature $c_s = \sqrt{\gamma RT}$ (R is the gas constant), the Jeans

wavelength can be expressed also as

$$\lambda_J \sim \sqrt{\frac{\gamma RT}{4\pi G \rho}} \sim \sqrt{\frac{\gamma R}{4\pi G m_H}} \sqrt{\frac{T}{n}} \sim 7 \sqrt{\frac{T \text{ [K]}}{n \text{ [H cm}^{-3}\text{]}}} \text{ [pc]} \quad (3.26)$$

The mass given by

$$M_J \sim \rho \lambda_J^3 \sim 23 \left(\frac{T}{1\text{K}}\right)^{3/2} \left(\frac{n}{1\text{H cm}^{-3}}\right)^{-1/2} M_\odot \quad (3.27)$$

is called the Jeans mass.

The Jeans wavelength, mass and free-fall time for typical interstellar clouds as well as for gaseous constituents in the universe are given in table 3.1. The masses estimated for molecular gas and cloud cores are typical for stars.

Cloud	ρ ($m_H \text{ cm}^{-3}$)	T (K)	λ_J (pc)	M_J (M_\odot)	t_J (y)
GMC core	$\sim 10^5$	10 - 30	~ 0.1	0.1 - 1	10^6 to stars
GMC	$\sim 10^3$	10 - 100	~ 1	~ 10	to stars
HI Cloud	~ 100	$10^2 - 10^3$	~ 10	$\sim 10^3$	
inter-cloud gas	~ 1				
Intra-cluster	$\sim 10^{-3}$				
Universe	$\sim 10^{-6}$				

Table 3.1: Jeans wavelength, mass and time (free-fall time)

3.1.5 Gravitational Instability

Hydro-dynamical equations describing a gas of density ρ are given as

$$\rho \frac{d\mathbf{v}}{dt} = -\nabla p + \rho \nabla \Phi, \quad (3.28)$$

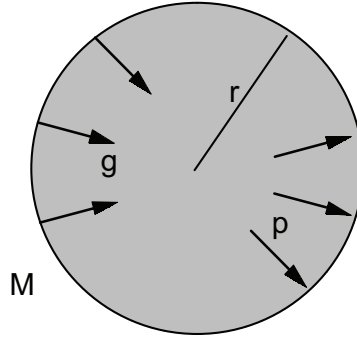


Figure 3.2: Gravitational contraction of a spherical gas cloud.

$$\frac{\partial(\rho v)}{\partial t} + \rho \nabla v = 0, \quad (3.29)$$

$$\nabla^2 \Phi + 4\pi G \rho = 0. \quad (3.30)$$

Here eq. (3.28), (3.29) and (3.30) are the equation of motion, fluid continuity, and Poisson's equation, respectively.

Consider a case when the density, pressure and the velocity are expressed as a superposition of a uniform component and a small perturbation:

$$\rho = \rho_0 + \delta\rho, \quad (3.31)$$

$$p = p_0 + \delta p, \quad (3.32)$$

$$v = v_0 + \delta v. \quad (3.33)$$

Remembering that ρ_0 , p_0 and v_0 satisfy eq. (3.28) - (3.30), we can rewrite the above equations as

$$\rho \frac{d\delta v}{dt} = -\nabla \delta p + \rho \nabla \delta \Phi, \quad (3.34)$$

$$\frac{\partial \delta p}{\partial t} = -\rho \Delta \delta v, \quad (3.35)$$

and

$$\nabla^2 \delta \Phi = -4\pi G \delta \rho. \quad (3.36)$$

Knowing that the pressure is related to the density by the adiabatic form, as $p \propto \rho^\gamma$, and that the sound velocity is related to ρ and p as

$$c_s^2 = \frac{dp}{d\rho} \simeq \frac{\delta p}{\delta \rho} = \gamma \frac{p}{\rho}, \quad (3.37)$$

we have

$$\frac{\delta p}{p} = \gamma \frac{\delta \rho}{\rho}, \quad (3.38)$$

or

$$\delta p = c_s^2 \delta \rho. \quad (3.39)$$

On the other hand, eq. (3.34) and (3.35) reduce to

$$\rho \frac{\partial}{\partial t} \Delta \delta v = -c_s^2 \nabla^2 \delta \rho + \rho \nabla^2 \delta \Phi. \quad (3.40)$$

Eliminating the terms including Φ from eq. (3.36) and (3.40), we obtain

$$\frac{\partial^2 \delta \rho}{\partial t^2} = c_s^2 \nabla^2 \delta \rho + 4\pi G \rho_0 \delta \rho. \quad (3.41)$$

This is a wave equation, and can be solved by introducing the exponential function

$$\delta\rho = \delta\rho_0 e^{i(\mathbf{k}\mathbf{r} + \omega t)}, \quad (3.42)$$

to yield the dispersion relation

$$\omega^2 = c_s^2 k^2 - 4\pi G \rho_0 = c_s^2 (k^2 - k_J^2), \quad (3.43)$$

with

$$k_J = \frac{1}{c_s} \sqrt{4\pi G \rho_0} \quad (3.44)$$

being called the Jeans wave number, or

$$\lambda_J = \frac{1}{k_J} = \frac{c_s}{\sqrt{4\pi G \rho_0}} \quad (3.45)$$

being the Jeans wavelength.

When $k < k_J$ or $\lambda > \lambda_J$, we have $\omega^2 < 0$, and the dispersion relation gives a growing wave: The instability grows, and the system is called to be unstable. The growth time is given by

$$t \sim \frac{1}{|\omega|} = \frac{1}{\sqrt{4\pi G \rho_0 - c_s^2 k^2}}. \quad (3.46)$$

For a small wavenumber $k \ll k_J$, or for a large wavelength $\lambda \gg \lambda_J$, we have

$$t \sim \frac{1}{\sqrt{4\pi G \rho_0}}, \quad (3.47)$$

which is approximately the same as the free-fall time.

On the other hand, if the wavenumber is large enough, so that the wavelength is, small ($k > k_J$ or $\lambda < \lambda_J$, $\omega^2 > 0$), the dispersion relation leads to an oscillation solution. This solution corresponds to

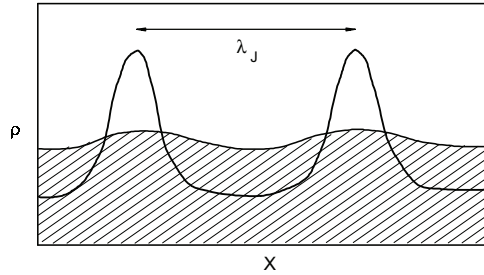


Figure 3.3: Gravitational instability (Jeans instability) of a density perturbation of a uniform gas.

a propagating compression wave: the small perturbation can not grow, but is smeared out with a sound wave. The instability, then, does not grow, and the system is stable.

3.1.6 The Birth of Stars

The fragmentation of cores of molecular gas clouds and GMCs into smaller and denser fragments (cloud-lets) is triggered by the gravitational instability. The fragments further contract gravitationally to form ‘proto-stellar’ clouds and then evolve to ‘proto-stars’. The time scale of the contraction is of the order of $t \sim 1/\sqrt{4\pi G\rho}$ and is $\sim 10^6$ yr in GMC cores. The Jeans mass of the instability is of the order of $\sim 0.1M_{\odot}$ for a gas of density $10^4 \text{ H}_2\text{cm}^{-2}$ and temperature 10 K. The Jeans mass gives a lower limit of the mass of proto-stellar clouds which can contract: gas fragments (cloud-lets) of mass larger than this critical mass can gravitationally contract. Therefore, stars that are born from a molecular cloud will have a distribution in a wide range of masses greater than the Jeans mass.

An ensemble of stars born from a single cloud or a group of clouds

form a cluster of stars. Groups of young stars born in a group are observed as OB associations and open clusters of stars. Globular clusters, comprising 10^5 stars, are suggested to be born from a larger mass cloud like as a GMC during a supersonic collision with another GMC.

The distribution of number density of stars as a function of mass of stars is called the initial mass function (IMF). The IMF is estimated by counting stars in a young cluster of stars or by counting local stars of various types (various masses). The IMF is known to have the form

$$f(M)dM \propto M^\mu dM$$

with $\mu \simeq -1.35 \sim -1.5$, and the lower and upper masses of stars are about $M_{\min} \sim 0.1M_\odot$ and $M_{\max} \sim 50M_\odot$. Although the number of lower-mass stars are larger, larger-mass stars more contributes the luminosity of a star cluster than lower-mass stars.

3.1.7 Other Instabilities

In astrophysics various types of instability are known to occur in the ISM. Typical instabilities are the thermal instability, Rayleigh-Taylor instability, Kelvin-Helmholtz instability, and the Parker-type instability.

3.1.8 . Thermal Instability

3.1.9 . Rayleigh-Taylor Instability

3.1.10 . Kelvin-Helmholtz Instability

3.1.11 . Parker Instability (Magnetic Inflation)

3.2 The Environment of Star Formation

3.2.1 Triggering of Cloud Compression

A galactic shock wave is induced by the density wave of stellar disk, and is the largest scale mechanism to compress the ISM in the Galaxy.

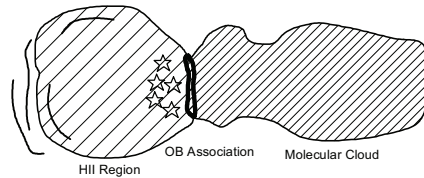


Figure 3.4: Star formation in molecular clouds.

The gas is compressed at the shock to form gaseous spiral arms, where the HI gas is transferred to molecular clouds. In the central region of the Galaxy, an oval potential of the inner stellar disk induces a stronger shock of gas, and the gas is rapidly accreted to the nuclear disk, where molecular clouds are formed and intense star formation occurs.

Stars are born through fragmentation of dense cores of molecular clouds and GMCs due to the gravitational instability of density perturbations (fluctuation). Such density fluctuations are triggered by local compression of gas either due to a shock wave penetration from outside, or due to stochastic collisions among turbulent eddies inside the cloud. In either case, collisions between gas clouds and cloud-lets (fragments) are the major sources of interstellar gas compression. Typical examples of collision phenomena are observed during mutual collisions of turbulent cloud eddies inside a cloud; collisions of two MCs or GMCs; encounter with expanding shell of supernova remnants; encounter by expanding HII regions; and injection of jets from the central region, etc..

3.2.2 Shock Wave

The shock wave is described by two discontinuous compressive gaseous flows 1 and 2. Let the temperature, velocity, density, pressure, and the

internal energy of the two gases be $T_1, u_1, \rho_1, p_1, U_1 = \frac{1}{\gamma-1}p_1$ and $T_2, u_2, \rho_2, p_2, U_2 = \frac{2}{\gamma-1}p_2$, respectively.

The basic equations describing the gases are: The equation of continuity:

$$\rho_1 u_1 = \rho_2 u_2, \quad (3.48)$$

The continuity of the momentum:

$$p_1 + \rho_1 u_1 u_1 = p_2 + \rho_2 u_2 u_2, \quad (3.49)$$

and the continuity of the energy:

$$u_1 p_1 + u_1 \left(\frac{1}{2} \rho_1 u_1^2 + U_1 \right) = u_2 p_2 + u_2 \left(\frac{1}{2} \rho_2 u_2^2 + U_2 \right), \quad (3.50)$$

or

$$u_1^2 + \frac{2\gamma}{\gamma-1} \frac{p_1}{\rho_1} = u_2^2 + \frac{2\gamma}{\gamma-1} \frac{p_2}{\rho_2}. \quad (3.51)$$

Eq. (3.48) to (3.50) are solved to give

$$\frac{p_2}{p_1} = \frac{2\gamma}{\gamma-1} M^2 - \frac{\gamma-1}{\gamma+1}, \quad (3.52)$$

and

$$\frac{u_2}{u_1} = \frac{\rho_1}{\rho_2} = \frac{\gamma-1}{\gamma+1} + \frac{2}{\gamma+1} \frac{1}{M^2}. \quad (3.53)$$

Here,

$$M = \frac{u_1}{c_1} = \sqrt{\frac{\rho_1 u_1^2}{\gamma p_1}} \quad (3.54)$$

is the Mach number, and

$$c_1 = \sqrt{\gamma RT_1} = \sqrt{dp/d\rho} \quad (3.55)$$

is the sound velocity.

When

$$u_1 \gg c_1 \quad (M \gg 1) \quad (3.56)$$

the gas is supersonic, and the solution reduces to

$$\frac{\rho_1}{\rho_2} \simeq \frac{\gamma - 1}{\gamma + 1}. \quad (3.57)$$

If the gas is adiabatic with the adiabatic index $\gamma = 5/3$, the supersonic shock compression gives

$$\frac{\rho_2}{\rho_1} \simeq 4. \quad (3.58)$$

If the gas is isothermal, or the temperature does not depend on the density and the pressure is proportional to the density ($p \propto \rho$; $\gamma = 1$), we have

$$\frac{\rho_2}{\rho_1} = M^2. \quad (3.59)$$

The interstellar gas during the galactic shock compression or during a cloud-cloud collision is almost isothermal, since the cooling time is shorter compared to the compression time scale. In a galactic shock wave, the velocity of in-flowing HI gas into a density-wave potential is of the order of $u_1 \sim 20 - 30 \text{ km s}^{-1}$ and the sound velocity is about $c_1 \sim 5 - 10 \text{ km s}^{-1}$, which yields a Mach number $M \sim 2 - 6$ and the compression of $\frac{\rho_2}{\rho_1} = M^2 \sim 4 - 36$. If two molecular clouds of internal sound velocity $\sim 0.1 - 1 \text{ km s}^{-1}$ collide at a velocity $u_1 \sim 5 \text{ km s}^{-1}$, the compression is as high as $\rho_2/\rho_1 \sim 25$ to 10^3 .

According to the Schmidt's law for the star formation rate and the gas density, the SFR can be expressed as $SFR \propto \rho_{\text{gas}}^\alpha$ with $\alpha \sim 1 - 2$.

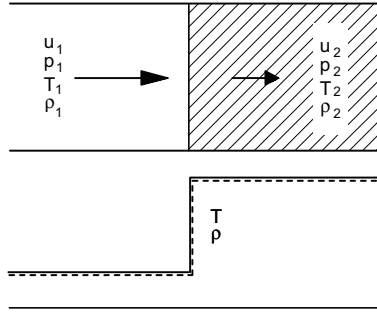


Figure 3.5: A shock wave due to supersonic collision of two gases.

The SFR, therefore, depends on the Mach number as

$$SFR \propto \frac{\rho_2^\alpha}{\rho_1} \sim M^{2\alpha}. \quad (3.60)$$

This relation, particularly when $\alpha \sim 2$, indicates that the starformation is most intense in the galactic shock region, and so is in the region near the galactic center, or in colliding gas clouds at a supersonic velocity.

3.2.3 Formation of Molecular Clouds

The formation of molecular clouds, particularly of giant molecular clouds (GMC), occurs during the large-scale compression of interstellar gas in the spiral arms. The mean density of ISM in the disk of the Galaxy is $n \sim 1 \text{ H cm}^{-3}$. The gas is compressed in the galactic shock by a compression rate of 10 to 30, or $n \sim 10 - 100 \text{ H cm}^{-3}$. The Jeans wave length in a compressed gaseous arm with $n \sim 10 \text{ H cm}^{-3}$ and sound velocity $c_s \sim 10 \text{ km s}^{-1}$ is then given by

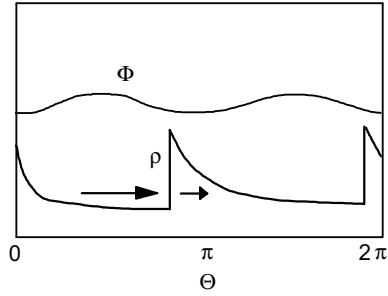


Figure 3.6: Compression of gas in the arm by galactic shock wave.

$$\lambda_J \sim \frac{c_s}{\sqrt{4\pi G \rho_{\text{gas}}}} \sim 100 \text{ pc.} \quad (3.61)$$

The Jeans mass is, therefore,

$$M_J \sim \rho \lambda_J^3 \sim 1.5 \times 10^5 M_\odot. \quad (3.62)$$

The contraction time of this cloud is given by

$$t \sim 1/\sqrt{G\rho} \sim 10^7 \text{ yr,} \quad (3.63)$$

which is comparable to the crossing time of the cloud through an arm.

3.2.4 Why spiral arms are bright

Molecular clouds are condensed along the galactic shock region in spiral arms. Since molecular clouds contain dust, the dense gaseous arm is observed as a dark lane. Stars are born in groups from dense molecular clouds. The mass function of born stars (mass M) (number of stars per unit volume per unit stellar mass) has the form

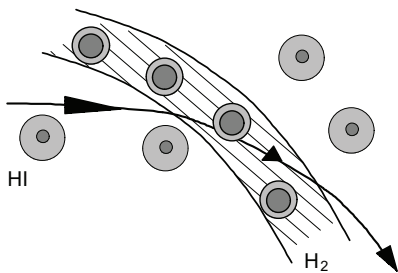


Figure 3.7: Compression of the gas in a spiral arm and the formation of molecular clouds.

$$f(M)dM \propto M^\mu dM \quad (3.64)$$

with $\mu \simeq -1 \sim -2$, and often quoted value is $\mu \sim -1.5$. This function is often called the initial mass function, and indicates that less massive stars dominate in number, and less number of massive stars are born compared to smaller stars.

The luminosity of a single star is approximately proportional to the mass as

$$L \propto M^{3.5} \quad (3.65)$$

The luminosity function per unit stellar mass is then written as

$$\phi(M)dM = Lf(M)dM \propto M^{3.5}M^\mu dM \sim M^2 dM. \quad (3.66)$$

The luminosity function per unit stellar luminosity is then related to the star luminosity L as

$$\phi(L)dL = L f(M)dL \propto L^{1+\mu/3.5}dL \sim L^{0.7}dL. \quad (3.67)$$

This shows that the luminosity per unit volume in the galactic disk is dominated by the light from most massive (luminous) stars, in spite of that their number is much less compared to smaller (less massive) stars.

The life time of a star can be related to the mass and luminosity as

$$t \sim M/L \sim M^{-2.5} \quad (3.68)$$

Massive stars evolve much more rapidly than smaller stars, and the life time of O- and B-type stars is as short as $\sim 10^5 - 10^7$ yr. The star-forming region soon after the formation of a star cluster shines predominantly due to OB stars, and the color is 'blue', emitting intense UV radiation. As the time elapses, massive stars evolve more rapidly than less massive stars do, and the OB stars explode to die and disappear. Thus, the luminosity of the region decreases rapidly within a few 10^7 years, and the color gets 'redder'.

By the galactic rotation the interstellar gas flows through a spiral arm, and the gas is compressed by the galactic shock during the passage through the arm. Molecular clouds form there, and are observed as the dark lane. OB stars are born from the clouds and shine in the down stream region of the dark lane for few 10^7 years, and are observed as a bright spiral belt. OB stars cannot survive till they leave the arm into the inter-arm region, for which it takes about 10^8 years. Because of these reasons, the belt of OB stars along the galactic shock wave is particularly bright in the disk. On the other hand, the luminosity per unit volume in the inter-arm region is far less than that along the bright arm.

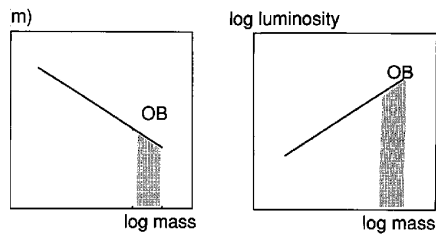


Figure 3.8: Mass function (number of stars per unit stellar-mass range per unit volume) and a luminosity function (luminosity of stars per unit stellar-luminosity range per unit volume).

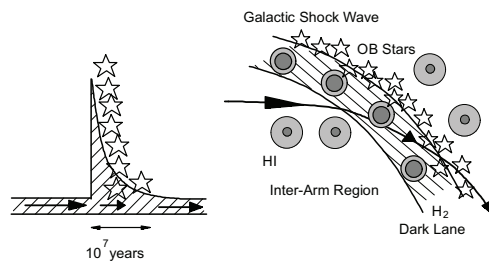


Figure 3.9: Why spiral arms shine.

3.3 HII Regions

3.3.1 Ionization sphere – Strömgren sphere –

Young stellar association soon after its formation contains massive stars of O and B types. The OB stars emit strong UV radiation, and ionize the ambient interstellar gas. Therefore, a star forming region is usually associated with an ionized gas, called HII regions.

Let $N_{\text{UV}} \simeq L_{\text{uv}}/h\nu$ be the number (production rate) of photon with wavelength shorter than $\lambda 912 \text{ \AA}$ emitted by an OB-star cluster, where L_{uv} is the luminosity of the cluster and $h\nu$ is the typical UV photon energy. The UV photons ionize hydrogen atoms in the ambient gas of density nh . On the other hand the ionized hydrogen recombines at a rate of $n_e n_i \alpha_r$, and absorb UV photons at this same rate. If the gas is composed of pure hydrogen, the rate of ionization and recombination in a sphere (radius r) of ionized gas around this OB star cluster is written as

$$4\pi r^2 n_{\text{H}} \frac{dr}{dt} = N_{\text{UV}} - \frac{4\pi}{3} n_e n_i \alpha_r r^3. \quad (3.69)$$

Here, the left-hand side is the rate of photo-ionization by the UV radiation, and the right-hand side is the rate of photo production by the OB stars and absorption by recombined atoms within the sphere. The shell of radius r is called the ionization front. The solution of this differential equation is given by

$$\frac{4\pi r^3}{3} = \frac{N_{\text{UV}}}{\alpha_r n_e n_i} \left(1 - e^{-\frac{n_{\text{H}}}{\alpha_r n_i n_e} t}\right). \quad (3.70)$$

In the initial phase of formation of the ionization, when the radius of the sphere is small enough, the recombination term in the right-hand side of eq. (3.69) is negligible:

$$\frac{4\pi r^3}{3} = V = \frac{N_{\text{UV}}}{n_{\text{H}}}t, \quad (3.71)$$

or

$$r \simeq \left(\frac{3N_{\text{UV}}}{4\pi n_{\text{H}}} \right)^{1/3}. \quad (3.72)$$

In the final phase of the expansion rate of the sphere (dr/dt) becomes zero, and the ionization and recombination balance with each other:

$$\frac{4\pi r^3}{3} \simeq \frac{N_{\text{UV}}}{n_{\text{i}}n_{\text{e}}\alpha_{\text{r}}}, \quad (3.73)$$

or

$$r \simeq \left(\frac{3N_{\text{UV}}}{4\pi n_{\text{i}}n_{\text{e}}\alpha_{\text{r}}} \right)^{1/3} \quad (3.74)$$

$$\sim 4.1 \left(\frac{n_{\text{i}}}{100 \text{ cm}^{-3}} \right)^{-1/3} \left(\frac{n_{\text{e}}}{100 \text{ cm}^{-3}} \right)^{-1/3} \left(\frac{\alpha_{\text{r}}}{4 \times 10^{-13} \text{ cm}^{-3} \text{ s}^{-1}} \right)^{-1/3} \quad (3.75)$$

$$\sim 4.1 \left(\frac{n_{\text{H}}}{100 \text{ cm}^{-3}} \right)^{-2/3} \left(\frac{\alpha_{\text{r}}}{4 \times 10^{-13} \text{ cm}^{-3} \text{ s}^{-1}} \right)^{-1/3} \cdot [\text{pc}] \quad (3.76)$$

This ionization sphere around OB stars in which the equilibrium between ionization and recombination is realized is called the ‘Strömgen’s sphere’.

The recombination rate α_{r} is related to the temperature T and metal abundance Z as

$$\alpha_{\text{r}} = 2A \left(\frac{2kT}{\pi m_{\text{e}}} \right)^{1/2} \frac{h\nu_0}{kT} Z^2 \phi \left(\frac{h\nu_0 Z^2}{kt} \right) \quad (3.77)$$

$$= \left(\frac{2.06^{-11} Z^2}{T^{1/2}} \right) \phi \left(\frac{h\nu_0 Z^2}{kt} \right) \text{ cm}^3 \text{ s}^{-1}. \quad (3.78)$$

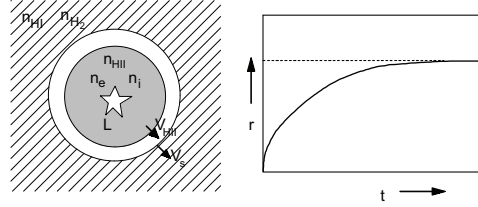


Figure 3.10: Expansion of ionization sphere of radius r around an OB-star cluster.

Here,

$$A = \frac{2^4}{3^{3/2}} \frac{he^2}{m_e c^3} = 2.105 \times 10^{-22} \text{ cm}^2 \quad (3.79)$$

($\propto \sigma$ = cross section of recombination) and ν_0 is the frequency at $\lambda 912\text{\AA}$, or $h\nu_0/k = 158,000 \text{ K}$. The ϕ is a slow function of T and Z (of order unity at $T > 10^5 \text{ K}$ and $\sim 10 - 100$ at $T \sim 10^5 - 10^4 \text{ K}$).

Suppose a single O5 star, or equivalently a cluster including 5 B0 stars, surrounded by a uniform hydrogen gas of density $n_{\text{H}} \sim n_{\text{i}} \sim n_{\text{e}} \sim 10 \text{ H cm}^{-3}$. The luminosity of the star(s) is $\sim 3 \times 10^5 L_{\odot} = 10^{39} \text{ erg s}^{-1}$, emitting $N_{\text{UV}} \sim 5.2 \times 10^{49} \text{ UV photons s}^{-1}$. For a recombination coefficient of $\alpha_{\text{r}} \sim 4^{-13} \text{ cm}^3 \text{ s}^{-1}$, we obtain the radius of the Strömngren sphere as $r \sim 20 \text{ pc}$.

3.3.2 Expanding Ionization Front

In the above expression of a spherical HII region we have ignored the flow (or expansion) of the gas inside the sphere. However, the ionized gas has been heated up to $\sim 10^4 \text{ K}$, much higher than the temperature of the surrounding gas ($\sim 100 \text{ K}$ for HI, and $\sim 10 - 100 \text{ K}$ for H_2 gas). This implies that the ionization sphere is not in a pressure equilibrium

with the ambient gas: it expands due to the higher internal pressure.

In initial phase of expansion, the expansion velocity of the sphere $v = dr/dt$ and the radius r are related to the internal energy E as

$$E \sim \frac{1}{2}Mv^2 \sim \frac{1}{2} \frac{4\pi r^3}{3} m_{\text{H}} n_{\text{H}} v^2, \quad (3.80)$$

where $M_{\text{s}} = \frac{4\pi}{3} r^3 m_{\text{H}} n_{\text{H}}$ is the plowed mass in the sphere from the ambient gas. The internal energy is related to the integrated photon energy that have been spent for ionization of the hydrogen gas minus radiated energy by the recombination:

$$E \sim L_{\text{uv}} t - \int \frac{4\pi r^3}{3} h\nu n_{\text{i}} n_{\text{e}} \alpha_{\text{r}} dt. \quad (3.81)$$

Alternatively, since the temperature of the HII region is known to be maintained at $\sim 10^4$ K due to radiative cooling as well as expansion, this energy can be written simply as

$$E \sim \gamma M_{\text{s}} RT \sim \gamma \frac{4\pi r^3}{3} n_{\text{H}} kT. \quad (3.82)$$

Using eq. (3.80) and (3.81), we obtain

$$v \sim \sqrt{2\gamma kT} \sim c_{\text{s}}. \quad (3.83)$$

This implies that the sphere expands at the sound velocity of the internal gas: $v \sim c_{\text{s}} \sim 10 \text{ km s}^{-1}$ for $T \sim 10^4$ K. Namely, the expansion velocity is large enough compared to the sound velocity in the ambient gas ($c_{\text{s}0} \sim 0.3 \text{ km s}^{-1}$ for H_2 gas; $\sim 1 \text{ km s}^{-1}$ for H gas): The expansion is supersonic with a Mach number $M \sim 10$, and therefore, a strong shock wave forms at the interface of the surrounding neutral gas and the expanding HII region (sphere).

In a later phase when a Strömngren sphere is realized, the ionization front at radius r expands faster (at a velocity V_{ion}) than the expanding

HII sphere of radius with a velocity v_{HII} and $n_e \sim n_i \sim \rho_{\text{HII}}$. From the Strömngren sphere condition we have

$$r_{\text{ion}}^3 n_e n_i \sim r_{\text{HII}}^3 \rho_{\text{HII}} \sim \text{const}, \quad (3.84)$$

which leads to

$$V_{\text{ion}} = dr_{\text{ion}}/dt \sim -\frac{2r_{\text{ion}}}{3\rho_{\text{HII}}} \frac{d\rho_{\text{HII}}}{dt}. \quad (3.85)$$

The HII sphere expands following

$$r_{\text{HII}}^3 \rho_{\text{HII}} \sim \text{const}, \quad (3.86)$$

to yield

$$v_{\text{HII}} = dr_{\text{HII}}/dt \sim -\frac{r_{\text{HII}}}{3\rho_{\text{HII}}} \frac{d\rho_{\text{HII}}}{dt}. \quad (3.87)$$

Since $r_{\text{HII}} \sim r_{\text{ion}}$, we have from eq. (3.85) and (3.87) we have

$$v_{\text{HII}} \sim \frac{1}{2} V_{\text{ion}}. \quad (3.88)$$

The expanding sphere of the HII gas forms an expanding shell at velocity $V_s \sim v_{\text{HII}} \sim 1/2 v_{\text{ion}}$, and the ambient HI gas of density ρ_{HI} (velocity=0) is accumulated. From the continuity condition of the shock front we have

$$\rho_{\text{HI}} V_s^2 = p_{\text{HII}} + \rho_{\text{HII}} \left(\frac{1}{2} V_s\right)^2. \quad (3.89)$$

Here, p_{HII} is the pressure of the HII region and is related to the density and sound velocity of the HII gas c_{HII} as ($\gamma \sim 1$);

$$p_{\text{HII}} \sim \rho_{\text{HII}} c_{\text{HII}}^2. \quad (3.90)$$

Then, we obtain an expression which relates the expanding velocity

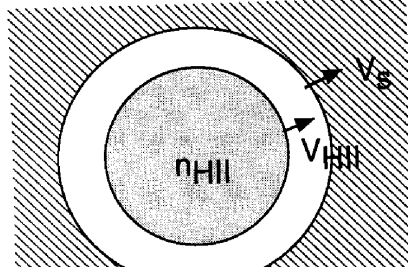


Figure 3.11: Expansion of a spherical HII region.

of the HII shell with the sound velocity and ambient HI density as

$$V_s \sim c_{\text{HII}} \sqrt{\frac{\eta}{1 - \frac{1}{4}\eta}}, \quad (3.91)$$

where η is the density ratio of the HII region and HI region.

$$\eta = \rho_{\text{HII}}/\rho_{\text{HI}}. \quad (3.92)$$

3.3.3 Shock Compression of Ambient gas

The above equations apply also for an HII region expanding into a molecular cloud, in which case the HI density can be read as H_2 density. When the HII region expands into an HI cloud or into a molecular cloud, the HII density is small enough compared to the ambient gas density; $\rho_{\text{HII}} \ll \rho_{\text{HI}}$ or $\rho_{\text{HII}} \ll \rho_{\text{mc}}$, and the expansion velocity is simply expressed as

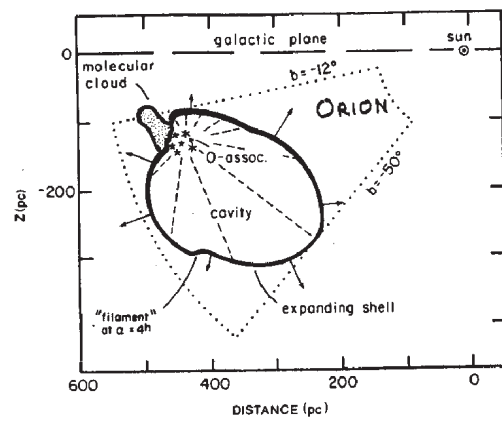


Figure 3.12: Expansion of an HII region into a small-density ISM, forming a huge shell.

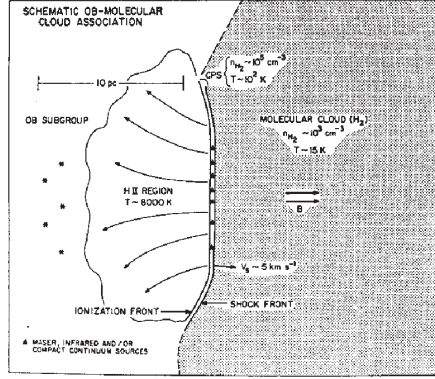


Figure 3.13: Shock compression of a molecular gas cloud by an expanding HII region.

$$V_s \sim c_{\text{HII}} \sqrt{\rho_{\text{HII}}/\rho_{\text{HI}}} \quad (c_{\text{HII}} \sqrt{\rho_{\text{HII}}/\rho_{\text{mc}}}). \quad (3.93)$$

In a normal HII region, we may assume $c_{\text{HII}} \sim 10 \text{ km s}^{-1}$ (for $T \sim 10^4 \text{ K}$) and $\rho_{\text{HII}} \sim 10^4 \text{ H cm}^{-3}$. If the shell expands into an HI cloud of density $\rho_{\text{HI}} \sim 100 \text{ H cm}^{-3}$, the expansion velocity is at $V_s \sim 3 \text{ km s}^{-1}$, and is supersonic. If the shell expands into a molecular cloud of density $\rho_{\text{mc}} \sim 10^3 \text{ H cm}^{-3}$, where the sound velocity is about 0.3 km s^{-1} , the expansion is at 1 km s^{-1} , and is still supersonic.

From these estimation we learn that an HII region expanding into an HI cloud or into a molecular cloud produces a shock wave and compresses the neutral gas to form a high density shocked layer. If we assume that the gas is isothermal, the compression of the gas at the shocked layer is of the order of $M^2 \sim 10$ for $c_s \sim 0.3 \text{ km s}^{-1}$ ($T \sim 10 \text{ K}$) and $V_s \sim 1 \text{ km s}^{-1}$. Such a strong compression of the neutral gas triggers further contraction of proto-stellar gas clouds.

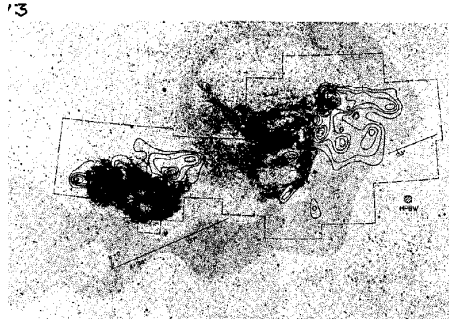


Figure 3.14: HII regions and compressed molecular gas at the edge of GMCs: M17 and W3 and GMCs.

3.4 Sequential Star Formation

3.4.1 Propagation of Shock Compression by an HII region

Once a cluster of stars including OB stars is formed in or near the surface of a molecular cloud, an HII region develops around the OB stars. The HII region expands, and produces a shock-compressed layer in the molecular cloud with compression by a factor of ~ 10 . The growth time ($\sim \sqrt{1/4\pi\rho}$) of the compressed layer is smaller than that of the ambient gas, and the gravitational instability grows more rapidly, resulting in an enhancement of further fragmentation of the layer into proto-stellar clouds.

Thus, the compression by an expanding HII region results in a further formation of stars in the molecular cloud, giving rise to a new HII region due to newly born OB stars. This new HII region, then, compresses the cloud to form another compression layer. In this way, the ‘star-forming layer’ propagates into the cloud interior. This process is

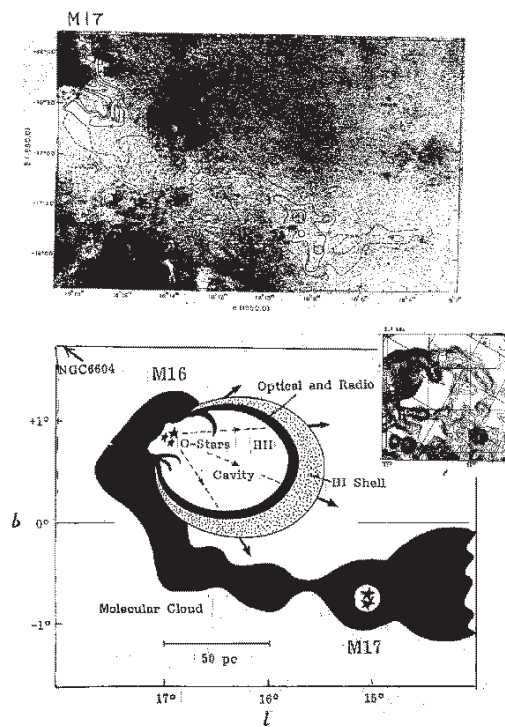


Figure 3.15: Ring of HII regions in the Scutum arm, surrounded by a molecular gas shell (seen in CO) and a larger-radius HI shell.

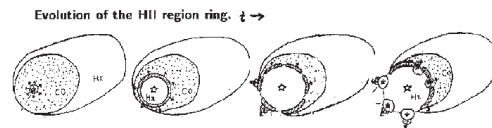
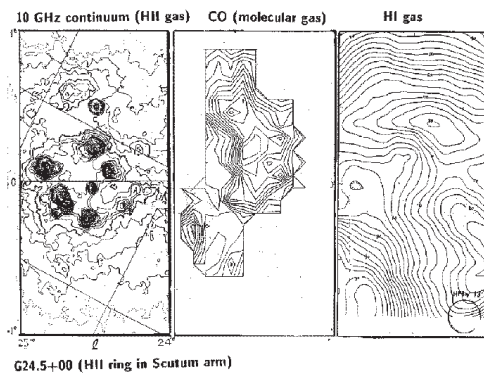


Figure 3.16: Ring of HII regions in the Scutum arm (continued).

called ‘the sequential star formation’ in a molecular cloud.

3.4.2 The Orion region

The Orion molecular cloud, particularly its core, is an intermediate class of star-forming region, where infrared sources indicating an on-going starformation have been found. It is known that this star forming region is associated with an HII region, called Ori A (in radio) and the Orion Great Nebula (in optical), whose age is approximately $10^6 - 10^7$ yr. The Orion star forming region is further associated with a young stellar association involving stars of age $\sim 10^7$ yr several pc away. Another association of stars with an age $\sim 10^8$ has been found in a farther location at about a few tens of pc. Furthermore, all these objects are surrounded by a diffuse HII shell of radius ~ 100 pc as seen in the $H\alpha$ emission. These facts show that the place of star formation has shifted toward the present molecular cloud region in the past 10^8 yr. Namely, a sequential star formation has occurred in the Orion molecular cloud for the past 10^8 yr, and is still on-going.

3.4.3 M16 - M17 Region

M17 is an intense HII region associated with giant molecular clouds which extend for about 100 pc along the galactic plane. The region is supposed to be the place where the sequential star formation is on-going.

M16 is an older HII region than M17 with an extended $H\alpha$ nebula and associated thermal radio emission region. A giant shell of diameter about 50 pc is found in the thermal radio emission and is also surrounded by an HI gas shell expanding at a velocity of about 20 km s^{-1} .

3.4.4 Sgr B2

Sgr B2 is a strong HII region in the central region of the Galaxy at $l = 1^\circ.2$, $b = 0^\circ$, comprising several compact radio emitting sources, and is observed to be expanding at an ultra-supersonic velocity (several tens of km s^{-1}). The Sgr B2 HII region is surrounded by clumpy shell of dense molecular cores each $\sim 10^4 M_\odot$, and the shell is in touch with the HII region and will be the sites of star formation in the near future. The dense molecular shell may be formed by a shock compression by the expanding HII gas, and the clumps would be formed by the gravitational fragmentation of such compressed shell. The whole region is located in the central region of giant molecular complex of diameter 50 pc and mass $10^6 M_\odot$.

The star-formation efficiency (SFE) defined by the ratio of the UV photon intensity necessary for the excitation of the HII gas to the mass of molecular gas (fuel for the star formation) is smaller compared to the SFE for the other regions. This indicates that Sgr B2 will be in an extremely young phase of star formation, embedded in a potential site of much more intense star formation in the future: Sgr B2 region is supposed to be in a “pre-burst” phase.

3.5 Supernova Remnants

3.5.1 Supernovae (SN) and Supernova remnants (SNR)

Stars with masses less than the Chandrasekhar limit ($1.3 M_\odot$) at the final stage of the evolution die “quietly” via white dwarfs. If the mass of a star at the final stage of the evolution exceeds the limit, which usually occurs for stars with masses of a few M_\odot during the main sequence after which the star loses the mass due to stellar wind, explodes as a supernova (SN). The rate of SN explosions in the Galaxy is estimated to be approximately 1 SN per 30 years : $r_{\text{SN}} \sim 1/30 \text{ yr}^{-1}$.

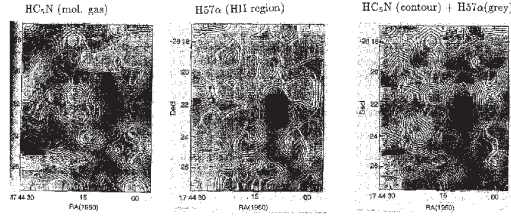


Figure 3.17: Sgr B2 HII region observed in the $H57\alpha$ line at 34.59561 GHz and a clumpy shell of dense molecular gas cores observed in the HC_5N ($J=13-12$) molecular line at 34.614386 GHz. Both the maps were obtained by a simultaneous observation using the 45-m telescope at Nobeyama equipped with a wide-band spectrometer.

During the explosion a huge amount of kinetic energy ($E_0 \sim 10^{49} - 10^{51}$) per SN is supplied to the interstellar medium, giving rise to a strong shock wave. The shock wave expands into the interstellar gas in a spherical shell of the shock front, and is called supernova remnants (SNR).

Type I SN: Supernovae as the result of explosion of population II (less massive) stars are classified as type I SN, and occur in the old population disk. Type I SN has the maximum absolute magnitude of about -20 mag., and the rising time scale is as fast as a few days, and as well the decaying time is also short as a couple of weeks. The energy released by type I SN is of the order of $10^{49} \sim 10^{50}$ erg, and the kinetic energy given to the ISM is smaller compared to type II SN as described below.

Type II SN: Massive stars of O and B types (population I) explode as type II SN, and are observed mainly in spiral arms. The maximum absolute magnitude of this type of SN is about 18 mag., and the light curve is more long-lasting for a month or more. Although the luminosity of type II SN is less than that of type I, they supply more amount of

kinetic energy to the ISM through their strong shock wave induced by larger amount of ejecta from the envelopes of the progenitor massive stars.

SNRs are subjects for the physics of gas dynamics and shock wave propagation through the interstellar gas and clouds. SNRs supply a considerable amount of kinetic as well as thermal energy to the interstellar gas, acting to maintain the turbulence in the ISM. SNRs are therefore deeply coupled to the heating and compression of gas clouds, star formation, excitation of turbulence, compression of magnetic fields and acceleration of cosmic rays, and are also the sources of heavy elements. These will further influence the ISM physics of the galactic disk and halo as well as the evolution of ISM in the Galaxy.

3.5.2 Classification of SNR

Shell-type SNR:

“Normally” observed SNRs are spherical shells with numerous thin filaments (or sheets), and is most naturally taken as expanding spherical shock waves driven by a point explosion at the center. The Cygnus Loop, IC 443 and S147 are the most typical examples of late stages. These SNR have diameters of about 10 to 30 pc and are expanding at a supersonic velocity of $\sim 100 \text{ km s}^{-1}$. Cas A is an example as the young shell type SNR, which is expanding at a velocity as high as $\sim 2000 \text{ km s}^{-1}$.

Filaments comprises various components of different temperatures between 10^3 to 10^5 K, emitting various emission lines characteristic of the temperatures. They are for, example, $\text{H}\alpha$, $\text{H}\beta$ ($n_e \sim 100 \text{ cm}^{-3}$; $\sim 10^4$ K), HeI , $[\text{NII}]$, OI , OIII , $[\text{OII}]$, $[\text{OIII}]$ ($n_e \sim 10^3 - 10^4 \text{ cm}^{-3}$; several 10^4 K), $[\text{NeIII}]$, or $[\text{SII}]$ lines. The interior of the shell is usually filled by high-temperature ($10^6 \sim 10^7$ K) ionized gas, emitting X-rays.

Shell type SNRs emit synchrotron radio emission from the filaments (sheets), having a steep spectral index ($\alpha \sim -0.5 - 1$). The radio

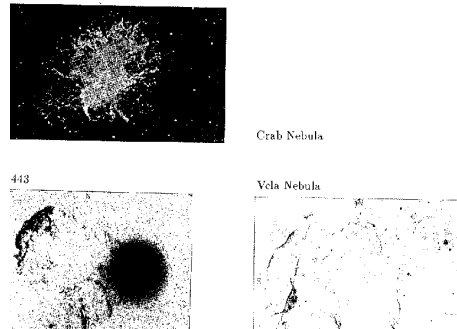


Figure 3.18: Supernova remnants in optical.

emission is usually polarized in the direction perpendicular to the shell surface, which is because the magnetic field is compressed along the shell surface.

Filled-center SNR:

There have been found many SNRs with amorphous morphology, which show no clear shell structure but have a filled-center morphology. These SNRs are called filled-center SNR. Their spectral index is more flat ($\alpha \sim 0$) than that for shell type, suggesting that younger cosmic-ray electrons are accelerated or supplied more constantly.

The Crab Nebula (Tau A) is a typical SNR of this type, which comprises numerous filaments that are more chaotic and distributed over the remnant. This type of SNR shows no clear shell structure, and the filaments are believed to be excited by injection of high-energy particles from the central neutron stars (pulsar). A number of filled-type SNRs have been discovered in the decade, which were difficult to be found in the early days because of their irregular shapes.

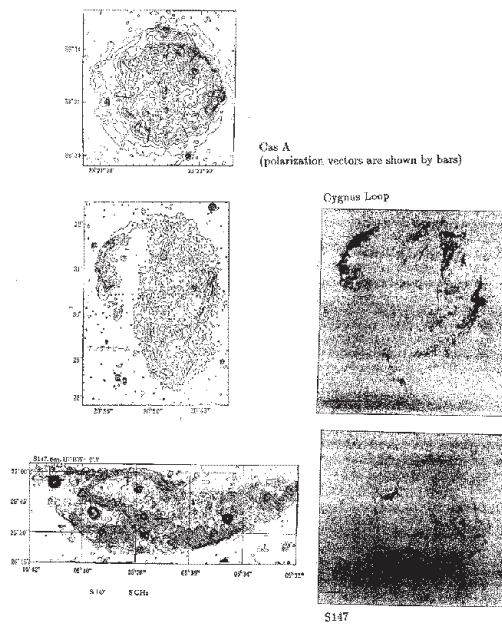


Figure 3.19: Supernova remnants in radio.

No. (l, b)	Ang Dia (min arc)	Dia. (pc)	Dist. (kpc)	$\Sigma_{1\text{GHz}}$ $\text{Wm}^{-2}\text{Hz}^{-1}\text{Str}^{-1}$	Classif.	Remarks
G004.5+6.8	3.8	3.3	3	$2.1 \cdot 10^{-19}$	Shell	1604 Kepler SN
G006.4-0.1	49	34	2.4	$2.0 \cdot 10^{-20}$	Shell	W28
G023.3-0.3	21	30	5.0	$2.0 \cdot 10^{-20}$	Shell	W41
G074.0-8.6	180	41	0.8	$9.3 \cdot 10^{-20}$	Shell	Cygnus Loop
G111.7-2.1	4.2	3	2.8	$2.9 \cdot 10^{-17}$	Shell	Cas A
G120.1+1.4	7.9	12	5.0	$1.4 \cdot 10^{-19}$	Shell	1572 Tycho 3C10
G180.0-1.7	166	79	1.6	$3.0 \cdot 10^{-22}$	Old shell	S147
G184.6-5.8	3.5	2.2	2.2	$1.2 \cdot 10^{-17}$	Fill Cen	1054 Crab Neb
G189.1+2.9	40	23	1.9	$1.5 \cdot 10^{-20}$	Shell	IC443
G263.9-3.0	256	44	0.6	$4.0 \cdot 10^{-21}$	Amorph	Vella Nebula
G327.6+14.0	34	13	1.3	$2.7 \cdot 10^{-21}$	Shell	1006 SN

Table 3.2: Typical SNRs and classification

3.5.3 The $\Sigma - D$ Relation and the Distribution of SNR

The $\Sigma - D$ Relation

The surface brightness of a supernova remnant is defined by

$$\Sigma_{\nu} = F_{\nu}/\Omega, \quad (3.94)$$

where F is the total flux density of the source at frequency ν and Ω is the apparent solid angle (in steradian) of the remnant. Empirically, the surface brightness is known to be related to the true linear diameter of a remnant D and its height from the galactic plane z as

$$\Sigma_{1\text{GHz}} \simeq 2.9 \times 10^{-14} D^{-4} \exp(-|z|/54 \text{ pc}), \quad (3.95)$$

or

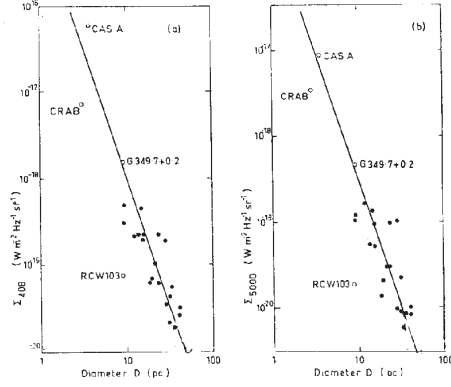


Figure 3.20: Surface brightness-Diameter ($\Sigma - D$) relation for SNRs.

$$D \simeq (3.2 \times 10^{13} \Sigma_{1\text{GHz}} \exp(|z|/54 \text{ pc}))^{-1/4} = 4.13 \times 10^{-4} \Sigma_{1\text{GHz}}^{-0.25} \exp(-|z|/216 \text{ pc}), \quad (3.96)$$

where $\Sigma_{1\text{GHz}}$ is the surface brightness at 1 GHz in $\text{W m}^{-2} \text{Hz}^{-1} \text{sr}^{-1}$, and D and z are in pc. This is called the $\Sigma - D$ relation, and is used to obtain the distance to a SNR by measuring the total flux density and apparent extent.

Distribution of SNR in the Galaxy

Given the diameter of a SNR, its distance d can be estimated by $d = D/\theta$, where θ is the angular diameter of the SNR. From d and the position on the sky (l, b) we can derive the three-dimensional position of the SNR.

About 25 SNRs have been discovered within 1 kpc from the Sun, which are supposed to be sampled completely. Although a more number of SNRs are found at larger distances, their sampling would be not complete because of the contamination by the galactic diffuse radio emission as well as the extinction. From the almost complete sampling

in the solar 1 kpc vicinity, the total number of SNRs in the Galaxy is estimated to be of the order of $25 \times (\pi 10 \text{ kpc}^2 / \pi 1 \text{ kpc}^2) \sim 2500$. Since the mean life time of a SNR is roughly 10^5 years, the rate of SN explosions can be estimated as $r_{\text{SN}} \sim 2500/10^5 = 1$ per 40 yr. (We know that the rate is about 1 per 20 to 30 years from a more accurate study.)

The distribution of SNRs in the Galaxy as projected on the galactic plane is shown in Fig. 3.21. Taking into account that the sampling is not complete beyond 1 kpc of the sun, we can see that that SNRs are distributed more concentrated in the galactic center region, and probably along the spiral arms. Fig. 3.22 shows a distribution of SNRs in the z direction as a function of the distance from the Galactic Center. Most of SNRs are distributed in a thin layer of about $|z| < 100$ pc, and the distribution can be fitted by an exponential law as

$$N_{\text{SNR}} \sim N_{0,\text{SNR}} e^{-z^2/z_{\text{SNR}}^2} \quad (3.97)$$

with $z_{\text{SNR}} \simeq 60$ pc. Note that the molecular gas layer has about the same scale thickness, suggesting a relation of the SN explosion and the molecular gas density.

Shaded areas denote spiral arms.

3.5.4 Evolution of a SNR

The evolution of a spherical shell of produced by a SN explosion can be approximated by a spherical shock propagation in a uniform medium. If the shell evolves in an adiabatic condition, namely if the radiative cooling time of the shell is short enough compared to the time scale of the expansion, the propagation of a spherical shock wave produced by a point explosion in a uniform medium can be described by a Sedov's similarity solution. Let the thermal+kinetic energy released by a SN explosion be E_0 , which is transformed to the kinetic energy of expansion of the surrounding gas of density ρ_0 . Suppose that the gas

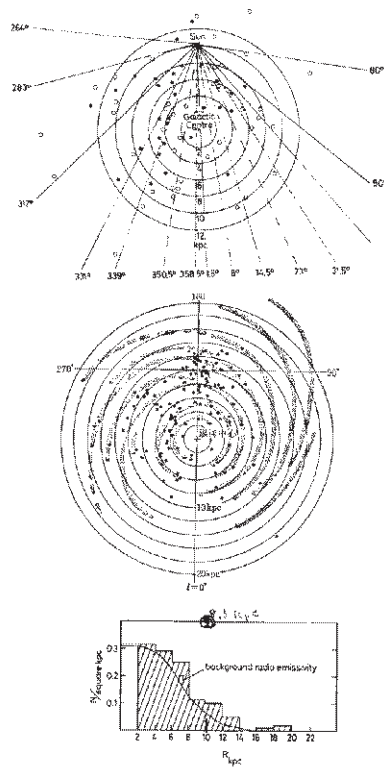


Figure 3.21: Distribution of SNRs projected on the plane of the Galaxy.

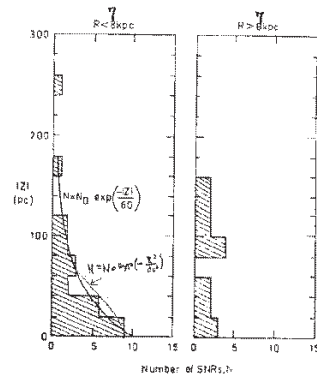
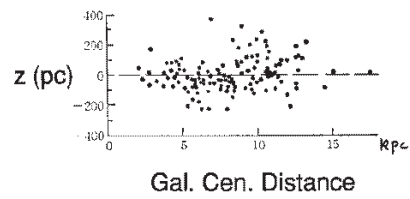


Figure 3.22: Distribution of SNRs in the z direction as a function of the galactocentric distance.

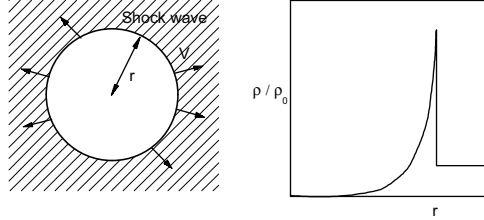


Figure 3.23: A spherical shocked shell produced by a point explosion in a uniform ISM by a SN.

is shock compressed in a thin shell of radius r which is expanding at a velocity v . Then, we have

$$E_0 \sim \frac{1}{2} \left(\frac{4\pi}{3} r^3 \rho_0 \right) v^2, \quad (3.98)$$

where $M = (4\pi/3)r^3\rho_0$ is the accumulated (snow-plowed) mass of the ISM in the shocked shell. Since $v = dr/dt$, we can solve the above equation to yield

$$v \sim \left(\frac{E_0}{\rho_0} \right)^{1/5} t^{-3/5}, \quad (3.99)$$

and the radius increases with t as

$$r \sim \left(\frac{E_0}{\rho_0} \right)^{1/5} t^{2/5}. \quad (3.100)$$

The energy given to the surrounding ISM is about $E_0 \simeq 10^{50} \sim 10^{51}$ erg for type I SN and $10^{49} \sim 10^{50}$ erg for type I.

These formulations apply only for a limited phase of the evolution of a SNR when the compressed gas in the shell is approximated to be adiabatic. In reality, however, a SNR experiences various phases according to the time elapsed from the explosion as well as depending

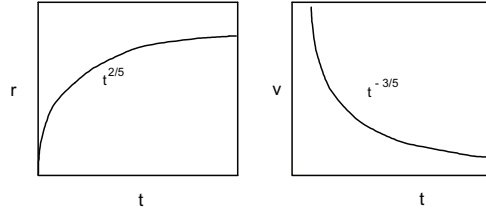


Figure 3.24: Time variation of the radius and expansion velocity of an adiabatic shell of a spherical shock wave.

on the physical condition of the surrounding ISM. A typical evolution of a SNR will be described as follows.

Free expansion phase ($t \sim 0 - 10^3$ yr)

At the very initial phase of expansion, when the mass of shock-accumulated gas from the ISM is smaller than the mass of ejecta from the SN, the ejecta expands almost freely at a velocity of v_0 , which is related to the energy as $E_0 \sim (1/2)v_0^2$. For a type II SN, the mass and explosive energy are about $M_0 \sim 5M_\odot$ and $E_0 \sim 10^{51}$ erg, respectively, and therefore, $v_0 \sim 5000$ km s $^{-1}$; for a type I SN, $M_0 \sim 1M_\odot$ and $E_0 \sim 10^{49}$ erg, and $v_0 \sim 1000$ km s $^{-1}$. The Crab Nebula is an example of this phase.

Adiabatic shocked-shell phase ($t \sim 10^3 - 10^4$ yr)

When the accumulated mass from the ISM ($M \sim (4\pi/3)r^3\rho_0$) begins to exceed the initial mass of the ejecta (M_0), the shell expansion begins to suffer deceleration, and a shocked shell forms. This occurs at about $t \sim 10^3$ yr and $r \sim 3$ pc. If the cooling time scale of the shell is smaller than the age (time scale of the expansion) $t_{\text{cool}} < t_{\text{exp}} \sim r/(dr/dt) \sim r/v$, the shell can be approximated by an adiabatic spherical shock

wave as described above. The cooling time for a shocked gas of density $n \sim 4n_0$ with $n_0 \sim 1 \text{ H cm}^{-3}$ and temperature 10^6 K corresponding to an expansion velocity 100 km s^{-1} is about 10^4 years. Therefore, the adiabatic expansion applies for SNR of $t < 10^4 \text{ yr}$.

Dense shell formation ($t \sim 10^4 - 10^5 \text{ yr}$)

At this stage the radiative cooling of shock-compressed gas cannot be ignored, since the cooling time becomes comparable to or shorter than the expansion time scale of the remnant. The adiabatic approximation does not apply any more, and the shell is more effectively compressed by the cooling: If the cooling is effective enough, the shock compression amounts to $M^2 \sim (v_{\text{shell}}/c_s)^2$, where M is the Mach number and c_s is the sound velocity. The shell is fragmented into numerous sheets and filaments by thermal as well as hydrodynamical instabilities. The shock-compressed filaments and sheets radiate line emissions and cool down to denser fragments with density $10^2 - 10^3 \text{ cm}^{-3}$. The thickness of the filaments is of the order of 0.1 pc , much smaller than the SNR radius, $20\text{-}30 \text{ pc}$. Typical examples are seen in the Cygnus Loop, IC 443 and S147.

Late phase; Fading into ISM

When the shell radius exceeds $\sim 30 \text{ pc}$ at $t > 10^5 \text{ yr}$, the expansion velocity decreases to a few tens km s^{-1} . The shell suffers from significant deformation due to the interaction with turbulent ISM and clouds. When the shell expands further and is decelerated, with the expansion velocity becoming comparable to the sound velocity of the ISM, the SNR fades into the ISM as sound waves. Any SNR disappears at this stage, finally reducing the kinetic energy to the turbulent motion of ISM.

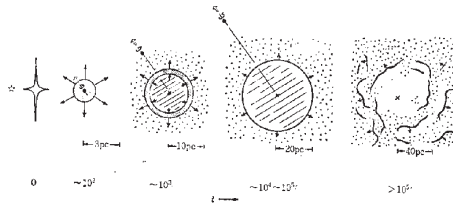


Figure 3.25: Evolution of a SNR.

3.5.5 Interaction with the ISM

Due to interaction with interstellar clouds the SNR shell deforms from spherical shape. When it encounters a cloud of similar size to the shell radius, the SNR will attain a highly asymmetric shape: Cygnus Loop and IC 443 are typical examples of such interaction. If the size and mass of the cloud is large enough, the propagation of a shock wave is strongly refracted, and a focusing shock into the cloud often occurs. The focusing shock compresses the cloud, resulting in an implosion of the cloud. On the other hand, a small cloud are often ‘evaporated’ by the shock heating.

Even if the surrounding ISM is uniform, the surface of the SNR shell are often fragmented due to hydro-dynamical instabilities. As the Sedov solution indicated, the SNR shell is decelerated by

$$d^2r/dt^2 \sim -t^{-8/5}. \quad (3.101)$$

In a coordinate system in which the shell surface is at rest, the acceleration points toward the outer region: The SNR shell lies on the ISM with the acceleration (apparent gravity) pointing from a denser region to a rare region. Therefore, a Rayleigh-Taylor instability grows. This instability is the major cause for filamentary structures observed

in SNRs, and also for clumpy structures observed in such early phase (and therefore, stronger deceleration) SNR as the Cas A. According to the compression of the gas as well as the interstellar magnetic fields, cosmic rays are accelerated, and such filaments and clumps are a strong radio emitting regions.

3.5.6 Implications of SNRs for the Galaxy Evolution

SNR and Star Formation

The life times of massive stars (O stars) are approximately 10^7 years (1.2×10^7 yr for $15 M_{\odot}$; 3×10^7 yr for $10 M_{\odot}$; 9×10^7 yr for $5 M_{\odot}$). Therefore, type II SNs explode in the vicinity of the places where the progenitor stars were born such as near to the SF region rich in MC and GMCs. The encounter of a SNR shock wave with a molecular cloud would, then, further compress it to create another SF region. Hence, a SN explosion followed by a shock wave (SNR) is another type of triggering mechanism of the sequential SF in the cloud complex.

It is also happens that large-scale shock waves produced by SNR hit more distant MCs and GMCs. This would further trigger SF inside the clouds, leading to a larger-scale ‘inter-cloud’ sequential SF. In this way, the SF propagates from clouds to clouds, and the inter-cloud sequential SF acts to a stochastic formation of spiral patterns of OB stars in a galactic disk in differential rotation.

Energy Supply to ISM Turbulence

If there is no energy supply, the interstellar turbulence (random motion of interstellar clouds) will decay within 10^7 years (\sim collision time among the clouds) due to dissipation through elastic collisions among clouds. The kinetic energy necessary for maintaining the turbulence is thought to be supplied by kinetic energy from SN explosions. Since the total mass of ISM is $M_{\text{ISM}} \sim 0.05 M_{\text{G}} \sim 10^{10} M_{\odot}$, the kinetic energy

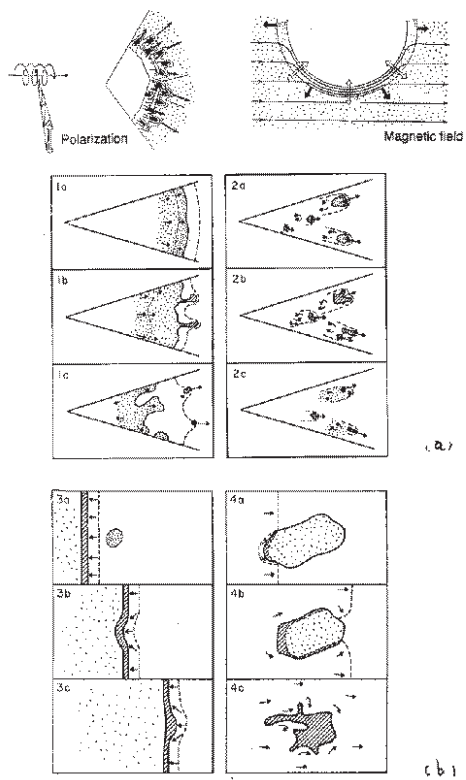


Figure 3.26: Interaction of a SNR shell with ISM. (a, b) Growth of Rayleigh-Taylor instability.

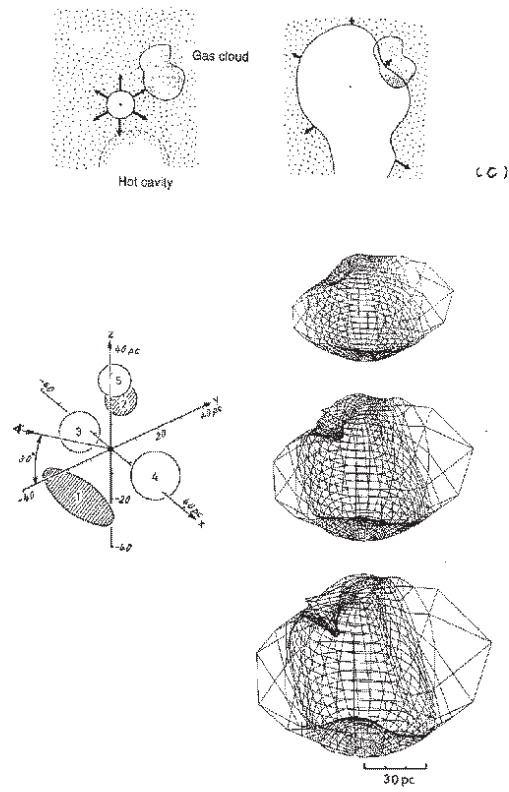


Figure 3.27: Interaction of a SNR shell with ISM. (c) Large-scale deformation of a shell due to collisions with large clouds by numerical simulation.

of turbulent motion is

$$E_{\text{turb}} \sim (1/2)M_{\text{ISM}}v_{\text{t}}^2 \sim 5 \times 10^{54} \text{ erg.} \quad (3.102)$$

The energy dissipation rate is of the order of

$$dE_{\text{t}}/dt \sim E_{\text{t}}/\tau \sim 5 \times 10^{47} \text{ erg/yr.} \quad (3.103)$$

If $\sim 10\%$ of the total energy released by SN explosions is finally given to the ISM turbulence as kinetic energy, the rate is estimated to be

$$dE/dt \sim 0.1 \times E_0 r_{\text{SN}} \sim 3 \times 10^{48} \text{ erg/yr,} \quad (3.104)$$

where

$$r_{\text{SN}} \sim 1/(30 \text{ yr}) \quad (3.105)$$

is the rate of type II SN explosions in the Galaxy. This is a much larger amount compared to the dissipation rate of the ISM turbulent energy: Thus, only a fraction of the energy released by SN explosions is sufficient for a steady excitation of the ISM turbulence.

Energy Supply to the Halo Gas and Galactic Winds

The rest of the kinetic energy from SN would be used for heating up the inter-cloud gas to high temperatures of $\sim 10^6 - 10^7$ K as well as for accelerating the heated gas to flow into the halo. As has been shown, the scale thickness of the SNR distribution is about $z_{\text{SNR}} \sim 60$ pc, which indicates that about 10% of SN explosions occurred in the space high above the galactic plane at $|z| > 100$ pc. At such heights, about a half of the explosive energy is used to accelerate the gas into the halo. In order for a gas to be blown into the halo, the shell speed must be greater than 100 km s^{-1} , which is realized if the shell radius is

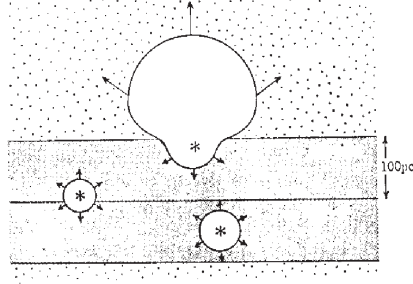


Figure 3.28: Shock wave due to an SN exploded at high z expands into the halo.

smaller than 20 pc and the accumulated shell mass $200 M_{\odot}$, assuming an efficiency of 10% for E_0 to kinetic energy. The total mass blown into the halo and the kinetic energy supplied to the halo gas are then estimated as

$$dM_{\text{gas to halo}}/dt \sim 0.1 \times 200M_{\odot} \times 1/30 \text{ yr}^{-1} \sim 0.7M_{\odot} \text{ yr}^{-1}, \quad (3.106)$$

and

$$dE_{\text{to halo}}/dt \sim 1.3 \times 10^{47} \text{ erg yr}^{-1}, \quad (3.107)$$

respectively.

Metal Abundance

The primeval galaxy had been composed of H, He and only small amount of heavy elements after the big bang at a ratio in mass of

$$X : Y : Z = 0.75 : 0.25 : 0.001. \quad (3.108)$$

On the other hand, the present heavy element ratio is about

$$Z \simeq 0.02 - 0.05 \quad (3.109)$$

in the solar vicinity. Therefore, the metal abundance has increased by one to two orders of magnitudes in the last 15 billion years since the formation of the Galaxy. This ‘pollution’ of the ISM occurred partly because of the stellar wind from massive stars and partly due to heavy element dissipation from the interiors of massive stars due to SN explosion.

Suppose that a single SN explosion distributes heavy elements of mass of $0.1 M_{\odot}$ into the interstellar space. Then, the total amount of heavy elements of the ISM in the Galaxy increases at a rate

$$dM_Z/dt \sim 0.1M_{\text{SN}}/20 \text{ yr}. \quad (3.110)$$

The rate of increase in the Z abundance is given by

$$dZ/dt \sim (dM_Z/dt)/M_{\text{ISM}}. \quad (3.111)$$

Since $M_{\text{ISM}} \sim 10^{10} M_{\odot}$, we have

$$dZ/dt \sim 1.7 \times 10^{-12}, \quad (3.112)$$

or

$$Z \sim 1.7 \times 10^{-12}t \quad (3.113)$$

for $M_{\text{SN}} \sim 5M_{\odot}$. For the age of the Galaxy $t \sim 1.5 \times 10^{10}$ yr, we have the present Z to be $Z \sim 0.03$. The sun was born 4.6×10^9 yr ago or $att = 10^{10}$ yr, at which time the metal abundance was $Z \sim 0.02$. This is approximately equal to the solar value ($Z = 0.017$).

Chapter 4

GALACTIC STRUCTURE

4.1 The Distance to the Galactic Center

The distance to the Galactic Center from the Sun (R_0) is the most fundamental parameter describing the Galactic Structure: The distance is related to such fundamental quantities as the mass and size of the Galaxy and those of individual objects, and so their luminosities, as well as spiral structures. The distance has been determined by various methods as follows, and the distance to the Galactic Center adopted today is $R_0 \simeq 8.5$ kpc.

4.1.1 Using Globular Clusters

Distances to globular clusters are measured by observing RR Lyr stars by applying the period-luminosity relation. Distances to clusters which do not involve RR Lyr stars are measured by the spectroscopic parallax method using their Hertzsprung-Russell diagrams.

From the distances and their positions on the sky, three-dimensional positions of the clusters, and therefore, the distribution in the Galaxy

are obtained. The galactic globular clusters are known to be distributed almost spherically in the galactic bulge and halo. If we simply assume that the center of this spherical distribution coincides with the Galactic Center, the distance R_0 is obtained to be about 8 to 10 kpc.

4.1.2 Using Maser Sources

Consider a spherical cloud near the Galactic Center, in which many H_2O maser sources are distributed spherically with their internal motion being random. Let the angular velocity (proper motion) of a cloud be $\mu = d\theta/dt$, the velocity dispersion perpendicular to the line of sight σ_p , and the velocity dispersion of the maser sources in the line of sight σ_r . If angular velocities of many maser sources are measured by VLBI observations and a dispersion of their proper motions with respect to the cloud center is obtained, we have

$$\sigma_p \simeq R_0 \langle \mu^2 \rangle^{1/2} \simeq R_0 \left(\frac{\sum \mu^2}{N-1} \right)^{1/2}. \quad (4.1)$$

On the other hand, σ_r is obtained by measuring the dispersion of radial velocities of the sources from maser-line observations. From the assumption of a spherical system, we have

$$\sigma_r \simeq \sigma_p, \quad (4.2)$$

and therefore,

$$R_0 \simeq \frac{\sigma_r}{\langle \mu^2 \rangle^{1/2}}. \quad (4.3)$$

Here, the quantities in the right-hand side of the equation are observables from the VLBI line observations. The Galactic Center distance determined by this method is $R_0 \simeq 8$ kpc.

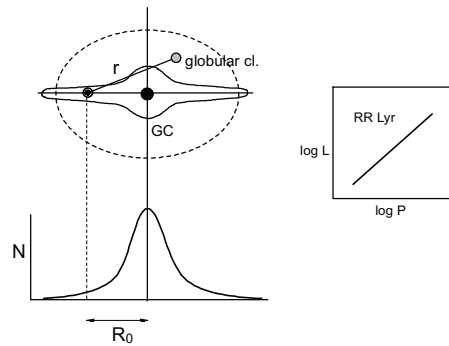


Figure 4.1: (a) The period-luminosity relation for RR Lyr stars in globular clusters. (b) The distribution of globular clusters around the Galaxy, and the distance to the Galactic Center from the Sun.

4.1.3 Using X-ray Bursters

When the luminosity of a star exceeds a threshold value, the envelope of the star is blown away by its own radiation pressure overcoming the stellar gravity. This threshold (critical) luminosity is called the Eddington limit, and is uniquely determined by the mass of a star. X-ray bursters are known to be extremely luminous at their bursting phase. However, this maximum luminosity should not exceed the Eddington limit. If we assume that the bursting-phase luminosity is approximately the Eddington luminosity, the distance can be estimated by comparing with the apparent magnitude. By applying this method to X-ray bursters in the galactic bulge, a distance of $R_0 \sim 7$ kpc has been obtained.

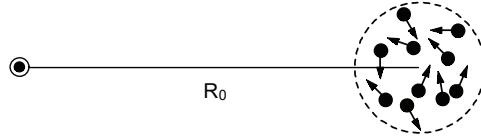


Figure 4.2: Radial velocity dispersion and a dispersion of proper motions in a spherical cloud composed of many maser-line sources give us the distance.

4.2 The Galactic Rotation

4.2.1 Oort's Constants

Suppose that the Sun is rotating around the Galactic Center on a circular orbit of radius R_0 at a velocity V_0 . A galactic object is located in the direction l ($b \sim 0^\circ$) at a distance r from the Sun, which is also rotating around the Galactic Center at a velocity V with radius R . The radial velocity of the object as seen from the sun is given by

$$v_r = V \cos \alpha - V_0 \sin l, \quad (4.4)$$

where α is the angle between the velocity vector of the object and the line of sight. Knowing that

$$\frac{\sin l}{R} = \frac{\cos \alpha}{R_0} \quad (4.5)$$

we have

$$v_r = \left(V \frac{R_0}{R} - V_0 \right) \sin l. \quad (4.6)$$

Introducing angular velocities $V = R\omega$ and $V_0 = R_0\omega_0$, we can

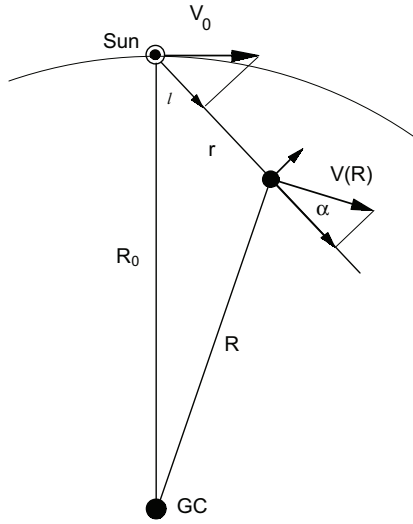


Figure 4.3: The Sun and a galactic object are rotating around the Galactic Center on circular orbits.

rewrite the equation as

$$v_r = (\omega - \omega_0)R_0 \sin l. \quad (4.7)$$

The velocity of the object perpendicular to the line of sight is written as

$$v_p = \frac{r}{R}(R_0 \cos l - r) - V_0 \cos l, \quad (4.8)$$

which is rewritten as

$$v_p = (\omega - \omega_0)R_0 \cos l - \omega r. \quad (4.9)$$

In the solar vicinity, $r \ll R_0, R$, we have

$$\omega - \omega_0 = \left[\frac{d\omega}{dR} \right]_{R=R_0} (R - R_0), \quad (4.10)$$

and

$$\frac{d\omega}{dR} = \frac{d}{dR} \left(\frac{V}{R} \right) = \frac{1}{R} \frac{dV}{dR} - \frac{V}{R^2}. \quad (4.11)$$

Therefore, the radial velocity can be written as

$$v_r = \left[\frac{dV}{dR} - \frac{V_0}{R_0} \right] (R - R_0) \sin l. \quad (4.12)$$

Since

$$R - R_0 \simeq r \cos l, \quad (4.13)$$

we have

$$v_r = \left[\frac{dV}{dR} - \frac{V_0}{R_0} \right] \frac{r \sin 2l}{2}. \quad (4.14)$$

Thus, we obtain

$$v_r = A r \sin 2l \quad (4.15)$$

with

$$A = \frac{1}{2} \left[\frac{V_0}{R_0} - \frac{dV}{dR} \right]_{R=R_0}. \quad (4.16)$$

Here, A is called the Oort's A constant.

The perpendicular component is given by

$$v_p = \left[\frac{dV}{dR} - \frac{V_0}{R_0} \right] (R - R_0) \cos l - \omega_0 r = \frac{1}{2} \left[\frac{V_0}{R_0} - \frac{dV}{dR} \right] r \cos 2l - \frac{1}{2} \left[\frac{V_0}{R_0} + \frac{dV}{dR} \right] r. \quad (4.17)$$

Or we can rewrite this as

$$v_p = (A \cos 2l + B) r \quad (4.18)$$

with

$$B = -\frac{1}{2} \left[\frac{V_0}{R_0} + \frac{dV}{dR} \right] \quad (4.19)$$

being called the Oort's B constant.

Introducing proper motion $\mu = d\theta/dt$ and $v_r = \mu r$, we rewrite the above expression as

$$\mu = \frac{A \cos 2l + B}{4.74} \text{ (''yr}^{-1}\text{)}. \quad (4.20)$$

Here, the Oort's constants A and B are measured in $\text{km s}^{-1}\text{kpc}^{-1}$.

By observing many stars (objects) with known distance r , proper motion μ , and radial velocity v_r , we can determine A and B by the least-square fitting using Eq. (4.15) and (4.20). The observations have given

$$A = 15 \text{ km s}^{-1} \text{ kpc}^{-1}, \quad (4.21)$$

and

$$B = -10 \text{ km s}^{-1} \text{ kpc}^{-1}, \quad (4.22)$$

4.2.2 The Solar Rotation Velocity

Equations (4.16) and (4.19) is used to obtain the rotation velocity of the Sun V_0 :

$$V_0 = (A - B)R_0, \quad (4.23)$$

and the differential rotation as

$$\frac{dV}{dR}_{(R=R_0)} = -(A + B). \quad (4.24)$$

Since we know the distance to the Galactic Center as $R_0 = 8.5$ kpc, and $A = 15 \text{ km s}^{-1}\text{kpc}^{-1}$ and $B = -10 \text{ km s}^{-1}\text{kpc}^{-1}$, we obtain the solar rotation velocity as

$$V_0 = 220 \text{ km s}^{-1}. \quad (4.25)$$

4.2.3 Rotation Curve within the Solar Circle

We have obtained the distance of the Sun from the Galactic Center R_0 and rotation velocity V_0 . This gives us opportunity to derive the rotation velocity $V(R)$ of the galactic disk as a function of galacto-centric distance R , which is called the rotation curve. We here assume that $V(R)$ varies smoothly with R . We then observe HI and/or CO line profiles of the interstellar gas distributed in the galactic plane toward l ($b \sim 0^\circ$). In the first quadrant of the disk ($0 < l < 90^\circ$) all the gas within the solar circle has positive radial velocity, and the gas outside the solar circle has negative velocity because of the motion of the Sun. A maximum velocity is observed coinciding with a position which is tangential to the line of sight, and we call this radial velocity the terminal velocity $v_{r \text{ max}}$. Given this terminal velocity from observation, the rotation velocity $V(R)$ at this position $R = R_0 \sin l$ is simply derived by

$$V(R) = v_{r \text{ max}} + V_0 \sin l. \quad (4.26)$$

By observing $v_{r \text{ max}}$ at various longitude l , and therefore, at various R , we obtain the rotation curve $V(R)$ of the disk in the first quadrant. For the third quadrant ($270^\circ < l < 360^\circ$), the terminal velocity must be negative, and hence, the rotation curve is given by

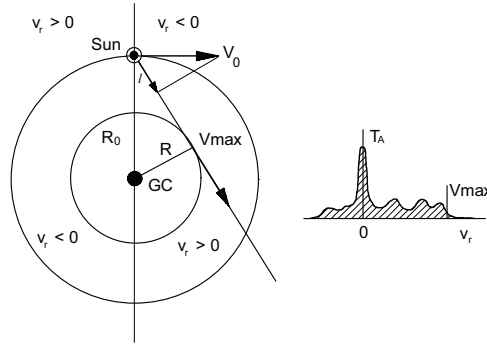


Figure 4.4: The terminal velocity is simply related to the rotation velocity of the disk within the solar circle.

$$V(R) = -v_{r \text{ min}} - V_0 \sin l. \quad (4.27)$$

4.2.4 Rotation Curve beyond the Solar Circle

The determination of the rotation curve beyond the solar circle ($R > R_0$) is not straightforward. Sources with *known distances* and their radial velocities are required. Let the distance to an object at (l, b) be r , then the galacto-centric distance R is uniquely determined by (l, b, r, R_0) . The rotation velocity and an observed radial velocity are related by

$$V(R) = \frac{v_r + V_0 \cos(l - 90^\circ)}{\cos(l + \theta - 90^\circ)}, \quad (4.28)$$

where θ is the galacto-centric longitude of the source.

The rotation curve has been obtained by observing HII regions, HI clouds and/or molecular clouds *associated with stars* whose distances have been measured independently by spectroscopic methods.

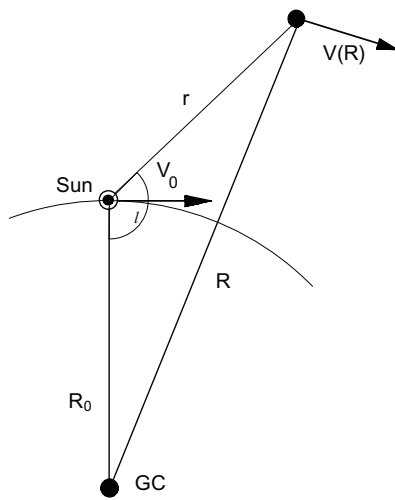


Figure 4.5: The rotation curve for the outer Galaxy is obtained by observing radial velocities of sources with known distance r .

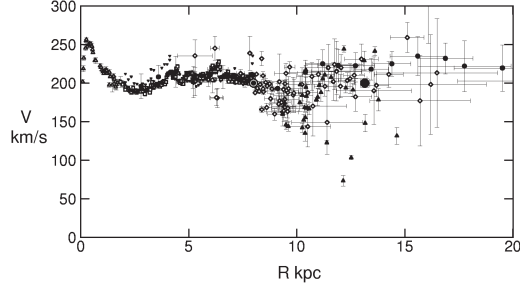


Figure 4.6: The Rotation curve of the Galaxy.

4.2.5 The Rotation Curve

The rotation curve of the whole galactic disk has been obtained by observations of HII regions in optical H_α and radio recombination lines, HI gas in the 21-cm line emission, and molecular gas by the CO line emission. The rotation curve is known to be almost flat from the central region at $R \sim 200$ pc till outer regions beyond $R \sim 20 - 30$ kpc.

4.2.6 The Mass of the Galaxy

Since the centrifugal force by the circular orbital rotation of the sun is in a balance with the gravity of the Galaxy mass within the solar circle, we may assume that

$$R_0 \omega_0^2 \simeq GM_0/R_0^2. \quad (4.29)$$

Or equivalently

$$M_0 = M(R_0) \simeq \frac{R_0 V_0^2}{G} \quad (4.30)$$

$$\simeq \frac{8.5 \text{ kpc} (220 \text{ km s}^{-1})^2}{G} \sim 1.0 \times 10^{11} M_\odot. \quad (4.31)$$

It is a good approximation to assume a flat rotation for all over the disk: $V(R) \simeq V_0 = 220 \text{ km s}^{-1}$. Then, the mass of the galaxy can be expressed as

$$M(R) \simeq 1.0 \times 10^{11} M_{\odot} \frac{R}{R_0}. \quad (4.32)$$

This implies that the mass of the Galaxy increases without limit, which is deeply related to the ‘missing mass’ problem in the outer region.

4.3 Distributions of Interstellar Gas in the Galaxy

4.3.1 Velocity-to-Space Transformation using a Radial-Velocity Diagram

Given a rotation curve $V(R)$, radial velocity v_r of any object near the galactic plane ($b \sim 0$) is calculated by knowing its (l, r) . Inversely, given the radial velocity and galactic longitude (v_r, l) of an object, its distance from the sun, and therefore, its position on the galactic disk can be calculated. Hence, positions and distribution of objects and gases can be obtained by their line emissions such as recombination lines (HII regions), $\lambda 21$ -cm line emission (HI clouds and diffuse gas), molecular lines such as CO (MCs and GMCs), and maser lines such as SiO (maser stars).

Let the rotation law of the Galaxy be $V(R)$, then radial velocity of an object at (R, θ) on (near) the galactic plane is calculated as

$$\begin{aligned} v_r &= R\omega \cos(90^\circ - l - \theta) - R_0\omega_0 \sin l \\ &= R\omega(\sin \theta \cos l + \cos \theta \sin l) - R_0\omega_0. \end{aligned} \quad (4.33)$$

Since $r \sin l = R \sin l$, $R \cos \theta = R_0 - r \cos l$, we have

$$v_r = R_0(\omega - \omega_0)\sin l = \left\{ \frac{R_0}{R}V(R) - V_0 \right\} \sin l. \quad (4.34)$$

Using Eq. (4.34) we can calculate a radial-velocity diagram of the Galaxy. The radial-velocity diagram is then used to obtain positions (distance r) of an object for which $(l, b; v_r)$ have been observed:

$$r = f(l, b; v_r). \quad (4.35)$$

Positions of objects outside the solar circle are uniquely determined by using this diagram. On the other hand, if the radial velocity is positive at $0 < l < 90^\circ$ and negative at $270 < l < 360^\circ$, the distance of a source is two-fold: there are two positions at which the observed v_r is satisfied. The discrimination of the near or far side solution is a rather sophisticated problem when obtaining the true distribution of matter. Additional informations such as apparent diameters of objects and their structural relation to the surrounding objects are required for the solution.

This procedure is called the velocity-to-space transformation (VST). VST is useful to obtain a “face-on” map of the density distribution of interstellar mass such as the HI and CO gases in the Galaxy. For example, as already given, the column density of the HI gas is expressed as

$$N_{\text{HI}} [\text{H cm}^{-2}] = C \int T_{\text{B}}(v) dv [\text{K km s}^{-1}] \quad (4.36)$$

with $C = 1.82 \times 10^{18}$ being the conversion factor. The local density of the gas is obtained by

$$n_{\text{HI}} = \frac{dN_{\text{HI}}}{dr} = \frac{dN_{\text{HI}}}{dv} \frac{dv}{dr}. \quad (4.37)$$

Using Eq. (4.35) and (4.36), we rewrite this to obtain the VST formula,

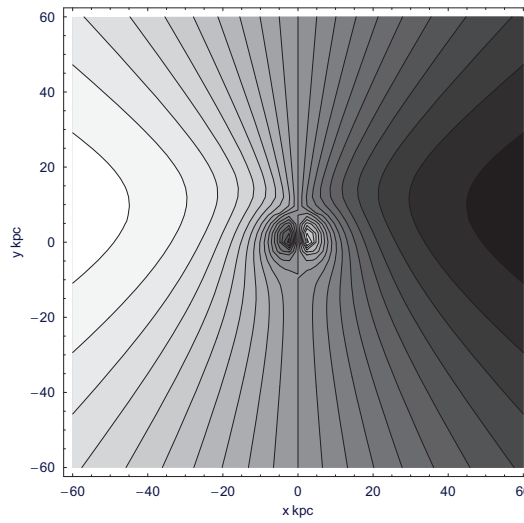
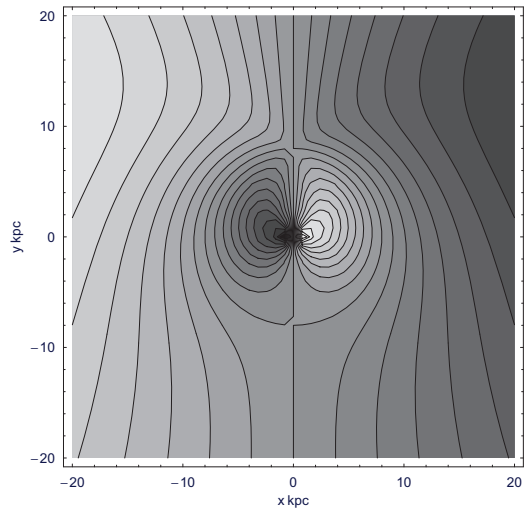


Figure 4.7: Radial-velocity diagram of the Galaxy at $b \sim 0$.

$$n_{\text{HI}} = C T_{\text{B}}(v_{\text{r}}) \left[\frac{df(l, b; v_{\text{r}})}{dv_{\text{r}}} \right]^{-1}. \quad (4.38)$$

4.3.2 (l, v_{r}) and (b, v_{r}) Diagrams

By observing velocity profiles of the HI and/or CO-lines at various longitudes, we can derive a diagram in which the intensity (brightness temperature) distribution is mapped in the position-velocity space, namely in the (l, v_{r}) plane. This is called a position-velocity diagram, or a (l, v_{r}) diagram for the galactic plane. The (l, v_{r}) diagram is used for studying the rotation characteristics of the galactic disk as well as to derive the spiral structure. In Figs. 4.8, 4.9 and 4.10 we show (l, v_{r}) diagram for the HI and CO line emissions as observed along the galactic plane ($b = 0^\circ$).

In a similar way, we can obtain a (b, v_{r}) diagram by scanning in the direction of the latitude (perpendicular to the galactic plane). A (b, v_{r}) diagram is used for obtaining informations about the disk thickness and distribution of the gas in the z direction. It is often used for studying the warping of the outer galactic disk. In Fig. 4.11 we show a (b, v_{r}) diagram obtained by scanning the HI emission perpendicular to the galactic plane at $l = 45^\circ$.

perpendicular to the galactic plane at $l = 45^\circ$. Gases with positive velocities represent those inside the solar circle ($R < R_0$), and negative-velocities to those outside the solar circle ($R > R_0$). A bending of the gas disk is seen in the negative-velocity part (outside the solar circle).

4.3.3 ‘Face-on View’ of the Galaxy

The (l, v_{r}) diagram is used for obtaining a “face-on” distribution of the density of interstellar gas in the Galaxy. In Fig. 4.12 we show a face-on view of the Galactic disk as seen in the HI line emission

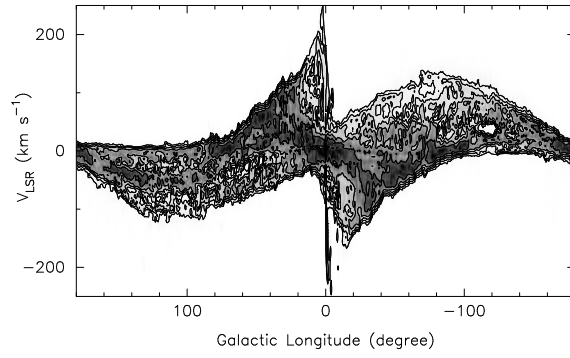


Figure 4.8: (a) A (l, v_r) diagram for HI gas along the galactic plane.

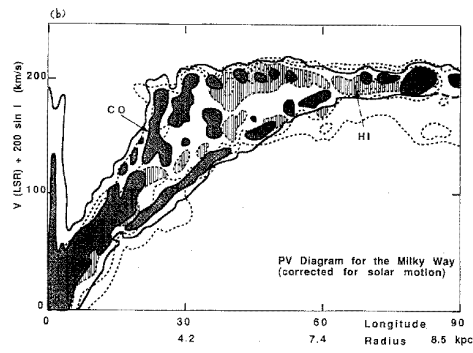


Figure 4.9: (b) The same as (a), but the solar rotation has been subtracted, so that as if the inner part of the Galaxy is seen from 'outside'.

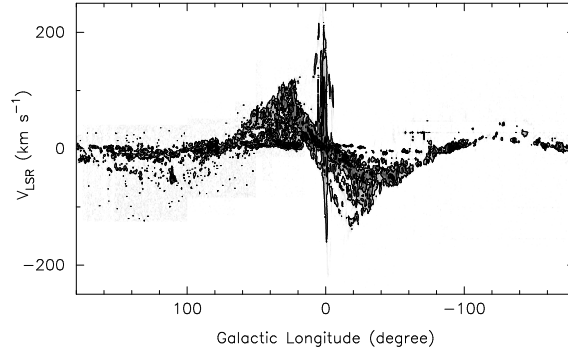


Figure 4.10: A (l, v_r) diagram for CO (molecular) gas along the galactic plane.

obtained by Dutch and Australian astronomers in the 1950's. Several spiral arms can be traced in this diagram. Here, a circular rotation is assumed, and the derived distribution depends on the validity of this assumption.

4.3.4 ‘Edge-on View’ of the Galaxy

The “edge-on” view of the Galaxy can be approximately imagined from a view of the Milky Way which is a projection of the Galaxy on the sky. There have been a number of all-sky surveys and galactic-plane surveys at various frequencies. We show all-sky maps of the galactic disk in the HI and CO line emissions, FIR (far infrared) emission at $60\mu\text{m}$ and in the radio continuum at 408 MHz (Fig. 4.14 to 4.18).

4.3.5 Radial Distributions of HI and CO and the Molecular Front

The distributions of HI and CO gases can be used to derive radial distributions of the ISM. A similar but more simplified method similar to VST which uses only data near the terminal velocities can be also

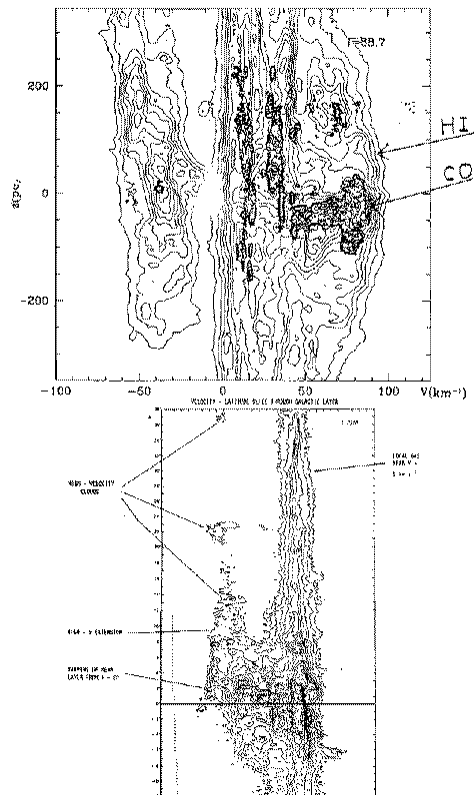


Figure 4.11: A (b, v_r) diagram for HI (thin contours) and CO (thick contours) gases

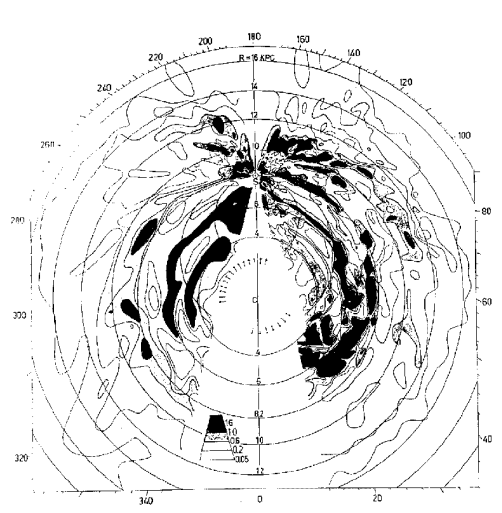


Figure 4.12: A distribution of HI gas density in the galactic plane derived by applying the VST to spectral data of the 21-cm line emission on an assumption of circular rotation of the gas.

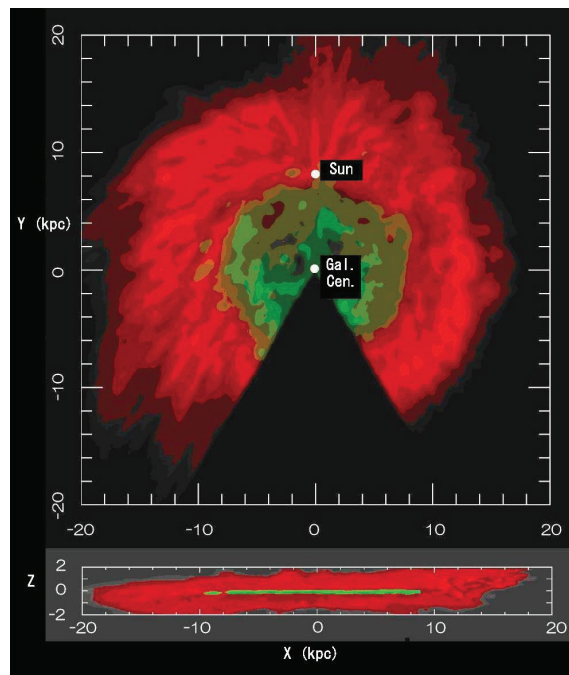


Figure 4.13: The newest HI view of the Galaxy (Nakanishi and Sofue 2003, 2006). [Top] Distribution of projected HI gas column density of the Galaxy. [Bottom] Cross section of the gas disk.

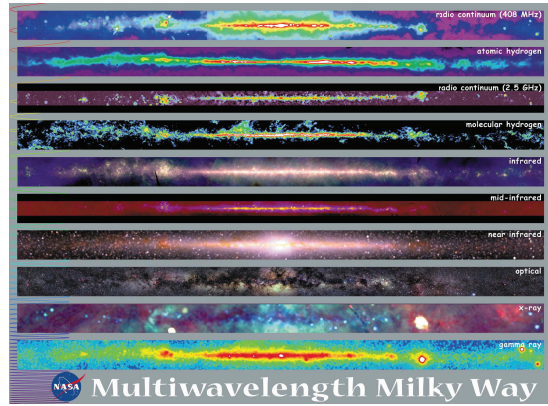


Figure 4.14: ‘Edge-on views’ of the Galaxy in the radio, FIR, optical emission and X-ray sources.

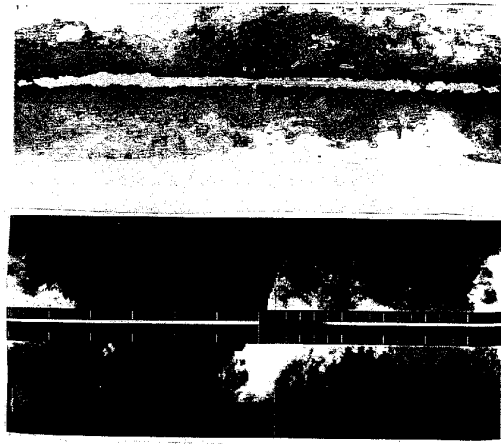


Figure 4.15: Edge-on view of the Galaxy in HI by integrated 21-cm line intensity.

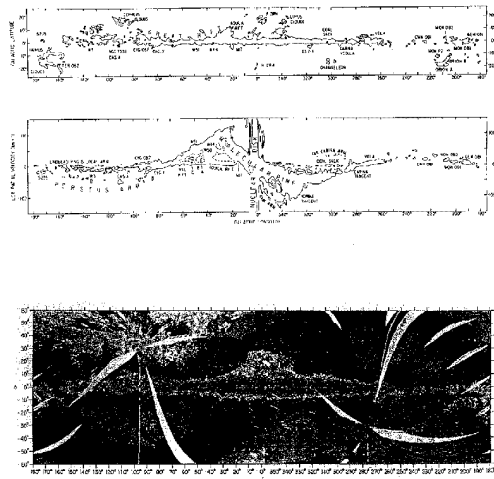


Figure 4.16: Edge-on view of the Galaxy in CO integrated 2.6-mm line intensity (molecular gas), and in FIR at $100 \mu\text{m}$ (dust).

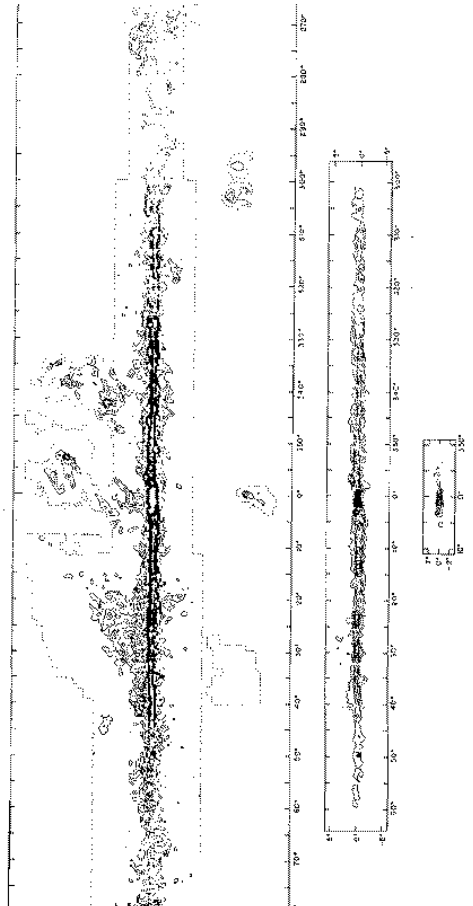


Figure 4.17: Edge-on view of the Galaxy in CO integrated 2.6-mm line intensity, and in FIR at $100 \mu\text{m}$ (continued).

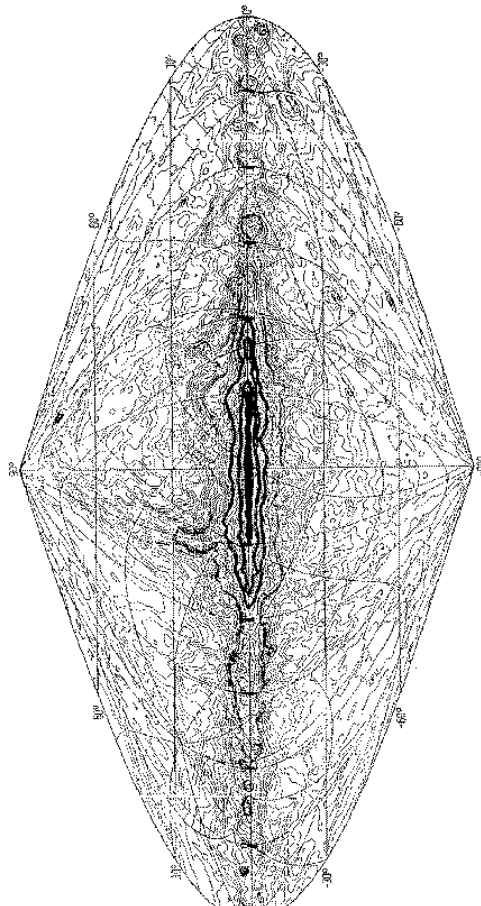


Figure 4.18: Edge-on view of the Galaxy in radio continuum at 408 MHz.

used to derive an approximate radial distribution of the gas.

Fig. 4.19 shows the radial variation of the HI and molecular hydrogen densities as a function of the galactocentric distance R . The HI gas is distributed widely in the galactic disk with an outskirts which extends to $R \sim 20$ kpc and the maximum density occurs at around $R \sim 10$ kpc. However, the HI gas is almost lacking in the central region. On the other hand, the molecular gas is distributed in a more inner region, with a maximum at $R \sim 4$ kpc and at the galactic center. The ring-like distribution of the molecular gas at $R \sim 4$ kpc is called the 4r-kpc molecular ring.

The molecular fraction as defined by

$$f_{\text{mol}} = \frac{\rho_{\text{H}_2}}{\rho_{\text{HI}} + \rho_{\text{H}_2}} \quad (4.39)$$

is almost unity at $R < 5$ kpc, indicating that the interstellar gas in the central region is almost totally molecular. On the other hand, the fraction is almost zero in the outer region beyond $R > 10$ kpc, where the ISM is almost totally neutral hydrogen. Fig. 4.20 shows the variation of f_{mol} as a function of R . The phase transition from HI to H_2 and vice versa is taking place in a narrow region of R at $R \sim 5 - 7$ kpc. We call this narrow transition region of the ISM phases the ‘molecular front’.

4.4 Mass Distribution in the Galaxy

4.4.1 Radial Mass Distribution for a Flat Rotation Curve

Approximately 95% of the mass of the Galaxy is possessed by stars, whose mass distribution can be obtained from kinematic information such as of the rotation curve and velocity dispersions. The mass involved within a radius R is given by

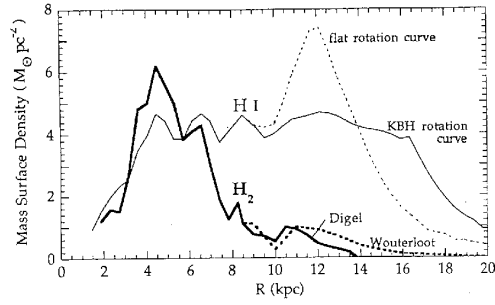


Figure 4.19: Radial distributions of the HI and H₂ densities in the Galaxy.

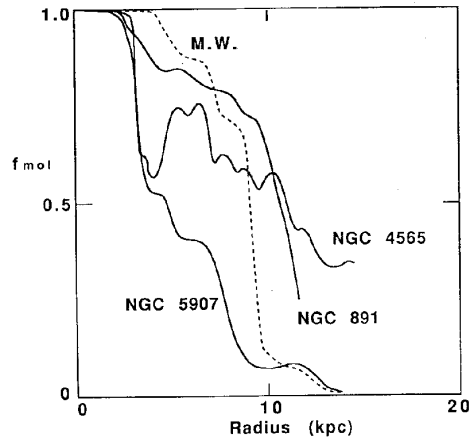


Figure 4.20: Radial variation of the molecular fraction f_{mol} for the Galaxy (dashed line) and edge-on galaxies. A phase transition from HI to H₂, and vice versa, takes place in a narrow range of R called the molecular front.

$$M(R) \sim \frac{RV(R)^2}{G}. \quad (4.40)$$

If the mass distribution is restricted in thin surface of an axisymmetric disk, the surface mass density σ is related to the mass $M(R)$ as

$$M(R) \sim \int_0^R \sigma 2\pi r dr, \quad (4.41)$$

or

$$\frac{dM(R)}{dR} = 2\pi R\sigma(R). \quad (4.42)$$

Hence,

$$\sigma \sim \frac{1}{2\pi GR} \left(V(R)^2 + 2RV(R)\frac{dV}{dR} \right) \sim \frac{1}{2\pi GR} V(R)^2, \quad (4.43)$$

where we assumed that $dV/dR \sim 0$. Therefore, the surface density decreases with the radius inversely proportional to R . This may be compared to the case of spherical distribution of mass, in which case the spatial density of mass decreases as $\propto R^{-2}$.

4.4.2 Mass Distribution perpendicular to the Disk

Since the centrifugal force due to rotation is balancing the gravity by the mass, the local distributions of stars and gas perpendicular to the galactic plane are described by a static equilibrium of the z -directional gravity (perpendicular to the disk) and the velocity dispersion in the z direction v_z . If we denote an equivalent pressure $p = \rho v_z^2$ of the matter concerned, the equilibrium in the z direction can be written as

$$\frac{dp}{dz} = \frac{d(\rho v_z^2)}{dz} = g_z \rho, \quad (4.44)$$

where g_z and ρ are the z -directional gravitational acceleration and

the density of the matter (either stars or gases). If we assume that the galactic disk is a flat plane of infinite surface area, the gravity can be approximated as

$$g_z \sim \alpha z, \quad (4.45)$$

and therefore,

$$\frac{d\rho}{dz} \sim -\frac{\alpha z}{v_z^2} \rho. \quad (4.46)$$

This can be solved if the velocity dispersion is about constant with z :

$$\rho = \rho_0 \exp\left(-\frac{z^2}{z_0^2}\right), \quad (4.47)$$

where ρ_0 and z_0 are constants depending on the species. The z_0 is called a z scale height representing the typical thickness of the disk, and is related to the velocity dispersion as

$$z_0 = \frac{v_z}{\sqrt{\alpha}} \sim v_z \sim \sqrt{T_{\text{gas}}}. \quad (4.48)$$

In table 4.1 we summarize the typical values of v_z and the disk scale-thickness z_0 for various species.

Component	v_z (km s ⁻¹)	$2z_0$ (pc)
GMC	5	60
OB stars	5	60
HI gas	10	100
Disk stars	20-30	300
Hot gas (10 ⁶ K)	100 ($\sim \sqrt{T}$)	$\sim 1kpc$

Table 4.1: Velocity dispersion in the z direction and scale thickness of the disk.

4.4.3 A Mass Distribution Law of the Whole Galaxy

The mass distribution $\rho(R, z)$ and the gravitational potential $\Phi(R, z)$ are related by the Poisson's equation:

$$\Delta\Phi = -4\pi\rho(R, z), \quad (4.49)$$

Let us recall that the potential for point mass is given by

$$\Phi = \frac{GM}{r} = \frac{GM}{\sqrt{R^2 + z^2}}, \quad (4.50)$$

with $r = \sqrt{R^2 + z^2}$ being the distance from the center. An extended spherical mass is often described by a Plummer's law:

$$\Phi = \frac{GM}{\sqrt{r^2 + b^2}} = \frac{GM}{\sqrt{R^2 + z^2 + b^2}}. \quad (4.51)$$

Here, b is a constant representing the scale radius of the spherical mass distribution.

The most convenient formula which describes the potential and realistic mass distribution of the Galaxy has been obtained by Miyamoto and Nagai, and the potential is a modified one from Eq. (4.51) for an axisymmetric spheroid:

$$\Phi = \frac{GM}{\sqrt{R^2 + (a + \sqrt{z^2 + b^2})^2}}. \quad (4.52)$$

Here, a is a constant representing the scale radius of the spheroid (disk).

The Galaxy can be described by three components: the central bulge of spherical distribution; the flattened spheroid corresponding to the disk; and the extended massive halo. The potential of the Galaxy is, therefore, a superposition of potentials due to these three mass components:

$$\Phi = \sum_{i=1}^3 \Phi_i = \sum_{i=1}^3 \frac{GM_i}{\sqrt{R^2 + a_i} + \sqrt{z^2 + b_i^2}}. \quad (4.53)$$

The potential of the Galaxy can be fitted by a set of parameters as given in table 4.2. Using the formula, we obtain the rotation curve and the mass distribution in the Galaxy as

$$V_{\text{rot}}(R) = \sqrt{\sum_{i=1}^3 R \frac{\partial \Phi_i}{\partial R}}, \quad (4.54)$$

and

$$\rho(R, z) = \frac{1}{4\pi} \sum_{i=1}^3 \Delta \Phi_i. \quad (4.55)$$

The third component leads to the flat rotation outside the solar circle. Fig. 4.21 shows a schematic rotation curve of the Galaxy and the distribution of the density.

Component	$M_i (M_{\odot})$	a_i (kpc)	b_i (kpc)
Bulge	2×10^{10}	0.0	0.5
Disk	2.5×10^{11}	7.0	0.5
Massive Halo	$\sim \text{several} \times 10^{12}$	~ 30	~ 20

Table 4.2: Parameters determining the Miyamoto-Nagai Potential of the Galaxy. See section VII for a more detailed model.

4.4.4 Massive Halo and the Missing Mass Problem

The rotation curve of the Galaxy has been measured up to the radius $R \sim 20 - 30$ kpc, and is known to be almost flat at $V_{\text{rot}} \sim 200 \text{ km s}^{-1}$. If we combine this fact with kinematical information about the orbital motion of the Large and Small Magellanic Clouds, which are satellites of the Galaxy, we find that the rotation curve does not decline until

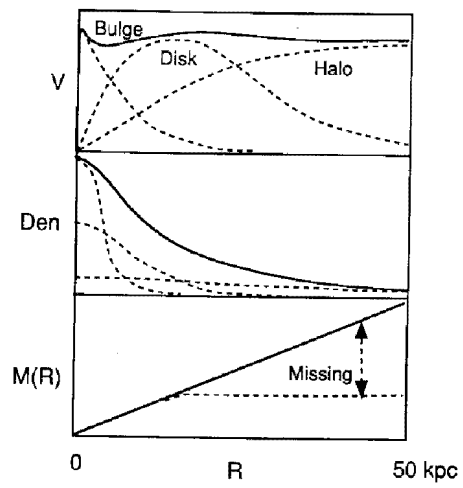


Figure 4.21: The distribution of mass density in the Galaxy, which is a superposition of the bulge, disk and massive halo components.

$R \sim 50$ kpc. Since the mass involved within radius R is approximately $M(R) \sim RV^2/G$, the fact of a flat rotation indicates that the mass of the Galaxy increases proportionally with the radius without limit.

The mass-to-light ratio in the inner region of a galaxy is roughly constant for normal galaxies until a certain radius. On the other hand, total luminosity of a whole galaxy is, of course, finite: the surface brightness of a galaxy decreases with radius as the surface density of mass decreases, and it reaches a very low level at a certain radius R_H beyond which no luminous matter is observed. As the radius increases, the luminosity attains its maximum value at a certain radius beyond which the luminosity does not increase. Therefore, it happens that the mass-to-light ratio $M(R)/L(R)$ begins to increase proportionally to R beyond this radius, $M(R)/L(R) \sim M(R)/L(R_H) \propto R$. There exists a huge amount of mass in the space surrounding the Galaxy, even though there is no light at all. The huge volume of halo is filled with ‘dark’ mass. In spite of the efforts to look for any light (from X-rays to radio), the mass has been not detected at all. This “unseen” mass has been called the ‘missing mass’, and the missing mass problem has been one of the most intriguing mystery in the astrophysics.

However, the recent great success in detecting MACHO (massive compact halo objects) by means of the micro-lensing effect on stars in the Magellanic Clouds appears to have solved this long standing problem: According to statistics of the detection probability of MACHOs and the observations, a significant fraction or all of the dynamical halo around the Galaxy can reasonably attributed to numerous dark and extremely dwarf stars which are not massive enough to shine by the nucleosynthesis reaction.

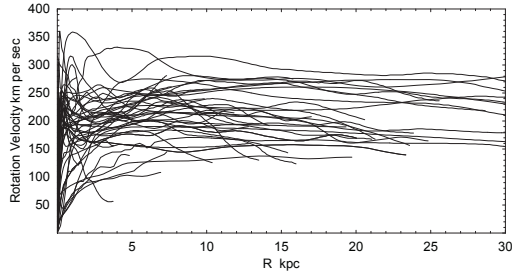


Figure 4.22: Rotation curves for spiral galaxies.

4.4.5 Dynamical Masses of Galaxies and of Cluster of Galaxies

Flat Rotation Curves

Flat rotation similar to that of our Galaxy has been observed for almost all galaxies for which rotation curves were measured in the HI line and optical line emissions such as $H\alpha$ line. In these galaxies, the mass increases with the radius almost infinitely, while the luminosity is finite, and again the missing-mass problem has been a challenging theoretical subject such as the cold-matter scenario.

Binary Galaxies

Mass of double galaxies and a galaxy with a companion (satellite) can be estimated by relative velocities of the two galaxies and their separation by assuming the inclination of the orbit. The orbital velocity of a galaxy around the other is expressed as

$$V_{\text{rot}} \sim \frac{1}{\sin i}(v_1 - v_2), \quad (4.56)$$

where i is the inclination of the orbital axis from the line of sight, v_1

and v_2 are the radial velocities of the two galaxies. The reduced mass of the two galaxies is related to the orbital velocity as

$$V_{\text{rot}}^2 \sim G \left(\frac{m_1 m_2}{m_1 + m_2} \right) \frac{1}{R}, \quad (4.57)$$

where m_1 and m_2 are the masses of the two galaxies, and R their separation.

Virial Mass of a Cluster of Galaxies

Masses of groups of galaxies and clusters of galaxies are estimated by virial mass from their size and velocity dispersion. Clusters of galaxies contain thousands of galaxies which are gravitationally bound to the center of mass of the cluster. The virial mass (dynamical mass) of a cluster is given by

$$M_c \sim \frac{R_c v_\sigma^2}{G} \quad (4.58)$$

where R and v_σ are the radius of the cluster and velocity dispersion of member galaxies. Observations have shown that $v_\sigma \sim 2000 \text{ km s}^{-1}$, and $R_c \sim 1 \text{ Mpc}$ for a normal-size cluster, and therefore, $M_c \sim 8 \times 10^{14} M_\odot \sim 10^4 M_{\text{Galaxy}}$. However, the total mass of individual galaxies cannot explain this huge amount of dynamical mass.

Missing Mass in the Universe

The majority of the mass contained by a cluster is not visible as galaxies. Hence, clusters of galaxies also contain invisible mass which amount about 10 times the mass of all member galaxies: A cluster of galaxies is filled with missing mass.

Therefore, we may consider that the ‘‘luminous mass’’ of galaxies which are observable by the classical astronomical means is much smaller than the dynamical mass of galaxies. We are ‘‘seeing’’ only

a very small fraction ($\sim 1 - 10\%$) of the real mass which may be either in such a form as invisible small (dark) stars or in some exotic form often quoted as the cold-matter.

4.5 Spiral Structure

4.5.1 Hubble Types and the Type of the Galaxy

Galaxies are categorized into E, S, and SB, where E stands for elliptical galaxies, S for spiral galaxies, and SB for barred spirals. Each type is further classified into subclasses: E into E0, E1 .. E7, where E0 is a round shaped galaxy, and E7 is most flattened elliptical. In between E and S we have S0, which is a type of galaxies without any spiral structure but have stellar disk and large bulge. S galaxies are sub-classified into Sa, Sb, Sc and Sd, where Sa has tightly wound spiral arms, Sb intermediate and Sc has open spiral arms with large pitch angles. Sa has a large bulge and Sc smaller bulge, and Sd has almost no bulge. E to S0 are called early type galaxies, and Sb to Sc are called late type. SB galaxies are those with a barred structure, and classified similarly to S as SBa, SBb, SBc according to the spiral arm winding and bulge size.

According to the spiral arm features as derived from HI and HII regions, or from CO-line observations, the Galaxy is classified as Sb type. The pitch angle of spiral arms is approximately 10° .

4.5.2 Origin of Spiral Arms

Spiral arms are regions of enhanced stellar density in the disk, where the excess of the mass density over the background is only a few %, $\delta\rho \sim 0.1\rho$. Accordingly, the local potential due to the arm is deeper than the background: $\delta\phi \sim 0.1\phi_0$. Due to the deeper potential and

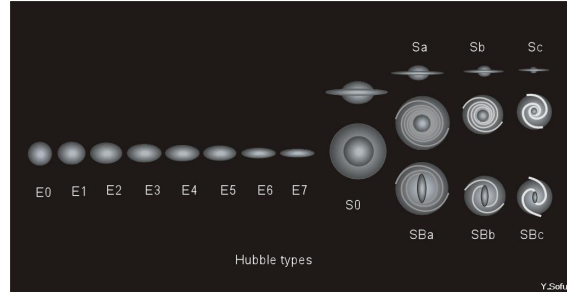


Figure 4.23: The Hubble classification of galaxies.

galactic shock waves, the gas is compressed to lead to enhanced star-formation. Spiral arms are, therefore, recognized as bright lanes of newly-born blue (OB type) stars in optical (B and V bands) photographs, as well as in $H\alpha$ emission. Arms are also traced by HI gas, H_2 (CO) gas, as well as in the radio continuum emission (magnetic fields and cosmic rays).

There have been proposed various hypotheses and theories which would explain the origin of spiral arms in disk galaxies. They may be summarized as the following:

Density wave theory

This most widely accepted theory explains the arms as due to a compression wave of the stellar density which propagate through the stellar disk. Since the angular speed of the propagation of the wave does not strongly depend on the galacto-centric distance, the pattern of the density enhancement remains unchanged. Once a spiral pattern is born, it is maintained for a long time.

Oval-potential-induced arms

If the density wave is strong and large-scale enough, the “arm” looks like a bar, and a barred spiral galaxy is formed. Often this bar forma-

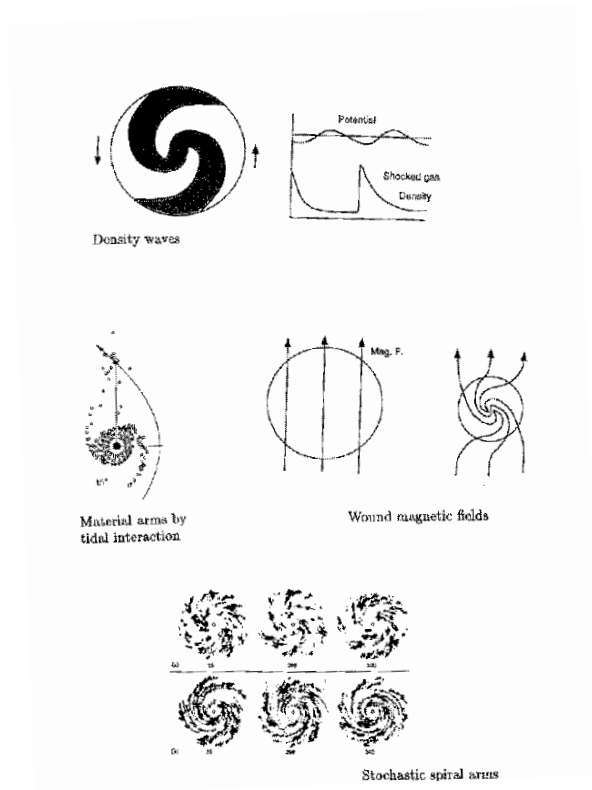


Figure 4.24: Origin of spiral arms.

tion applies in the central bulge region. Once a galactic bulge attains an oval shape as projected on the disk, the distorted potential will cause spiral-like density disturbance in the whole disk, particular outside the bar ends. This leads to formation of secondary spiral patterns.

Material arm hypothesis

This applies to such a system where tidal interaction by a companion stretches a tail of stars and gas that exhibits a spiral feature. The arms are not density wave, but are real matter arms, and the angular speed is about the same as the galactic rotation angular speed. Hence, the arms will be wound tightly during the galactic rotation, and the arms are more or less transient.

Magnetic arms

Magnetic fields frozen into the interstellar gas are stretched by the differential rotation of the disk, and form magnetic spiral arms. Since the magnetic field is somehow related to the gas density enhancement or rarefaction through a magneto-hydrodynamical (MHD) coupling, this may cause also gaseous spiral arms. Due to the winding up of the lines of force by rotation, the field direction becomes to change from a spiral arm to the other. Such a magnetic spiral pattern will be maintained in a steady spiral, if the oppositely directed magnetic lines of force reconnect in a time scale comparable to or shorter than the rotation period, or if the dissipation into the halo is rapid enough. If this is the case, the galactic halo will be a reservoir of magnetic fields supplied from the disk. In fact, radio continuum observations have indicated a thick disk and extended magnetic halos in many edge-on spiral arms.

Explosion hypothesis

An exotic idea had been proposed to explain some peculiar arms which apparently emerge from the nuclear region of a galaxy. Suppose that a

gaseous as well as magnetic jet is ejected from the nucleus within the disk of a galaxy. Then, the jet propagation will be strongly affected by the rotating disk gas and magnetic fields. Therefore, such a jet inside the disk plane will be bent to form a spiral-like structure. This has indeed been applied to the disk galaxy NGC 4258 which possesses a radio arm which appear to run independent of the optical spiral arms at a much larger pitch angle than the disk arms.

Stochastic spiral arms of SF regions

According to the sequential star formation scenario as it is applied to ‘inter GMC’ propagation, a ‘front’ consisting of individual star forming regions expands through the galactic gas disk, as if a ring of fire expands in a field of grass. These rings of star forming front are, then, stretched by the differential rotation of the galactic disk into filamentary arcs which align on spiral fragments over the disk. As a result, the galaxy disk will be covered by numerous spiral fragments of star formation regions, which shine by their OB stars and HII regions. Indeed, there exist many galaxies which do not show up any grand-designed spiral pattern, but show rather stochastic spiral arms. This scenario is called the stochastic spiral arm formation.

4.5.3 Density Waves

Gravitational instability of a disk

Suppose an infinite plane of stars whose surface mass density and velocity dispersion are σ and v_d , respectively. Let the disk be perturbed by a density enhancement of radius λ . If the gravity by a mass of the density-enhanced region $M = \pi\lambda^2\sigma$ exceeds the pressure due to the velocity dispersion ρv^2 of a mass element, then the region will contract by the self gravity. Namely, the disk is unstable against the gravitational fragmentation if

$$\rho v_d^2 < \left(\frac{G\pi\lambda^2\sigma}{\lambda} \right) \rho \quad (4.59)$$

or if

$$\lambda > \lambda_c = \left(\frac{v_d^2}{\pi G\sigma} \right). \quad (4.60)$$

For a galaxy disk for which $v \sim 30 \text{ km s}^{-1}$, and $\sigma \sim M_{\text{gal}}/(\pi R_0^2) \sim 0.1 \text{ g cm}^{-3}$, the critical wave length is estimated to be $\lambda_c \sim 0.1 - 1 \text{ kpc}$. Therefore, if the galaxy is not rotating, the disk will be unstable against fragmentation into pieces of radius 0.1 to 1 kpc.

However, since disk is differentially rotating, the effective velocity dispersion is much higher:

$$v^2 \sim v_d^2 + \Delta V_{\text{rot}}, \quad (4.61)$$

where

$$\Delta V_{\text{rot}} \sim \frac{dV_{\text{rot}}}{dR} \lambda \sim (A - B)\lambda = \omega\lambda. \quad (4.62)$$

Even in a case without velocity dispersion ($v_d \sim 0$), we have a larger critical wavelength: The disk is unstable if

$$\lambda > \lambda_c \sim \frac{\pi G\sigma}{(A - B)^2} = \frac{\pi G\sigma}{\omega^2}. \quad (4.63)$$

For a normal disk galaxy the critical wave length is about $\lambda_c \sim 1 - 10 \text{ kpc}$. Therefore, the galaxy disk is unstable for perturbation of a scale length of a few kpc, and the whole galaxy disk suffers from a bar-like oval deformation. According to such deformation of the disk shape, and therefore of the disk potential, individual orbits of stars are also deformed to attain ‘rosette’ orbits.

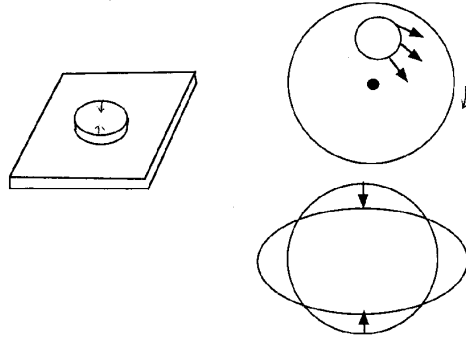


Figure 4.25: Gravitational instability in a plane and rotating disk of stars.

Density Waves

There are three kinds of frequencies characterizing the stellar disk: the galactic rotation frequency ω , the frequency of rotation of the axis of a rosette orbit ω_p of a star, and the epicyclic frequency κ related to the oscillation of a star on the orbit in the direction of R . The frequency ω_p is called also the frequency of pattern rotation, or the pattern (angular) speed. In a normal galactic disk, the pattern speed is approximately given by

$$\omega_p \simeq \omega - \frac{1}{2}\kappa. \quad (4.64)$$

Therefore, if the disk of stars is perturbed so that all stars begin to rotate on individual rosette orbits, their mutual spatial relation remains about the same for many rotations: Once a ‘bar’ of density enhance region is formed, the bar shape is maintained for a long time.

It is a natural consequence that a such distorted bar shape will be affected by the differential rotation, so that the shape is stretched

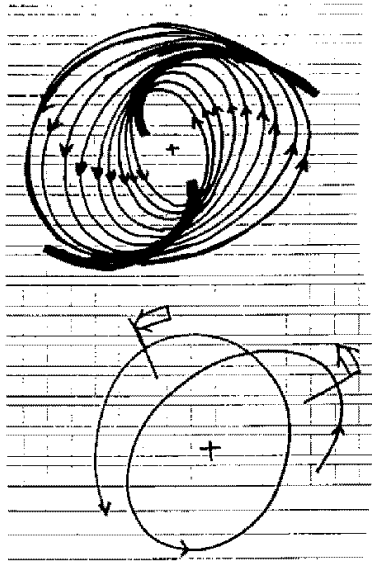


Figure 4.26: Rosette orbits of stars in a disk.

to achieve a spiral pattern. Suppose that the rosette orbits happen to have shifting major axis directions so that orbits of stars become close to each other twice on their orbital motion. Then the orbits and therefore the star distribution attain a self-sustaining spiral pattern along which the potential becomes deeper. This pattern of density enhancement with deeper potential is called the spiral density wave.

Pattern speed and resonances

The frequencies ω_p and κ are related to the galactic parameters as

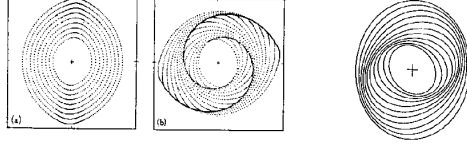


Figure 4.27: Many rosette orbits as seen in a rotating frame at ω_p .

$$\omega_p = \omega - \frac{1}{2}\kappa, \quad (4.65)$$

where κ is the epicyclic frequency, related to the Oort's constants as

$$\kappa = \sqrt{-A(A - B)}. \quad (4.66)$$

Because of the condition that the pattern speed ω_p is a slowly varying function of the radius, it can be taken as a constant over the disk. Therefore, once a pattern of density wave is formed (either a bar or spiral), the pattern of the potential is maintained for a much longer time than the rotation period of the disk, and the potential rotates rigidly at ω_p .

The pattern velocity near the sun is about $\omega_p R_0 \simeq 100 \text{ km s}^{-1}$. Since the true rotation velocity of stars and gas is $\omega_0 R_0 = V_0 = 220 \text{ km s}^{-1}$, the density pattern (potential) propagates through the galactic disk at

$$\Delta V_p = (\omega_p - \omega_0)R_0 \sim -120 \text{ km s}^{-1}, \quad (4.67)$$

when it is observed from a rotating frame with the disk. Equivalently, the stars and gas rotate at a relative velocity $-\Delta V = (\omega_0 - \omega_p)R_0 \sim 120 \text{ km s}^{-1}$ with respect to the density pattern, when it is observed from a rotating frame with the pattern.

The rotation velocity increases steeply near the galactic center, and is then almost constant over the disk. On the other hand, the pattern velocity $\omega_p R$ increases with R . Therefore, there appears a radius at which the rotation velocity becomes equal to the pattern velocity, and the guiding center of the rosette orbit rotates with the potential, when

$$\omega_p = \omega. \quad (4.68)$$

This radius is called the co-rotation radius, and the ‘co-rotation resonance’ occurs there.

There occur more resonances, which are called the ‘Lindblad resonances’, when

$$n(\omega_p - \omega) = \pm\kappa \quad (4.69)$$

with n being integer. At this radius, a star encounters the potential successively and regularly during its epicyclic oscillation. If $\omega_p - \omega = \kappa/n$, the star overtakes the potential, and this is called an inner Lindblad resonance. If $\omega_p - \omega = -\kappa/n$, stars are swept by the more rapidly rotating potential, and this is called an outer Lindblad resonance.

4.5.4 Galactic Shock Waves

Shocked Stream Line

Along the density maximum on a density wave pattern, the gravitational potential is deeper compared to the inter-arm regions. Since stars are collision-less, the density enhancement is approximately inversely proportional to the velocity of stars, and the excess depth of the potential due to this density enhancement is considered to be about 10% of the background (unperturbed) potential:

$$\frac{\delta\rho}{\rho} \sim \frac{\delta\Phi}{\Phi} \sim 0.1. \quad (4.70)$$

Velocity excess over the circular rotation is of the order of

$$\frac{\delta V}{V} \sim \frac{1}{2} \frac{\delta \Phi}{\Phi} \sim 0.05, \quad (4.71)$$

or we have $\delta V \sim 10 \text{ km s}^{-1}$.

The density wave potential with a spiral pattern of pitch angle p sweeps the interstellar gas at a speed

$$v_{\text{perp}} \sim (\omega - \omega_p)R \sin p. \quad (4.72)$$

In the Galaxy the pitch angle is about $p \sim 10^\circ$, and so $v_{\text{perp}} \sim 20 \text{ km s}^{-1}$. Since the gas is not collision-less, it happens that gas already swept up and compressed near the center of the potential pattern is encountered by a gas flowing into the arm due to attraction by the potential. The velocity difference between the gas which is about to flow out from the potential and the gas which is flowing in is a few tens of km s^{-1} in the direction perpendicular to the spiral. This velocity difference is supersonic, and a shock wave occurs at the contact surface of the gases flowing out and into the potential. This non-linear response, which causes a shock wave, strongly compresses the interstellar gas and acts to produce stars and bright spiral arms.

Consider a stream line (tube) of gas along an orbit on which the interstellar gas is rotating. If we look at the stream in a rotating frame with the pattern speed ω_p , the gas stream encounters twice the arms per rotation. The encounter of the gas stream occurs at a tilted angle p , and the condition which describes the shock wave is the velocity component of gas perpendicular to the spiral arm

$$v \sim (v_{\text{perp}}^2 + \delta V^2)^{1/2} \sim 20 - 30 \text{ (km s}^{-1}\text{)} \quad (4.73)$$

Since this velocity is supersonic,

$$M = v/c_s \sim 2 - 3, \quad (4.74)$$

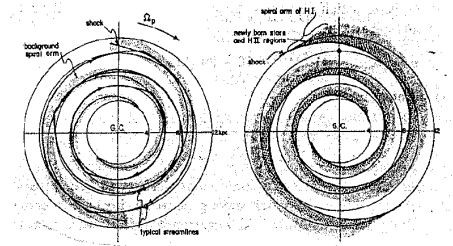


Figure 4.28: Galactic shock waves.

a shock wave is generated along the arm in the sense the compression occurs perpendicular to the arm. On the other hand, the velocity component parallel to the spiral arm has nothing to do with the arm regarding the shock wave generation, because it concerns the flow parallel to the arm along which the potential variation is very slow.

Density and Velocity Jumps and Inflow of Gas

According to the shock wave, the stream line is bent at the shock: The velocity component perpendicular to the arm drastically changes across the arm in such a sense that the mass flow is conserved:

$$\rho_1 v_1 = \rho_2 v_2, \quad (4.75)$$

where subscripts 1 and 2 denote the status before and after the shock passage. As shown in section 3.2.2, the density jump for an isothermal gas such as the ISM is given by

$$\rho_2/\rho_1 \sim M^2 \sim 10, \quad (4.76)$$

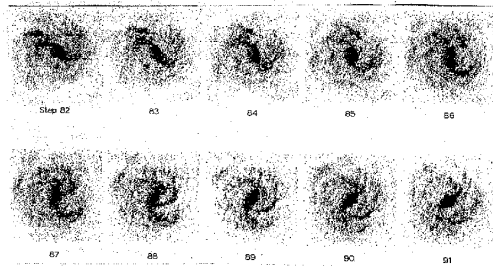


Figure 4.29: Non-circular motion in the gas disk caused by oval (spiral or bare) potential and galactic shock waves.

where $M \sim v/c_s \sim 2 - 3$ is the Mach number, and so

$$v_2 \ll v_1. \quad (4.77)$$

This results in loss of kinetic energy as well as in angular momentum of the stream. On the other hand the velocity parallel to the arm does not change:

$$v_{\text{para}} \sim (\omega - \omega_p)R \cos p. \quad (4.78)$$

Hence, the stream line becomes oval with its concave part coinciding with the spiral shock wave. Moreover, because of the loss of kinetic energy and angular momentum, the stream line (orbit) does not close, but the gas gradually spirals into the galactic center.

Star Formation in the Arms

The galactic shock wave has an essential implication for the star formation and arm brightening in spiral galaxies: According to the compression of gas along the spiral arm due to the galactic shock wave, the star formation rate increases by a factor of

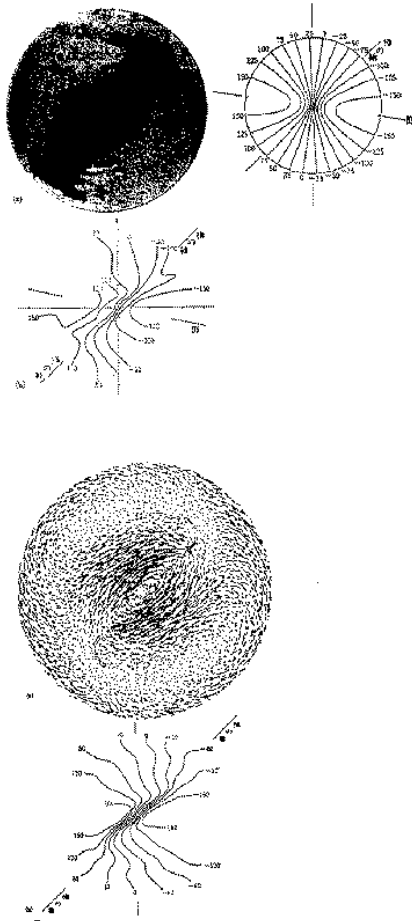


Figure 4.30: Non-circular motion in the gas disk caused by oval (spiral or bare) potential and galactic shock waves. (continued)

$$SFR \propto (\rho_2/\rho_1)^\alpha \sim 10^2 \quad (4.79)$$

($\alpha \sim 1 - 2$: Schmidt's law). This is the reason why the spiral arms are observed to be so bright, in spite of the weak (a few percent) density enhancement of background disk stars by the density waves.

Magnetic and Radio Arms

Since magnetic fields are frozen into ISM because of the large magnetic Reynolds number, compression of gas at the galactic shock wave results in compression of the magnetic fields in the direction perpendicular to the arm. By this two-dimensional compression, the strength of the parallel component of the field to the arm is increased by a factor proportional to the gas compression:

$$\frac{B_2}{B_1} \sim \frac{\rho_2}{\rho_1} \sim M^2. \quad (4.80)$$

According to the compression of magnetic field, the cosmic ray intensity also increases due to obeying an adiabatic compression law of a relativistic gas:

$$P_{CR} \sim \langle NE \rangle \propto \frac{\rho_2^\gamma}{\rho_1} \quad (4.81)$$

with $\gamma = 4/3$ being the adiabatic power index for a relativistic gas. Particle density is proportional to gas density, $N \propto \rho$, so

$$\langle E \rangle \propto \rho^{\gamma-1} \sim \rho^{1/3}. \quad (4.82)$$

Thus, the synchrotron emissivity at the arm is increased by a factor

$$\frac{\varepsilon_2}{\varepsilon_1} \sim \frac{\langle NB^2E^2 \rangle_2}{\langle NB^2E^2 \rangle_1} \sim \left(\frac{\rho_2}{\rho_1}\right) \left(\frac{\rho_2}{\rho_1}\right)^2 \left(\frac{\rho_2}{\rho_1}\right)^{2/3} \sim \left(\frac{\rho_2}{\rho_1}\right)^{3.67} \sim M^{7.3}. \quad (4.83)$$

Therefore, the synchrotron brightness of an arm is by a factor of $M^{7.3} \sim 10^2 \sim 10^3$ times that of the inter arm region. In fact, radio continuum observations of spiral galaxies have shown that the radio brightness is much stronger along the spiral arms than in inter-arm regions, particularly along dark lanes which are places where the shock compression is highest.

Nuclear Fueling by a Bar

The galactic shock wave has also kinematical as well as gas-dynamical implications for the evolution of a gas disk, as well as fueling of the nuclear region by gas. According to the loss of the velocity component perpendicular to the spiral arms, the rotation velocity of gas becomes highly non-circular, particularly near the spiral arms. Such a non-circular rotation of gas has been observed as the deformation of iso-velocity contours from those expected for a circular rotation.

By this mechanism, it happens also that the orbit of interstellar gas shrinks. If the potential is deep enough, in such a case for a bar potential, this causes a rapid supply of gas toward the nuclear region of a galaxy. In fact, barred spiral galaxies are shown to experience such gas inflow. This bar-shock contraction of disk gas is considered to be the most efficient fueling mechanism for the nucleus activity and/or starburst in the central region.

Chapter 5

THE GALACTIC CENTER AND ACTIVITY

5.1 The Galactic Center in Radio

5.1.1 Radio Continuum Emission

Radio continuum features in the galactic center region are a superposition of various active radio sources: star-forming regions distributed in thin thermal disk; vertical structures which are mostly non-thermal closely related poloidal magnetic fields; and the Galactic center known as the radio source Sgr A. The radio emission is therefore a mixture of thermal and non-thermal emissions. In this chapter, we discuss the properties of the radio emission, reviewing the methods to distinguish thermal and nonthermal emissions. We then summarize various exotic structures, which are mostly perpendicular to the galactic plane, and discuss them in relation to vertical magnetic fields and to manifestation of energy release from the nuclear disk. We comment on the similarity of large-scale ejection features to some radio bubble features in external galaxies. Vertical cylinder structures of expanding rings of

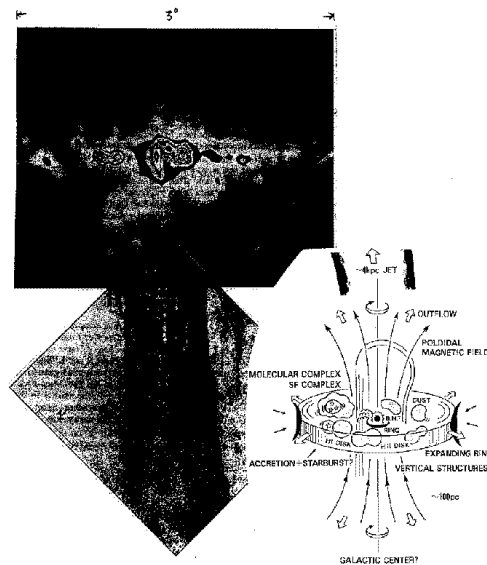


Figure 5.1: Various features around the Galactic Center.

molecular gas are also discussed.

5.1.2 Flat Radio Spectra

The radio continuum emission from the galactic center region of $\sim 3^\circ \times 3^\circ$ is a mixture of nonthermal (synchrotron) and thermal (free-free) emissions. In order to investigate the various observed structures it is essential to clarify their emission mechanisms. We describe the methods to separate these two emission components.

The conventional method to investigate the emission mechanism is to study the spectral index. Thermal emission shows a flat spectrum of $\alpha = -0.1$ with $S \propto \nu^\alpha$, while nonthermal emission usually shows steeper spectrum. Radio emission from the galactic center has a flat

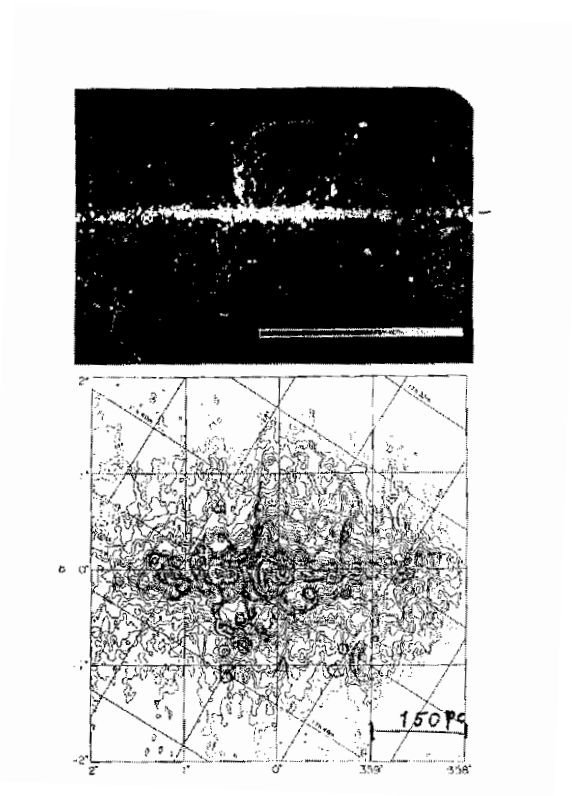


Figure 5.2: The whole-sky 408 MHz map and a 10 GHz map of the central 4° region of the Galaxy.

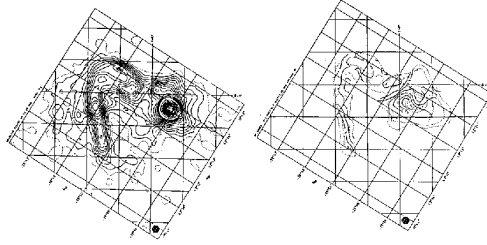


Figure 5.3: Spectral index distribution for the radio Arc and Sgr A region as determined using data at 843 MHz, 10 GHz, and 43 GHz.

spectral index, and it was thought that the extended component comprises an ellipsoidal disk of diffuse thermal gas of a size of $\sim 300 \times 100$ pc. However, a spectral index study of radio data in large frequency separation, from 845 MHz to 43 GHz, has shown that the spectral index in the radio Arc and bridge region near Sgr A is flat or even inverted (positive). It was shown that the spectral index in the central 3° region is almost everywhere flat. Flat spectra are obtained even in regions where strong linear polarization was detected.

Hence, the flat spectrum observed near the galactic center must no longer be taken as an indicator of thermal emission. We note that many active galactic nuclei in extragalactic systems often show flat radio spectra for their nonthermal characteristics. However, the question why the spectra are so flat, or how high-energy electrons are supplied so efficiently in such a wide area of the galactic center, is not answered as yet.

5.1.3 Linear Polarization

A direct and more convincing way to distinguish synchrotron radiation is to measure the linear polarization. However, an extremely high

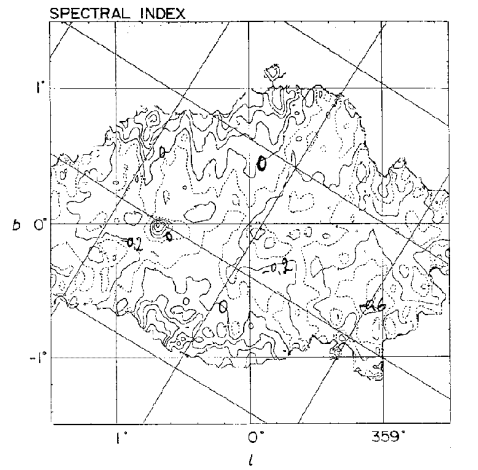


Figure 5.4: Radio spectrum distribution in the central 3° region of the Galaxy as observed at 10 and 2.7 GHz.

Faraday rotation caused by the dense interstellar matter and long path length through the galactic plane de-polarizes the emission by the finite-beam and finite-bandwidth effects, which makes the measurement difficult. This difficulty has been resolved by the development of a multi-frequency, narrow-band Faraday polarimeter as well as by high-resolution and high-frequency observations using the VLA. Very large rotation measure ($RM > \sim 10^3 \text{ rad m}^{-2}$) and high degree (10 - 50%) polarization have been observed along the radio Arc and on the eastern ridge of the Galactic Center Lobe.

At high frequencies the Faraday de-polarization becomes less effective. The detection of polarization as high as $p \sim 50 \%$ along the Arc at mm wavelengths is reported. This is nearly equal to the theoretical maximum, $p_{\text{max}} = (\alpha + 1)/(\alpha + 7/3) \simeq 47 \%$, for the Arc region where the spectral index has the value of $\alpha \simeq +0.2$. This fact implies that the magnetic field is almost perfectly ordered. This is also consistent with the VLA observations showing straight filaments suggestive of highly ordered magnetic field. From these observations of linear polarization it is clear that the radio emission near the galactic center, in particular around the radio Arc, is nonthermal despite their flat or inverted spectra.

5.1.4 Infrared-to-Radio Ratio

Separation of thermal and nonthermal radio emission can be done in a more efficient way even for the regions where no polarization data are available. The method uses comparison of far-IR (e.g. $60 \mu\text{m}$ data from IRAS survey) and radio intensities (both in Jy/str): thermal emission regions, mostly composed of HII gas, have high IR-to-radio ratio, $R = I_{\text{FIR}}/I_{\text{R}} \simeq 10^3$. On the other hand, nonthermal emission regions, such as supernova remnants, have small IR-to-radio ratio, $R = 0 \sim 300$. Using this characteristics we are able to distinguish thermal and non-thermal emission regions in a wide area near the galactic center. The

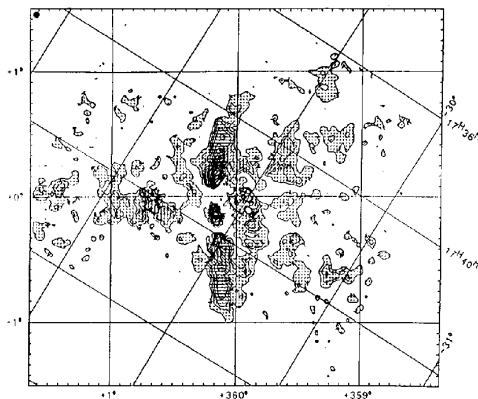


Figure 5.5: Linearly polarized radio intensity distribution at 10 GHz of the Galactic Center region.

region near the galactic plane is dominated by thermal emission and many strong radio sources like Sgr B2 appear thermal (HII). These regions are closely associated with dense molecular clouds and therefore related to star formation from the clouds. On the other hand we find many of the prominent features like the Radio Arc, Sgr A and regions high above the galactic plane including the GCL (galactic center lobe) are nonthermal.

5.2 Thermal Emission in the Galactic Center

5.2.1 The Thermal Disk and Star Formation

The nuclear disk about 50 pc thick and 200 pc in radius consists of numerous clumps of thermal emission regions, most of which are active star-forming regions and HII regions, are detected in the hydrogen recombination lines. Typical HII regions are named Sgr B, C, D and

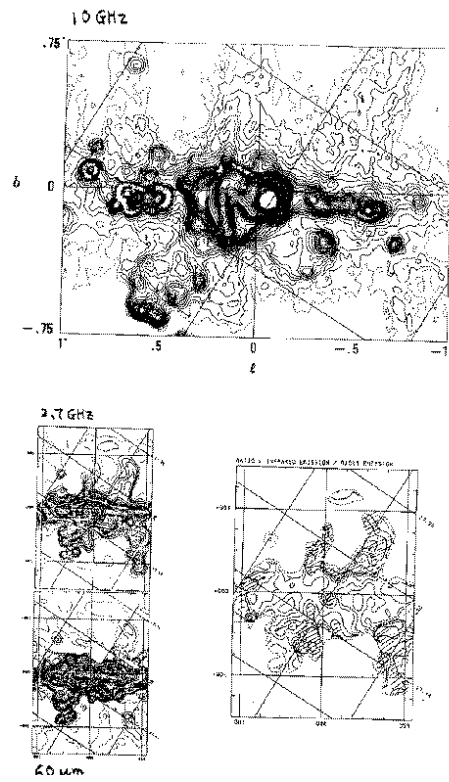


Figure 5.6: Radio continuum (2.7 GHz), IR 60 μm , and radio-to-FIR intensity ratio in the Galactic Center region

E. The total HII mass of $2 \times 10^6 M_{\odot}$ has been estimated, and the production rate of Ly continuum photons of $3 \times 10^{52} \text{ s}^{-1}$ is required to maintain this amount of HII gas. The star forming rate, which is assumed to be proportional to the Ly continuum photon flux, of the central few hundred pc region reaches almost 10% of the total star forming rate of the Galaxy. The HII regions are surrounded by expanding shells and cylinders of molecular gas.

Because of the high concentration of molecular gas in the central few hundred pc region, the star-formation efficiency (SFR/molecular gas mass) in the central region is not high as in the normal SF regions. Or, in turn, the ratio (γ) of the gaseous mass to the SF rate can be taken as the “youngness” of SF region, and the value of γ is large compare to HII regions in the outer disk: The central SF region, particularly such SF region as Sgr B2, are “younger” in the sense that the “fuel” gas is over abundant compared to newly born stars.

5.2.2 Molecular Clouds and Star Forming Regions

The galactic center region has also been observed intensively at various molecular lines. In particular, CO line observations have shown a global distribution of the molecular gas and have revealed a high concentration in the central few hundred pc. This fact clearly indicates that intense star formation in the central region occurs deeply coupled with the wealth of molecular gas.

Correlation between Continuum and Molecular Sources

Figure 5.7 shows positional relationship between the distributions of the ^{13}CO and the continuum emission features. It is obvious that the intensity distributions both for the continuum and molecular line emissions are significantly asymmetric with respect to the galactic center (Sgr A). They are both stronger in the positive longitude side than in the negative longitude regions. For various thermal radio sources,

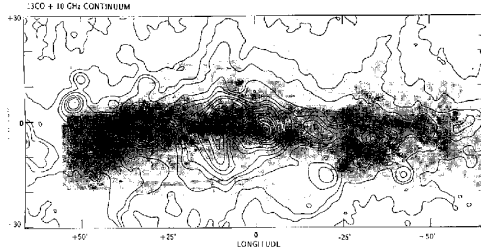


Figure 5.7: Superposition of radio continuum features on the CO line map.

velocity data from hydrogen recombination line observations are available, and are summarized in table 1 together with their galactic coordinates.

Sgr B2 and a Molecular Complex

The radio source Sgr B2 consists of compact HII regions with strong thermal emission with recombination-lines at a velocity of $V_{\text{LSR}} = 65 \text{ km s}^{-1}$. A dense molecular cloud with an angular size of about $0^{\circ}.05$ at $V_{\text{LSR}} = 60 \sim 70 \text{ km s}^{-1}$ is associated not only regarding velocity, but also positionally coincides with Sgr B2. The continuum radio emission suffers from strong H_2CO molecular line absorption at $V_{\text{LSR}} = 62.5 \text{ km s}^{-1}$. This indicates that the molecular cloud lies in front of the continuum source, and that probably Sgr B2 (HII region) and the molecular cloud are in contact with each other along the line of sight. Namely, star formation in Sgr B2 may be taking place at the farther end of the molecular cloud along the line of sight.

The Sgr B2 molecular cloud is a part of even larger molecular complex: At a similar velocity, $60\text{-}70 \text{ km s}^{-1}$, the cloud is embedded in

a wide outskirts with a diameter of approximately $0^{\circ}25$. We call this complex the "Sgr B2 molecular complex". The total mass of this complex can be estimated using the integrated intensity and the extent as read from the ^{13}CO maps. We use the relation $\sigma = 32I$, with σ being the surface mass density of molecular gas in $M_{\odot} \text{ pc}^{-2}$ and I being the ^{13}CO line intensity in K km s^{-1} . The total mass of the Sgr B2 molecular complex, including its outskirts, is estimated to be $1.5 \times 10^6 M_{\odot}$. The thermal source Sgr B1 lies close to Sgr B2. At the same velocity as Sgr B1 (45 km s^{-1}) there exists a molecular complex which extends for an angular extent of $\Delta l \times \Delta b \simeq 0^{\circ}.4 \times 0^{\circ}.3$. It is remarkable that this molecular complex makes a large loop with its clearest appearance at $V_{\text{LSR}} = 30 \sim 40 \text{ km s}^{-1}$.

This loop feature has a systemic velocity of about 40 km s^{-1} and can be recognized over a wide velocity range from $V_{\text{LSR}} = 70 \text{ km s}^{-1}$ to $V_{\text{LSR}} \simeq 20 \text{ km s}^{-1}$. We emphasize that the recombination-line velocity ($V_{\text{LSR}} = 45 \text{ km s}^{-1}$) of Sgr B1 coincides with the velocity of this molecular loop, which indicates that the loop is physically related to Sgr B1, possibly driven by the activity of this HII region. From these facts we may interpret that the loop feature is a molecular shell surrounding Sgr B1; we call it the "Sgr B1 molecular shell".

The large velocity dispersion of the shell ($V_{\text{LSR}} = 20 \sim 70 \text{ km s}^{-1}$) suggests that it is expanding at a velocity of about 25 km s^{-1} referring to its center velocity. The size of this shell is about $40 \text{ pc} \times 30 \text{ pc}$ for a distance of 8 kpc. If the expanding velocity is 25 km s^{-1} , the age of the shell would be of the order of 10^6 years. Hence, the expansion of the shell may have started about 10^6 years ago when Sgr B1 was still more active than today. The total mass of the shell is estimated to be $2 \times 10^6 M_{\odot}$. This leads to a kinetic energy of the expanding motion of about 1.3×10^{52} ergs.

Table 5.1 summarizes the position and velocity relationship between the molecular and HII features in the Galactic Center region.

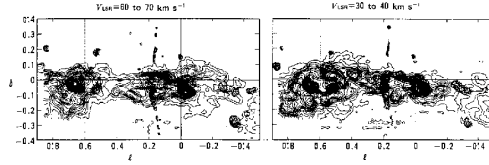


Figure 5.8: CO clouds around Sgr B2.

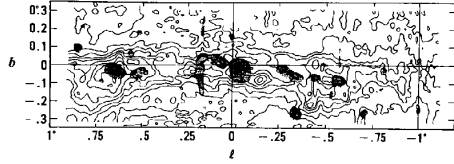


Figure 5.9: Molecular clouds and continuum sources in the Galactic Center region.

H II	Cont. G(<i>l</i> , <i>b</i>)	$V_{LSR,HII}^{(a)}$ (km s ⁻¹)	MC	$V_{LSR,CO}$ (km s ⁻¹)	V_{exp} (km s ⁻¹)	M_{MC} (M_{\odot})	E_{kin} (erg)
Sgr B1	G+.52-.05	45	shell	30-40	25	2×10^6	1.3×10^{52}
Sgr B2	G+.66-.04	65	complex	60-70	...	1.5×10^6	...
G-0.27	G-.27-.03	-43	Arcs		25	$\sim 10^5$	$\sim 6 \times 10^{50}$
	G-.34-.07		G-.3+.05	-70			
	G-.45-.06		G-.3-.12	-20			
		...	Barrel ^(b)	20	70	10^5--6	10^{52--53}
Sgr C	G-.56-.08	-60	Complex	-60

Table 5.1: Molecular clouds and continuum sources in the Galactic Center region.

Molecular Gas Avoidance near a Continuum Chain

An elongated molecular feature of ^{13}CO is found which is aligned parallel to the galactic plane at $b \simeq 0^\circ.02$ and the velocity varies continuously from $V_{\text{LSR}} = -50 \text{ km s}^{-1}$ ($l \sim -0^\circ.2$) to -90 km s^{-1} ($\sim -0^\circ.5$). Another arc-shaped molecular feature is found at $b \sim -0^\circ.2$ and runs parallel to the negative-velocity arc but at lower latitude in the opposite side of the continuum chain. This lower arc has a continuously changing velocity from $V_{\text{LSR}} = -20 \text{ km s}^{-1}$ ($l \sim -0^\circ.2$) to -40 km s^{-1} ($l \sim -0^\circ.5$). At $V_{\text{LSR}} = -30 \sim -50 \text{ km s}^{-1}$ there are several small clouds which are more closely associated with the continuum chain, and the velocity coincides with that of G-0.27. The clouds seem to be related to the southern molecular arc at its larger velocity ends.

Note that the continuum chain lies near the center of the molecular arcs and positionally coincides with a region of empty molecular gas: The continuum and molecular features seem to avoid each other. We emphasize that these molecular arcs are concave with respect to each other, and that they appear to surround the continuum chain, comprising an elliptical ring with its center at G-0.27-0.03. This suggests that the two arcs comprise opposite parts of an expanding ring at a velocity of about 25 km s^{-1} . The ring radius, as estimated from its angular extents, will be about 30 pc, and it is tilted by about 20° from the galactic plane, so that its age of the order of 10^6 y. The radial velocity of G-0.27 ($V_{\text{LSR}} = -43 \text{ km s}^{-1}$) is nearly equal to the mean velocity of the two molecular arcs. However, on the velocity-position diagrams it is not clear that these two arcs are connected to each other. The upper arc might be an isolated cloud.

Molecular Rings and Cylinders

From CS ($J = 1 - 0$) line observations a barrel-shaped shell of radius 20 pc at G-0.3-0.1 has been noticed. The "barrel" has a central LSR

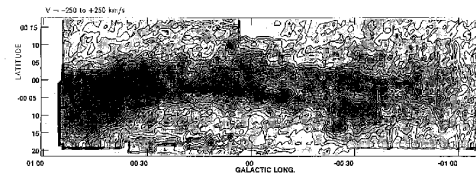


Figure 5.10: ^{13}CO line intensity distribution in the galactic center.

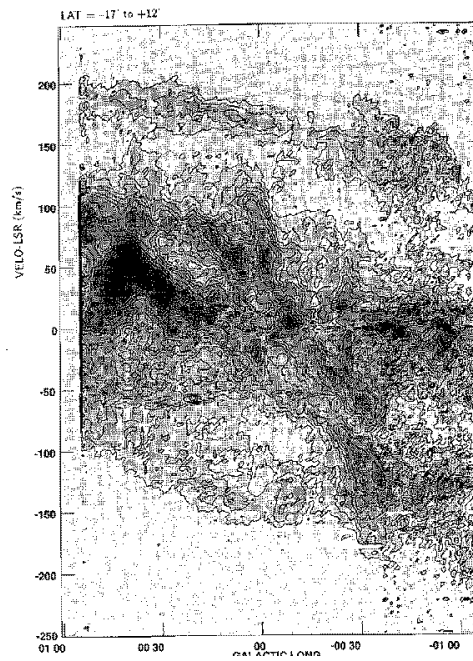


Figure 5.11: The (l, V) (longitude-velocity) diagram of the ^{13}CO line emission of the galactic center.

velocity of $V_{\text{LSR}} \sim +20 \text{ km s}^{-1}$. On the $l - V_{\text{LSR}}$ map it makes a ring-like feature fitted with an expanding loop at a velocity of 70 km s^{-1} and radius 20 pc . This may be attributed to an expanding shell at a velocity of 70 km s^{-1} , which was caused by an explosion with an energy of 10^{52-53} ergs.

The center position of this barrel apparently coincides with the continuum source G-0.27-0.03, which has $V_{\text{LSR}} = -43 \text{ km s}^{-1}$, and the negative velocity side of the ring on the $V_{\text{LSR}} - l$ diagram at $V_{\text{LSR}} = -40 \sim -50 \text{ km s}^{-1}$ is close to the recombination-line velocity of G-0.27-0.03. The source G-0.27-0.03 may be a shock-triggered star-forming site on the surface of this expanding barrel. From the ring radius, 20 pc , and the expansion velocity, 70 km s^{-1} , the barrel's age must be of the order of 3×10^5 years. This time scale might be too short for other star formation to be triggered. Hence, it is not clear if the barrel and the continuum source G-0.27 are related to each other. We also note that no continuum source, and therefore no recombination source, has been found near the center velocity of the barrel.

Sgr C and Molecular Complex

On the integrated ^{13}CO map the continuum source Sgr C lies near a position where the molecular emission has depression. On the channel maps of the $\text{CS}(J = 2 - 1)$ line emission we find a complex of molecular gas at $V_{\text{LSR}} = -40 \sim -60 \text{ km s}^{-1}$ which though associated with Sgr C, is positionally shifted toward the south-east by about $5'$. Again we notice that the continuum source does not positionally coincide with the peak position of its associated molecular complex.

The Sgr C molecular complex extends for approximately $0^{\circ}25$ (35 pc) not only along the galactic plane but also in the direction perpendicular to the plane. In particular, it has a negative-latitude extension at $V_{\text{LSR}} = -50 \sim -60 \text{ km s}^{-1}$. Another molecular feature at high negative velocity, $V_{\text{LSR}} = -100 \sim -140 \text{ km s}^{-1}$, is associated with this

region. This high-negative velocity feature comprises of two symmetrical plumes extending from G-0.50-0.05 vertically to the galactic plane about $\pm 0^\circ.2$. This might be associated with possible high-velocity ejection along the Galactic Center Lobe.

Origin of the shells

The shells and rings are probably driven by activities in the star-forming regions, such as stellar winds and/or supernova shocks. In fact, the kinetic energies of the shells, $E \sim 10^{50-52}$ ergs, can be supplied by several supernovae. According to the starburst-ring formation scenario, successive SN explosions and stellar winds cause high pressure in the central region of a dense nuclear molecular disk, and a cavity forms near the center. Then, the upper and lower parts of the disk are blown off while forming a cylindrical outflow perpendicular to the disk. Accordingly an expanding molecular ring forms within the disk. It is possible that similar cavity-ring formation takes place within a single massive cloud near the galactic center triggered by interior star formation or mini-burst: namely mini-rings/shells can be formed by mini-bursts associated with individual clouds.

In this scenario the HII region Sgr B2 may still be embedded within or in contact with a dense molecular complex, and star formation (or a mini burst) in Sgr B2 has possibly been triggered by the expanding Sgr B1 shell. The molecular shell centered by Sgr B1 is in a cavity phase and expanding. The molecular ring around G-0.27 is in a late ring phase, in which the upper and lower parts of the cloud had already been blown off. It is thus possible that the G-0.27 ring is the oldest, the Sgr B1 shell is moderate, and the Sgr B2 complex the youngest star-forming (mini-burst) regions. The fact that they are not necessarily located close to each other suggests that star-burst sites are wandering around the galactic center.

5.3 Galactic Nucleus and its Surrounding Magnetic Structures

5.3.1 Sgr A: The Nucleus

Sgr A* is the nucleus of the Galaxy which is unresolved even with the use of a VLBI, and is supposed to be a very compact radio source of a size less than 1 milliarcsec, or $\sim 10^9$ km ~ 10 AU. The nucleus is surrounded by a nebula which exhibits three-armed peculiar spirals of a size ~ 3 pc, showing thermal radio spectrum. These features are further surrounded by a tilted ring of molecular gas of radius ~ 3 pc, which is rotating at a velocity of about 100 km s^{-1} . These features are called Sgr A West, which shows a flat-spectrum in radio. A shell-type supernova remnant is superposed on the eastern edge of these features, and is called Sgr A East, having a steep spectrum indicating a nonthermal emission. All these features are further embedded in an extended halo of radius about 10 pc, and the radio emitting region containing all these are called Sgr A.

5.3.2 Thermal Filaments

Complex filaments are extending from Sgr A toward the north, composing a bridge between the radio Arc and Sgr A. Detection of hydrogen recombination lines and the association of molecular gas at negative velocities indicate its thermal characteristics, and the structures are often called the thermal arched filaments.

In spite of thermal radio emission, a large Faraday rotation has been detected toward the bridge, which indicates the existence of a magnetic field along the thermal filaments. A magneto-ionic jet model in which the gas is flowing out of Sgr A and collides with the ambient poloidal



Figure 5.12: Sgr A* and the three-armed mini spirals.

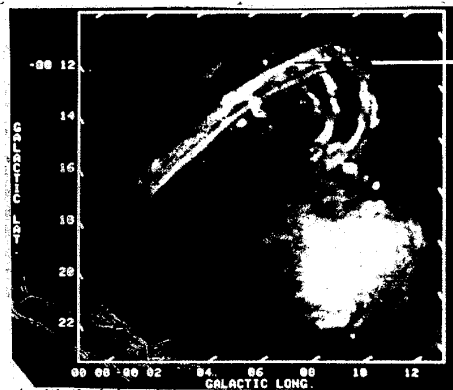


Figure 5.13: Sgr A with the halo and the radio arc.

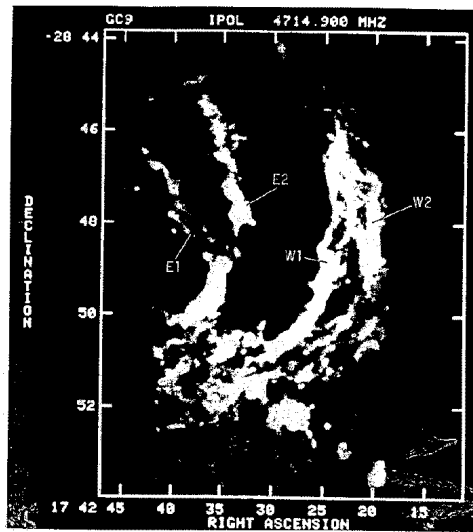


Figure 5.14: Thermal filaments as observed with the VLA.

magnetic field at the radio Arc has been proposed. Observations of molecular lines showed that the gas is flowing toward the center and an accretion model has been proposed by analyzing the velocity field. The complex structure in the bridge indicates high turbulent motion inside the bridge. In fact, velocity dispersion as high as $30\text{-}50 \text{ km s}^{-1}$ has been observed in the bridge from recombination-line observations, and it increases drastically near the Arc ($60\text{-}70 \text{ km s}^{-1}$), which suggests a dynamical interaction of the bridge with the Arc. High-resolution maps of the radio arc have shown that the Arc (straight filaments) and the arched filaments are interacting with each other.

5.3.3 Vertical Magnetic Tubes: Radio Arc and Threads

The radio Arc was originally found in the radio continuum survey maps of the galactic plane, and has been resolved into many straight filaments with the use of VLA. The straight filaments run perpendicular to the galactic plane, and extend more than $\sim 100 \text{ pc}$ toward positive latitudes. The mid point of the arc is strongly polarized ($\sim 20 - 50 \%$), and shows a high Faraday rotation ($RM \sim \text{a few } 10^3 - 10^4 \text{ rad m}^{-2}$). The theoretically maximum polarization of 50% along the Arc indicates a highly ordered magnetic field and is consistent with the VLA straight filaments. The magnetic field direction, as determined from the intrinsic polarization angles, is parallel to the filaments and vertical to the galactic plane. Field strength as high as $\sim 1 \text{ mG}$ has been estimated in the Arc and in some radio filaments.

Interferometric observations of the filaments in the Arc at 43 GHz revealed that some filaments are not visible at this high frequency. Assuming the field strength of the order of 1 mG, we could estimate the life time of cosmic-ray electrons emitting at 43 GHz to be about 4000 years. This implies that the filaments of strong magnetic field may be a time variable, or transient feature, being temporarily illuminated by recently accelerated high-energy electrons. It would be, therefore,

interesting to perform a time-variation watch of the thin nonthermal filaments in the Arc by high-resolution VLA observations.

The higher latitude extensions of the Arc, both toward positive and negative latitudes for more than 100 pc, are also polarized and are called polarized plumes. The degree of polarization reaches as high as 20% at 10 GHz. The magnetic field directions are parallel to the radio arc, or vertical to the galactic plane. High Faraday rotation ($\sim \pm 10^3$ rad m^{-2}) has been detected. The sense of rotation measure reverses from positive to negative latitude sides, indicating a reversal of the line sight component of the magnetic field above and below the galactic plane. The field strength is estimated to be 10-100 μG . The polarized spot and the plumes are parts of a large-scale poloidal magnetic field twisted by the disk rotation (see next section).

Besides the filaments in Arcs, numerous straight filaments, called “threads”, are observed. They appear to be distributed rather independently of the other major radio sources. They are roughly perpendicular to the galactic plane. The threads intersect the other features without interaction. From the very thin and straight appearance the threads are likely magnetic structures, and the vertical nature is consistent with a large-scale poloidal field in the central region.

5.4 Ejection: Lobes and Jets

5.4.1 The Galactic Center Lobe

The galactic center lobe (GCL) is a loop structure of about 200 pc diameter extending vertically over the galactic plane. The cross section of the lobe parallel to the galactic plane indicates its cylindrical structure. The eastern ridge of the lobe is an extension from the radio Arc and is strongly polarized. The magnetic field is shown to run parallel to the ridge. The ridge also extends toward negative latitude, where a symmetric polarized plume is found. The western ridge emerges from

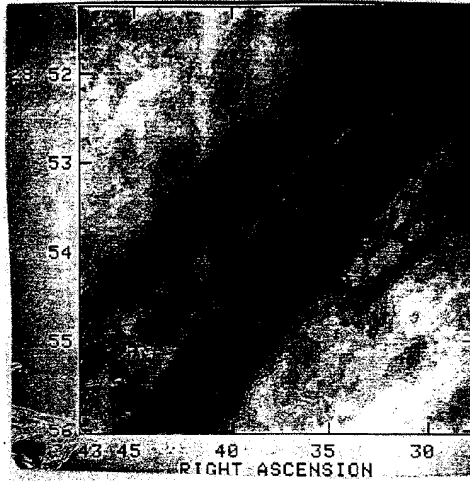


Figure 5.15: Radio Arc.

Sgr C and is clearly the extension of the VLA filament. The detection of filament and polarization in the western ridge indicates the existence of magnetic field. Recently, a complex of molecular gas and warm dust associated with the western ridge of the lobe has been detected, and a velocity jump in the CO-line spectra with a shock front coinciding with the western ridge has been found.

Formation of the lobe structure has been modeled in various ways: An explosion hypothesis requires an explosive energy injection near the nucleus, which produces an expanding propagating the disk and halo. An MHD acceleration model in which the gas is accelerated via a twist of poloidal magnetic field by the accretion gas disk has been proposed.

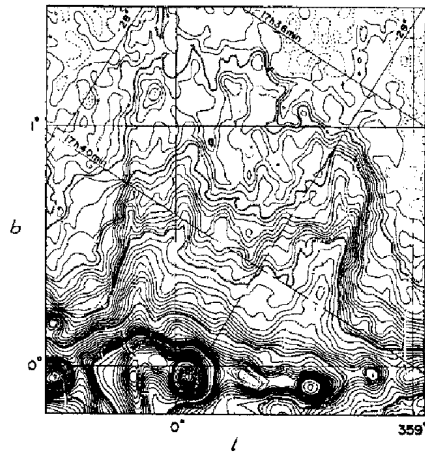


Figure 5.16: The Galactic Center Lobe.

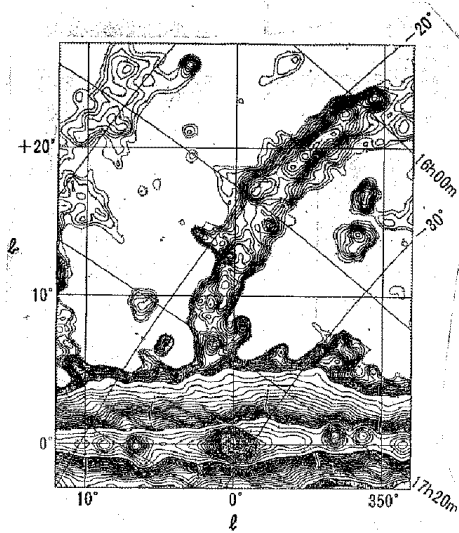


Figure 5.17: The 4-kpc Galactic Center Jet.

5.4.2 The 4-kpc Jet

On a much larger scale of a few kpc above the galactic plane, a giant spur has been found, which emanates from the galactic center toward positive latitude, $b \sim 25^\circ$. A ridge connecting the spur to the galactic center has been detected by 1408 MHz observations. This feature, which is 4-kpc long and some 200-pc in diameter, may be cylindrical in shape and extends roughly perpendicular to the galactic plane. This structure might be a jet (or the remnant of a relativistic beam from the nucleus), or it might be magnetic tornado produced by the differential rotation between the halo and the nuclear disk. Recently, a VLBI mini-jet in the central few mas region of Sgr A* has been found at 43 GHz. The jet direction appears to point the largest scale jet at high latitude, and they have suggested a possible connection of both objects.

5.4.3 Giant Shock Wave in the Halo: the North Polar Spur

The whole sky radio map at 408 MHz shows numerous radio spurs. The most prominent spur is called the North Polar Spur (NPS), which traces a giant loop on the sky of diameter about 120° , drawing a huge Ω over the galactic center. There have been various interpretations of this prominent feature, particularly related to a nearby supernova remnant. Here, we comment on a rather exotic idea, which presumes an explosion at the galactic center: The giant Ω -shape of the NPS could be a shock front due to a gigantic explosion or a sudden energy input at the galactic center of the order of $10^{55} \sim 10^{56}$ erg. In this model, the NPS must lie at a distance of a few kpc away. On the other hand, the current supernova remnant hypothesis predicts a distance of a few tens of pc. A key to explore the distance is the X-ray absorption by the galactic disk. If it is a galactic-scale bubble beyond the HI disk, the X rays must be absorbed near the galactic plane: the optical depth (H column density) changes as a function of $\text{cosec } b$. On the other hand, if the NPS is a local object embedded in the galactic HI disk, the optical depth does not change with b , and hence, the NPS ridge should be visible even near the galactic plane at $b < 10^\circ$ where the radio brightness is the highest. Indeed, X-ray all-sky maps reveal X-ray features associated with the NPS as well as those making up a well-defined large-scale shocked features.

5.4.4 Extragalactic Radio Bubbles

Similar huge bubbles in radio continuum have been found in many spiral galaxies. Edge-on galaxy NGC 3079 has S-shaped double lobes which extend for 3 kpc size in both directions of the galactic plane. NGC 4258 is known for its symmetrical S-shaped radio features perpendicular to the major axis. These bubbles would look like similar to the NPS if the observer is sitting inside the galaxies.

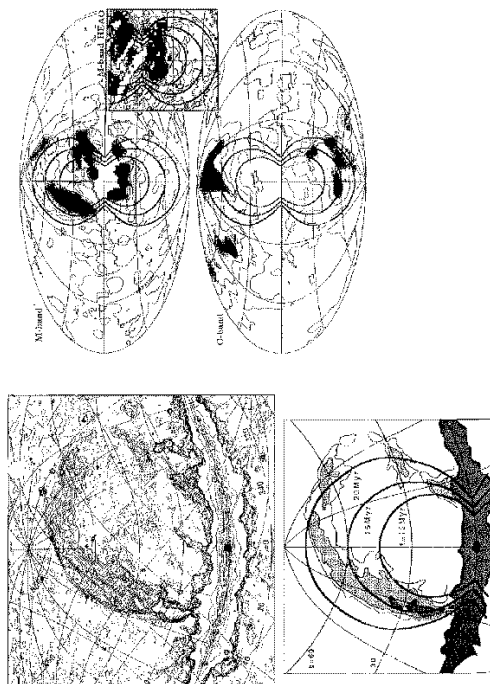


Figure 5.18: The North Polar Spur in radio and X-rays. A model shock front associated with an explosion at the nucleus or with a starburst some 10^7 yr ago is superposed.

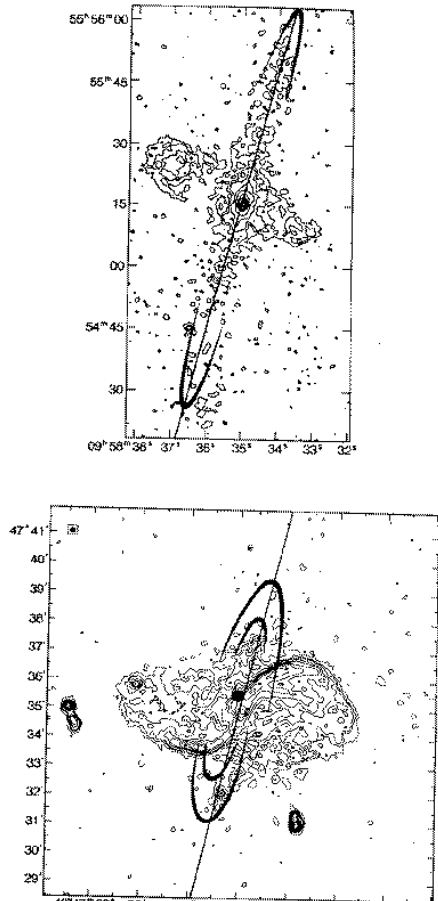


Figure 5.19: NGC 3079 at 1420 MHz, showing a large-diameter bubble in the halo, NGC 4258 at 1420 MHz, and the North Polar Spur (Milky Way).

5.5 Origin of Vertical Structures

5.5.1 Poloidal fields

Polarization observations of the galactic center region show that the field direction projected on the sky along the radio Arc and the eastern ridge of the galactic center lobe is perpendicular to the galactic plane. The polarization is visible in a wider area of $1.5^\circ \times 1.5^\circ$ area around Sgr A, and showed that magnetic field is widely distributed in the galactic center region. Measurements of the Faraday rotation show that the rotation measure (RM) reverses from the lower side of the galactic plane to the upper side, indicating reversal of the line-of-sight component of the field. The reversal of the RM is also observed across the rotation axis of the Galaxy. From these, a poloidal field model has been proposed in which the field lines are twisted by the disk rotation. However, it is often claimed that the very straight nature of the filaments in the radio Arc is suggestive of a field lines not bending. If this is the case, the Faraday reversal should be attributed to intervening fields between the Arc and the Sun. Since the RM reversal happens in $\sim 10'$ -scale and the RM amplitude is as large as $RM \sim 10^4$ rad m^{-2} , it is reasonable to suppose that the Faraday effect occurs in the nuclear disk.

If we stand on the primordial origin hypothesis of galactic magnetic fields, we should inevitably consider the evolution of the vertical component of the primordial field. The time scale with which a magnetic field component perpendicular to the disk plane diffuses away from the galaxy may be estimated as $\tau_{\text{vert}} \sim r^2/lv \sim 10^{11}$ y. Therefore, the vertical component trapped from the intergalactic space can never escape from the galaxy, but is transferred to the central region when the galaxy contraction proceeds. A rough estimation shows that the field strength of the vertical component in the galaxy is proportional to the surface mass density, and a strong vertical field, some $10 \mu\text{G}$, is

expected to exist in the central 1-kpc region. On the other hand, the disk component parallel to the galactic plane annihilates in the central region more efficiently than in the outer region and a rather weaker disk field is expected there.

This scenario of evolution of the galactic field thus predicts that a vertical field dominates in the central region, while the disk spiral field has the maximum in the outer disk several kpc away from the central region. This is consistent with the fact that our Galaxy possesses a twisted poloidal field in the center, while the disk field (parallel to the galactic plane and spiral arms) is strongest at $r \sim 5$ kpc. Similar characteristics have been found in spiral galaxy M31: the central radio source shows polarization consistent with the vertical field. The projected field direction is perpendicular to the major axis, while the disk field, which is a superposition of ring and spiral, has the maximum at $r \sim 10$ kpc.

Given a large-scale poloidal field, which penetrates the rotating dense nuclear disk, twist of the field is inevitable. The twist will then propagate toward the halo, accelerating the gas perpendicular to the disk plane. This will result in a cylindrical outflow of gas and cosmic rays, which will account for the formation of the galactic center lobe. The large-scale poloidal field in the halo will also be twisted by the differential rotation between the disk and halo gases. The twist will amplify the field strength near the rotation axis, and will be observed as the galactic center jet (or tornado) of 4-kpc length.

5.5.2 Explosion

A sudden energy release at the galactic center such as an explosion or a star burst also results in vertical gaseous structure. In fact molecular and hydrogen line observations of the disk gas exhibit various expanding ring features. We here discuss the possibility that an explosion at the center will produce the vertical structures and examine

if the expanding rings in the disk plane are associated with vertical structures.

An explosion and an energy release in a short time like a star burst at the center of a rotating disk can be theoretically traced by hydrodynamic and MHD codes. A shock wave which is initially spherical expands more rapidly in the direction perpendicular to the disk plane because of the smaller gas pressure and mass in this direction compared to those in the disk plane. Then the shock front attains an Ω shape elongated perpendicular to the disk, mimicking the GCL at some stage. Further propagation of the shock front through the nuclear disk has been numerically simulated: Refraction of the shock waves due to the density variation in the disk results in focusing onto a ring of radius about twice the scale height of the disk gas density (~ 200 pc) in the nuclear disk. Such a ring has been indeed observed as the 200-pc expanding ring as follows.

5.5.3 The 200-pc Expanding Molecular Cylinder

Expanding ring features of various scales are found in the galactic plane, which are mainly observed in the molecular and hydrogen line emissions. The molecular expanding ring of 200 pc radius is the most typical example, which has a radius of 200 pc and is expanding at a velocity of 50 km s^{-1} . The tangential points to the 200-pc ring on the $l - v$ diagram appear at $l = 1^\circ.6$ and at $l = -1^\circ.2$. Cross sections of the ring in CO emission at these longitudes indicates that they compose walls of 150 pc height perpendicular to the galactic plane with a thickness of about 20 pc. Namely, the expanding ring is a cylinder about 150 pc long. The kinetic energy of the expansion motion is of the order of 10^{54} ergs, which is comparable to that involved in the galactic center lobe. The coincidence between the energies in the 200-pc cylinder and the GCL is consistent if the GCL will focus on the ring in the future, and the 200-pc ring is the consequence of the shock

focusing of a past GCL some 10^6 y ago.

A cylindrical molecular ring has been also found in the starburst galaxy M82. The "200-pc ring" in M82 is thought to be the consequence of an energy release, while far more intense than that in our Galaxy center, by successive explosions of supernovae in the central region of the dense molecular disk, which is followed by a vertical wind of high-temperature gas as well as the formation of an expanding ring and a cylinder. Existence of vertical magnetic field is not known, while the intense nonthermal radio emission suggests field strength as high as some $10 \mu\text{G}$.

5.5.4 Infalling-Clouds and "Galactic Sprays"

The energy required to produce many of the expanding shells and cylinders is typically $10^{52} - 10^{54}$ ergs. The energy source could be supernova explosions or explosion at the nucleus. We here suggest an alternative possibility of external energy source to create such vertical structures: These structures could be attributed to infalling gaseous debris from the companion galaxies, LMC and SMC. According to the ram-pressure stripping-and-accretion model of gas clouds in a companion galaxy by its parent's gaseous halo and disk, interstellar clouds are stripped and accreted toward the disk of the larger galaxy. If we apply this idea to the Magellanic Clouds and the Galaxy, gas clouds in LMC and SMC are stripped, which soon form the Magellanic Stream, and finally infall toward the galactic disk. If the clouds' orbit is retrograde with respect to the galactic rotation, the clouds hit the nuclear disk, where their sprays would exhibit various vertical ridges and peculiar kinematics. The kinetic energy given to the nuclear disk by a collision of an infalling cloud of mass of $10^6 M_{\odot}$, a typical GMC, is $\sim 4 \times 10^{53}$ erg for an infalling velocity of 200 km s^{-1} . This energy is enough to produce any of the vertical and dynamical (expanding) phenomena as discussed in this article.

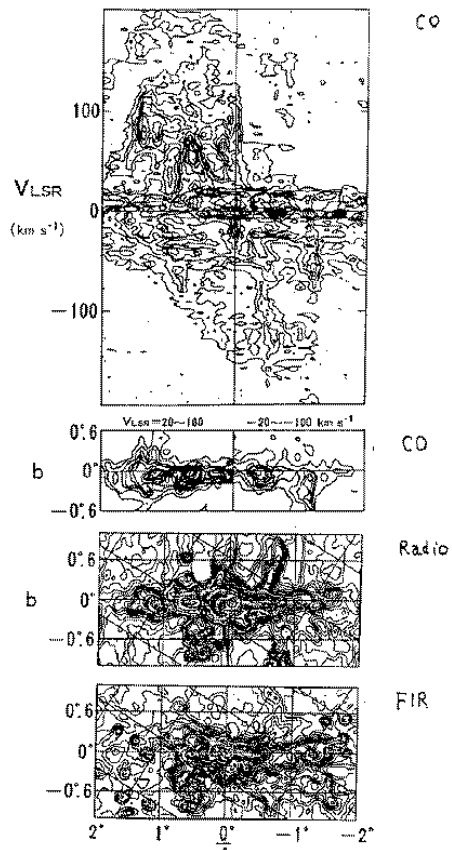


Figure 5.20: The 200-pc expanding ring in a CO line PV diagram, and associated features seen at various wavelengths.

Chapter 6

NONTHERMAL EMISSION AND MAGNETIC FIELDS

Radio observations of the synchrotron radiation from the galactic disk and its polarization give us information about the magnetic field structure. Analyses of polarization vectors and of Faraday rotation measures along the line of sight give us information about three-dimensional orientation of magnetic fields in galaxies.

6.1 Synchrotron Emission and Polarization

6.1.1 Synchrotron intensity and magnetic field strength

The intensity of synchrotron (non-thermal) emission is related to the electron density N , electron energy E and the magnetic field strength B as

$$I_\nu \propto B^2 E_E^2 N. \quad (6.1)$$

On the assumption that the magnetic and cosmic-ray energy densities are in equilibrium,

$$\frac{B^2}{8\pi} \sim N_E E (= \int_{E_1}^{E_2} E N(E) dE) \quad (6.2)$$

and

$$\nu \propto BE^2, \quad (6.3)$$

we have an approximate formula which relates B and intensity I of the emission:

$$B \sim 3.3 \times 10^2 \nu_{1 \text{ GHz}}^{-1/7} \varepsilon^{2/7} \text{ (G)}, \quad (6.4)$$

where

$$\varepsilon = \frac{\int I_\nu d\nu}{L} \sim \frac{\nu I_\nu}{L} \text{ (erg s}^{-1} \text{ cm}^{-3}) \quad (6.5)$$

is the emissivity with L being the line-of-sight depth of the emitting region. Thus, the field strength can be estimated from the synchrotron emissivity (intensity) of the source.

The brightness temperature of the sky at the galactic poles of the Galaxy at $\nu = 1$ GHz (\sim face-on brightness of the Galaxy at the sun) is $T_B \sim 10$ K. So, if we take a thickness of the radio disk to be 500 pc, the emissivity is

$$\varepsilon \sim \nu I_\nu / L \sim 2kT_B \nu / \lambda^2 L \sim 2 \times 10^{-30} \text{ erg s}^{-1} \text{ cm}^{-3}. \quad (6.6)$$

From the above expressions we obtain $B \sim 1 \mu\text{G}$ for an averaged value in the thick disk. If the disk is as thin as $L \sim 200$ pc, then $B \sim 1.4 \mu\text{G}$. From a more precise estimation the local magnetic field strength has been obtained to be about $3 \mu\text{G}$.

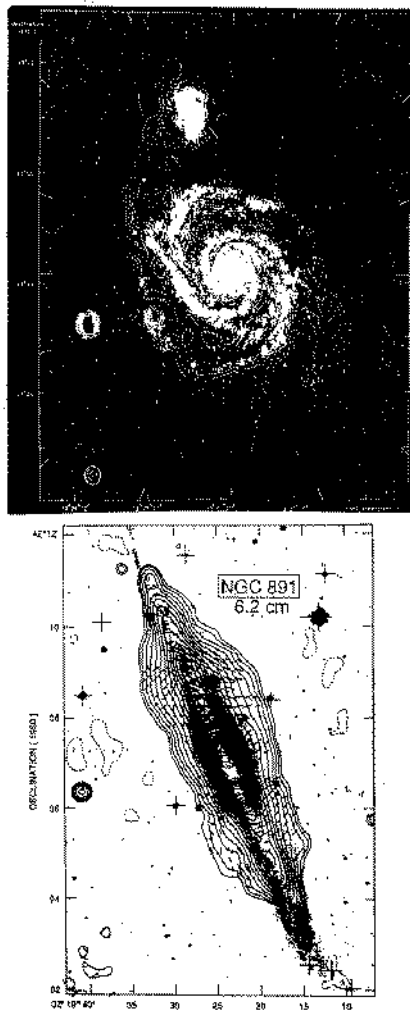


Figure 6.1: Radio continuum emission in galaxies. (a) M51: a face-on view, and (b) NGC 891: an edge-on view.

6.1.2 Linearly Polarized Emission

A single electron emits a polarized radio wave, whose electric vector is parallel to the direction of acceleration, and so the wave is polarized perpendicular to the lines of force of magnetic field. For an ensemble of electrons with an energy spectrum of the form $N(E)dE \propto E^{-\beta}dE$, the total synchrotron intensity has the maximum polarization degree of

$$p_{\max} = \frac{\beta + 1}{\beta + 7/3} = \frac{-\alpha + 1}{-\alpha + 5/3}, \quad (6.7)$$

where $\beta \sim 2.4$ for the solar vicinity value and $\alpha = -(\beta - 1)/2 \sim -0.7$ is the spectral index of the emission ($I_\nu \propto \nu^\alpha$). Therefore, the maximum polarization degree from a source with an ideally aligned magnetic field is 70%. However, interstellar magnetic fields are usually not so well aligned, but are more tangled and random. Also the galactic radio emission is the mixture with thermal radiation. So, the galactic emission is usually polarized by about $p \sim$ a few %.

In such a region as the galactic center where the radio spectrum is flat, the maximum polarization degree is smaller. For example, the Radio Arc has a spectral index of $\alpha \sim 0.2$, which yields the maximum polarization degree of $p_{\max} \sim 54\%$. Polarization observations at 30 - 50 GHz using the 45-m telescope at Nobeyama and with the Bonn 100-m telescope have shown that the Arc is polarized by about 50%. This high degree of polarization indicates that the Arc consists of almost perfectly aligned magnetic lines of force. Such field lines of force have been indeed observed with the VLA.

The direction of intrinsic polarization vectors is perpendicular to the magnetic field direction. Hence, if we can correct for the Faraday rotation as described below, we can obtain the direction of the magnetic field as projected on the sky.

6.1.3 Faraday Rotation

A linearly polarized radio wave can be expressed by a superposition of two circularly polarized waves whose electric vectors rotate in the clockwise and counter-clockwise directions, respectively, which are called the right-hand (R) and left-hand (L) polarizations, or waves of ordinary and extra-ordinary modes. If an ISM involves both ionized gas (including partially ionized one) and magnetic field, the ISM is not isotropic for the wave propagation, because the magnetic field defines a certain fixed direction in the medium. Since thermal electrons of the gas rotate in the same direction around the field lines of force by Lorentz force, interaction by the R mode electric wave vector is different from that by L mode waves. This situation causes a Faraday effect on the propagating wave, so that the refractive indices n of the R and L waves are different:

$$1 - n^2 = \frac{1.24 \times 10^4 n_e (\text{cm}^{-3})}{\nu^2 (1 \pm \nu_H \cos \theta)}, \quad (6.8)$$

where θ is the angle between the line of sight and field direction, and ν_H is the Larmor frequency of the field B . Because of a phase shift of the two modes, the resultant linear polarization vector rotates as the wave propagates. This is called the Faraday rotation of linearly polarized radio waves, and the variation of the position angle ϕ of the wave is given by

$$\phi = \phi_0 + RM\lambda^2, \quad (6.9)$$

where $\phi_0 = \phi_{\text{mag}} + 90^\circ$ is the intrinsic polarization angle with ϕ_{mag} being the position angle of the field lines projected on the sky. RM is called the rotation measure, and is given by

$$RM = 0.81 \int_0^x n_e B_p dx \text{ (rad m}^{-2}\text{)}. \quad (6.10)$$

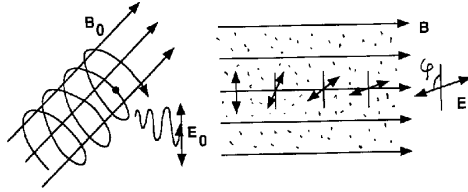


Figure 6.2: Linear polarization and Faraday rotation.

Here, n_e (in cm^{-3}) is the thermal electron density, x (in pc) is the distance along the line of sight, $B_p = B \cos\theta$ (in μG) is the line-of-sight component of the field.

RM is defined to be positive when the field line runs away from the observer, and RM is negative if the field line is toward the observer. If we observe position angles ϕ of linearly-polarized radio waves at different wavelengths and plot it as a function of λ^2 , we can determine $RM \sim 0.81n_e B_p L$. If we assume a certain value for the thermal electron density n_e and the depth L , we can approximately determine the line-of-sight component of the field.

6.1.4 Determination of Magnetic Field Orientation

In galaxies and ISM, radio emitting sources are mixture of synchrotron source and thermal gas. In such circumstances, the three-dimensional orientation of the magnetic field can be determined as follows:

- (a) Observed intensity I_ν of synchrotron radiation gives the field strength $B = (B_t^2 + B_p^2)^{1/2}$.
- (b) Intrinsic polarization angle $\phi_0 - 90^\circ$ gives the transverse direction of the field line on the sky B_t .
- (c) Faraday rotation measure RM , which is determined from multi-wavelength measurement of polarization angle, gives the line-of-sight

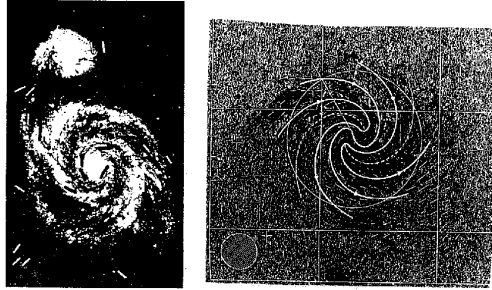


Figure 6.3: Transverse component of magnetic fields in a spiral galaxy, indicating a spiral field configuration.

field component B_p .

6.2 Magnetic Fields in Disk Galaxies

6.2.1 RM in Disk Magnetic Field

The magnetic field configuration in disk galaxies can be determined by the Faraday rotation observations, which give us information about the transverse and line-of-sight components of the field as described above. A widely adopted method to determine magnetic field configuration is called the RM vs Θ (azimuthal angle) method. In this method we plot the value of RM (or equivalently $\Delta\phi = \phi - \text{arbitrary const.}$) as a function of Θ , where Θ is the azimuthal angle along a circle on the disk plane of the galaxy at a fixed radius.

If the magnetic field of the galaxy disk is either a ring or axisymmetric (as if the field apparently have non-zero divergence), RM shows a single sinusoidal variation with Θ . If the field is a bisymmetric spiral (BSS) configuration, in which the field line flows in from one edge of the galaxy and flow out from the opposite edge, the RM variation is

double peaked sinusoidal.

There have been a number of galaxies for which the field configurations have been determined in this way. The Galaxy, M51, M81, NGC 4258, etc have a BSS field; M31 has a ring field, and NGC 6946 appears to show a spiral field with an apparent non-zero divergence.

6.2.2 BSS Magnetic Fields and the Primordial Origin Hypothesis

The magnetic field configuration of spiral galaxies is shown to be predominantly bisymmetric spiral (BSS), while a few ring and axisymmetric cases are reported. As to the origin of the BSS configuration we may envision two possibilities:

(a) a primordial field trapped into a primeval galaxy and wound up by the disk rotation, where a steady spiral configuration is maintained by the dynamo action; and

(b) a dynamo-generated large-scale spiral field which was created from infinitesimally weak random fields.

The BSS configuration in spiral galaxies can be more naturally understood on the basis of the primordial origin hypothesis. The primordial hypothesis can also explain the ring configuration as the result of a reconnection of field lines wound up in the inner region of the galaxy.

6.2.3 Vertical Fields in spiral Galaxies

In addition to the disk fields, numerous evidences for vertical magnetic fields have been observed, which may be more or less related to the activities of the disk and the nucleus.

Vertical Structures out of the Galactic Disks

The radio-continuum maps of the Milky Way show vertical structures emerging from the galactic plane. Their appearance parallel to each

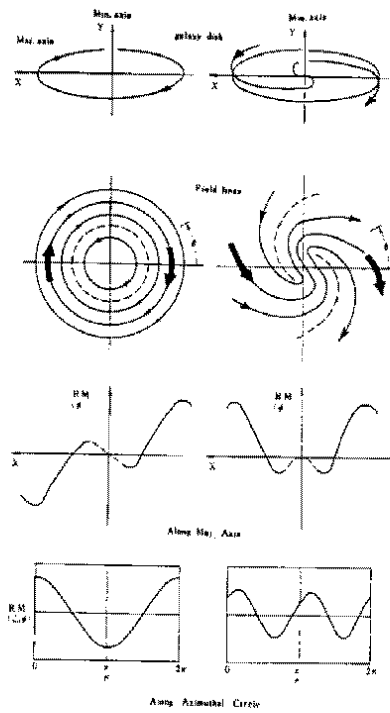


Figure 6.4: Variation of R_M with Θ according to the field configuration (ring and axisymmetric, or BSS)

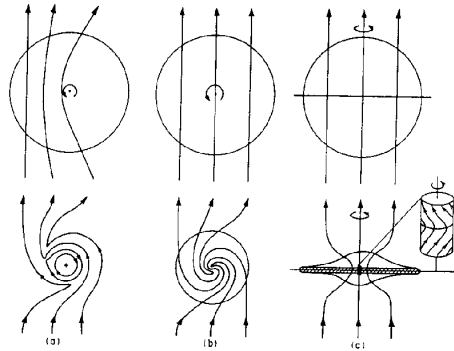


Figure 6.5: Primordial origin of the BSS and ring fields in galaxies. Primordial magnetic field trapped into a protogalaxy: (a), (b) Field in the disk; (c) Vertical field.

other suggests their coherent origin, likely driven by magnetic lines of force emerging normal to the disk plane.

External edge-on galaxies often show vertical dust lanes. Long, coherent and thin filaments running normal to the disk of some dust-rich spirals suggest the existence of a large-scale vertical field running across the disk plane. These vertical structures are found at radii of a few kpc and run for more than a kiloparsec in the halo.

Vertical Magnetic Fields in the Galactic Nuclei

In the central region of the Galaxy direct evidence for a vertical field has been found with high-resolution and/or polarization observations of the synchrotron radio emission: A large number of straight filaments extending for a hundred pc scale run almost perpendicular to the disk plane near the Arc and are well understood as the trace of a magnetic field running vertical to the disk. Some parts of these structures show

strong polarization and Faraday rotation directly showing the poloidal magnetic field .

Polarization observations of the nuclear radio source in M31 shows the magnetic field orientation perpendicular to the major axis. Since the galaxy is nearly edge-on, this may be attributed to a poloidal magnetic field in the nucleus. Besides M31, however, no obvious magnetic structures are known for nuclei in external galaxies.

Vertical Ejections from Nuclei of Galaxies

Nuclei of spiral galaxies often reveal jet-like features emerging perpendicular to the disk plane and/or central radio sources elongated perpendicular to the major axis. These ejection features may be the manifestation of a vertical field running across the nucleus.

6.2.4 Magnetic Fields in the Galactic Halo

Observational data for halo fields are still crude. A few edge-on galaxies like NGC 4631 show extended nonthermal radio halo. The field strength from the radio emissivity is estimated to be a few μG . There are many galaxies for which no evidence for radio halo is seen.

Magnetic fields in the halo of the Galaxy can be derived from RM analysis for external radio sources and pulsars. If we plot $|RM|$ (rotation measure) against $|\cot b|$ for radio galaxies and quasars, the upper envelope of the plot can be fitted by a relation,

$$|RM|_{\text{RG,Quasar}} \simeq 30 |\cot b| \text{ (rad m}^{-2}\text{)}. \quad (6.11)$$

On the other hand if we plot the same for pulsars, we obtain

$$|RM|_{\text{Pulsar}} \simeq 10 |\cot b| \text{ (rad m}^{-2}\text{)}. \quad (6.12)$$

The difference between the coefficients for the two plots is considered

to be due to Faraday rotation in the space above a disk of thickness of about 500 pc in which most of pulsars are distributed, namely it may be due to a halo beyond a few hundred pc from the galactic plane:

$$|RM|_{\text{Halo}} \sim 20 |\cot b|. \quad (6.13)$$

If we take an electron density and a thickness of the halo to be approximately 10^{-3} cm^{-3} and a few kpc, respectively, the field strength in the halo is estimated to be a few μG , about the same as in the disk.

6.3 Evolution of Magnetic Fields in Spiral Galaxies

6.3.1 Primordial Origin of Galactic Magnetic Fields

On the primordial hypothesis, the BSS field is interpreted as the fossil of an intergalactic field wound up by the primordial galaxy disk. The field is then maintained in a steady state by the induction-dynamo mechanism. Even a ring field can be produced from the primordial one, if we allow for an initial asymmetry with respect to the center.

Vertical Component of the Primordial Magnetic Fields

It is natural that a large-scale field component parallel to the rotation axis existed, when a galaxy formed. This field component is also trapped to the primeval gas sphere [phase I]. Since the disk radius is large enough and the diffusion time is longer than the galaxy evolution time, the vertical field is almost frozen into the disk gas. The vertical field then follows an evolution as described below.

Evolution of Vertical Fields in Primeval Galaxies

Starting from a uniform gas sphere (disk) and initial star formation in a proto galaxy, an exponential disk is realized by the viscosity-driven

angular momentum transfer and on-going star formation. Since the field is frozen into the gas, the magnetic flux conservation results in a radial distribution of the field strength obeying the exponential law, provided the initial field was uniform. In the central region the gas density attains an excess by an order of magnitude over the value given by a simple exponential disk, and the field strength is correspondingly high. The initial star formation then finishes when the gas is fed into stars and the density decreases to a certain threshold value, after which the magnetic field is no more frozen into the stellar disk.

Strong Vertical Fields near the Galactic Nuclei

The vertical magnetic field is then frozen into the gas left behind the initial star formation. At this stage the gas may have a constant threshold density below which the initial star formation did not take place, and shares a few percent of the total mass. The "interstellar" gas then follows its own evolution governed by the density wave shock, cloud-cloud collisions, and star formation. Through the shock- and viscosity-driven inflow the gas accretes toward the center. In the central region a bar-induced shock will enhance the accretion. Since the diffusion time of the vertical field is shorter than the dynamical time scale, this results in a formation of a strong vertical field in the center. In the early universe when galaxy formation took place, galaxy-galaxy collision will have been frequent and the tidal encounter may have enhanced the bar-induced inflow of gas, and therefore strong vertical field near the center.

If the present intergalactic or intra-cluster magnetic field is of the order of $10^{-9}\sim 10^{-10}$ G, the vertical field strength in the central 1 kpc of normal spiral galaxies is expected to be of the order of mG, which dominates in the central region. On the other hand spiral fields within the disk is weaker in the central few kpc, while it dominates in the outer disk.

6.3.2 Loss of Angular Momentum by the Vertical Fields

The interstellar gas in turn suffers magnetic torque from the vertical field which is twisted by the galactic rotation. The time scale with which the rotating gas element loses angular momentum is given by $\tau = Vr/(B^2/4\pi\rho)$, where V , r , B , and ρ are the rotation velocity, radius, magnetic field strength, and gas density, respectively. The time is then calculated to be $\tau \sim 10^{11}$, 10^8 , and 10^5 years, respectively at $r = 5, 1$ and 0.1 kpc. This shows that the magnetic to and the accumulation of vertical field is accelerated by the magnetic-torque/angular-momentum-loss mechanism.

6.4 Nuclear Activities and the Vertical Fields

6.4.1 Jets from the Nuclei

The twisted vertical magnetic field near the nucleus accelerates a screwing outflow of gas, and results in a vertical jet from the nucleus. This mechanism will explain many of the observed vertical radio features near the nuclei of spiral galaxies. It is suggested that quasars are nuclei of distant galaxies. According to our scenario about vertical field component in protogalaxies, nuclei of these galaxies may have a strong vertical field and intense accretion of gas at its initial stage. This particularly applies in such a stage when the central density enhancement of the primeval exponential disk is present. Long, energetic jets from quasars could be the manifestation of such an intensive accretion of vertical magnetic fields in the nuclei of protogalaxies.

Chapter 7

HI and CO IN GALAXIES

The major constituents of the ISM in spiral galaxies are the HI and H₂ gases, which make up about a few percent of the total mass.

Distributions of HI gas in galaxies have been obtained for many galaxies by mapping with high-resolution observations using large-aperture single dishes such as the 100-m telescope and by interferometers like the WSRT and VLA. It is, however, only recent that a number of galaxies have been mapped in the molecular lines at mm-wavelengths, particularly in the ¹²CO($J = 1 - 0$) line emission. The CO line data, such as those obtained at high angular resolutions with the Nobeyama 45-m and IRAM 30-m telescopes, have been used to obtain distributions of the molecular hydrogen gas on the assumption that the CO intensity is proportional to the molecular hydrogen column mass.

It is well known that the HI gas is distributed in the outer region of galaxies, while it is deficient in the central several kpc. On the other hand, the molecular gas is known to be more concentrated in the central several kpc region, often showing a nuclear concentration in the central 1 kpc making a nuclear disk and/or a compact ring.

This general tendency of the ISM distribution is the manifestation of galactic-scale phase transition between HI and H₂ during the evolution of galaxies.

7.1 HI in Galaxies

7.1.1 HI Gas Distributions

The column density of H atoms is obtained by integrating brightness temperature T_{mb} in velocity or in frequency:

$$N_{\text{HI}} \text{ (H cm}^{-2}\text{)} = 1.83 \times 10^{18} \int_{V_{\text{min}}}^{V_{\text{max}}} T_{\text{B}} dv \text{ (K km s}^{-1}\text{)} = 3.88 \times 10^{20} \int_{\nu_{\text{min}}}^{\nu_{\text{max}}} T_{\text{B}} d\nu \text{ (K MHz)}. \quad (7.1)$$

The mass is estimated by

$$M_{\text{HI}} = m_{\text{H}} \int N_{\text{HI}} dx dy = m_{\text{H}} \int N_{\text{HI}} D^2 d\Omega, \quad (7.2)$$

where x, y are extents in the galaxy, D is the distance, and Ω is the angular solid angle.

Figs. 7.1 and 7.2 shows observed HI distributions for several spiral galaxies together with their radial velocity distributions. The neutral hydrogen (HI) gas is widely distributed in the outer region of a galaxy, while HI is missing in the central 1 kpc region. The HI distribution in the disk is very broad, and radially extends up to $R \sim 20 - 30$ kpc. Total mass of the HI gas in a normal spiral galaxy of Sb type is typically 2–3% of the dynamical mass.

7.1.2 Rotation and Velocity Fields of HI Gas

Spectral HI data provide us of kinematical information of the intermediate and outer disk. The variation of radial velocity v as a function of the distance from the center along the major axes gives almost directly

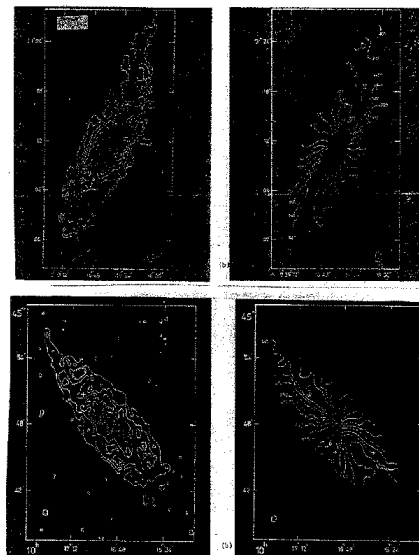


Figure 7.1: HI gas distributions and velocity fields in spiral galaxies.

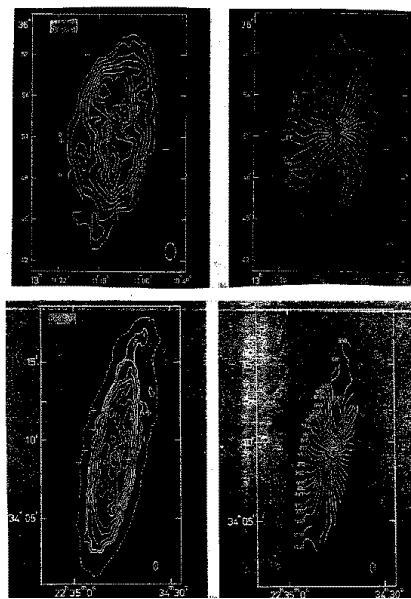


Figure 7.2: HI gas distributions and velocity fields in spiral galaxies (continued).

the rotation curve $V(R)$:

$$V(R) = v/\sin i, \quad (7.3)$$

where i is the inclination angle of the galaxy ($i = 0^\circ$ for face-on galaxy; $i = 90^\circ$ for edge-on). The radial velocity distribution as plotted in the form of iso-velocity contours is called the velocity field. A velocity field gives information about not only the rotation but also such non-circular motions caused by spiral arms (density waves and galactic shock waves) and by warping of the disk.

Fig. 7.3 shows velocity fields for many galaxies. The nodal line as defined by loci of maximum (recession side of the disk rotation) and minimum (approaching side) velocity is often bending. This is caused mainly by large-scale warping of the disk, particularly in the outermost regions. Also wavy variation of the iso-contours is recognized in almost every galaxy, and is due to non-circular motions superposed on the circular rotation due to density wave and galactic shocks.

7.2 CO and Molecular Gas in Galaxies

7.2.1 Distribution of Molecular Gas

The column density of H_2 molecules is obtained by integrating the brightness temperature of CO line:

$$N_{\text{H}_2} (\text{H}_2 \text{ cm}^{-2}) = C \int_{V_{\min}}^{V_{\max}} T_{\text{B}} dv \quad (\text{K km s}^{-1}), \quad (7.4)$$

where C is the conversion factor for which we often adopt the empirical value obtained for molecular clods in the Galaxy on the assumption of virial equilibrium of individual clouds. Conventionally, a value $C = 2.8 \times 10^{20}$ is used, and sometimes 3.6×10^{20} is adopted. However, the conversion factor has been shown to be clearly dependent on the metallicity of galaxies, and a simple relation between C and metal

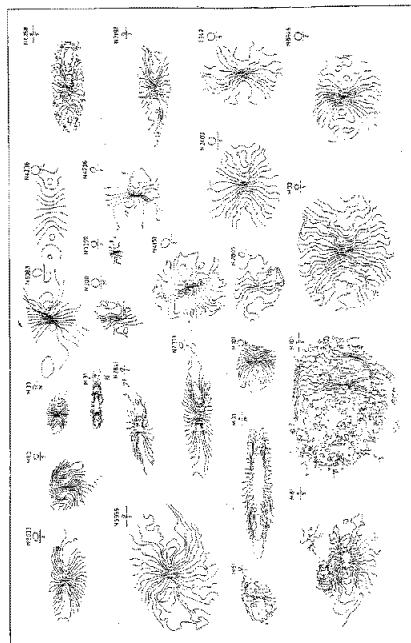


Figure 7.3: Velocity fields for galaxies (Bosma 1980).

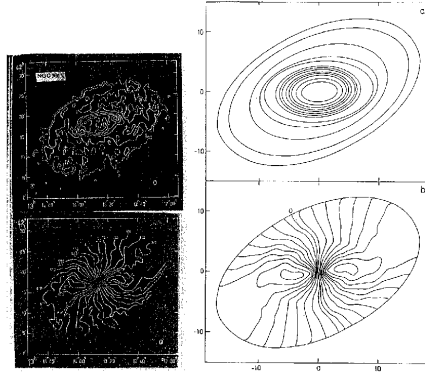


Figure 7.4: Warping of galactic disk and disturbed velocity field.

abundance has been derived, as shown in subsection 7.2.3.

In contrast to the HI distribution, CO emission comes from more inner and nuclear regions. Fig. 7.5 shows the HI and CO intensity distributions for the face-on galaxy M51 (HI: Rots 1990; CO: Nakai et al 1994; Kuno et al 1995). HI is widely spread over the whole galaxy and has a hole (depression) near the nucleus. On the other hand, CO emission has the peak near the nucleus, and the spiral arms are more clearly traced by the CO emission.

In subsection 7.4.1 we show radial variations of the HI and H₂ densities as plotted against the galacto-centric distances for several edge-on galaxies. It is remarkable that HI makes up the outer disk and the outskirts, whereas CO makes up the nuclear disk and inner disk, where star formation is taking place most intensively. The inner molecular disk and outer HI disk appears to be replacing at a certain narrow range of radius at $R \sim 5 - 10$ kpc, which we call later the molecular front.

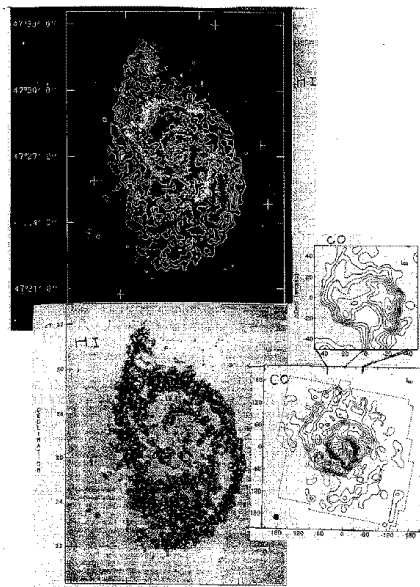


Figure 7.5: HI and CO intensity distributions in the face-on galaxy M51.

7.2.2 Inner CO Kinematics

Since the molecular gas is more concentrated in the inner disk and in the nuclear disk, the emission can be used to obtain the kinematics of the central region, where HI emission is almost missing. Fig. 7.8 shows the PV diagram in the CO emission for the edge-on galaxy NGC 891 plotted together with an HI PV diagram. It is impressive that the CO emission has a large-velocity component near the center indicating the existence of a rapidly rotating dense nuclear disk, while HI is not detected in the inner 2 kpc. The rotation characteristics of the nuclear disk as derived from CO observations as combined with that from HI observations will be discussed in detail in section 7.6.

7.2.3 The CO-to-H₂ Conversion Factor in Galaxies

Variation of the Conversion Factor among Galaxies

Deriving the mass of molecular hydrogen gas is the fundamental process for the interstellar physics of galaxies. The principal method has adopted conversion from the intensity (or luminosity) of the ¹²CO(*J* = 1 – 0) molecular line emission (*I*_{CO} or *L*_{CO}) into the column density (or mass) of H₂ molecules (*N*_{H₂} or *M*_{H₂}).

The conversion factor $C(= N_{\text{H}_2}/I_{\text{CO}} = M_{\text{H}_2}/L_{\text{CO}}) = C^* \times 10^{20}$ H₂/K km s⁻¹ has been derived for molecular clouds in the solar vicinity on the assumption of a virial equilibrium of individual clouds and the large-velocity-gradient for the CO line. This method has been used for deriving the conversion factor in nearby external galaxies such as M31, M33 and the Magellanic Clouds, where individual clouds can be resolved. A more global value in our Galaxy has been derived by using a correlation between the distribution of γ -ray intensity, which is assumed to be proportional to the column mass of hydrogen atoms and molecules, and that of CO intensity along the galactic plane. A correlation between the CO intensity and optical extinction (*A_v*), which is

assumed to be correlated with the column mass of hydrogen, has been also used, and has been applied to well-studied galaxies like M51.

The conversion factor obtained for the Milky Way Galaxy appears to be well-defined around $C^* \sim 3$ within a factor of 1.3. However, the value seems to be largely scattered among galaxies on the order of magnitude, from our Galaxy and galaxies of “normal metallicity” to such low-metallicity galaxies as the Magellanic Clouds ($C^* \sim 15$). Hence, it is a natural consequence from these facts that one supposes a dependency of C on metallicity. It is also natural to consider that the conversion factor is a function of the distance from the galaxy centers, since the metallicity exhibits a general exponential decrease with the galacto-centric distance.

Metallicity Dependence of the Conversion Factor

The metallicity dependence of the conversion factor has been extensively studied recently. Fig. 7.6 plots the conversion factor C^* against the oxygen abundance $12 + \log \text{O}/\text{H}$ for various galaxies for which metal abundance and the factor are known (e.g., M51, M31, the Milky Way Galaxy, M33, IC10, NGC6822, LMC, and SMC). The diagram demonstrates that the conversion factor depends on the metallicity of gas clouds. A simple least squares fit gives

$$\log C^* = -0.80(12 + \log \text{O}/\text{H}) + 7.60 \quad (7.5)$$

or equivalently,

$$C \propto Z(\text{O})^{-0.8}. \quad (7.6)$$

Here, $Z(\text{O}) = [\text{O}/\text{H}]$ is the oxygen abundance. We note that Eq. (7.5) applies both for various regions within a single galaxy and for different galaxies with different metallicities.

This plot suggests that, among various properties of interstellar

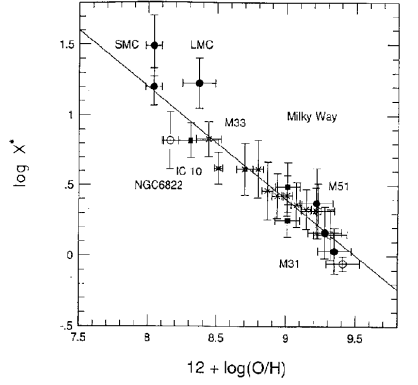


Figure 7.6: The conversion factor (C^*) vs oxygen abundance relation for eight disk galaxies. Different symbols indicate different galaxies. The solid line gives a least square fit.

medium such as the gas density and excitation temperature, the metallicity is a fundamental parameter that controls the CO-to-H₂ conversion factor. It will be reasonable to suppose that the conversion factor is somehow dependent on the CO abundance $Z(\text{CO})$. If we assume that O and C abundance are proportional to each other, the above equations indicate that the conversion factor is mainly controlled by $Z(\text{CO})$ as

$$C \propto Z(\text{CO})^{-0.8}. \quad (7.7)$$

Radial Variation of the Conversion Factor

The Milky Way Galaxy and M51 exhibit conspicuous radial gradients of the conversion factor. In Fig. 7.7, we plot the values of C^* for these galaxies as well as M31 as a function of a radius r/r_e , where r_e is an effective radius obtained from the stellar surface brightness

distribution. The figure suggests that within uncertainties associated with data acquisition $\log C^*$ vs r/r_e relation holds universally for the Milky Way Galaxy, M31 and M51, although r_e of each galaxy is not the same; $r_e = 6.19$ kpc for the Milky Way Galaxy, $r_e = 7.37$ kpc for M31, and $r_e = 7.26$ kpc. A least-squares fit gives:

$$\log C^* = 0.37 + 0.40(r/r_e - 1). \quad (7.8)$$

Since the radial distributions of C^* in these galaxies merely reflect the radial abundance gradient of oxygen, it is reasonable to have such a tight correlation between C^* and r/r_e . Indeed the oxygen abundance at any galactocentric distance in the disk of a spiral galaxy can be written as:

$$(\text{O}/\text{H}) = (\text{O}/\text{H})_e 10^{-0.39(r/r_e - 1)}, \quad (7.9)$$

where $(\text{O}/\text{H})_e$ is the oxygen abundance at the effective radius of a galaxy. By putting Eq.(7.5) into Eq.(7.9), we obtain:

$$\log C^* = \log C_e^* + 0.31(r/r_e - 1), \quad (7.10)$$

where C_e^* is the conversion factor at the effective radius r_e . Eq.(eq:2-3-(6)) gives a nearly identical slope to that given by Eq.(eq:2-3-(4)). This formula requires a knowledge of C_e^* alone and can be used for any galaxy to which the oxygen abundance gradient is not actually known. Note that the values of C_e^* of galaxies shown in Fig. 7.7 are nearly identical, which is the reason why one gets apparently universal C^* vs r/r_e relation for these galaxies. Of course if C_e^* is considerably different from these galaxies, a galaxy should have a different C^* vs r/r_e relation from that shown in Fig. 7.7 (eg., M33).

The Conversion Factor and Galaxy Evolution

The formula, Eq.(7.5), has a great potential in chemical evolution study of disk galaxies. In particular, once the simple model of galactic

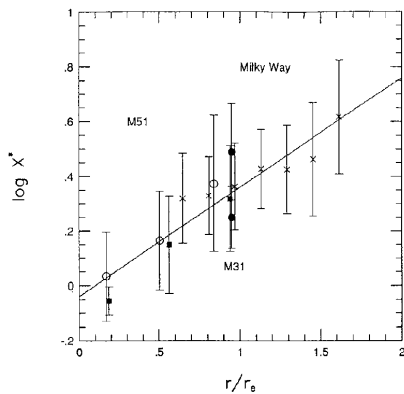


Figure 7.7: Radial distribution of conversion factor (C^*) for the Milky Way Galaxy, M31, and M51. The solid line gives least square fit.

chemical evolution is assumed, it is possible to derive the distribution of the yield of oxygen, and probably those of other elements, in disk galaxies. The yields of heavy elements are one of the most important properties in chemical evolution study as they give informations directly related to the stellar initial mass function (IMF) and thus to the stellar nucleosynthesis.

However, except for the solar neighborhood disk of the Milky Way Galaxy, the true yields of heavy elements such as carbon and oxygen in disk galaxies are not yet known. A difficulty of getting the precise mass distribution of H_2 molecule was the major obstacle for this. To derive the distribution of the yield, one needs to know 1) the abundance distribution of heavy element, eg., oxygen, $12 + \log(O/H)$, 2) the stellar mass surface density Σ_* , 3) HI density distribution Σ_{HI} , and 4) H_2 density distribution Σ_{H_2} . Σ_* is derived from the surface brightness by assuming that the mass distribution follows the light distribution with a constant mass-to-light M/L ratio. Eq.(7.5) can be used to estimate

the radial distribution of H_2 molecule gas in disk galaxies. If the radial distribution of oxygen is known, Eq.(7.5) gives the distribution of the conversion factor C^* which one can use to derive the H_2 distribution from the CO data. Defining the gas density fraction $\mu = \Sigma_{\text{gas}}/\Sigma$ as the ratio of total gas mass density ($\Sigma_{\text{gas}} = \Sigma_{\text{HI}} + \Sigma_{\text{H}_2}$) to the total density of stars and gas ($\Sigma = \Sigma_{\text{gas}} + \Sigma_*$), one finally gets the yield of oxygen as $y_{\text{O}} = -Z(\text{O})/\ln(\mu)$, where $Z(\text{O})$ is the abundance of oxygen in mass.

7.3 CO vs HI in Galaxies

7.3.1 CO vs HI in the Position-Velocity Diagram for Edge-on Galaxies

The CO emission generally originates in high-density interstellar regions, while the HI in more diffuse interstellar gas, and therefore, a CO-plus-HI PV diagram represents the “true” distribution of interstellar gas. Using the observed PV diagrams, we derive the radial distribution of gas densities of H_2 and HI, and further, the molecular gas fraction.

In Figs. 7.8 and 7.9 we present composite PV diagrams, in which CO and HI PV diagrams are superposed, for the NGC 891, NGC 4565, and NGC 5907. Primarily, these diagrams are useful to obtain rotation properties of the galaxies both in the HI and CO: The CO as well as HI rotation curves already attain the maximum at the galacto-centric distance $R \sim 3 - 10$ kpc, and are followed by a flat rotation of the outer gas. The fact that both the HI and CO emitting regions attain the same maximum rotation velocity at $R \sim 5 - 10$ kpc have been used to argue for a coincidence of the total line profiles in CO and HI and has been used to establish the CO-line Tully Fisher relation. The diagrams can also be used for deriving dynamical as well as structural informations such as about a bar potential and a bar-shocked gas ring

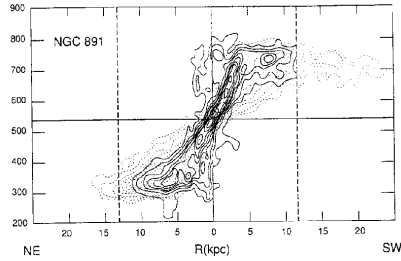


Figure 7.8: Composite PV diagrams for CO and HI emissions for edge-on galaxies (NGC 891).

in the central region. In this paper we use these diagrams for deriving the molecular and HI gas fractions in the galaxy disks as functions of the distance from the galactic center.

NGC 891

This is a typical Sb galaxy with an almost perfect edge-on orientation, and is supposed to be the most similar galaxy to the Milky Way. This galaxy has been extensively mapped in the CO line and in the HI line. The CO diagram is characterized by the 4-kpc molecular ring feature, which makes an apparently rigid-rotation ridge running across the origin of the diagram. In addition to this ring, the central high-velocity enhancement is evident, which comprises a steep and rigid rotation feature at $R < 1$ kpc corresponding to the rapidly-rotating nuclear disk. The HI gas is distributed in a larger radius region in a broad ring and outskirts at $R > 10$ kpc.

The rotation curve of the galaxy is almost flat at $R < 15$ kpc, and is followed by a gradually declining rotation in the outermost region.

It is remarkable that the 4-kpc CO ring is located just inside the main HI ring, and that the HI and CO gases generally avoid each

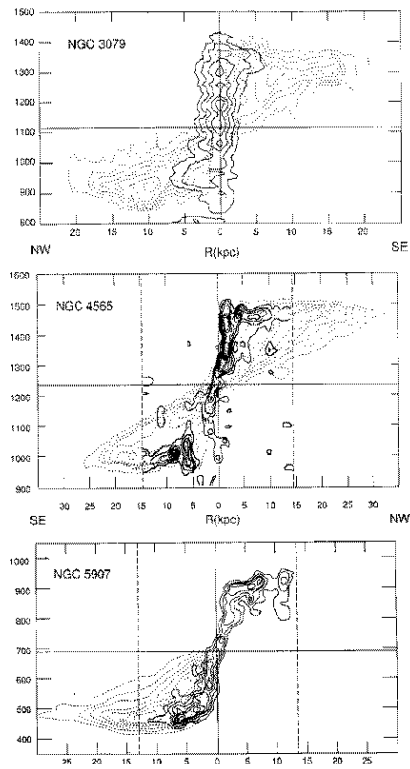


Figure 7.9: Composite PV diagrams for CO and HI emissions for edge-on galaxies (NGC 3079, NGC 4565, NGC 5907).

other. It is also impressive that the CO nuclear ring is not associated with HI at all: the HI emission is not detected in the central 3 kpc, indicating depression of HI gas in the center.

NGC 4565

This is an Sb galaxy at a distance of 10.2 Mpc and with a large inclination angle of $i \simeq 86^\circ$. The CO PV diagram shows a significant lopsidedness in the sense that the CO in the SW side is lacking. However, the HI diagram shows an almost perfect symmetry. Again, the displacement between the CO and HI is evident. Particularly, the nuclear CO disk is not associated with HI gas.

NGC 5907

This is an edge-on Sc galaxy. This CO + HI PV diagram demonstrates the overall displacement of molecular and atomic hydrogen gases most clearly. The HI gas is distributed over a large ring of 12 kpc radius, while the CO gas makes up a ring of 4 to 7 kpc radius. It is peculiar that this galaxy shows a central depression also in the CO line.

7.4 Radial Variations of HI and H₂ Densities

7.4.1 Deriving the Density Distribution from a PV diagram

The gaseous distributions in the observed galaxies are characterized by a major molecular ring of a few kpc radius and an extended HI outskirts with spiral arms as well as the nuclear disk of molecular gas. Using the observed PV diagrams, we are able to derive radial density distributions both for the HI and molecular hydrogen by applying a de-convolving method as described below. The HI and H₂ densities in the galaxy disk at a radius R can be obtained by

$$n(\text{HI}) = C_1 b_1^{-1} I_{\text{HI}}/L, \quad (7.11)$$

$$n(\text{H}_2) = C_2 b_2^{-1} I_{\text{CO}}/L, \quad (7.12)$$

where,

$$L = 2|R| \sqrt{V_{\text{rot}}^2/V_{\text{min}}^2 - 1}. \quad (7.13)$$

Here, C_1 and C_2 are the conversion factors from the intensities to column densities of H atoms and H₂ molecules, respectively and are given as $C_1 = 1.82 \times 10^{18} \text{ H cm}^{-2}/(\text{K km s}^{-1})$ and $C_2 = 3.6 \times 10^{20} \text{ H}_2 \text{ cm}^{-2}/(\text{K km s}^{-1})$. The coefficients b_1 and b_2 are correction factors for the beam dilution in the z direction:

$$b_1 = 2z_{\text{HI}}/\theta_1 D \quad (7.14)$$

and

$$b_2 = 2z_{\text{H}_2}/\theta_2 D, \quad (7.15)$$

where $2z_{\text{HI}} = 250 \text{ pc}$ is the scale thickness of the HI disk, $2z_{\text{H}_2} = 150 \text{ pc}$ is the scale thickness of the molecular gas disk, θ_1 and θ_2 are the beam widths of the HI and CO observations, respectively, and D is the distance of the galaxy. The integrated CO intensity is given by

$$I_{\text{HI}} = \int_{V_{\text{min}}}^{V_{\text{max}}} T_{\text{mb}; \text{HI}} dV \quad (\text{K km s}^{-1}), \quad (7.16)$$

and

$$I_{\text{CO}} = \int_{V_{\text{min}}}^{V_{\text{max}}} T_{\text{mb}; \text{CO}} dV \quad (\text{K km s}^{-1}), \quad (7.17)$$

where $T_{\text{mb}; \text{HI}, \text{CO}}$ are the main beam temperatures of the HI and

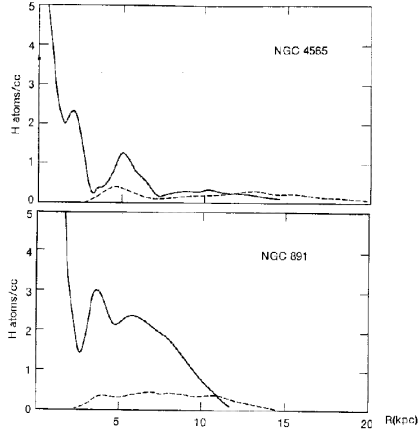


Figure 7.10: Radial density distributions for edge-on galaxies.

CO emissions. The adopted values of V_{\min} , V_{rot} and V_{\max} in our calculations are listed in table 7.1. The values of V_{\max} are taken to be larger than the rotation velocity V_{rot} by $20\sim 30 \text{ km s}^{-1}$ in order to cover all the emission apparently beyond the terminal velocity due to the velocity dispersion in the interstellar gas.

Fig. 7.10 shows the obtained distributions of HI and H_2 gas densities plotted against the radius for NGC 891, NGC 4565, and NGC 5907. The unit of abscissa is H atoms cm^{-3} , where $n(\text{H}) = 2n(\text{H}_2)$ for the molecular gas.

NGC 891

This galaxy contains a large amount of molecular gas, clearly showing the $R = 4\text{-kpc}$ molecular ring and the nuclear disk. In larger scale the density of the H_2 gas decreases almost exponentially with the radius. On the other hand, the HI density is nearly constant throughout the major part of the disk, as widely known for normal galaxies. It is

also remarkable that the HI gas exhibits significant depression in the central region at $R < 2$ kpc. We note that the total gas density at $R \sim 8$ kpc is about $0.5 \text{ H atoms cm}^{-3}$, and this is comparable to the value of 0.7 in the solar neighborhood in our Galaxy.

NGC 4565

In this galaxy, similarly to NGC 891, the 5-kpc molecular ring and the nuclear molecular disk are evident, as well as the approximately exponential decrease of the density with radius. On the other hand, the HI distribution is almost flat in the major disk extending to such large radius as 20 kpc or more. It is interesting to note that the 5-kpc molecular ring is also associated with a significant enhancement of HI gas.

NGC 5907

This galaxy shows a significant difference in the H_2 distribution from the other galaxies in the sense that the H_2 gas does not exist in the central 2 kpc region. As we have already seen in the PV diagram, this is due to the lack of the high-velocity component in the central region and the assumption of constant rotation velocity. We cannot ascertain the validity of this assumption for this galaxy, but it is worthwhile to note that there are some galaxies like M31 which show a central depression of interstellar gas.

7.5 The Molecular Front

7.5.1 Radial Variation of Molecular Fraction

Using the distributions of the molecular and HI gases, we can derive radial variation of molecular-gas fraction against the total gas density. We define the molecular fraction by

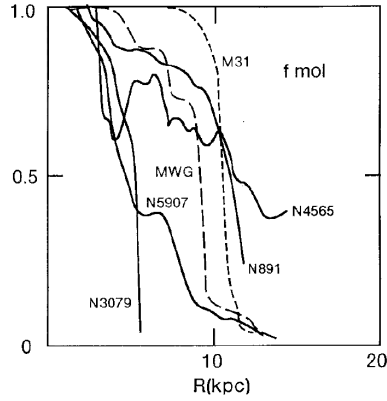


Figure 7.11: Radial variations of the molecular fraction in galaxies.

$$f_{\text{mol}} = \frac{\rho_{\text{H}_2}}{\rho_{\text{HI}} + \rho_{\text{H}_2}} = \frac{2n_{\text{H}_2}}{2n_{\text{H}_2} + n_{\text{H}}}. \quad (7.18)$$

Fig. 7.11 plots the obtained variation of the molecular fraction as a function of the radius for several galaxies.

7.5.2 Molecular Front

All the plots in Fig. 7.11 show that the H_2 gas is dominant in the inner region of the galactic disk, while HI is dominant in the outer region. The molecular fraction is almost unity in the central few kpc region, and it decreases drastically at a critical radius. It is remarkable that the sudden decrease in the molecular fraction occurs in positional coincidence with the molecular ring of a few kpc radius: The sudden decrease occurs at $R \sim 3 - 4$ kpc in NGC 891, NGC 4565 and NGC 5907, and at $R \simeq 4 - 5$ kpc in our Galaxy. The molecular fraction, then, decreases to almost zero at $R \sim 10$ kpc. The galaxy disk is, therefore, separated into two parts at this critical radius; the inner molecular region, where the interstellar gas is almost totally H_2 , and

the outer HI region, where the gas is almost totally HI.

We stress that the transition from HI to H₂, and vice versa, is taking place within the very narrow range of radius, at the inner edge of which the molecular ring is located. We call such a clear border between the two regions of the disk the ‘molecular front’. This front may be the manifestation of a galactic-scale phase transition between HI and H₂, and can be deeply coupled with the evolution of the interstellar gas. It is remarkable that *all* the galaxies studied here have shown similar variations of the molecular fraction.

7.5.3 Phase Transition between HI and H₂

Suppose that a single spherical cloud is composed of two zones (an inner H₂ core and an outer HI envelope) and is embedded in a uniform ISM in a pressure balance. Then, given the mass of the cloud, the transition from HI to H₂, and vice versa, simply depends on the gas pressure (P), the strength of the dissociative-radiation (UV photon) field (U), and the heavy element abundance (Z) related to the amount of interstellar dust which shields the UV photon. The molecular fraction of the cloud increases, if the pressure and/or the heavy-element abundance increase, and if the dissociative UV intensity decreases. The transition is particularly sensitive to the heavy-element abundance and gas pressure. The fraction is also an increasing function of increasing mass of the cloud. Once a distribution function of cloud masses is given, we can integrate molecular fractions for individual clouds to yield an averaged value of the molecular fraction (f_{mol}) in a certain area of the gas disk of a galaxy.

It is known that the temperature and velocity dispersion of the molecular as well as HI gas clouds do not vary so steeply with the radius in a galaxy disk. We may, therefore, assume that the pressure is proportional to the total (HI + H₂) gas density, which can be approximately expressed by an exponential disk of scale radius of a few

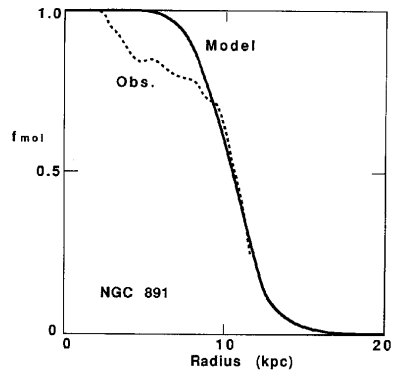


Figure 7.12: Radial variation of the molecular fraction for a galaxy as calculated from the phase-transition theory between HI and H₂, compared to the observation of NGC 891.

kpc. The radiation field can be assumed to be proportional to the star-formation rate which is a simple power-law function of the gas density. The metal abundance is known to be an exponential decreasing function of the radius. The molecular front phenomenon can be well reproduced by a simple simulation based on such simple assumptions as above in the scope of the phase-transition theory.

7.6 Rotation Curves of Galaxies

7.6.1 Rotation of Galaxies

The rotation curves of galaxies have been obtained by optical (H α) and HI 21-cm line emission observations along the major axes. It is well known that the HI gas distribution generally shows depression in the central few kpc region, which has yielded an apparently solid rotation curve for the central a few kpc region. Optical measurements are affected by the contamination of the bright bulge light,

which has also increased the uncertainty of the curve near the center. Moreover, because of the dust absorption in the gaseous disk, optical observations cannot be obtained of the central regions of highly-tilted galaxies, whereas edge-on galaxies are most suitable for determining the rotation curves without ambiguity of correction for inclination.

On the other hand, the CO-line emission is concentrated in the central region, so that rotation curves of the inner few kpc region can be most accurately obtained by CO position-velocity (PV) diagrams. It has been shown that the CO rotation curves of edge-on galaxies do not necessarily coincide with those obtained by HI and/or optical observations: The central rotation by CO is much flatter than that from HI and optical data, or even increases near to the center, exhibiting rapidly rotating compact disk component.

By compiling CO-line PV diagrams along the major axes of nearby late type galaxies which have been observed with large-aperture telescopes and interferometers, the most accurate rotation curves have been derived for nearby galaxies. Particularly, CO-line data from the Nobeyama 45-m telescope with an angular resolutions $15''$ have been extensively used. PV diagrams from these data have a linear resolution better than 700 pc (angular resolution $15''$ at 10 Mpc) to 100 pc ($5''$ at 5 Mpc). The inner rotation curves from the CO PV diagrams are combined with outer HI and optical rotation curves from the literature.

7.6.2 . Definition of Rotation Curves

Fig. 7.13 shows an example of the composite PV diagrams for NGC 891. The CO gas is concentrated in the central region, while HI is distributed in the outer disks, having a void in the central region. The rotation curve of a galaxy can be derived by using the loci of terminal velocity (V_t) in the PV diagram after correction for the inclination of galaxy disk. Thereby, the velocity dispersion of the interstellar

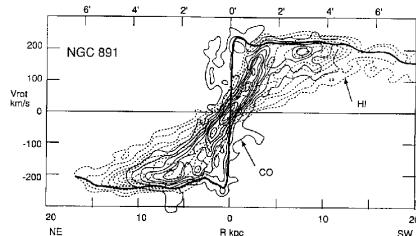


Figure 7.13: CO + HI composite position-velocity diagram for NGC 891. A fitted rotation curve is superposed by the thick line.

gas (σ_{ISM}) and the velocity resolution of observations (σ_{obs}) must be corrected by

$$V_{\text{rot}} = V_t - (\sigma_{\text{obs}}^2 + \sigma_{\text{ISM}}^2)^{1/2}. \quad (7.19)$$

The velocity resolution is usually $\sigma_{\text{obs}} \sim 10 \text{ km s}^{-1}$, while the interstellar velocity dispersion may be taken as $\sigma_{\text{ISM}} \sim 7 \text{ km s}^{-1}$. So, we adopt a correction for the ISM velocity dispersion and velocity resolution as $V_{\text{rot}} \simeq V_t - 12 \text{ km s}^{-1}$. Since the accuracy of measuring V_t is about 10 km s^{-1} , the accuracy of determination of rotation velocities is not largely dependent on the values of the velocity dispersion and resolution.

The terminal velocity is defined by a velocity at which the intensity becomes equal to

$$I_t = [(0.2I_{\text{max}})^2 + I_{\text{lc}}^2]^{1/2} \quad (7.20)$$

on observed PV diagrams. This defines a 20% level of the intensity profile at a fixed position, $I_t \simeq 0.2 \times I_{\text{max}}$, if the signal-to-noise ratio is sufficiently high. On the other hand, if the intensity is not strong enough, the equation gives $I_t \simeq I_{\text{lc}}$ which approximately defines the

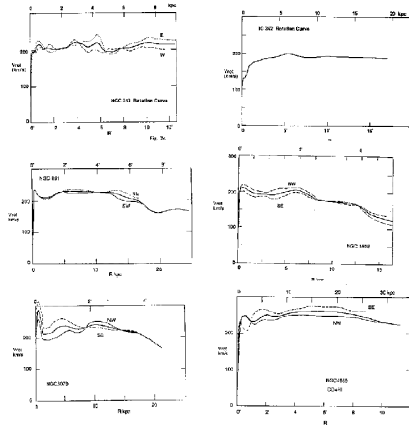


Figure 7.14: Most accurate rotation curves for nearby galaxies derived from CO + HI composite position-velocity

loci along the lowest contour level (usually $\sim 3 \times$ rms noise).

In Fig. 7.13 we superpose the thus obtained rotation curve for NGC 891 as an example. The HI gas indicates the rotation of the outer disk, whereas the CO emission indicates the rotation in the innermost region including the rapidly rotating nuclear disk. The rotation curve as a function of the radius can be obtained by averaging the absolute rotation velocities in both sides of the galaxy nucleus.

7.6.3 Rotation Curves for Nearby Galaxies

In the following subsections, we describe the thus obtained rotation curves for individual galaxies. Generally, the rotation curves are almost flat even in the very inner region, much flatter than those obtained from HI or optical observations. We describe individual galaxies below. The rotation curves are shown in Figs. 7.14 and 7.15.

Galaxy	Type	Incl. (deg)	Dist. (Mpc)	Line	A. Reso. (arc sec)	L. Reso. (kpc)	References
N253	Sc	78.5	2.5	CO	45	0.55	Scoville et al (1985)
				H α	–	–	Pence (1981)
				HI	120	1.5	Combes et al (1977)
IC342	Sc	25	3.9	CO	15	0.28	Hayashi et al (1987)
				CO	4	0.076	Ishizuki et al (1990)
				CO	45	0.85	Young&Scoville (1982)
				CO	45	0.85	Sage and Solomon (1991)
				HI	50	0.9	Rogstad&Shostak (1972)
N891	Sb	88.3	8.9	CO	4	0.17	Scoville et al (1993)
				CO(2-1)	13	0.55..	Garcia-Burillo et al (1992)
				CO	15	0.65	Sofue&Nakai (1993)
				HI	20	0.86	Rupen (1991)
N1808	Sbc	58	11.4	CO	15	0.83	Sofue et al (in prepara.)
				CO	45	2.40	Dahlem et al (1990)
				HI	20	1.1	Saikia et al (1990)
				HI	20	1.1	Koribalski et al (1993)
N3079	Sc	~ 90	15.6	CO	4	0.30	Sofue&Irwin (1992)
				CO	45	3.4	Young et al (1988)
				HI	20	0.15	Irwin&Seaquist (1991)
N4565	Sb	86	10.2	CO	15	0.74	Sofue&Nakai (1993)
				HI	20	1.0	Rupen (1991)
N5194 (M51)	Sc	20	9.6	CO(2-1)	13	0.60	Garcia-Burillo et al(1993)
				H α	–	–	Tully (1974)
N5907	Sc	88	11.6	CO	15	0.84	Sofue (1994)
				HI	40	2.2	Casertano (1983)
N6946	Sc	30	5.5	CO	4	0.11	Ishizuki et al (1990)
				CO	15	0.40	Sofue et al (1988)
				CO(2-1)	13	0.35	Casoli et al (1993)
				HI	20	0.5	Tacconi&Young (1986)
				HI	50	0.9	Rogstad&Shostak (1972)
Galaxy Gal.Cen.	Sb	90	0	²³¹ CO, HI, HII	–	–	Clemens (1985)
¹³ CO				2'	5 pc	Bally et al (1987) Sofue (1995)	

Table 7.1: Parameters for galaxies and references for PV diagrams and rotation curves.

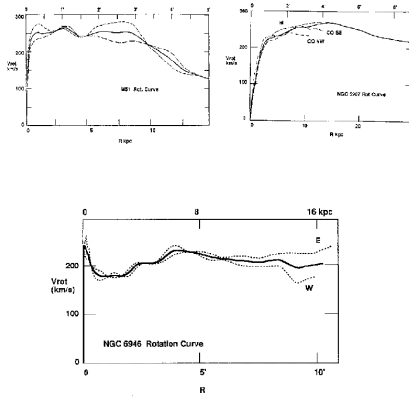


Figure 7.15: Most accurate rotation curves for nearby galaxies derived from CO + HI composite position-velocity (continued)

NGC 253

A PV diagram obtained using the 14-m telescope at FCRAO with resolution $45''$ (545 pc for 2.5 Mpc distance) indicates a steep increase of the rotation velocity near the nucleus within $R \sim 0.5$ kpc. An optical rotation curve indicates a flat rotation at 2 to 5 kpc radius. More outer rotation characteristics can be derived from an HI velocity.

This is a nearby (2.5 Mpc distance) highly inclined Sb galaxy rich in the molecular gas. By combining rotation curves derived by using published CO and HI PV data, a rotation curve has been obtained as shown in Figs. 7.14 and 7.15, where the inclination of $i = 78^\circ.5$ has been corrected. The rotation velocity increases steeply in the central region, and attains a maximum velocity of 210 km s^{-1} at $R \sim 0.3$ kpc. Then, the curve is almost perfectly flat until $R \sim 9$ kpc

IC 342

This is an almost face-on ($i = 25^\circ$) Sc galaxy at 3.9 Mpc distance. It has been extensively studied in the CO and HI lines, and various PV diagrams have been obtained. High-resolution PV diagrams have been obtained with the Nobeyama 45-m telescope at a resolution of $15''$ (284 pc) and a $4''$ -resolution mm-Array PV diagram. Fig. 7.14 shows the obtained rotation curve for IC 342 using the PV diagrams.

The rotation velocity increases almost rigidly in the innermost region at $R < 10'' = 190$ pc, and reaches $V_{\text{rot}} \sim 130 \text{ km s}^{-1}$ at $R \sim 15''$ (280) pc. Then, it increases gradually to reach a maximum velocity at 190 km s^{-1} at $R \sim 2 - 3'$ (2-3 kpc), followed by a flat HI rotation at 195 (at 8 kpc) to 190 km s^{-1} (at 20 kpc).

NGC 891

This edge-on Sb galaxy at a distance of 8.9 Mpc has been extensively observed in the CO line using the IRAM 30-m telescope, NRO 45-m, and OVRAO interferometer. It has been mapped in the HI line at a comparable resolution to the CO observations. In Fig. 7.13 we show a composite PV diagram of the CO and HI lines. The CO diagram is characterized by the 4-kpc molecular ring and the high-velocity nuclear disk at $R < 1$ kpc. The HI gas is distributed in a broad ring and outskirts at $R > 10$ kpc. For deriving the rotation curve near the nucleus, we also made use of the IRAM CO($J = 2 - 1$) observation at a $13''$ resolution and the higher resolution PV diagram obtained by interferometer observations.

Fig. 7.14 shows the rotation curve of IC 342. After a steep rising up near the nucleus, the rotation velocity attains a steep maximum over 250 km s^{-1} , followed by a dip at $R = 2$ kpc. Then, it becomes almost flat at $R \sim 3$ kpc, and remains so until $R \sim 15$ kpc. Beyond this radius, the rotation velocity gradually declines toward the outermost region. The rotation curve is very similar to that of our Galaxy.

NGC 1808

NGC 1808 is an Sbc galaxy known for its dusty jet, and the distance is 11.4 Mpc for a Hubble constant of $75 \text{ km s}^{-1}\text{Mpc}^{-1}$, and the inclination angle is $i = 58^\circ$. HI observations using the VLA indicated a circular rotation ring of about 7 kpc radius. HI-line absorption in the nuclear region has been mapped with the VLA, and a nuclear ring of cold, dense rotating gas disk of radius 500 pc has been found. The observations with the SEST 15-m telescope to map NGC 1808 in the CO line emission at an angular resolution of $43''$ have revealed a central condensation of molecular gas. We have mapped the central $1'$ region using the Nobeyama 45-m telescope at a resolution of $15''$ in the CO emission, and obtained a high-resolution PV diagram along the major axis. This diagram shows a high-velocity rotating nuclear disk, consistent with the HI line observations. These PV diagrams have been used to construct a rotation curve as shown in Figs. 7.14 and 7.15. The rotation speed increases steeply to 210 km s^{-1} at $R \sim 10''$ (500 pc) in the nuclear region, and then decreases to 190 km s^{-1} at $R \sim 3$ kpc. It increases again to a maximum of 210 km s^{-1} at $R \sim 2'$ (7 kpc) in the HI rotation curve. Beyond this radius, the rotation declines to $V_{\text{rot}} \sim 130 \text{ km s}^{-1}$ at $R \sim 6'$ (18 kpc). Such a declining rotation in the outskirts is rather exceptional among the galaxies studied here except M51 outskirts, suggesting a small-mass massive halo.

NGC 3079

This is an amorphous edge-on galaxy classified as Sc type, showing an anomalously high concentration of CO gas in the center. The distance is taken to be 15.6 Mpc for the galacto-centric HI systemic velocity as below with $H_0 = 75 \text{ km s}^{-1}\text{Mpc}^{-1}$. Figs. 7.14 and 7.15 show the rotation curve produced by using the composite CO + HI PV diagram, where a VLA HI PV diagram and CO data from the Nobeyama mm Array have been integrated. This galaxy exhibits an exceptionally high

concentration of CO emission in the galactic center. This high-density nuclear disk is clearly visible as the absorption feature in the HI line.

The rotation velocity shows a steep rising-up to a maximum as high as 320 km s^{-1} in the SE side and 260 km s^{-1} in the NW, followed by a dip at a few kpc radius. The rotation velocity of this nuclear disk component is highly asymmetric with respect to the nucleus. The asymmetric rotation continues until $r \sim 8 \text{ kpc}$. The HI gas is widely distributed in the broad ring at $R = 1' - 2'$ (5 - 10 kpc) and in the outskirts showing a symmetric flat rotation.

NGC 4565

This is an almost edge-on ($i \simeq 86^\circ$) Sb galaxy at a distance of 10.2 Mpc. The CO PV diagram shows a significant asymmetry in the intensity distribution: the CO emission in the SE few kpc region is very weak, so that the CO rotation in this region is not clear. However, except for this region, the total rotation characteristics is almost symmetric, and mimics that of NGC 891. On the other hand, the HI diagram shows an almost perfect symmetry both in intensity and rotation velocity.

The rotation curve as obtained from these diagrams is shown in Figs. 7.14 and 7.15, which is similar to that for NGC 891. It has a nuclear-disk component rotating at 260 km s^{-1} , followed by a flat rotation until 20-25 kpc at velocity as high as $\sim 250 \text{ km s}^{-1}$. This galaxy is one of those with extremely flat rotation even in the outskirts, suggesting a large extended massive halo.

NGC 5194 (M51)

This nearly face-on Sbc galaxy at an inclination 20° and distance 9.6 Mpc has been extensively studied in all wavelengths. A rotation curve from optical spectroscopic data has been obtained for a wide area. High-resolution CO PV diagram has been obtained, while no HI PV diagram has been obtained.

Combining these PV diagrams and correcting for the inclination of $i = 20^\circ$, we obtained a full rotation curve, and present it in Figs. 7.14 and 7.15. The rotation velocity increases steeply near the nucleus within 0.5 kpc, reaching a maximum of 260 km s^{-1} . Then, it remains flat up to 9 kpc, beyond which the rotation velocity declines to 130 km s^{-1} at $R \sim 15 \text{ kpc}$. This declining rotation is similar to that observed in NGC 1808.

NGC 5907

A CO + HI composite PV diagram for NGC 5907 has been obtained using CO data from Nobeyama and HI data from the WSRT. The HI gas is distributed over a large ring of 12 kpc radius, while the CO gas makes up a ring of 4 to 7 kpc radius. It is peculiar that this galaxy shows a central depression in the CO line. This causes an apparent rigid-rotation near the nucleus, rising gradually from $R \sim 0$ to 2 kpc, as it is indicated by the rotation curve in Figs. 7.14 and 7.15. Then, the rotation is almost flat until 20 kpc, beyond which it is gradually declining. Because of the lack of the nuclear disk in the CO emission, it is not clear if the rotation curve mimics that of NGC 891 or it is indeed rigid-body like.

NGC 6946

This is an nearly face-on galaxy at a 5.5 Mpc distance, and has been observed in high resolution in the CO line. A wide-area rotation curve is obtained by combining CO data from the NRO 45-m observations with an HI rotation curve. The rotation is almost perfectly flat from the very center to the outskirts at $R \sim 15 \text{ kpc}$. The CO PV diagram from IRAM 30-m observations shows that the rotation is almost flat toward the center. The innermost CO PV diagram has been obtained by using the Nobeyama mm Array at a resolution of $4''$, which showed a very steep rising of the rotation velocity up to a sharp maximum at

220 to 230 km s⁻¹ within the central 2'' (53 pc).

We have combined all these data and obtained a rotation curve as shown in Fig. 6.2.1 after correcting for the inclination of $i = 30^\circ$. The steep rising near the nucleus is followed by a decrease to a dip at about 1 kpc, followed by a flat minimum at 185 km s⁻¹ until 3 kpc. Then, the rotation velocity gradually increases to attain 220 km s⁻¹ at $R \sim 7$ kpc, beyond which the rotation is nearly flat. The flat rotation appears to continue until the observed edge of the galaxy at $R \sim 16$ kpc. The rotation curve mimics the one for our Galaxy as shown in the next subsection.

The Milky Way

The Milky Way Galaxy has long been observed both in HI and CO, and many longitude-velocity ($l-V_{\text{LSR}}$) diagrams have been published. These diagrams have been used to obtain a rotation curve of the Galaxy. The central 1° region has been observed extensively in the ¹³CO line emission at a resolution of 2' (5 pc). Detailed PV diagrams from the Bell Telephone Laboratory data have been used to derive a rotation curve in the central 150 pc. Fig. 7.16(a) shows a ¹³CO($J = 2 - 1$)-line PV diagram averaged in $b = -17'$ to $12'$ (47 pc width). The diagram shows several rigid-body like ridges, and are identified with rotating ring and arcs of about 120-pc ring. Fig. 7.16(b) is a PV diagram across Sgr A, which shows a steep ridge near $l \sim 0^\circ$, indicating a nuclear gas concentration rotating at a velocity of about 150 km s⁻¹, and therefore a compact nuclear mass. We use these ridges to obtain possible rotation curves, and superpose the thus obtained rotation curves by thick lines in the figures. Note that the two symmetrical high-velocity arcs at $V_{\text{LSR}} \sim \pm 150$ to 200 km s⁻¹ are parts of the expanding molecular ring, and do not indicate the rotation of the gas. Moreover, these expanding features makes up only a few percent of the total emission of the displayed region.

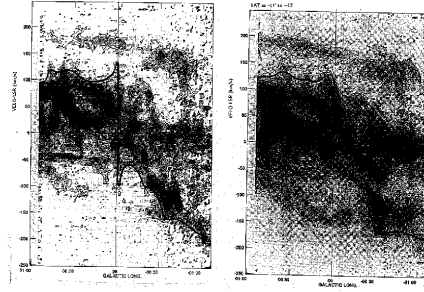


Figure 7.16: (a) Longitude- V_{LSR} ($l - V_{\text{LSR}}$) diagram across Sgr A. of the $^{13}\text{CO}(J = 1 - 0)$ line emission of the inner 1° region of the Galaxy. A possible rotation curve is indicated by the thick line. (b) Averaged $l - V_{\text{LSR}}$ diagram at $-17' < b < +12'$ for the inner 1° possible rotation curve is indicated by the thick line.

Fig. 7.17(c) shows a rotation curve of the inner 150 pc of the Galaxy by averaging the curves obtained above. By combining this rotation curve with that given for outer region, the most accurate rotation curve of the Galaxy has been obtained, as shown in Fig. 7.17(d). The solar rotation and radius are taken to be 220 km s^{-1} and 8.5 kpc, respectively.

7.6.4 Comparison of Rotation Curves

All the rotation curves obtained in this work are shown in the same scale in Fig. 7.18. Generally, the rotation velocity rises steeply within a few hundred pc, indicating the existence of a central compact mass component. Many galaxies (the Milky Way, NGC 891, NGC 3079, NGC 6946) exhibit a sharp maximum at $R \sim$ a few hundred pc, reaching a velocity as high as ~ 200 to 300 km s^{-1} . On the other hand, the maximum velocity corresponding to this component is not so high

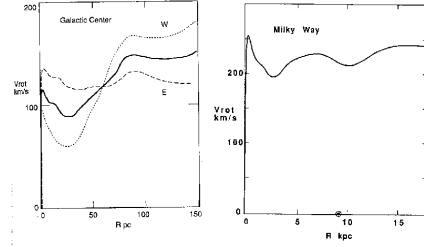


Figure 7.17: (c) An inner rotation curve at $-1^\circ < l < +1^\circ$ of the Galaxy. (d) Total rotation curve of the Galaxy obtained by using (c) and a fitting to the plot.

in such galaxies as NGC 253, IC 342, and M51, where the existence of the steep and sharp rising near the nucleus is also evident. One exception is NGC 5907, which shows a more gentle (solid-body like) increase of rotation velocity within $R \sim 3$ kpc.

7.6.5 Fitting by Miyamoto-Nagai Potential

We try to fit the rotation curves by the Miyamoto-Nagai potential. The modified Miyamoto and Nagai's potential with n mass components is expressed in a (R, z) coordinate as the following. Here, R denotes the distance from the rotation axis and z is the height from the galactic plane.

$$\Phi = \sum_{i=1}^n \frac{GM_i}{\sqrt{R^2 + (a_i + \sqrt{z^2 + b_i^2})^2}}, \quad (7.21)$$

where M_i , a_i and b_i are the mass, scale radius, and scale thickness of the i -th mass component of the galaxy. For a spherical mass distribution, we have $a_i = 0$, and b_i becomes equal to the scale radius of the sphere. The rotation velocity is calculated by

$a_3 = 6$ kpc and thickness $b_3 = 0.5$ kpc; and (4) a massive halo of $M_4 = 3 \times 10^{11} M_\odot$ and scale radius of $a_4 = b_4 = 15$ kpc. The rotation of NGC 891 can be reproduced by the same model with a similar parameter combination.

Similarly, the rotation curve observed for NGC 6946 is fitted by the one shown in Fig. 7.20, in which a table presenting the parameter combination is inset. The flat valley at $R \sim 1$ to 2 kpc region can be fitted well by introducing the four-component model, which was difficult to reproduce by the three-component model. The rotation of NGC 3079 can be fitted by a similar model. The rotation curves of NGC 253 and IC 342 can be fitted by the same model with a smaller-mass nuclear component, as shown in Figs. 7.21 and 7.22. Rotation curves for the other galaxies can be also reproduced by this model assuming parameters in between Figs. 7.19 and 7.22.

Only an exception is NGC 5907, which shows an apparently rigid rotation at $R < 3$ kpc. It is difficult to judge if this is indeed due to lack of the nuclear mass and the rotation velocity is indeed rigid, or if this is due to lack of CO-line emitting gas (hole of gas) as the tracer of rotation curve in spite of a more flat rotation.

We have so far called the obtained diagrams the “rotation curves”. However, they actually meant observed loci of the highest velocity envelopes in the position-velocity diagrams. However, non-circular motion such as due to barred potential and density waves would be superposed on the actual motion of gas, particularly in the central regions. We, therefore, estimate the deviation of the tangential velocity represented by the observed PV diagrams along the major axis from that of a circular rotation. Suppose that gas clouds are orbiting on elliptical orbits of eccentricity e . Then, the orbital velocity of a cloud at the perigalactic passage is given by

$$V_0 = V_{\text{rot}} \sqrt{1 + e}, \quad (7.23)$$

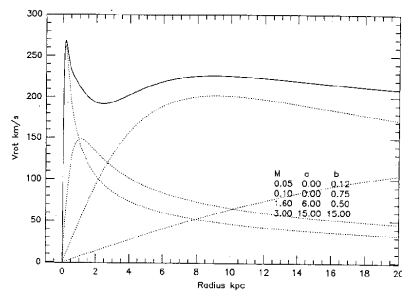


Figure 7.19: Rotation curve of our Galaxy as calculated for the Miyamoto-Nagai potential with four components: (1) Nuclear mass component; (2) Bulge component with scale radius a few hundred pc; (3) Disk component; and (4) Massive halo component. The mass M in $10^{11}M_{\odot}$, scale radius a and the thickness b in kpc of each component are indicated by the inset table. The inset table shows the mass M , scale radius a and thickness b for the four mass components of the modified Miyamoto-Nagai potential in equation (3). Dashed lines indicate rotation velocities corresponding to each mass component.

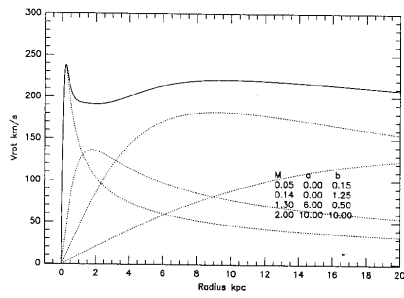


Figure 7.20: Galactic rotation curve as calculated for the Miyamoto-Nagai potential (continued), mimicking that of NGC 6946.

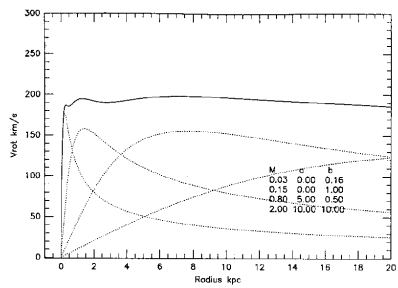


Figure 7.21: Galactic rotation curve as calculated for the Miyamoto-Nagai potential, mimicking that of NGC 253 with a smaller-mass nuclear component.

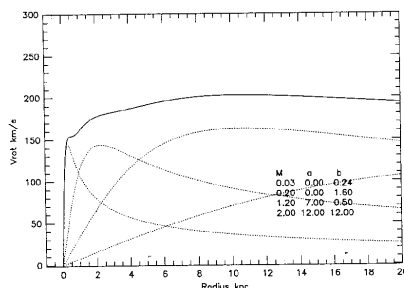


Figure 7.22: Galactic rotation curve as calculated for the Miyamoto-Nagai potential, mimicking that of IC 342.

where V_{rot} is the circular velocity corresponding to the mass distribution as calculated by eq. (eq:6-4-(4)). The loci of maximum velocity on the PV diagram will approximate this perigalactic (maximum) orbital velocity.

Therefore, the “rotation curve” may indicate a slightly over-estimated circular velocity by a factor of $\sqrt{1+e}$. For a highly disturbed orbits of gas in a strong bar as numerical simulations have shown, the eccentricity is found to be of the order of $e \sim 0.5$. Hence, the apparent rotation velocity from the PV diagrams would be only $\sim 20\%$ higher than a purely circular velocity even in such an extreme barred-shocked condition. This would, however, result in an overestimation of the mass component by a factor of $1+e$, causing an overestimation of a few tens of percent. We mention that the rotation of the gas disk in the central 150 pc of our Galaxy has been shown to be almost circular from a detailed analysis of the CO PV diagrams.

7.6.6 The Four-Mass Component Model

We have compiled position-velocity (PV) diagrams along the major axes of nearby galaxies, which have been observed in the CO line

(central regions), H_α emission (star forming disk), and in HI lines (disk and outskirts). We used these PV diagrams to obtain total rotation curves from the nuclear region to outskirts. The obtained total rotation curves are shown to be approximately flat from the nuclear region of a few hundred pc radius to outer $R \sim 10 - 30$ kpc region, except for the inner few hundred pc.

The most striking feature obtained in the present study is the steeply rising nuclear peak of the rotation curves at $R \sim 100$ to 200 pc, which is generally observed in the central regions. This steep rotation peak can be fitted by a mass model in which a compact nuclear mass component of a 100 to 150 pc radius and a mass of several $10^9 M_\odot$ is assumed. From a fitting of the observed rotation curves by the Miyamoto-Nagai potential, this nuclear mass component has turned out to be an additional new component to the well known central bulge: The rotation curves of galaxies can be thus generally fitted by a model with four mass components: the nuclear compact mass, central bulge, disk, and the massive halo.

The nuclear mass component would have an essential implication for the formation and evolution of the galactic bulge and the central mass condensation of galaxies. A theoretical model has shown that the flat rotation curve and exponential-law mass distribution in disk galaxies may be a consequence of a viscous protogalactic disk contraction with on-going star formation, where the time scales of viscosity and star formation are of the same order, or of the order of the Jeans time of the disk instability. Their model has also produced a central enhancement of the rotation velocity at $R \sim 0.05R_0$ with R_0 being the scale radius of the disk. This is due to a raider contraction of the central gas disk compared to the star formation time because of a stronger shearing-viscosity in the central disk. The model rotation curves could somehow mimic even the central velocity peak of the observed curves such as in the Milky Way, NGC 891 and NGC 6946.

However, the model appears to be still not satisfactory in reproducing in detail the steep central peak of rotation curves at $R < \sim 200$ pc corresponding to the compact nuclear mass component. In order for such a compact mass component to appear, a much raider contraction of protogalactic gas disk would have been necessary. Such a rapid contraction of gas disk prior to star formation may be possible if we could modify (increase) the viscosity in the central gas disk. Alternatively, we may need to take into account a rapid gas accretion through strong galactic shocks in a central oval (bar) potential during the proto-galactic disk contraction.

7.7 The HI and CO Tully-Fisher Relation and mm-wave Cosmology

7.7.1 HI Tully-Fisher Relation

Rotation velocity and size of a galaxy are directly related to the galaxy mass, and therefore, to the galaxy luminosity.

$$L \propto M = \frac{RV_{\text{rot}}^2}{G}. \quad (7.24)$$

If the galaxy luminosity is related to the surface area of the disk as

$$L \propto R^2, \quad (7.25)$$

or

$$R \propto M^{1/2}, \quad (7.26)$$

then, eq. (7.24) reduces to

$$L \propto M \propto V_{\text{rot}}^4. \quad (7.27)$$

Or, using absolute magnitude M_B in B band, for example, we obtain

$$M_B \sim -10 \log V_{\text{rot}} + \text{const.} \quad (7.28)$$

Indeed, a good relation has been found between the total velocity width of the HI line emission and the absolute magnitude. In reality, however, an empirical relation has been obtained for nearby galaxies with calibrated distances:

$$M_B = -7.58(\log W_i - 2.50) - 19.55 \quad (7.29)$$

where $W_i = 2V_{\text{rot}} = W_{\text{obs}}/\sin i$ is the line width after correction for the inclination of the galaxy. This relation is called the ‘‘Tully-Fisher relation’’.

The Tully-Fisher relation is one of the most powerful tools to estimate distances to galaxies using total line widths of the 21-cm HI line emission. However, distances to galaxies so far reached by HI observations are limited to around 100 Mpc, or recession velocities of 10,000 to 15,000 km s⁻¹ even with the use of the largest telescope.

7.7.2 CO instead of HI

However, we have no routine method to determine distances to galaxies beyond this distance, except for the possible use of CO line using a large-aperture mm-wave telescopes.

Beyond this distance, angular resolutions of a few arc-minutes in HI observations becomes too large to resolve individual galaxies in a cluster. Interferometers like VLA are not useful for the purpose because of the limited number of spectral channels (velocity resolution) due to the limited number of auto-correlator channels. Furthermore, more red-shifted HI frequency results in increases in beam size as well as in interferences, which also makes resolution of distant cluster galaxies difficult.

On the other hand, CO facilities have much sharper beams (e.g., 15

arc-sec with the Nobeyama 45-m telescope), with the use of which we would be able to resolve individual member galaxies in a cluster more easily, making it possible to avoid contamination by other member galaxies in a beam. Moreover, the larger is the redshift of an object, the lower becomes the CO frequency, which results in a decrease in the system noise temperature due to atmospheric O₂ emission near 115 GHz: the more distant is a galaxy, the lower becomes the noise temperature. Only the disadvantage of the use of CO line would be its sensitivity, particularly for distant galaxies. Actually, we need a few mK rms data for line-width measurements with a velocity resolution of 10 km s⁻¹ for normal galaxies beyond $cz \sim 10,000$ km s⁻¹, for which an integration time of about ten or more hours are required, and such observations are possible only by a long-term project with the largest mm-telescopes. However, although noise temperatures of current CO receivers, which are some hundred K in the present status, are still worse than those used in HI observations, we have the hope that they will be much improved in the near future to several tens K, which may result in an increase of the sensitivity by one or two orders of magnitudes.

Since the distribution of HI gas is broad in a galaxy, HI line profiles are easily disturbed by interactions among galaxies, which is inevitable in the central region of a cluster. Such disturbance might cause uncertainty in the HI line profiles for Tully-Fisher relation. On the other hand, CO gases are more tightly correlated with the stellar distribution, and are less affected by the tidal interaction. Of course, CO gas is distributed enough to a radius of several to ten kpc, so that the integrated line profiles manifest the maximum velocity part of the rotation curve.

7.7.3 CO vs HI Line Profiles Correlation

In recent studies, the CO line profiles have been found to coincide with the HI profiles. In particular, an almost perfect coincidence has

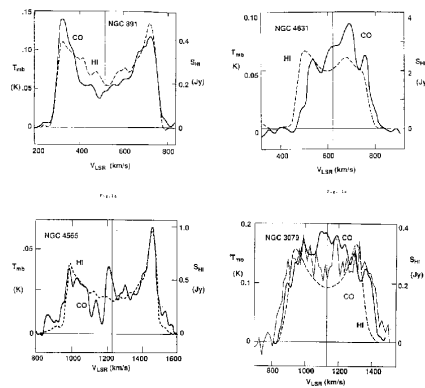


Figure 7.23: Total line profiles of the $^{12}\text{CO}(J = 1 - 0)$ line emission observed with the 45-m telescope (full line), and HI (dashed line) for edge-on galaxies.

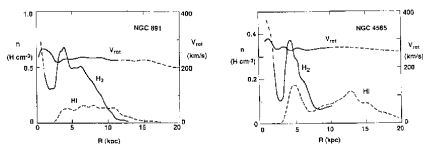


Figure 7.24: Radial distributions of the H_2 and HI gas densities. Their CO and HI rotation curves are indicated by the thick and dashed lines, respectively.

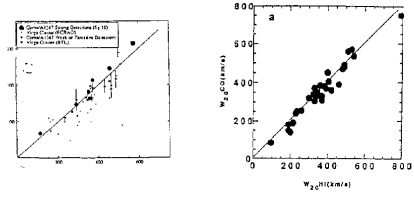


Figure 7.25: CO vs HI line width correlation for galaxies in Coma cluster of galaxies, and for nearby galaxies and for intermediate-distance galaxies.

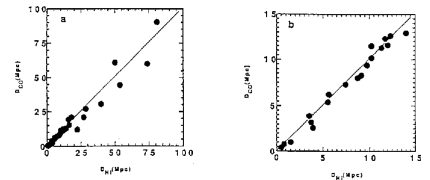


Figure 7.26: CO vs HI TF distances as determined using data as plotted in the previous figure.

been found in such non-disturbed galaxies like NGC 891 and NGC 4565. Generally, rotation curves are almost flat beyond 1 kpc from the galactic center, attaining a broad maximum at around galactocentric distance of $R \sim 3 - 5$ kpc. The rotation and/or dispersion is higher in the central few hundred pc, which contributes to the high-velocity wing in the total profile. The radial distribution of CO gas has two major density maxima: one near the center and the other at around $R \sim 3.4$ and 4.5 kpc for NGC 891 and NGC 4565, respectively. When the line emission is integrated over an entire galaxy, contribution from the outer ring/disk becomes dominant, because the total amount of gas involved in the outer ring/disk is much larger than that in the central region, simply for the disk's surface-area effect. Hence, the ring/disk component becomes the major source for the total line profile.

Although the HI gas is distributed in a broader disk than CO, its densest region is close to the CO disk. Namely, the densest HI disk appears at 3–10 kpc for NGC 891 and at 5–10 kpc for NGC 4565. Moreover, the rotation curve attains its broad (nearly flat) maximum at these radii. Hence the CO and HI double horns arise from almost the same radii, at which the rotation curve is nearly flat.

We now show a detailed comparison of CO and HI profiles for 32 spiral and irregular field galaxies in Figs. 7.23 to 7.26. This is the basic step toward establishing the CO Tully-Fisher relation not only for distant galaxies using the Nobeyama 45-m mm-wave telescope, but also for nearby galaxies as well as for galaxies in the central region of clusters where tidal interaction is inevitable.

Many of the sample galaxies show peculiar features like active nuclei or interaction with a companion. Despite such peculiarities, there is still a correlation between CO and HI. We apply the calibration of the B-band Tully-Fisher relation to determine the distances of the galaxies using the CO linewidth. We thereby use the CO linewidths just instead of HI without any own calibration. Finally we compare

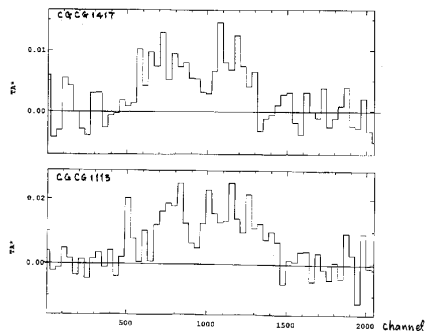


Figure 7.27: CO line profile for very distant galaxies.

the resulting distances with the distances obtained from the HI Tully-Fisher relation.

The results are shown in Figs. 7.23 to 7.26: These figures indicate that the CO and HI-line Tully-Fisher relation lead to an almost the same distances, and therefore, CO would be the powerful mean to replace HI for the distance determination of galaxies of cosmological distances.

7.7.4 The CO Tully-Fisher Relation: mm-wave Cosmology

Based on the arguments so far obtained for the CO-line Tully-Fisher relation, it will be reasonable to perform a routine observations of distance determination for galaxies and clusters beyond $cz > 10,000 \text{ km s}^{-1}$ using large-aperture mm-wave telescopes. There have been already some attempts to observe CO line widths for such distant galaxies using the IRAM 30-m telescope and the Nobeyama 45-m telescope. In the course of our preliminary observations at Nobeyama using the 45-m telescope, we have obtained CO line profiles of several galaxies in

Abel clusters at $cz \sim 20,000 \text{ km s}^{-1}$. Combining with the increasing sensitivity of the mm-wave observational technique in the near future, we have the hope that the CO Tully-Fisher relation using such large telescopes as the Nobeyama 45-m telescope will become the promising tool to measure the distances to high- z clusters of galaxies.

For applying the Tully-Fisher relation for the distance determination, however, it is necessary to obtain the apparent magnitude of a galaxy as well as its inclination i which is necessary in order to obtain the inclination-corrected velocity width $W_i = W_{\text{obs}}/\sin i$. For this purpose we need photometric data of target galaxies, as well as accurate inclinations. In order to obtain accurate inclination angles for galaxies with $cz > 20,000$, which are faint and of small angular extents, high-angular resolution imaging of sub arc-sec resolution would be necessary.

Combination of CO-line width measurement using the Nobeyama 45-m mm-wave telescope and high-quality imaging and photometry using the large 8-m optical telescope at Hawaii under construction would provide us of a promising situation in observational cosmology.

Chapter 8

STARBURST

8.1 Starburst Galaxy M82

M82, a nearby starburst galaxy, has been observed in various frequency ranges, from radio to X-rays. To get information about dynamics and physical conditions for the molecular gas, the star-forming block, extensive observations have been made of the line emissions of CO ($J=1-0$) and CO ($J=2-1$) transitions for the central ~ 1 kpc region at resolutions as high as $5 - 15''$ using large-aperture telescopes and mm interferometers. In this chapter we review the current progress in the study of starburst in M82, and present the newest observational data. We combine the data with the existing data at various wavelenghts to get insight into what is occurring in M82. We then give an interpretation of the data and propose a possible scenario of starburst in M82 as follows.

A tidal interaction of M82 with M81, the giant parent galaxy, gave a dynamical impact some 10^8 yrs ago, which led to a self-sustaining barred structure in the central region of M82. Being shocked by the barred potential, interstellar gas was rapidly accumulated toward the central region, and a sudden increase in the gas density took place there. Obeying the modified Schmidt's law, the star-formation rate

increased suddenly near the center by the accretion of gas. By strong shocks and winds from supernovae and young massive stars, a chain reacting cycle of active star formation proceeded in a ring-like region surrounding the nucleus. The energy released by the starburst and accumulated in the disk blew off the gas into the halo, forming a high-velocity outflow perpendicular to the disk. The flow consists of central high-temperature gas which emits X-rays and optical lines and of a cylindrical wall of dusty molecular gas emitting the CO lines. When the central gas is exhausted, the starburst stops. If the galaxy contains more gas and the tidal disturbance comes again, the same process repeats and a recurrent starburst goes on, while if there exists no more gas or no further trigger, the burst finishes in one time, which we call an impulsive starburst.

8.1.1 What is a starburst galaxy?

By definition “starburst” is a phenomenon that a high rate of star formation (say $\sim 10^3$ times that in normal interstellar place) is realized in a specific volume of a galaxy within much shorter duration (say $< 10^8$ years) than the time scale of the galaxy’s evolution time. In this sense any star-forming regions in the Galaxy, which contain massive OB stars, HII regions and molecular clouds, may be regarded as starbursting regions, when they are picked up individually. However, we here define a starburst galaxy as galaxy which contains a coherent ensemble of star-forming regions within a region of ~ 1 kpc scale, in most cases near the galactic nucleus.

8.1.2 How a Starburst Galaxy Looks Like?

We summarize how the starbursting galaxy, and therefore star-forming regions, look like at various wavelength ranges (Fig. 8.1). Stars are born from dense molecular clouds which are seen most representatively in spectroscopic mm-wave radio observations of CO, HCN, H₂CO,

HCO⁺, OH, etc. (Morris and Rickard 1982). As the gas is to be supplied from the outer region of the galaxies by some dynamical mechanism, the galaxy must contain rich envelope of gas often seen in the HI 21-cm line emission. Newly born stars, in particular OB stars, radiate intense UV and optical lights that ionize the very nearby gases to produce HII regions that emit thermal bremsstrahlung (free-free) radio radiation with a flat spectrum. However, most of the UV and optical lights are absorbed by dust grains which are richly contained in the molecular clouds. The UV-heated dust of temperature 10–60 K re-emits black-body radiation in the far-infrared (FIR) domain peaking at $\sim 100 \mu\text{m}$. Hence, the starburst region, and star-forming regions, are the strongest emitter of FIR radiation.

High-mass stars (OB stars) inject thermal and kinetic energies into the interstellar media through high-velocity stellar winds by their mass loss process. As well, OB stars explode at the end of their life as supernovae, and inject much energy into the interstellar space through cosmic rays and shocked gas. Through the interaction with interstellar magnetic field, which is in an energy equipartition with the turbulent gaseous component and cosmic rays, cosmic-ray electrons emit diffuse nonthermal (synchrotron) radio emission with steep spectrum. Remnants of supernova explosions are also strong nonthermal radio emitters, but are observed as individual compact sources. Finally, the heated interstellar gas radiates diffuse optical, UV and X-ray emissions, depending on their temperatures. The thermal and kinetic energies, and therefore the pressure, often become large enough to blow off the disk gas, which is observed as an outflow of gas in the direction perpendicular to the galactic plane.

Figure 8.2 shows a comparison of spectra of typical starburst galaxy M82 and typical star-forming regions in our Galaxy. As is readily seen the spectra resemble very much each other and without doubt the two sources are composed of similar, or almost the same, materials, except for the total luminosity. Namely we need only a pack of $\sim 10^4 - 10^5$

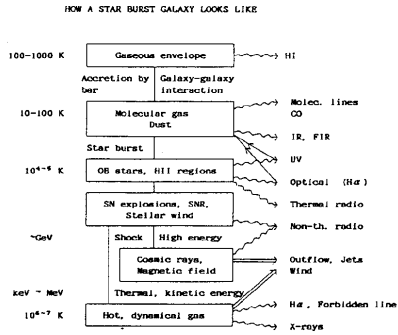


Figure 8.1: Diagram illustrating how a starburst galaxy looks like.

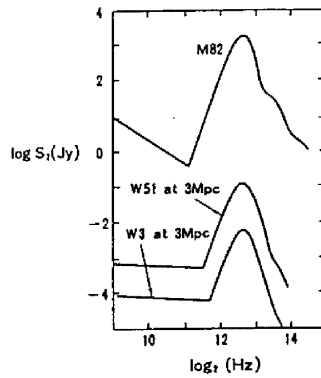


Figure 8.2: FIR and radio spectrum of M82 compared with the galactic star-forming regions W3 and W51 which are put at the same distance of 3.25 Mpc. Data are taken from Hargraves (1974), Telescope and Harper (1980), and Thronson and Harper (1979).

objects equivalent to a galactic star-forming region like W51 or W3 in the central ~ 1 kpc region in order to reproduce the emissions of M82 from radio to infrared.

In table 8.1, we compare the FIR luminosities of the central 1 kpc of M82 with that of the central 1 kpc of our Galaxy (Lugten et al 1986). We also compare their total masses and molecular gaseous masses. Obviously M82 radiates $\sim 10^2$ times more energetic radiation in the FIR domain. As the FIR emission is an almost perfect indicator of energy released by OB stars, we may conclude that high mass stars are about hundred times more produced there than in the same volume of our galactic center region, although the gas contents are almost the same. This means that the efficiency of star formation per unit gas mass is $\sim 10^2$ times higher in M82. We also note that the fraction of mass in the form of gas in M82 is much higher than in the Galaxy.

	M82	Galaxy
FIR luminosity, L_{FIR}	$4 \times 10^{10} L_{\odot}$	$5 \times 10^8 L_{\odot}$
Dynamical (total) mass, M_{dyn}	$10^9 M_{\odot}$	$10^{10} M_{\odot}$
Molecular hydrogen mass, M_{H_2}	$2 \times 10^8 M_{\odot}$	$2 \times 10^8 M_{\odot}$
$L_{\text{FIR}}/M_{\text{tot}}$	$40 L_{\odot}/M_{\odot}$	$0.05 L_{\odot}/M_{\odot}$
$M_{\text{gas}}/M_{\text{tot}}$	0.2	0.02

Table 8.1: Comparison of the ISM in the central 1 kpc of M82 and the Milky Way (Lugten et al 1986).

8.1.3 Implication of Starburst

Starburst galaxies, for their high luminosities at any frequencies, provide opportunity to detect and measure the emissions more easily compared to normal galaxies, and are much easier to be found, even if they are at cosmological distances. As often is the case, the starburst galaxies exhibit peculiar morphological features like ejection of matter

or some explosive nature, and show much dynamical characteristics. Many observers are attracted by such enthusiastic properties. Because of the high luminosity and therefore high signal-to-noise ratio in observations, as well as by attracting many observers to challenge, a wealth of good quality data at various wavelengths are available, in particular for such nearby starburst galaxies like M82 and NGC 253. This provides us good opportunity to investigate their physical properties in a great detail.

Physics which must be studied, of course, is the mechanism and origin of the active star formation. To do this, we need to know such parameters like the efficiency and rate of star formation from molecular clouds, initial mass function of stars being born there, the life time of the bursting phase and evolution. To determine these quantities by measuring the emissions from bursting regions, we must see first the physical conditions in the regions, namely the temperature, excitation condition, optical depth of the emission, density and size of gas clouds, etc., and also the transfer of emission is an important subject.

As a bursting galaxy is in a violent phase, it is essential to understand its dynamical circumstances, namely the motions of gas, the existence of shock waves, the outer inflowing motion, the turbulence, etc. Information of such dynamical phenomena can be obtained only through spectroscopic observations of radio line emissions like HI and CO as well as from optical line emissions like the $H\alpha$ and forbidden lines.

Further implication of the study of starburst galaxies is their role in the evolution of normal galaxies. Namely, whether starburst is really a peculiar phenomenon occurring in some very specific galaxies, or it occurs rather commonly in any galaxy during its evolution. Does starburst occur only once during the galaxy evolution, or is it a recurrent phenomenon? All these questions may significantly affect understanding the chemical evolution of galaxies, for the drastic increase in the

star-formation rate causes a significant change of the interstellar chemical abundance on which depends the evolution of a galaxy significantly.

8.1.4 Starburst History in M82

M82 (NGC 3034; Arp 337; 3C231) was recognized as a peculiar edge-on galaxy in the M81 group of galaxies early in 1950's and was known to be a companion to M81. M82 was classified as Irr II (Holmberg 1950; Sandage 1961) or I0 (de Vaucouleurs and de Vaucouleurs 1964). From its peculiar morphology that exhibits a numerous filamentary structures in emission and in absorption extending out of the galactic disk, the galaxy was suggested to be either exploding or colliding. In 1960's an explosion hypothesis was advocated by optical measurements of velocity gradient along the minor axis in the H α emission (Lynds and Sandage 1963; Burbidge et al 1964; Axon and Taylor 1978). A high expansion velocity of $\sim 500 \text{ km s}^{-1}$ was reported which suggested a gigantic explosion some 10^6 yrs ago at the nucleus.

In 1970's, linear polarization measurements of scattered light in the halo showed the existence of a wealth of dust high above the galactic plane over 2 kpc (e.g., Bingham et al 1976; Schmidt et al 1976; Visvanathan and Sandage 1972). However, the detection of redshifted scattered light of the H α line brought some complication in the interpretation of the expanding-halo model on the basis of a moving mirror hypothesis.

A large-scale extension of gas around the galaxy was also known from the HI line observations (Gottesmann and Weliachew 1973; Cottrell 1977). The HI velocity showed a large-scale distortion from circular motion of the gas in the HI halo, strongly suggesting a tidal interaction with the galaxy M81, and gives a hint to a triggering dynamical mechanism of the bursting star formation in the inner region. In fact, a prominent HI bridge connecting M81 and M82 has been observed. More inner region was mapped in HI absorption against the radio continuum emission showing a dense HI condensation in the central $2 \times$

0.3 kpc region (Weliachew et al 1984).

In this decade, in 1980's, ground-based and satellite observations at infrared wave range became available. Based on their pioneering work on near and mid-infrared observations ($2 - 20 \mu\text{m}$) Rieke et al (1980) have shown that many aspects of the observed IR characteristics of M82 and NGC 253 are well understood by a starburst hypothesis (see also Rieke 1987). FIR observations became available and thorough IR spectra of these galaxies became to be known (Telescope and Harper 1980), addressing similarity between galactic star-forming regions and the galaxies at IR domain. The starburst hypothesis could well explain the wealth of young stellar clusters detected in optical emission line observations (O'Connell and Manago 1978). Of course, the IRAS observations put M82 among the most luminous FIR sources in the sky. The IRAS discovery of luminous FIR galaxies, far more luminous than M82 in some cases, forwarded much to ascertain the importance of the study of starburst galaxies, since most of them could be of similar nature to M82 as is readily indicated from their similar FIR spectra (Becklin 1987).

X-ray imaging of M82 with the use of Einstein Observatory (Watson et al. 1984) revealed that a high-temperature ($\sim 10^7$ K) gas coexists in the central region with the hot gas being extending perpendicularly to the galactic plane toward the halo as high as ~ 1 kpc. This suggested an energetic heating mechanism of interstellar gas in the nuclear region. Indeed, high-resolution radio-continuum mapping of the galaxy has shown a large number of young supernova remnants of $\sim 10^2$ years or rather less concentrating in the central 400×100 pc region (Kronberg et al 1981, 1985; Kronberg 1987). This suggests a high rate of supernova explosions, \sim one SN per a few years, giving a hint to the energy source of the high-temperature component. Earlier continuum mapping showed an extended nonthermal emission (Hargraves 1984; Condon and Gerin 1985), which indicated a magnetic field as strong as $35 \mu\text{G}$ mixed up with high energy cosmic-ray particles.

Being stimulated by those observations results and by the high resolution CO observations described later, several theoretical models have been proposed to simulate the large-scale outflow of gas and wind driven by the starburst activity in the center (Chevalier and Clegg 1986; Tomisaka and Ikeuchi 1987; Tomisaka 1987; Umemura et al 1987).

8.1.5 CO Observations of M82

M82 contains a large amount of molecular gas and was the firstly detected galaxy in the molecular lines (Rickard et al 1975; Solomon and de Zafra 1975; Morris and Rickard 1982). In early 1980's, three important papers reporting more detailed CO line observations appeared. Sutton et al. (1983) made $^{12}\text{CO}(J = 1 - 0)$ and $(J = 2 - 1)$ observations using the Caltech. 10-m dish, and showed that the brightness temperature in the $J = 2 - 1$ transition is about 2–3 times higher than that in the $J = 1 - 0$ transition. This indicated that the molecular gas in the central region of M82 is optically thin for the CO line. Young and Scoville (1984) obtained a map of the CO ($(J = 1 - 0)$) covering an area as wide as $8' \times 5'$ (8×5 kpc) using the FCRAO 14-m telescope, and showed that molecular gas has a highly concentrated core as well as a largely-extended halo up to $\sim 2'$ (2 kpc) out of the galactic plane. The rotation curve showed a rather small dynamical mass, $\sim 10^{10} M_{\odot}$ within the radius 3 kpc. Olofsson and Rydbeck (1984) used the Onsara 20-m telescope to map the inner region, showing that the CO ($J = 1 - 0$) emission has an elongated disk structure along the major axis. They showed also the large-scale molecular halo. Their velocity field map showed a velocity gradient along the minor axis, suggesting a significant non-circular motion. These observations were made with a resolution of $30 - 60''$ so that the core region was not sufficiently resolved.

Recently significant progress was made in the CO ($J = 1 - 0$ and

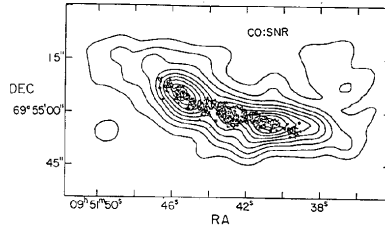


Figure 8.3: Interferometer map of integrated CO intensity of M82 at a resolution of $13''$ (Lo et al. 1987) superposed on a radio-continuum VLA map at 6 cm (Kronberg 1985).

2 – 1) observations of the central regions of M82 with the use of large aperture single dishes, e.g. NRO 45-m telescope and IRAM 30-m telescope (Nakai 1985; Nakai et al. 1987; Louiseau et al 1987), and of mm interferometers, e.g. the Owens Valley mm interferometer (Lo et al. 1987) and the Hat Creek mm interferometer (Calstrom 1987). These observations have made it possible to obtain high resolution maps with resolutions of $5\text{--}15''$, and have provided opportunity to compare in a more detail with other observations at various wave ranges. In section 8.2 we describe the newest CO observations.

8.2 High-Resolution CO Observations of M82

Recent progress in molecular line observations, in particular in the CO lines, using large aperture mm wave telescopes and mm interferometers have revealed detailed structures of molecular gas in the central ~ 1 kpc of M82. We review the recent observational results and discuss them in comparison with other observations at various wavelengths.

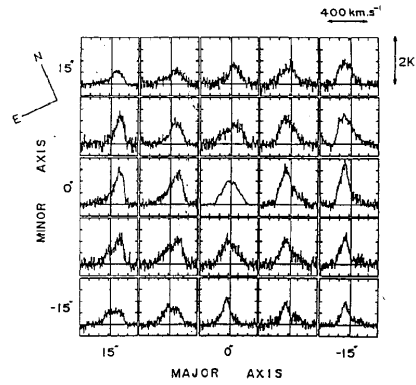


Figure 8.4: $^{12}\text{CO}(J = 1 - 0)$ line profiles of the central region of M82 taken with the NRO 45-m telescope (Nakai et al. 1987).

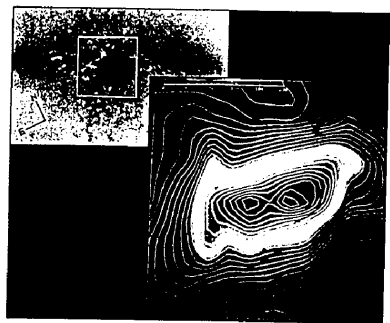


Figure 8.5: CO intensity map of M82 taken with the NRO 45-m telescope (Nakai et al. 1987). Inserted is the $\text{H}\alpha$ photograph reproduced from Lynds and Sandage (1961).

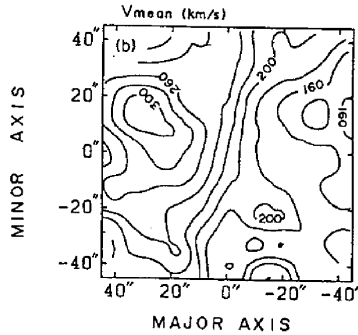


Figure 8.6: Distribution of the mean velocity of the CO emission in M82.

8.2.1 Interferometer Observations

Lo et al. (1987) performed a high-resolution $^{12}\text{CO}(J = 1 - 0)$ line mapping of the central 1 kpc of M82 using the Owens Valley mm interferometer at a HPBW of $7''$ with a simultaneous velocity coverage/channels of $150 \text{ km s}^{-1}/32$ channels. Their map (Fig. 8.3) shows a high concentration of CO gas toward the galactic plane within 700×100 pc associated with a weak extended component up to ~ 300 pc from the galactic plane. The map resolved the disk into two major peaks which appear on both sides of the $2 \mu\text{m}$ central source (Rieke et al. 1980). They showed a good spatial correlation of the CO emission feature with the HI absorption feature obtained by Weliachew et al. (1984) and with the $10 \mu\text{m}$ map of Rieke et al (1980). A detailed comparison was made with the radio continuum and supernova remnant distributions obtained by VLA (Kronberg et al. 1985). It is shown that SN explosions are occurring in the central $\sim 500 \times 600$ pc region, and the SNR distribution seems to be peaking near the region where

the CO shows a depression between the two peaks. Lo et al. (1987) also found a large shell-like structure in a channel map at $V_{\text{LSR}}=172$ km s^{-1} , and they attributed it to some violent activity.

More recently the highest-resolution map of the CO and some other molecular lines were obtained using the Hat Creek mm interferometer with a resolution of $5 - 10''$ (see Calstrom 1987). A radio-continuum map at 3 mm wavelength was also obtained. The maps are well in agreement with the CO map by Lo et al. (1987). However, with the high resolution, they could resolve the third peak of CO intensity nearer to the center in between the two CO peaks in a spatial coincidence with the region where the SNR density is highest. The 3-mm continuum emission indicates high density ionized thermal gas coexists with the molecular gas.

8.2.2 NRO 45-m Observations

The 45-m telescope at the Nobeyama Radio Observatory was used to map the ^{12}CO ($J = 1 - 0$) line emission toward the central 1×1.5 kpc region at a resolution of $15''$. The grid interval and pointing accuracy were $7.5\text{-}15''$ and $3\text{-}5''$, respectively, which resulted in an effective angular resolution on the final map of $18''$ (~ 250 pc at 3.25 Mpc distance). The simultaneous velocity coverage and channel number were 650 km s^{-1} and 2048, respectively, with the velocity resolution of 0.3 km s^{-1} . Results are described in detail by Nakai (1985) and Nakai et al. (1986, 1987). Observational parameters are given in Table 8.2.

Obtained spectra are shown in Fig. 8.4 and the integrated intensity distribution in Fig. 8.5. As is readily seen in the intensity map, the CO distribution well agrees with the interferometer results, showing the two-peaked distribution of molecular gas. Also remarkable in the figure is the horn-like spurs running perpendicular to the major axis in the four corners of the contours. As described in more detail in section 8.3, the two peaks and the spurs are interpreted in terms of a rotating

Distance of M82	3.25 Mpc (Tammann and Sandage 1961)
Center position (2.2 μm peak)	RA(1950) = $9^{\text{h}}5^{\text{m}}43.9^{\text{s}}$ Dec(1950) = $69^{\circ}55'01''$ (Rieke et al. 1980)
Systematic velocity	vlsr = 220 km s $^{-1}$ (Olofsson and Rydbeck 1984)
Position angle of major axis	65°
Inclination angle	81.5° (Lynds and Sandage 1963)
Mapped area in CO	1.5×1 kpc
Telescope	45-m telescope at NRO (HPBW = $15''$)
Effective Resolution	$18''$ (250 pc)
System temperature	500 – 700 K
Spectrometer	250 MHz / 2048 ch. Acousto-optic type
Velocity resolution	0.3 km s^{-1} (= $650 \text{ km s}^{-1}/2048$ channels)
Observing period	1983 – 1985

Table 8.2: Parameters for M82 CO observations using the 45-m telescope (Nakai et al. 1987)

ring (torus) of molecular gas with a radius of 200 pc and of cylindrical distribution of molecular gas extending toward the halo perpendicular to the disk plane.

The velocity field is shown in Fig. 8.6. Along the major axis we obtain a rotation of velocity 100 km s^{-1} . We note here that the mean velocity along the major axis is about 40 km s^{-1} larger than the velocity measured optically by O’Connell and Mangano (1978). Namely the optical rotation curve is blue-shifted by about 40 km s^{-1} from the CO rotation curve. This velocity discrepancy may be explained, if the optical rotation curve represents motion of a foreground part (near side) of the galactic disk in expansion, and this is likely if we consider the large amount extinction due to the dust, while the CO rotation curve results from the emission from the whole galactic disk.

In Fig. 8.6 it is clearly seen that there is a velocity gradient along the minor axis, showing a non-circular motion in the halo. Considering the

Material	Mass	Area	References
Molecular hydrogen (H ₂)	$1.1 \times 10^8 M_{\odot}$	within $r < 700$ pc	Nakai et al.(1987)
Atomic hydrogen (HI)	5×10^7	$r < 700$ pc	Crutcher et al.(1978)
Ionized gas (HII)	7×10^7	$r < 600$ pc	Willner et al.(1977)
Dust	5×10^5	$r < 300$ pc	Telesco & Harper (1980)
Dynamical (total) mass	$(1.1 - 1.2) \times 10^9$	$r < 700$ pc	Nakai et al.(1987)

Table 8.3: Summarized masses of the various contents in M82.

inclination of the disk plane, $i=82^\circ$, this velocity gradient is naturally attributed to an expanding motion or an outflow of gas perpendicular to the disk plane at a velocity of $40 \text{ km s}^{-1} / \cos i \sim 300 \text{ km s}^{-1}$. Such a high velocity outflow is observed not only along the minor axis but also along the spur-like features, indicating that the cylinder (or the molecular chimney) is moving at the same velocity out of the plane.

Mass (H ₂) ^a	$5 \times 10^7 M_{\odot}$
Velocity ^b	$\sim 300 \text{ km s}^{-1}$
Height	$> \pm 500$ pc
Kinetic energy	$\sim 5 \times 10^{55}$ erg

a. within the region of $|z| > 100$ pc and $|r| < 500$ pc.

b. assuming the inclination angle of 82° (90° is edge-on).

Table 8.4: The observed parameters for the outflowing molecular gas.

8.2.3 IRAM 30-m Telescope Observations of the CO($J = 2 - 1$) Line

To get more detailed information with sufficient resolution about the physical conditions like the optical depths and excitation of molecules, Louiseau et al. (1987) performed a mapping of the central 1 kpc in the ¹²CO ($J = 2 - 1$) line at 230 GHz. The observations were made using the IRAM 30-m telescope near Granada in Spain. The mapped

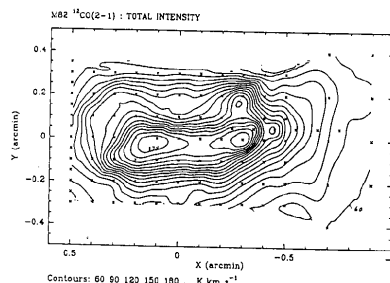


Figure 8.7: CO ($J = 2 - 1$) intensity map of M82 taken with the IRAM 30-m telescope (Loiseau et al. 1987).

area was 1000×500 pc of the center. A shottky-barrier diode-mixer receiver of system temperature 1000-2000 K and a 512-channel filter bank spectrometer were used with the velocity resolution of 1.3 km s^{-1} and the simultaneous velocity coverage 600 km s^{-1} . The angular resolution of the antenna was $13''$ and the pointing accuracy was better than $3''$. High antenna temperature of 3-6 K was recorded toward the central region, approximately twice the $J = 1 - 0$ line.

Figure 8.7 shows the integrated intensity map of the ^{12}CO ($J = 2 - 1$) line emission of M82. The distribution of the emission is almost the same as that obtained in $J = 1 - 0$ line, and most of the structures seen in the 45-m CO map are well seen in this figure, e.g. the two-peaks and the spur-like extensions toward the halo.

In Fig. 8.8 we compare the ^{12}CO ($J = 2 - 1$) line profiles with the $J = 1 - 0$ transition profiles for the 200-pc ring region and for outer regions. As was the case for $J = 1 - 0$, we get the highest antenna temperature toward the 200-pc ring at $X \sim +15''$ and $T_{\text{B}}(2 - 1) = 8 \text{ K}$ was recorded, where we have $T_{\text{B}}(1 - 0) = 3.5 \text{ K}$. The $J = 2 - 1$ emission shows generally higher temperature, twice that of $J = 1 - 0$ for the inner region of $|X| < 20''$ and $|Y| < 10''$, while the two temperatures

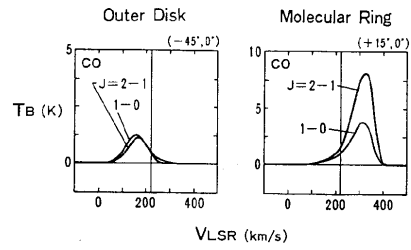


Figure 8.8: Line profiles of ^{12}CO $J = 2 - 1$ and $1 - 0$ transitions toward the outer region (optically thick) and toward the 200-pc ring (optically thin) (Nakai 1987; Loiseau et al. 1987).

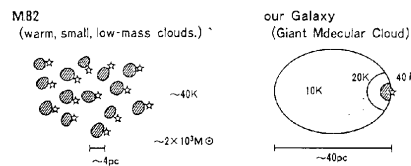


Figure 8.9: Warm, small-size and low-mass molecular clouds in M82 in comparison with giant molecular clouds in our Galaxy (Nakai 1987).

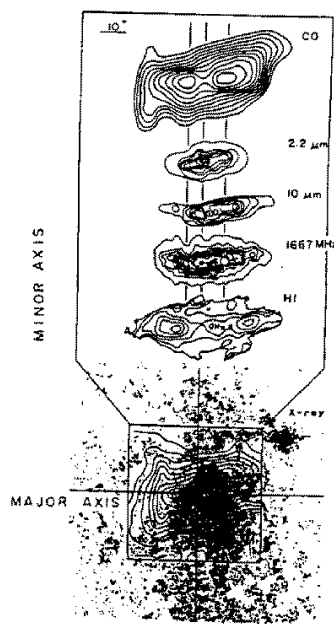


Figure 8.10: Comparison of maps of M82 in various emission. See the text for references (After Nakai et al. 1987).

are almost the same in the outer regions. This fact implies that the inner region is optically thin for the CO ($J = 1 - 0$) line, and we get an optical depth of $\tau \sim 0.5$, if we assume the same excitation temperature of $T_{\text{exc}} = 40$ K as the dust temperature determined from the infrared observations. In the outer regions, on the other hand, the emission is optically thick.

Although we need a more detailed analysis to obtain accurate figures, we can make an order-of-magnitude estimate about the cloud size, mass, etc. for the inner region (ring region) (Nakai 1987). We assume that the region contains a large number of spherical clouds of size a and each cloud has mass M and density n_{H_2} , and that the length along the line of sight of the observed region is l .

Then the cloud size a is related to l and the volume and surface filling factors f_v and f_s through $a = f_v/f_s$. Here f_v is approximated by $1/n_{\text{H}_2}$ and f_s is given by $T_{\text{B}}/T_{\text{ex}}(1 - e^{-\tau})$. For an assumed temperature $T_{\text{ex}} = 40$ K, $l \sim 1$ kpc and $\tau \sim 0.5$ we obtain $a \sim 3(n_{\text{H}_2}/10^3 \text{cm}^{-3})^{-1}$ pc. The mean mass of individual clouds is obtained to be $M \sim 2 \times 10^3 M_{\odot} (n_{\text{H}_2}/10^3 \text{cm}^{-3})^{-2}$ and the total number of clouds in the ring (torus) $N_{\text{cl}} \sim (M_{\text{H}_2}/M \sim 10^5 (n_{\text{H}_2}/10^3 \text{cm}^{-3})^2)$. Mean distance among clouds is about 10 pc. Here we assumed the torus radius of 300 pc and cross section of 200×100 pc. Thus we conclude that the ring is filled with low-mass, small-size clouds with high excitation temperature. Figure 8.9 illustrates the cloud distribution in the molecular ring in comparison with giant molecular clouds in the Milky Way Galaxy (Nakai 1987).

The outer regions of the 200 pc ring and the halo region are optically thick against the ^{12}CO line emission. This fact suggests that the molecular gas is distributed in a more diffuse way and with lower temperature than in the ring and more or less similar to giant molecular clouds in the Milky Way.

8.2.4 Comparison with Other Observations

The high resolution CO observations have made it possible to compare the molecular hydrogen distribution in more details with other observations at various wavelengths from X-ray to radio. Figure 8.10 summarizes the comparison among them (see also Figs. 8.3 and 8.5).

IR and FIR Emissions

The 2.2 μm map (Rieke et al. 1980) shows the distribution of low temperature stars like supergiants associated with circumstellar dust shells of high temperature, 500-800 K. The 2.2 μm peak, which we assume to be the nucleus of M82, is located in the minimum position of the CO emission between the two peaks. Namely the 2.2 μm star cluster is located in the center of the ring where the molecular gas density is much lower. The extended 2.2 μm emission feature coincides with the molecular ring and shows the existence of such stellar population mixed up with the molecular gas clouds there.

The 10 μm emission shows a similar distribution to that of the molecular hydrogen. The 10 μm emission comes from dust of temperature ~ 100 K mixed up with ionized HII gas near star formation regions heated by O and early B stars. In the present resolution this hot dust component coexists with the molecular ring composed of warm (40 K), small clouds. The warm dust component radiates in the FIR range peaking around 100 μm . The energy source of the FIR emission is the absorbed UV and optical lights from OB stars.

HI Gas

The HI gas distribution as determined from the 21-cm absorption features (Weliachew et al. 1984) has also two peaks which coincide with the CO peaks as determined from the interferometer observations (Lo et al. 1987), showing that the HI gas also composes a ring. The total mass of HI gas, and therefore the density, involved in the central 1 kpc

is about a half of that of molecular hydrogen (table 8.3). Such high density of HI, comparable to H₂ density, in the central region seems extraordinary, since normal galaxies have generally a deep depression (or a hole) of HI in their centers while H₂ (molecular gas) dominates there. The high HI content in the central (< 500 pc) region of M82 may suggest an intense inflow (accretion) of gas from the outer region of HI envelope.

Radio Continuum Emission

The radio continuum emission of M82 consists of two components: The extended component is mainly due to synchrotron radiation by the strong interstellar magnetic field ($\sim 35 \mu\text{G}$) and cosmic rays (Hargraves 1974) and partly, in particular in the mm wave range, due to the thermal (free-free) emission from ionised gas (Carlstrom 1987). Another component consists of numerous discrete sources of small diameters, which are mostly attributed to young supernova remnants (Kronberg et al. 1985). Some of the sources have been resolved with VLBI observations and show extended structure, but no shell-like nature has been found (Kronberg 1987). The global distribution of the two components is essentially the same and well coincides with the CO intensity distributions.

However, the two peaks observed in the CO line are not clearly seen in the continuum emission; the continuum emission seems to be more uniformly distributed with slight concentration toward the third CO peak (Carlstrom 1987). This fact seems not consistent with the expectation that SN explosions take place in the densest region of molecular gas where the intense star formation is going on. Two alternative explanations may be possible: (i) By the dense ionized gas as shown by the mm continuum observations (Carlstrom 1987) the centimetric and decimetric continuum radio emission is no more transparent but absorbed significantly in the disk and ring, so that the observed SNRs

and diffuse radio component are those in the foreground, or nearer side of the center, and the ring (two peaks) does not show up. In fact the sources show a turnover spectra at the lower frequencies (Kronberg 1987). Note that the mm continuum is transparent and coincides with the molecular distribution. In this case the SN rate could be significantly higher than the current estimate (one SN per a few years) which is based on the statistics of the detected SNRs. (ii) Alternatively, provided the centimetric and decimetric emission is transparent, SN explosions are taking place in more inner side of the molecular ring, not necessarily coinciding with the present star-forming region. It is also probable that, if supernovae are exploding, being berried in dense molecular gas in the ring, their radiation is absorbed and reemitted moslly in the infrared emission (Wheeler et al. 1980). Such berried SNRs evolve very rapidly and are not observed in the radio domain. In this case the IR emission from the M82 disk may partly be due to SN energy release. Again the SN rate must be higher than the current estimate.

Optical Images

In Fig. 8.4 we compare the CO intensity distribution with the optical photograph (Lynds and Sandage 1963). Because of the large extinction the optical image cannot be compared with the central features in the CO distribution. However, it is interesting to compare the spur-like CO features in the halo (the molecular cylinder or chimney) with the optical filamentary structures. The longest optical filaments running perpendicular to the disk plane are well located within the “wall” of the molecular cylinder. According to the model described in the next section the filaments are due to mixture of $H\alpha$ emission from the high velocity ionized gas inside the cylinder and dust filaments associated with the molecular cylinder which surrounds the high temperature flow.

X-ray Emission

Watson et al. (1984) have obtained an IPC X-ray image of M82 using the Einstein Observatory. Figure 8.10 shows a superposition of the X-ray image and the CO distribution. The X-ray emission is elongated along the minor axis, originating near the center of the molecular 200-pc ring. As is readily seen, the CO cylinder just surrounds the X-ray feature. The X-ray emission indicates that a high-temperature gaseous component is produced in the central region, being heated by some energetic phenomena like SN explosions. The configuration elongated perpendicular to the galaxy plane suggests that the gas is outflowing toward the halo, being collimated by the molecular wall.

8.3 Model of M62 Starburst

8.3.1 Ring-and-Outflowing Cylinder Model

The results of the various observations can be interpreted in terms of a ring-and-outflowing cylinder model by Nakai et al. (1987; see also Nakai 1985), and is schematically illustrated in Figure 8.11. The molecular hydrogen gas in the central region of M82 consists of two major components; the “200-pc ring” in the galactic plane and the cylindrical halo with high-velocity outflow.

The 200-pc molecular ring is associated with the HI gas ring at the same radius, and involves a large amount of warm dust ($T_d \sim 40$ K). The high luminosity FIR (10–100 μm) dust emission coming from the ring is due to reradiation after absorbing UV and optical lights from massive stars which are being born in a bursting star forming phase from the molecular clouds. The central region of the ring, or near the nucleus, is rather scarce in gas, where circum-nuclear supergiant stars with circumstellar dust shells emit IR emission responsible for the 2.2 μm peak. Molecular clouds in the ring are of small size of a few pc, small mass of $\sim 10^3 M_\odot$ and high temperature of ~ 40 K. The ring

is rotating at a velocity of 100 /kms . The large velocity width in CO toward the center suggests that the ring is expanding at $\sim 40\text{--}50 \text{ km s}^{-1}$ in the radial direction. Many young SNRs are found in or near the ring structure.

The 200-pc ring is associated with spur-like features which can be deconvolved to a cylindrical distribution of molecular gas in case of an axisymmetric case. Total molecular mass involved in the cylinder is about $5 \times 10^7 M_{\odot}$ which is the mass integrated above 100 pc of the galactic plane. The radius of the cylinder is about 300 pc with thickness ~ 200 pc. It extends perpendicular to the disk plane as high as ~ 1 kpc. From the velocity gradient perpendicular to the disk plane, the gas in the cylinder is flowing out of the plane at a velocity $\sim 300 \text{ km s}^{-1}$ for the inclination of $i = 82^{\circ}$. The total kinetic energy of the outflow is about 10^{56} erg.

The energy of the expanding motion can be supplied by SN explosions: According to the star burst model by Rieke et al. (1980) and to the SNR statistics from radio observations (Kronberg et al. 1985), the SN rate in the ring is about one SN / a few year. If the fraction of conversion of SN energy to kinetic and thermal energy of interstellar gas is η , we can estimate the energy given to the gas in and near the ring as

$$E_{\text{kin}} = \eta E_{\text{SN}} R_{\text{SN}} t_{\text{cyl}} \quad (8.1)$$

Here $E_{\text{SN}} \sim 10^{51}$ erg is the energy of one SN explosion, $R_{\text{SN}} \sim 1\text{--}0.3 \text{ yr}^{-1}$ is the SN rate and $t_{\text{cyl}} \sim Z/V_{\text{exp}} \sim 1 \text{ kpc} / 300 \text{ km s}^{-1} \sim 3 \times 10^6$ yr. The conversion rate, η , may be taken as ~ 0.1 (Chevalier 1974). Then we obtain $E_{\text{kin}} \sim 10^{56}$ erg, comparable to the observed value of outflowing kinetic energy.

From the fact that the optical depth of the CO line is large we may consider that the molecular gas distribution in the halo (cylinder) is diffuse in larger clumps than in the ring region. It is likely that the

gas clouds are stretched in the direction of the flow. In fact optical photographs show numerous filamentary dust lanes being stretched perpendicular to the disk, which are most likely due to such stretched molecular gas clouds in the cylinder by the high-velocity flow. The observed peculiar morphology of the vertical $H\alpha$ filaments is explained by the cylinder model: At the contact surface of the low temperature molecular “wall” (cylinder) and the high temperature ionized gas (X-ray halo) there appears a transient region with temperature 10^{4-5} K, which radiates $H\alpha$ emission. The $H\alpha$ emission is seen through the molecular wall containing numerous stretched dust clouds which are silhouetted against the $H\alpha$ emission. The mixture of $H\alpha$ and dust filaments are thus observed as running perpendicular to the galactic plane.

Thus from the view point of energetics the observed high-velocity molecular outflow perpendicular to the disk and the extended X-ray emission can be naturally attributed to the intense energy release by the star burst in the nuclear ring. The peculiar optical morphology with $H\alpha$ and dust filaments can be also explained by this cylinder outflow model. In the next section we consider this model in more quantitative way on the basis of numerical simulations.

8.3.2 Numerical Models of the Ring+Cylinder Structure

We discuss the formation mechanism of the ring and cylinder structure on the basis of numerical computations of hydrodynamic and magnetohydrodynamic behaviours of the gas with a high rate of energy input near the center.

Explosion Model

To account for and reproduce extragalactic jets various models have been proposed, which deal with collimation of outflowing gas driven

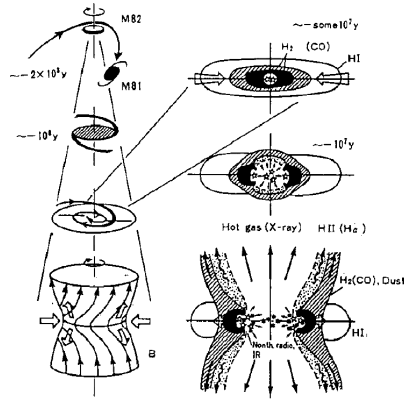


Figure 8.11: Possible evolution of M82 and formation of ring + cylinder structure.

by an explosion or a sudden energy release at the nucleus of a disk system. The suddenly heated gas expands and causes strong shocks by encountering with the ambient matter. The shock propagates much faster in the direction perpendicular to the disk plane blowing off into the halo, resulting in a collimated flow along the minor axis, while it propagates slowly in the disk blocked by the dense gas in the disk.

Sofue (1984) has applied the jet model of Sakashita (1971) to a galactic-scale disk system computing an explosion and associated shock propagation from the center through the disk and halo. The method was a modified self-similar shock propagation in a variable density medium. The shock wave propagates faster in the direction perpendicular to the disk and the disk is blown off toward the halo, forming an elongated Ω -shaped shock front in the halo, partly composing a cylindrical structure (Fig. 8.12). By treating with magnetohydrodynamic blast wave, Sofue (1977) showed that a considerable fraction of the shock front focuses on a ring (focal ring) with the radius about

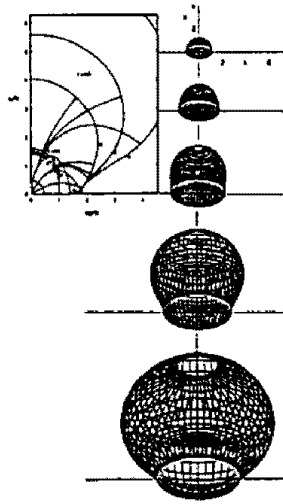


Figure 8.12: Explosion model of other ring + cylinder (lobe) structure (Sofue 1977, 1984).

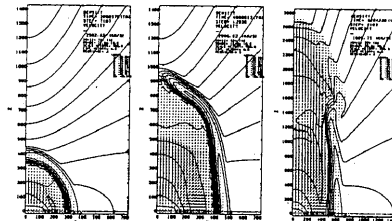


Figure 8.13: Vertical outflow model of M82 driven by continuous energy supply at the center (Tomisaka and Ikeuchi 1987).

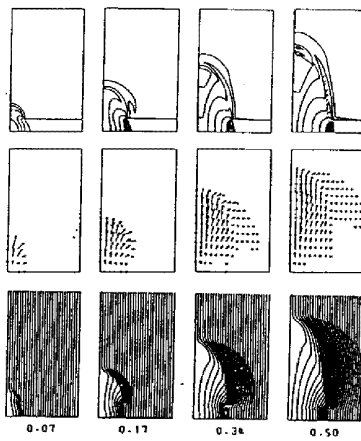


Figure 8.14: Shock propagation in M82 under the existence of a vertical magnetic field (Umemura et al. 1987).

twice the disk scale height. For a scale height of 100 pc the compressed focal ring appears at $r \sim 200$ pc.

The shock wave model in a disk+halo system can already explain some essential features observed in M82, namely the ring structure in the disk plane and the cylindrical collimated flow perpendicular to it. The high temperature in the cavity surrounded by the shock front may explain the X-ray emission. For the cold molecular disk to form, the cooling time in the shock compressed region must be short enough compared with the time scale of the flow. In case of M82 the cooling time must be shorter than $\sim 10^7$ years, which is realized even in the halo region where the free-free cooling time is estimated to be $\sim 10^6$ years.

Wind Model

Chevalier and Clegg (1985) modeled a one dimensional wind of gas in M82 driven by a constant energy input near the center by successive SN explosions.

They showed that a high-velocity, high temperature streaming motion of gas enriched with heavy element transfers the gas from the central region to the outer parts. They suggest that the wind is expected to create a hole of gas in which the galaxy is embedded.

Two dimensional hydrodynamic model of outflow in a rotating disk was recently computed by Tomisaka and Ikeuchi (1987). They showed that a sudden energy input at the nucleus produces a flow of gas perpendicular to the disk plane and blows off into the halo where the shock front forms an elongated Ω shape (Fig. 8.13). The result is essentially similar to the explosion model, showing that the star burst energy, mainly released through stellar winds and SN explosions near the nucleus, causes a collimated outflow surrounded by a dense cylinder.

Magnetic Model

Radio continuum observations showed the existence of strong magnetic fields of $\sim 35 \mu\text{G}$, although the observations do not tell about the orientation of magnetic field (Hargraves 1974). It was shown that the central region of a disk galaxy likely possesses a strong vertical magnetic field running perpendicular to the disk plane, often dominating over the field parallel to the galactic plane (Sofue and Fujimoto 1987).

By such a strong vertical magnetic field the flow of gas is significantly affected: The flow is better collimated in the direction parallel to the field. Umemura et al. (1987) showed, by their MHD computations in two dimensional axisymmetric case, that the ring + cylinder structure observed in M82 can be better reproduced with a vertical field of $\sim 30 \mu\text{G}$ than without magnetic field (Fig. 8.14).

An alternative model to magnetically driven outflow has been proposed by Uchida and Shibata (1986): When an accretion of gas in the disk is rapid enough, the angular momentum conservation of the gas causes a twist in the vertical magnetic field. The twist propagates toward the halo along the field, accelerating the disk gas perpendicular to the disk and a “mild jet” appears. The magnetic twist model needs no violent heating of gas but can create even a cold (molecular) gas flow in a vertical cylinder. This may better explain the molecular gas cylinder in M82, while it is hard to account for the central high temperature gas, for the model does not require any explosion or strong energy release at the center.

In reality, however, the wind/explosion model and the magnetic twist model may be combined. The intensive accretion of gas toward the center, which is necessary to trigger the star burst (see the next section), would produce a magnetic-twist acceleration of cold gas from the dense disk, creating the molecular gas cylinder. The star burst causes a high-temperature Gas flow in the inner region.

8.3.3 Accretion of Gas and Formation of Dense Nuclear Disk

The central region of M82 is rich in molecular, atomic and ionized gases. The star burst phenomenon, triggered by the enhanced star formation rate, is intimately related to high density of gas. We here consider the mechanism to produce a dense gaseous core in a galaxy (see also Lo et al. 1987; Lo 1987; Combes 1987).

Formation of a Bar by Tidal Interaction

Noguchi (1986) has shown that a tidal interaction during an encounter of galaxies produces a barred structure in the innermost region of the disturbed galaxy. As shown by the HI observations and from the optical photographs (Cottrell 1977; Gottesman and Weliachew 1977), M82 is a companion to the giant spiral, M81, and a clear indication of tidal interaction is seen from the HI bridge between the two galaxies (Fig. 8.15). It must be also noted that M82 is embedded in dense HI envelope, and a highly disturbed velocity distribution is observed in the HI envelope, indicating a strong gravitational disturbance on M82.

Tidal disturbance is the strongest when the orbit of M81 around M82 is “direct”, namely when the orbital angular momentum aligns with that of M82. Suppose that an encounter took place in the past and the disturber, M81, is now receding M82. The systemic velocity of M81 is 200 km s^{-1} smaller than that of M82 (Cottrell 1977). From these, and modifying the proposed orbit by Cottrell (1977), we may suppose possible orbits of M81 and M82 as illustrated in Fig. 8.15. If the distance between the two galaxies is about $\sim 60 \text{ kpc}$ ($\sim \sqrt{2}$ times the projected distance) and the recession velocity of M81 from M82 is $\sim 300 \text{ km s}^{-1}$ ($\sim \sqrt{2} \cdot 200 \text{ km s}^{-1}$), the close encounter is considered to have occurred about 2×10^8 years ago. In this case, the orbit of M81 around M82 is direct, while the orbit of M82 around M81 is retrograde and this may be the reason why M81 is not significantly disturbed.

By such a direct tidal disturbance on M82 a bar structure is formed in the central region in a few galactic rotation, or some 10^7 years after the perigalactic passage of M81. The bar structure lasts more than several rotation ($> 10^8$ years), and in this sense the bar is already a self-sustaining structure (Noguchi 1986; Fig. 8.16).

If there exists a non-axisymmetric potential in a disk galaxy, a non-linear response of gas against the potential causes a galactic shock wave (Fujimoto 1968; Roberts 1969). If the potential is much deeper than that for normal spiral density waves, as it is the case for a barred galaxy, the shock along the bar is far stronger, so that the gas loses its angular momentum and kinetic energy quickly (Sorensen et al. 1976; Huntley et al. 1978; Roberts et al. 1979, Fig. 8.17). This results in a rapid inflow of gas toward the central region and makes a dense gaseous core around the nucleus. In fact such a high density core of molecular gas associated with a star burst nature in the nucleus has been found in the barred spiral galaxy, M83 (Handa et al. 1987).

It is likely that the HI gas, which was distributed widely in M82, was accreted by the formation of a bar $\sim 10^8$ years ago triggered by the tidal encounter of M81 $\sim 2 \times 10^8$ years ago. Namely the accretion suddenly began $\sim 10^8$ years ago and formed a dense gaseous core near the center some 10^7 years ago. This triggered the sudden increase in star formation rate and therefore the star burst there.

8.3.4 Trigger of Starburst

The star formation rate (SFR) in a galaxy has been shown to be related to the gas density (Schmidt 1965) through

$$SFR \sim \rho^a . \quad (8.2)$$

From statistics of OB associations, HII regions, and blue light distributions in comparison with the HI and molecular gas distributions, the power a has been estimated as 1~2 (Tosa and Hamajima 1975;

Nakai and Sofue 1984; Young 1987).

In the above formula, velocity dispersion has not been taken into account, which may be an important factor when considering cloud-cloud collision, in particular, in such a highly turbulent region as the nuclear disk of M82. We therefore propose the following modified Schmidt's law for SFR.

$$SFR \sim \rho^a \sigma^b . \quad (8.3)$$

If the frequency of collisions is the major factor, the power b is about unity. If the shock compression in a cloud due to collision, which is proportional to the square of Mach number for an isothermal shock, is taken into account, the power b will be higher. We may take b as between 1 and 3.

In the central region of M82 the average gas density is $\rho \sim 10\text{--}100$ H cm^{-3} and the velocity dispersion $\sigma \sim 50\text{--}100$ km s^{-1} , which are both 5 to 10 times those in normal interstellar space in galaxies. For $a \sim 2$, $b \sim 2$, we obtain SFR about 100 to 1000 times that in normal galaxy disks. Such a high SFR attains within a few 10^7 years triggered by the sudden accretion of gas by a bar.

The high SFR results in a high rate of birth of massive stars (OB stars) which radiate intense UV and optical lights. The lights are absorbed by the dust in molecular clouds, heat them and are re-radiated in the IR emission. The high rate of SN explosions and intense stellar winds from OB stars follow. The energy thus released and injected into the interstellar medium is then transformed to thermal and turbulent (kinetic) energies of the gas, creating high-temperature ionized gas and large-dispersion of the clouds. According to the heat up of gas the pressure increases, which results in compression of gas in the 200-pc ring and in an outflow of gas from the disk (see section 3.2).

The shock compression will result in increases both in the density and collisions. This may further increase the SFR, and more extensive

star formation is triggered. This chain reaction of star formation, or the star burst, will last until the gas clouds in the nuclear disk are all exhausted or blown off from the disk through the galactic wind. In this sense the star burst (chain reacting star formation) is an ensemble of numerous star forming regions where the sequential star formation is proceeding (Elmegreen and Lada 1977).

8.3.5 Unified Scenario of Starburst

We have discussed various mechanisms likely responsible for the star burst in M82 on the basis of observational data and theoretical models. The star burst process may be summarized as in the diagram in Fig. 8.18, and the scenario of star burst can be described as below.

(i) Galaxy-galaxy collision (encounter) causes a strong tidal disturbance in the companion galaxy (M82). The disturbance is stronger when the disturber (M81) is massive and the orbit is "direct" (orbiting in the same sense as the rotation of the disturbed). (ii) The tidal disturbance produces a long standing (self-sustaining) barred structure in the innermost region of the disturbed galaxy. (iii) The barred potential causes a strong galactic shock in the rotating gas, resulting in a rapid accretion into the nuclear region. The accretion creates a dense core in the center of the disk. Coupled with strong vertical magnetic field, the accretion triggers a vertical outflow of cold matter from the disk through the twist of the magnetic lines of force. (iv) The increase in the gas density and turbulent motion in the central region results in a sudden increase of SFR according to the modified Schmidt's law, and new stars are intensively born. (v) UV and optical lights from thus born massive stars are absorbed by dust clouds, heat them, and are reradiated in intense IR emission. (vi) Stellar winds from massive stars and SN explosions excite the interstellar medium to high temperature and highly turbulent state. This results in a rapid expansion of the central region and forms a shock-compressed ring. (vii) According to

the compression in the ring the SFR increases and further star formation is enhanced. Stages (iv) to (vii) are repeated in a chain-reacting way. (viii) When the pressure of heated gas becomes large enough, the upper part of the disk is broken and blown off vertically, and a collimated flow of high temperature gas is formed. The flow is surrounded by the cold (molecular) gas cylinder which was partly accelerated via the magnetic twist by the accretion. (ix) Through the outflowing wind and expansion of the ring in the disk, the central gas is exhausted. As the overall gas density decreases, the SFR decreases and the star burst stops. (x) If the galaxy contains no more gas in the surroundings or no more trigger (stage (i) through (iii)) is expected like as in hyperbolic orbit case of galaxy encounter, the star burst finishes in one time. This type may be called an impulsive star burst (ISB). (xi) If there exists enough gas in the surroundings and if either the galaxy encounter repeats on an elliptical orbits or the bar structure is self-sustaining for longer time, the stages from (i) or (ii) will repeat. This type may be called a recurrent star burst (RSB). (xii) A shorter-period cycle of star burst is also possible, when the gravitational potential of the central region is large so that the gas blown off by a star burst falls down again, as suggested for our galactic center region (Krügel et al. 1983; Loose et al. 1982). This is another type of RSB, or a mini RSB.

M82 has been understood as being in a bursting phase of a RSB galaxy triggered by a cyclic tidal interaction by orbiting around M81. We stressed the importance of a bar, which is often formed by the tidal interaction, to accrete gas and create a high density core of gas for star burst. Since the inclination of the galaxy is finite, $i \sim 82^\circ$, it would be possible to detect a noncircular velocity field produced by such a barred potential. As the projected length of the bar would be \sim one tenth the ring radius, this is possible if we are able to obtain a velocity field map $\sim 1''$ angular resolution. The bar may form through the tidal interaction with M81 and we suggested a possible orbit configuration. A detailed analysis and modeling of the orbit of M81-M82 interacting

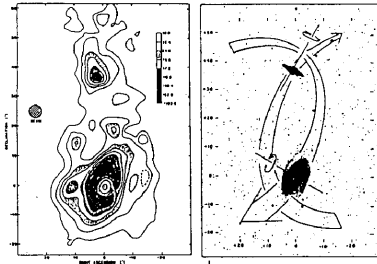


Figure 8.15: HI gas in the M81-M82 system (Gottesman and Weliachew 1977) and a reproduction of the red PSS print. Possible orbits of M81 and M82 are illustrated, in which M82 experiences a “direct” encounter by M81, while M81 is encountered by M82 in a “retrograde” sense.

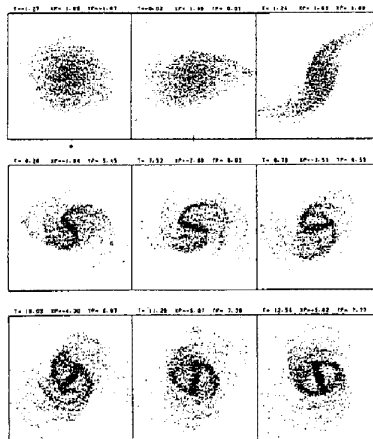


Figure 8.16: Tidal encounter by another galaxy causes a self-sustaining bar in the central region of the disturbed galaxy (see Noguchi 1986).

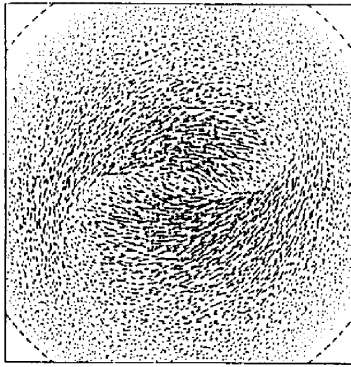


Figure 8.17: Strong shock of gas rotating across a barred potential results in a rapid accretion of gas toward the center (Roberts et al. 1979).

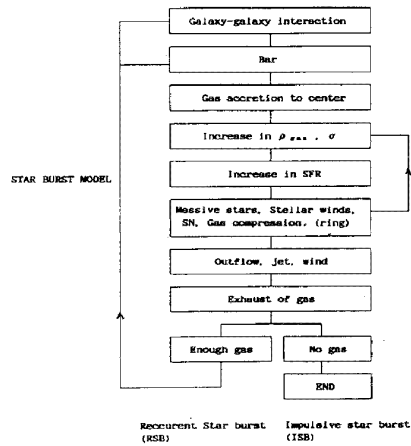


Figure 8.18: Schematic diagram summarizing a possible starburst mechanism.

system are highly desired.

NGC 253 is the second most active star bursting galaxy among the nearby galaxies exhibiting high IR luminosity (Pieke et al. 1980). CO observations at a resolution $\sim 30''$ have shown a high concentration of molecular gas toward the center and a molecular gas ring of radius 3 kpc (Scoville et al. 1985). However, no higher resolution observations have been made so that no detailed distribution of molecular gas in the nuclear disk is known as yet, partly because of the observational difficulty due to its low declination.

Measurements of velocity field in the central region have shown a large noncircular motion indicating a barred structure (Ulrich 1978; Pence 1981). Evidence for outflow of gas from the nuclear region has been obtained by optical and radio emission line measurements (Ulrich 1978; Turner and Ho 1985; McCarthy et al. 1987). X-ray observations (Fabbiano and Trinchieri 1984) show an extended emission asso-

ciated with the nuclear region elongated in the direction perpendicular to the major axis, indicating a vertical outflow of high-temperature gas, similar to the M82 case. All these observations, in particular the high IR luminosity show that the nucleus is active and a star burst is taking place.

Recently a large scale vertical outflow of gas was suggested by a detailed inspection of dust filaments in optical photographs (Sofue 1987): Numerous dark filaments of length more than 1 kpc are running vertically to the major axis in the inner region of radius 2–3 kpc. The vertical filaments are either due to a vertical magnetic field accelerating cold gas from the disk toward the halo, or due to a vertical outflow (or wind) driven by star burst activity in the central 1–2 kpc.

LMC (the Large Magellanic Cloud) composes a close dynamical system with the SMC (Small Magellanic Cloud) and the Galaxy, which are gravitationally interacting each other (Fujimoto and Sofue 1976, 1977; Fujimoto 1984). It was shown that LMC and SMC experienced a close collision some 10^8 years ago (Fujimoto 1984). It is therefore likely that the tidal interaction caused a bar in the central region of LMC, which is really observed. It was also suggested that a burst of star formation occurred some 10^8 years ago triggered by the interaction, which is indeed confirmed by the detection of many blue globular clusters. Such a burst likely results from an accretion of gas from outer region by the bar. In fact we note that LMC and SMC are rich in HI gas and are embedded in an HI envelop.

REFERENCES

References are given for individual chapters. Except for monographs and conference proceedings with titles, key words to each reference are given in square parentheses.

1. INTRODUCTION

- Akabane, K., Kaifu, N., Tabara, H. 1988, *Cosmic Radio Astronomy* (Kyouritsu Publ. Co, Tokyo; in japanese).
- Brown, R. L., Lockman, F. J., Knapp, G. R. 1978, *ARAA* 16, 445. [Recombination lines]
- Gardner, F. F., Whiteoak, J. B 1966, *ARAA* 4, 245. [Polarization]
- Ginzburg, V. L. Syrovatskii, S. I. 1965, *ARAA* 3, 297. [Synchrotron radiation]
- Kraus, J. D. 1966, *Radio Astronomy* (McGraw-Hill Book Co., New York).
- Landau, Lifshitz 1960, *Classical Theory of Field* (Pergamon Press, New York).
- Pacholzyk, A. G. 1977, *Radio Astrophysics* (Pergamon Press).
- Schklovsky, I. S. 1960 *Cosmic Radio Waves*, (Harvard Univ. Press).
- Syrovatskii, S. I., 1981, *ARAA* 19, 163. [Synchrotron emission]
- Vershuur, G. L., K. I. Kellermann, K.I. (ed) 1988, *Galactic and Extragalactic Radio Astronomy* (Springer Verlag, Berlin).

2. INTERSTELLAR MATTER

- Allen, C. W. 1973, *Astrophysical Quantities* (University of London, The Athlone Press, London).
- Arimoto, N., Sofue, Y., Tsujimoto, T. 1995, *ApJ*, submitted. [CO-H₂ Conversion factor]
- Bloemen, J. B. G. M., Strong, A. W., Blitz, L., Cohen, R. S., Dame, T. M., Grabelsky, D. A., Hermsen, W., Lebrun, F., Mayer-Hasselwander, H. A., Thaddeus, P. 1985, *AA*, 154, 25. [CO₀H₂ conversion factor]
- Chandrasekhar, S. 1968, *Hydrodynamic and Hydromagnetic Stability* (Oxford Univ. Press, London).
- de Boer, K. A., Savage, B. D. 1983, *ApJ*, 265, 201. [Ionized gas]
- Dickey, J. M., Lockman, F. J. 1990, *ARAA*, 28, 215. [HI gas]
- Dickman, R. L., Snell, J. S., Young, J. S. (ed) 1988, *Molecular Clouds in the Milky Way and External Galaxies* (Springer-Verlag).
- Downes, D., Goss, W. M., Schwarz, U. J., Wouterloot, J. G. A. 1978, *AAS*, 35, 1. [Continuum sources; Recombination lines]
- Downes, D., Wilson, T. L., Beiging, J., Wink, J. 1980, *AA Suppl.* 40, 379. [ibid]
- Elmegreen, B G 1993, *ApJ* 411, 170. [HI-H₂ transfer]
- Kaplan, S. A, Pikel'ner, S. B. 1974 *ARAA* 12, 113. [ISM]
- Maloney, P., Black, J. H. 1988, *ApJ* 325, 389. [CO-H₂ Conversion factor]
- Maloney, P. M. 1990, in *The Interstellar Medium in Galaxies*, ed. H. A. Thronson & J. M. Shull (Dordrecht, Kluwer), 493. [ibid]
- Mezger, P. G., Pankonin, V., Schmidt-Burke, J., Thum, C., Wink, J. 1979, *AA* 80, L3. [HII regions in Galaxy]
- Shull, J. M., Beckwith, S. 1982, *ARAA* 20, 163. [Interstellar mol. hydrogen]
- Sofue, Y., Honma, M., Arimoto, N. 1994, *AA*, in press. [HI-H₂ in galaxies]
- Spitzer, L. 1962, *Physics of Fully Ionized Gases* (Princeton Univ. Press, Princeton, N.J.).
- Spitzer, L. 1978, *Physical Processes in the Interstellar Medium* (Wiley,

San Fransisco).

Verschuur, G. L. 1975, ARAA, 13, 257. [HI in Galaxy]

Young, J. 1988, in Molecular Clouds in Galaxies and the Milky Way,
eds. R. L. Dickman, R. L. Snell, J. S. Young, Spirnger-Verlag, p.
326. [Molecular gas in galaxies]

3. STAR FORMATION AND DEATH

Akabane, K., H.Hirabayashi, Sofue, Y. 1986 PASJ 38, 775. [W3 in
mm wave]

Akabane, K., Sofue, Y., H.Hirabayashi, M.Morimoto, M.Inoue 1988
PASJ 40, 459. [Sgr B2 in mm wave]

Caswell, J. L. 1988, in Supernova Remnants and the Interstellar Mat-
ter, IAU Col. 101, ed. R. S. Roger , T. L. Landecker (Cambridge
Univ. Press, Cambridge), p. 269. [Radio SNR]

Chevalier, R. A. 1977, ARAA 15, 175. [SNR; ISM]

Clarc, D. H., Caswell, J. L. 1976 MNRAS 174, 267. [SNRs]

Danziger, J., Gorenstein, P. 1983, in Supenova Remnants and their
X-ray Emission, IAU Symp. No. 101, (D. Reidel Pub., Dordrecht)

Elmegreen, B., Lada, C. 1976, AJ 81, 1089. [SF propagation]

Elmegreen, B., Lada, C. 1977, ApJ 214, 725. [SF propagation]

Green, D. A. 1984, MNRAS 209, 449. [SNR statistics]

Green, D. A. 198u6, MNRAS 221, 473. [IC443 radio]

Handa, T., Sofue, Y., W.Reich, E.Fürst, I.Suwa, Y.Fukui 1986 PASJ
38, 361. [10GHz continuum in SF region]

Kennicutt, Jr. R. C. 1989 ApJ 344, 685. [Star formation in galaxies]

Lada, J. 1987, in Star Forming Regions, Peimbert, IAU Col 101, eds.
M., Jugaku, J. (D. Reidel Pub. Co., Dordrecht), p. 1.

Larson, R. B. 1974 MNRAS, 169, 229. [Star formation; mass function]

Manchester, R. N., Taylor, J. H. 1977, Pulsar (W.H.Freedman and
Co.).

- McKee, C. F., Hollenbach, D. J. 1980, ARAA 18, 219. [Interstellar shock]
- Peimbert, M., Jugaku, J. (ed) 1987, Star Forming Regions (D. Reidel Pub. Co., Dordrecht).
- Raymond, J. C. 1984, ARAA 22, 75. [SNRs]
- Reich, W., E.Fürst, Sofue, Y. 1984 AA 133, L4. [Filled center SNR]
- Rieke, G. H., Lebofsky, M. J., Thompson, R. I., Low, F. J., Tokunaga, A. T. 1980, ApJ, 238, 24. [Starburst]
- Roger, R. S., Landecker, T. L. (eds) 1988, Supernova Remnants and the Interstellar Medium, IAU Col. 101 (Cambridge Univ. Press, Cambridge).
- Scalo, J. M. 1986, Fund. Cosmic Phys. 11, 1. [Initial mass function]
- Seiden, P. E., Gerola, H. 1982, Fund. Cosm. Phys., 7, 241. [Stochastic SF]
- Shu, F. H., Adams, F. C., Lizano, S. 1987 ARAA 25, 23. [Star formation]
- Weiler, K. W. 1983, in Supernova remnants and their X-ray Emission, IAU No. 101, eds. J. Danziger and P. Gorenstein (D. Reidel Pub., Dordrecht), p. 299
- Weiler, K. W., Sramek, R. A. 1988, ARAAA 26, 295. [SN; SNR]
- Woodward, P. R. 1978, ARAA 16, 555. [ISM shock; cloud instability]

4. GALACTIC STRUCTURE

- Altenhoff, W. J., Downes, D., Pauls., T., Schraml, J. 1979, AAS, 35, 23. [11-cm radio survey]
- Binney, J. & Tremaine, S. 1987, In Galactic Dynamics, p146 Princeton Univ. Press., New Jersey
- Beichman, C. A., Neugebauer, G., Habing, H. J., Clegg, P. E., Chester, T. J. (ed.) 1985, IRAS Explanatory Supplement 1985, JPL D-1855 (Jet Propulsion Laboratory, Pasadena). [IRAS galactic plane]

- Cleary, M. N., Heiles, C., Haslam, C.G.T. 1979, AAS 36, 95.
- Dame, T. M., Koper, E., Israel, F. P., Thaddeus, P. 1993 ApJ 418, 730. [CO in Galaxy]
- Dame, T. M., Ungerechts, H., Cohen, R. S., de Geus, E. J., Grenier, I. A., May, J., Murphy, D. C., Nyman, L.-A, Thaddeus, P. 1987, ApJ, 322, 706. [ibid]
- Burton, W. B. (ed) 1979, The Large-scale characteristics of the lGalaxy, IAU Symp. No. 84 (D. Reidel, Drodrecht)
- Burton, W. B. 1976, ARAA 14, 275. [HI morphology of Galaxy]
- Burton, W B 1988, in Galactic and Extragalactic Radio Astronomy, ed. G. L. Verschuur, K. I. Kellermann (Springer Verlag, Berlin), pp.295-358. [HI in Galaxy]
- Burton, W. B., Gordon, M. A. 1978, AA 63, 7. [CO, HI rot.curve of MW]
- Burton, W. B., Verschuur, G. L. 1973, A. Ap. S. 12, 145-202. [HI in Galaxy]
- Clemens, D. P. 1985 ApJ 295, 422. [Rotation curve of Galaxy]
- Combes, F. 1992 ARAA, 29, 195. [CO; dynamics of Galaxy]
- Contopoulos, G. & Papayannopoulos, T. 1980, AA, 92, 33. [Galaxy kinematics]
- de Boer, K. A., Savage, B. D. 1983, ApJ, 265, 201. [Halo gas]
- Dickey, J. M., Lockman, F. J. 1990, ARAA, 28, 215. [HI in Galaxy disk]
- Dickman, R. L., Snell, R.L., Young, J. S. (eds) 1988, Molecular Clouds in Galaxies and the Milky Way (Spirnger-Verlag, New York.)
- Fujimoto, M. 1966, in Non-stable Phenomena in Galaxies, IAU Symp. No 29, ed. Arakeljan (Academy of Sciences of Armenia, USSR), p.453.
- Fujimoto, M., Sørensen, S. A., 1977, AA, 60, 251. [Bar; gas]
- Fukunaga, M., Tosa, M. 1991, PASJ, 43, 469. [Gas accretion in disk]
- Georgelin, Y. M., Georgelin, Y. P. 1976, AA 49, 57.
- Handa, T., Sofue, Y., Nakai, N., H.Hirabayashi, M.Inoue 1987 PASJ

- 39, 709. [10 GHz galactic plane survey]
- Haslam, C.G.T., Salter, C.J., Stoffel, H., Wilson, W.E., 1982, AA Suppl. 47, 1. [408 MHz all sky survey]
- Holmberg, E. 1950, Medd Lunds Astr. Obs. Ser. II, 128, 1. [Brightness distribution in galaxies]
- Heiles, C., Habing, H. J. 1974, A. Ap. Suppl. 14, 1-555 [HI at high b]
- Huntley, J. M., Sanders, R. H., Roberts, W. W., 1978, ApJ, 221, 521. [Bar; shock]
- McCammon, D. 1990, ARAA 28, 657. [X-ray of Galaxy]
- Miyamoto, M., Nagai, R. 1975, PASJ, 27, 533. [Galaxy potential]
- Nagai, R., Miyamoto, M. 1976, PASJ, 28, 1. [ibid]
- Noguchi, M. 1987, MNRAS, 228, 635. [Bar; shock]
- Noguchi, M. 1988, AA, 203, 259. [ibid]
- Oort, J. H., Kerr, F. T., Westerhout, G. 1958, MNRAS 118, 379. [HI view of the MW]
- Roberts, W. W. 1969, ApJ 158, 123. [Galactic shock]
- Reich, W., Fürst, E., Steffen, P., Reif, K., Haslam, C. G. T. 1984, AAS, 58, 197 [11-cm galactic plane survey]
- Roberts, W. W., Huntley, J. M., van Albada, G. D. 1979, ApJ, 233, 67. [Bar; shock]
- Rubin, V. C., Ford, W. K., Thonnard, N. 1980, ApJ, 238, 471. [Rotation curves for Sc galaxies]
- Rubin, V. C., Ford, W. K., Thonnard, N. 1982, ApJ, 261, 439. [ibid for Sb]
- Savage, B. D., Mathis, J. S. 1979, ARAA, 17, 73. [Ionized halo gas]
- Saio, H., Yoshii, Y. 1990, ApJ 363, 40. [Exponential disk]
- Sandage, A. 1961, in The Hubble Atlas of Galaxies, Carnegie Institution of Washington, Washington D. C.
- Sandage, A., Tammann, G. A. 1981, A Revised Shapley-Ames Catalog of Bright Galaxies, Carnegie Institution of Washington, Washington, D.C., p.13.
- Shlosman, I., Noguchi, M. 1993, ApJ414, 474. [Bar; shock]

- Sofue, Y. 1995, ApJ submitted. [Rotation curves of galaxies]
- Sørensen, S. -A., Matsuda, T., Fujimoto, M. 1976, Ap. Sp. Sci. , 43, 491. [Bar; shock]
- Toomre, A. 1977 ARAA 15, 437. [Spiral structure]
- van Woerden, H., Allen, R. J., Burton, W.B. (ed) 1985, The Milky Way Galaxy, IAU No. 105 (Reidel Publ. Co., Dordrecht).
- Verschuur, G. L. 1975, ARAA 13, 257. [HI; high-velo. clouds]
- Verschuur, G. L., K. I. Kellermann, K.I. (ed) 1988, Galactic and Extragalactic Radio Astronomy (Springer Verlag, Berlin).
- Wada, K., Habe, A. 1992, MNRAS 258, 82 . [Bar; shock]
- Yoshii, Y., Sommer-Larsen, J. 1989, MNRAS, 236, 779. [Exponential disk]

5. THE GALACTIC CENTER AND ACTIVITY

- Backer, D. (ed) 1987, The Galactic Center (American Inst. Phys. New York)
- Brown, R.L, Liszt, H.S. 1984, ARAA 22, 223. [Gal. Center]
- Burton, W. B., Liszt, H. S. 1978, ApJ, 1225, 815. [ibid]
- Güsten, R. 1989, in The Center of the Galaxy (IAU Symp. 136), ed. M.Morris (D.Reidel Publ. Co., Dordrecht) p. 89. [Molecular gas in GC]
- Güsten, R. 1987, in The Galactic Center, ed. D. Backer (American Inst. Phys. New York), p. 19 [ibid]
- Kaifu, N., Iguchi, T., Kato, T. 1974, PASJ 26, 117. [Expanding mol. ring]
- Kaifu, N., Kato, T., Iguchi, T. 1972, Nature 238, 105. [ibid]
- Koyama, K., Awaki, H., Kunieda, H., et al 1989, Nature 339, 603. [X-ray in GC]
- Liszt, H. S., Burton, W. B. 1978 ApJ 236, 779. [HI in GC]
- Lo, K. Y. 1986, PASP, 98, 179 [Radio continuum in GC]

- Lo, K. Y. 1987, in *The Galactic Center*, ed. D. Backer (American Inst. Phys. New York), p. 30 [ibid]
- Mezger, P. G., Pauls, T. 1979, in *The Large-scale characteristics of the Galaxy*, IAU Symp. No. 84, ed. W. B. Burton (D. Reidel, Dordrecht), p. 357 [SF in GC]
- Morris, M. (ed) 1989, *The Center of the Galaxy* (IAU Symp. 136),
- Morris, M. (ed) 1989, in *The Center of the Galaxy*, IAU Symp. 136 (D.Reidel Publ. Co., Dordrecht). [Radio; magnetic field in GC]
- Morris, M., Yusef-Zadeh, F. 1985, *AJ*, 90, 2511 [ibid]
- Oort, J. 1977, *ARAA* 15, 295. [Review of GC region]
- Oort, J. H. 1986, in *The Milky Way Galaxy*, IAU No. 105, eds. H. van Woerden et al (D. Reidel Pub., Dordrecht), p. 349 [ibid]
- Pauls, T., Downes, D., Mezger, P. G., Churchwell, W. 1976, *AA*, 46, 407. [Radio sources in GC]
- Reich, W., Sofue, Y., E.Fürst 1987 *PASJ* 39, 573. [Radio vs FIR in GC]
- Reich, W., Sofue, Y., R.Wielebinski, J.H.Seiradakis 1988 *AA* 191, 303. [Radio Spectra in GC]
- Reid, M. 1993, *ARAA* 31, 345. [Gal. cen. distance]
- Scoville, N. Z. 1972, *ApJ*, 175, L127 [Expanding ring]
- Serabyn, E., Güsten, R. 1986, *AA*, 161, 334 [IR in GC]
- Serabyn, E., Lacy, J. H. 1985, *AA*, 293, 445 [ibid]
- Sofue, Y., Handa, T. 1984 *Nature* 310, 568. [GC radio lobe]
- Sofue, Y. 1985 *PASJ* 37, 697. [ibid]
- Sofue, Y. 1984 *PASJ* 36, 539. [Shock from GC]
- Sofue, Y., W.Reich, P.Reich 1989 *ApJ* 341, L47. [Jet from GC]
- Sofue, Y. 1990 *PASJ* 42, 827. [CO vs radio continuum in GC]
- Sofue, Y., Murata, Y., Reich, W. 1992, *PASJ*, 44, 367. [Radio arc in mm wave]
- Sofue, Y., 1994, *ApJ*, 431, L91. [Shock from GC]
- Sofue, Y. 1994, *PASJ* submitted [Molecular arms in GC]
- Tsuboi, M., Inoue, M., Handa, T., Tabara, H., Kato, T., 1985, *PASJ*,

- 37, 359. [Polarization; magnetic field in GC]
- M.Tsuboi, M.Inoue, Handa, T., H.Tabara, T.Kato, Sofue, Y., N.Kaifu
1986 AJ 92, 818. [ibid]
- Uchida, Y., Shibata, K. 1986, PASJ, 38, [Jet mechanism]
- Uchida, Y., K.Shibata, Sofue, Y. 1985 Nature 317, 699. [ibid]
- Wrixon, G. T., Sanders, R. H. 1973, A. Ap. Suppl. 11, 339. [HI in
GC]
- Yusef-Zadeh, F., Morris, M., Chance, D. 1984, Nature, 310, 557.
[VLA radio map; magnetic field in GC]
- Yusef-Zadeh, F., Morris, M. 1987, AJ, 94, 1128. [ibid]
- Yusef-Zadeh, F., Morris, M., Slee, O. B., Nelson, G. J. 1986, ApJ,
310, 689. [ibid]
- Yusef-Zadeh, F., Morris, M., Slee, O. B., Nelson, G. J. 1986, ApJ,
300, L47. [ibid]

6. NONTHERMAL EMISSION AND MAGNETIC FIELDS

- Axon, D. J., Taylor, K. 1978, Nature 274, 37. [Star polarization]
- Beck, R., Gräve, R. (ed) 1987, Interstellar Magnetic Fields (Springer
Verlag, Heidelberg).
- Chandrasekhar, S. 1968, Hydrodynamic and Hydromagnetic Stability
(Oxford Univ. Press, London), Chap. X, XI.
- Ford, H. C., et al. 1985, ApJ, 293, 132. [Star polarization]
- Ford, H. C., Crane, P. C., Jacoby, G. H., Lawrie, D. G., van der Hulst,
J. M. 1985, ApJ, 293, 132. [Star polarization]
- Fujimoto, M., Tosa, M. 1980, PASJ, 32, 567 [Magnetic field in M51]
- Gardner, F. F., Whiteoak, J. B 1966, ARAA 4, 245. [Polarization]
- Ginzburg, V. L. Syrovatskii, S. I. 1965, ARAA 3, 297. [Synchrotron
radiation]
- Heiles, C. 1976 ARAA 14, 1. [Interstellar mag. field]
- Parker, E. N. 1972, ApJ, 163, 255. [Dynamo]

- Parker, E. N. 1979, *Cosmical Magnetic fields* (Oxford Univ. Press).
- Sawa, T., Fujimoto, M. 1986, *PASJ*, 38, 133. [Spiral magnetic field]
- Sofue, Y., Fujimoto, M., Kawabata, K. 1979 *PASJ* 31, 125. [Inter-galactic magnetic field]
- Sofue, Y., Fujimoto, M., Wielebinski, R. 1986 *ARAA* 24, 459. [Magnetic field in galaxies]
- Sofue, Y., W.Reich, M.Inoue, J.H.Seiradakis 1987 *PASJ* 39, 95. [Magnetic field in GC]
- Syrovatskii, S. I., 1981, *ARAA* 19, 163. [Synchrotron radio emission]
- Verschuur, G. L. 1975, *ARAA*, 13, 257. [Interstellar magnetic field]
- Yusef-Zadeh, F., Morris, M., Chance, D. 1984, *Nature*, 310, 557 [Magnetic field in GC]

7. HI AND CO IN GALAXIES

- Aaronson, M., Bothun, G., Mould, J., Huchra, J., Shommer, R. A., Cornell, M. E. 1986, *ApJ*, 302, 536. [TFR (Tully-Fiser relation) in H band]
- Allen et al. 1986, *Nat*, 319, 296. [HI in M83]
- Allen, R. J., Baldwin, J. E., Saicisi, R. 1978, *AA*, 62, 397. [Radio in Galaxies]
- Arimoto, N., Yoshii, Y. 1986, *AA*, 164, 260. [Galaxy evolution]
- Arimoto, N., Sofue, Y., Tsujimoto, T. 1995, *ApJ*, submitted. [CO-H₂ Conversion factor]
- Arp, H. C. 1966, *Atlas of Peculiar Galaxies* (California Institute of Technology, Pasadena).
- Arp, H. C., Madore, B. F. 1987 *A Catalogue of Southern Peculiar Galaxies and Associations*, Vol. II (Cambridge Univ. Press, Cambridge).
- Athanasoula, E. (ed) 1983, *Internal Kinematics and Dynamics of Galaxies*, IAU Symp. No. 100, (D. Reidel Publ. Co., Dordrecht).

- Bajaja E., van den Burg G., Faber S. M., et al., 1984, AA 141, 309
[HI in M31]
- Bajaja E., Krause M., Dettmar R.-J., Wielebinski R., 1991, AA 241,
411 [ibid]
- Ball, R., Sargent, A. I., Scoville, N. Z., Lo, K. Y., Scott, S. L. 1987,
ApJ, 298, L21. [CO in IC342]
- Barnes, J. E. 1989, Nat, 338, 123. [Galaxy merger]
- Bosma, A. 1981, AJ, 86, 1791. [HI in galaxies]
- Bosma, A. 1981, AJ, 86, 1825. [ibid, velocity fields]
- Bosma, A. H. 1980, AAS, 41, 189. [HI in galaxies]
- Bosma, A., van der Hulst, J. M., Sullivan, W. T., 1977, AA, 57, 373.
[ibid]
- Bothun, G. D., Aaronson, M., Shommer, B., Mould, J., Huchra, J.,
Sullivant III, W. T. 1985, ApJS, 57, 423. [TFR]
- Bottinelli, L., Gouguenheim, L., Fouqué, P., Paturel, G. 1990, AAS,
82, 391. [HI catalog for TFR]
- Braine, J., Combes, F., Casoli, F., Durpaz, C., Gerin, M., Klein, U.,
Wielebinski, R., Brouillet, N. 1993, AAS, 97, 887. [CO in galaxies]
- Braine, J., & Combes, F. 1992, AA, 264, 433. [CO in galaxies]
- Brinks, E., Bajaja, E. 1986, AA, 169, 14. [HI in M31]
- Brinks, E., Shane, W. W. 1984, AA, 55, 179. [ibid]
- Canzian, B., Mundy, L. G., Scoville, N. Z. 1988, ApJ, 333, 157. [CO
bar in NGC 253]
- Casertano, S. 1983, MNRAS, 203, 735. [HI in N5907]
- Casoli, F., Clausset, F., Viallefond, F., Combes, F., Boulanger, F.
1990, AA 233, 357. [CO in NGC 6946]
- Casoli, F., Viallefond, F., Combes, F., & Boulanger, F. 1990, AA, 233,
357 [CO in M31]
- Casoli, F., et al. 1992, AA, 264, 55 [ibid]
- Claussen, M. J., & Lo, K. Y. 1986, ApJ, 308, 592. [CO in IC 342]
- Combes, F. 1988, in Galactic and Extragalactic Star Formation, edited
by R.E. Pudritz and M. Fich (Kluwer, Dordrecht), p. 475 [CO in

- galaxies; dynamics]
- Combes, F., Cassoli, F. (de) 1990, Dynamics of Galaxies and Molecular Clouds Distribution, IAU Symp. 146 (Kluwer Academic Publishers, Dordrecht).
- Combes, F., Gottesman, S. T., Weliachew, L. 1977 AA 59, 181 [HI in M82-81 system]
- Condon, J. J. 1992, ARAA 32, 575. [Radio emission from galaxies]
- Cram et al. 1980, AAS, 40, 215. [HI in M31]
- Dahlem, M., Salto, S., Klein, U., Booth, R., Mebold, U., Wielebinski, R., Lesch, H. 1990, AA, 240, 237. [CO in NGC 1808]
- de Vaucouleurs G., de Vaucouleurs A., Corwin H. G. Jr., et al., 1991, in Third Reference Catalogue of Bright Galaxies (New York Springer Verlag)
- Dickey, J. M., Kazès, I. 1992, ApJ, 393, 530. [CO TFR]
- Dickman, R. L., Snell, J. S., Young, J. S. (ed) 1988, Molecular Clouds in the Milky Way and External Galaxies (Springer-Verlag).
- Duric, N., Seaquist, E. R., Crane, P. C., Bignell, R. C., Davis, L. E., 1983, ApJ, 273, L11. [Radio lobe in NGC 3079]
- Duric, N., Seaquist, E. R. 1988, ApJ, 326, 574. [ibid]
- Ekers, R. D., Sancisi, R. 1977, AA, 54, 973. [Radio in edge-on galaxies]
- Ekers, R. D., van Gorkom, J. H., Schwarz, U. J., Goss, W. M. 1983, AA, 122, 143 [ibid]
- Emerson et al. 1976, MNRAS, 176, 321. [HI in M31]
- Ferrini, et al 1991, in The Interstellar Disk-Halo Connection in Galaxies, IAU Symp 144, ed. J. B. G. M. Bloemen (Kluwer, Dordrecht), p. 397. [Dust in galaxy halo]
- Foqué, P., Bottinelli, L., Gouguenheim, L., Paturel, G. 1990, ApJ, 349, 1. [HI TFR]
- Fujimoto, M., Sofue, Y. 1976 AA 47, 263. [LMC-SMC-Galaxy; Magellanic Stream]
- Fujimoto, M., Sofue, Y. 1977 AA61, 199. [ibid]

- Fukugita, M., Okamura, S., Tarusawa, K., Rood, H. J., Williams, B. A. 1991, *ApJ*, 376, 8. [B-band TFR]
- Garcia-Rurillo, A., Guélin, M., Cernicharo, J. 1993, *AA*, 274, 123. [CO in M51]
- Garcia-Burillo, S., Guélin, M., Cernicharo, J., Dahlem, M. 1992, *AA*, 266, 210. [CO in NGC 891]
- Giovanelli, R., Haynes, P. 1988, in *Galactic and Extragalactic Radio Astronomy*, ed. G. L. Verschuur, K. I. Kellermann (Springer Verlag, Berlin), pp.522-562. [HI in galaxies]
- Gottesman, S. T., Weliachew, L. 1977, *ApJ* 211, 47. [HI in M82-M81]
- Habing, H. J., Miley, G., Young, E., Baud, N, Bogges, N., Clegg, P. E., de Jong, T., Harris, S., Raimond, E., Rowan-Robinson, M., Soifer, B. T. 1984, *ApJ*, 278, L59. [IRAS images of M31]
- Handa, T., Nakai, N., Sofue, Y., M. Hayashi, Fujimoto, M. 1990 *PASJ* 42, 1. [CO in M83]
- Haynes, M. P., Giovanelli, R., Chincarini, G. L., 1984 *ARAA* 22, 445. [HI; galaxies]
- Haynes, M. P., Giovanelli, R., Roberts, M. S. 1979, *ApJ*, 229, 83. [HI in galaxies]
- Heckman, T. M., van Breugel, W., Miley G. K., & Butcher, H. R. 1983, *AJ*, 88, 1077. [Gas outflow from starburst galaxies]
- Heckman et al 1989, *ApJ* 342, 736 [Seyfert galaxies]
- Helou, G., Kahn., I. R., Malek, L., & Boehmer, L. 1989, *ApJS*, 68, 151. [IRAS galaxies]
- Holmberg, E. 1950, *Medd Lunds Astr. Obs. Ser. II*, 128, 1 [Galaxy brightness distribution]
- Hodge, P. W. 1966, *Atlas and Catalog of HII regions in M31* (Univ. of Washington, Seattle)
- Huchtmeier, W., K., Richter, O. -G. 1989 *General Catalog of HI Observations of Galaxies* (Springer-Verlag, Heidelberg)
- Hummel, E., Kotanyi, G. G., van Gorkom, J. H. 1983, *ApJ*, 267, L5 [Radio from edge-on galaxies]

- Hummel, E., Sancisi, R., Ekers, R. D. 1984, AA, 133, 1. [Radio from galaxies]
- Hummel, E., van der Hulst, J. M., Keel, W. C., & Kennicutt, R. C. 1987, AAS, 70, 517. [ibid]
- Irwin, J. A., Seaquist, E. R. 1988, ApJ, 335, 658. [Lobes from NGC 3079]
- Irwin, J. A., Seaquist, E. R. 1991 ApJ 371, 111. [ibid]
- Ishiguro, M., Kawabe, R., Morita, K. -I., et al 1989, ApJ, 344, 763. [CO in Maffey 2]
- Ishizuki, S. Kawabe, R., Ishiguro, M., Okumura, S. K., Morita, K. -I., Chikada, Y., Kasuga, T. 1990a, Nature 344, 224. [CO in IC342]
- Ishizuki, S., Kawabe, R., Ishiguro, M., Okumura, S. K., Morita, K. -I., Chikada, Y., Kasuga, T., Doi, M. 1990b ApJ 355, 436 [CO in GC N6946]
- Kaneko, N., Morita, K., Fukui, Y., et al 1989, ApJ, 337, 691. [CO in NGC N1068]
- Kawara, K., Nishida, M., Phillips, M. M. 1989, ApJ, 337, 290. [Excitation in galaxy nuclei]
- Keel, W. C., Kennicutt, Jr. R. C., Hummel, E., van der Hulst, J. M. 1985, AJ, 90, 708. [Galaxy interaction]
- Kennicutt, Jr. R. C. 1989 ApJ 344, 685. [SF in galaxy disks]
- Kenney, J., Young, S. J. 1988 ApJS 66, 261. [CO in Virgo galaxies]
- Koper, E., Dame, T. M., Israel, F. P., Thaddeus, P. 1991, ApJ, 383, L11. [CO in M31]
- Koribalski, B., Dickey, J. M., Mebold, U. 1993, ApJL 402, L41. [HI in NGC 1808]
- Kuno, N., Nakai, N., Handa, T., Sofue, Y. 1995, PASJ submitted. [CO in M51]
- Lada, C., M.Margulis, Sofue, Y., Nakai, N., Handa, T. 1987 ApJ 328, 142. [CO; HI in M31 arm]
- Laustsen, S., Madsen, C., West, R. M. 1987, in Exploring the Southern Sky, Springer-Verlag, Heidelberg, p.31.

- Lo, K. Y., Ball, R., Masson, C. R., Phillips, T. G., Scott, S., Woody, D. P. 1987, *ApJ*, 317, L63. [CO in M51]
- Lo, K. Y., Berge, G. L., Claussen, M. J., Hieligman, G. M., Leighton, R. B., Masson, C. R., Moffet, J. 1984, *ApJ*, 282, L59. [CO in M82]
- Loiseau, N., Nakai, N., Sofue, Y., R.Wielebinski, H-P.Reuter, U.Klein 1990 AA 228, 331. [CO(2-1) in M82]
- Lonsdale, C. J., Helou, G., Good, J. C., Rice, W. L. 1985, *Catalogued Galaxies and Quasars Observed in the IRAS Survey*, US Government Printing Office, Washington, D. C. .
- Lynds, C. R., Sandage, A. R. 1963, *ApJ* 137, 1005. [M82]
- Mathewson, D. S., Cleary, M. N., Murray, J. D. 1974, *ApJ*, 190, 291. [HI Magellanic Stream]
- Mathewson, D. S., Schwarz, M. P., Murray, J. D. 1977, *ApJ*, 217, L5. [ibid]
- Mathewson, D. S., Ford, V. L., Buchhorn, M. 1992, *ApJS*, 81, 413. [HI and rotation curves]
- Mirabel I. F., Sanders D. B., 1988, *ApJ* 335, 104. [CO in starburst galaxies]
- Murai T., Fujimoto M. 1980, *PASJ* 32, 581 [Magellanic Stream]
- Nakai, N., Sofue, Y. 1982 *PASJ* 34, 199. [SF rate in M31]
- Nakai, N., M.Hayashi, Handa, T., Sofue, Y., T.Hasegawa, M.Sasaki 1987 *PASJ* 39, 685. [CO in M82]
- Nakai, N., Kuno, N., Handa, T., Sofue, Y. 1994, *PASJ* 46, 527. [CO in M51]
- Persic, M., Salucci, P. 1995, *ApJS* in press [Rotation curves]
- Pierce, M. J., Tully, R. B. 1988, *ApJ*, 330, 579. [TFR]
- Rickard, L. J., Palmer, P., Morris, M., Zuckerman, B., Turner, B. E. 1975, *ApJ* 199, L75. [CO in galaxies]
- Rieke, G. H., Lebofsky, M. J., Thompson, R. I., Low, F. J., Tokunaga, A. T. 1980, *ApJ*, 238, 24. [Starburst galaxies]
- Roberts, M. S., Whitehurst, R. N., 1975, *AJ*, 26, 483. [HI in M31]

- Rogstad, D. H., Shostak, G. S. 1972, ApJ. 220, L37. [HI in IC 342, NGC 6946]
- Rots, A., 1980, AAS, 41, 189. [HI in galaxies]
- Rots, A. H., Bosma, A., van der Hulst, J. M., Athanassoula, E., Crane, P. C. 1990, AJ, 100, 387. [HI in M51]
- Rubin, V. C., Burstein, D., Ford, W. K., Thonnard, N. 1985, ApJ, 289, 81. [Rotation curves]
- Rubin, V. C., Ford, W. K., Thonnard, N. 1980, ApJ, 238, 471. [ibid for Sc]
- Rubin, V. C., Ford, W. K., Thonnard, N. 1982, ApJ, 261, 439. [ibid for 23Sb]
- Rupen, M. P., 1991, AJ, 102, 48. [HI in NGC 891, NGC 4565]
- Sage, L. J., Solomon, P. M. 1991 ApJ 380, 392. [CO in IC342]
- Saikia, D. J., Unger, S. W., Pedlar, A., et al. 1990, MNRAS, 245, 397. [HI in NGC 1808]
- Sancisi, R. 1976, AA 53, 159. [Radio in edge-on galaxies]
- Sancisi, R., Allen, R. J. 1979, AA, 74, 73. [ibid]
- Sancisi, R., Thonnard, N., Ekers, R. D. 1987, ApJ, 315, L39. [ibid]
- Sandage, A. 1961, in The Hubble Atlas of Galaxies, Carnegie Institution of Washington, Washington D. C.
- Sandage, A., Tammann, G. A. 1981, A Revised Shapley-Ames Catalog of Bright Galaxies, Carnegie Institution of Washington, Washington, D.C., p.13.
- Sanders, D. B., Solomon, P. M., Scoville, N. Z. 1984, ApJ, 276, 182. [CO in FIR luminous galaxies]
- Sanders et al 1988, ApJ 325, 74 [FIR galaxies - QSO]
- Sanders D. B., Mirabel I. F., 1985, ApJ 298, L31. [ibid]
- Sanders D. B., Young J. S., Scoville N. Z., et al., 1987, ApJ 312, L5 [ibid]
- Sanders, D. B., Scoville, N. A., Young, J. S., Soifer, B. T., Schloerb, F. P., Rice, W. L., Danielson, G. e., 1986, ApJ, 305, L45. [ibid]
- Sargent, A. I., Welch, W. J. 1993, ARAA 31, 297. [mm-wave images]

- of galaxies]
- Scoville N. Z., Young J. S., 1983, ApJ 265, 148. [CO in galaxies]
- Scoville N. Z., Young J. S., Lucy L. B., 1983, ApJ 270, 443. [CO in galaxies]
- Scoville, N. Z., Soifer, B. T., Neugebauer, G., Young, J. S., Mattheus, K., Yeka, J. 1985, ApJ., 289, 129. [CO in NGC 253]
- Scoville, N. Z., Thakker, D., Carlstrom, J. E., Sargent, A. E., 1993 ApJL 404 L63. [CO in NGC N891]
- Shostak G. S., 1978, AA 68, 321. [HI in galaxies; warping]
- Sofue, Y., T.Kato 1980 PASJ 33, 449. [HI in M31]
- Sofue, Y. 1987 in Galactic and Extragalactic Star Formation, ed. R.Pudritz, D.Reidel Publ. Co., pp.409-438. [Starburst in M82]
- Sofue, Y., M.DoI, S.Ishizuki, Nakai, N., Handa, T. 1988 PASJ 40, 511. [CO in NGC 6946]
- Sofue, Y., Reuter, H.-P., Krause, M., Wielebinski, R., Nakai, N. 1992, ApJ, 395, 126. [CO(2-1) in M82]
- Sofue, Y., Irwin, J. A. 1992, PASJ, 44, 353. [CO in NGC 3079]
- Sofue, Y. 1992, PASJ, 44, L231. [CO TFR]
- Sofue, Y., Wakamatsu, K., Taniguchi, Y., Nakai, N. 1993, PASJ, 45. [CO in Arp galaxies]
- Sofue, Y., Wakamatsu, K. 1993, PASJ, 45, 529. [CO in ellipticals]
- Sofue, Y., Honma, M., Arimoto, N. 1994, AA, in press [HI-H₂ transition; Molecular front]
- Sofue, Y. 1995, ApJ submitted. [Rotation curves]
- Sofue, Y., Nakai, N. 1993, PASJ 45, 139. [CO in NGC N891]
- Solomon, P. M., Sage, L. J. 1988, ApJ, 334, 613. [CO in interacting galaxies]
- Sukumar, S., Allen, R. J. 1991, ApJ, 382,100. [Radio continuum in NGC 891]
- Tacconi, R., Young, J. S. 1986, ApJ 308, 600. [HI in NGC 6946]
- Telesco, C. M. 1988, ARAA, 26, 343. [Starburst]
- Thronson, H. A, Jr. et al. 1989, ApJ, 344, 747. [S0/Sa galaxies]

- Tully, R. B. 1974, *ApJ.S.* 27, 437. [$H\alpha$ in M51]
- Tully, R. B. 1987, *Catalog of Nearby Galaxies* (Cambridge Univ. Press, Cambridge)
- Tully B., Fisher J. R., 1977, *AA* 64, 661. [TFR]
- Tully B., Fouqué P., 1985, *ApJS* 58, 67. [TFR]
- Unwin, S. C. 1980, *MNRAS*, 192, 243. [HI in M31]
- van Albada, R. D. 1980, *AA Suppl.* 39, 283. [Radio; HI in NGC N4258]
- van den Bergh, S. 1989, *AA Rev.* 1, 1111. [Cosmological distances]
- van der Kruit, P. C., Allen, R. J. 1976, *ARAA* 14, 417. [Galaxies in radio continuum]
- van der Kruit, P. C., Allen, R. J. 1978, *ARAA* 16, 417. [Kinematics of galaxies]
- van Gorkom, J. H., Knapp, G. R., Ekers, R. D., Ekers, D. D., Laing, R. A., and Polk, K. S. 1991, *AJ*, 97, 708. [Radio from ellipticals]
- Véron-Cetty, M. -P., Véron, P. 1985, *AA*, 145, 425. [Outflow galaxy NGC 1808]
- Vogel, S., N., Boulanger, F., Ball, R. 1987, *ApJ*, 321, L145. [CO in M31 arm]
- Wainscoat, R. J., de Jong, T., Wesselius, P. R. 1987, *AA*, 181, 225. [IRAS galaxies]
- Weliachew, I., Casoli, F., Combes, F. 1988, *AA*, 199, 29. [HI in NGC 6946; Maffey 2]
- Weliachew, L., Sancisi, R., Guélin, M., 1978, *AA*, 65, 37. [???
- Weliachew, L., Fomalont, E. B., Greisen, E. W. 1984, *AA*, 137, 335 [???
- Wiklind, T., Rydbeck, G. 1986, *AA*, 164, L22. [Molecular gas in ellipticals]
- Wilson, C., D., Scoville, N. 1990, *ApJ* 363, 435. [CO in M31]
- Wilson, C., D., Scoville, N. 1992, *ApJ* 385, 512. [CO in M33]
- Young, J. 1988, in *Molecular Clouds in Galaxies and the Milky Way*, eds. R. L. Dickman, R. L. Snell, J. S. Young, Springer-Verlag, p.

326. [Molecular clouds in galaxies]
- Young, J. S., Kenney, J. D., Tacconi, L., Claussen, M. J., Huang, Y.-L., Tacconi-Garman, L., Xie, S., Schloerb, F. P., ApJ, 311, L21.
[ibid]
- Young, J. S., Claussen, M. J., Scoville, N. Z. 1988, ApJ, 324, 115.
[ibid]
- Young, J. S., Scoville, N. 1982, ApJ, 258, 467. [ibid]
- Young J. S., Scoville, N. Z., 1984, ApJ 287, 153 [ibid]
- Young, J S , Scoville, N Z 1992, ARAA, 29, 581. [ibid, review]
- Young J. S., Tacconi L. J., Scoville N. Z., 1983, ApJ 269, 136 [CO in M83]

8. STARBURST

- Axon, D.J., and Taylor, K. 1978, Nature, 274,37.
- BeckKlin, 1987, in this volume.
- Bingham, R.G., McMullan, D., Pallister, W.S., White, C., Axon, D.J., and Scarrott, S.M. 1976, Nature, 259, 463.
- Burbidge, E.M., Burbidge, G.R., and Rubin, V.C. 1964, ApJ, 140, 942.
- Carlstrom, 1987, in this volume.
- Chevalier, R.A. 1974, Astrophys. J., 188, 501.
- Chevalier, R.A., and Clegg, A.W. 1985, Nature, 317, 44.
- Combes, F. 1987, in this volume.
- Condon, F., and Gerin, M. 1985, ApJS, 53, 459.
- Cottrell, G.A. 1977, MNRAS, 178, 577.
- Crutcher, R.M., Rogstad, D.H., and Chu, K. 1978, ApJ, 225, 784.
- de Vaucouleurs, G., and de Vaucouleurs, A. 1964, Reference Catalogue of Bright Galaxies (Universiry of Texas Press, Austin).
- Elmegreen, B. G., and Lada, C.J. 1977, ApJ, 214, 725.
- Fabbiano, G., and Trinchieri, 1984, ApJ, 286, 491.

- Fazio, G.G. 1978, in *Infrared Astronomy*. eds. G. Setti and G.G. Fazio (D. Reidel Publ. Co., Dordrecht), p.25.
- Fujimoto, M. 1968, in *Nonstable Phenomena in Galaxies*, IAU Symp. No. 29, ed. M. Arakeljan (Armenian Academy of Sci., Yerevan), p.453.
- Fujimoto, M. 1984, in *Structure and Evolution of the Magellanic Clouds*, IAU Symp. No.108, eds. S. van den Bergh and K.S. de Boer (D. Reidel Publ. Co., Dordrecht), p.115.
- Fujimoto, M., and Sofue, Y. 1976, *A&A*, 47, 263.
- Fujimoto, M., and Sofue, Y. 1977, *A&A*, 61, 199.
- Gottesman, S.T., and Weliachew, L. 1977, *ApJ*, 211,47.
- Hargraves, 1974, *MNRAS*, 168, 491.
- Holmberg, E. 1950, *Medd Lunds astr. Obs. Ser.* 11, Vol. 128, 1.
- Huntley, J.M., Sanders, R.H., and Roberts, W.W. 1978, *ApJ*, 221, 521.
- Kronberg, P.P. 1987, in this volume.
- Kronberg, P.P., Biermann, P., and Schwab, F.R. 1981, *ApJ*, 246, 751.
- Kronberg, P.P., Biermann, P., and Schwab, F.R. 1985, *ApJ*, 291, 693.
- Krügel, E., Tutukov, A., and Loose, H. 1983, *A&A*, 124, 89.
- Lo, K.Y. 1987, in *Star Formation in Galaxies*, NASA Conf Pub. 2466, ed. C.J.L. Persson (NASA Office of Space Sci. Appl., Washington, D.C.), p.367.
- Lo, K.Y., Cheung, K.W., Masson, C.R., Phillips, T.G., Scott, S.L., and Woody, D.P. 1987, *ApJ*, 312, 574.
- Loose, H.H., Krügel, E., and Tutukov, A. 1982, *A&A*, 105, 342.
- Louiseau, N., Nakai, N., Klein, U., Wielebinski, R., and Sofue, Y. 1987, in preparation.
- Lugten, J.B., Watson, D.M., Crawford, M.K., and Genzel, R. 1986, preprint
- Lynds, C.R., and Sandage, A.R. 1963, *ApJ*, 137, 1005.
- McCarthy, P.J., Heckman, T., and van Breugel, W. 1987, *AJ*, 92, 264.
- Morris, M., and Rickard, L.J. 1982, *ARAA*, 20, 517.
- Nakai, N. 1985, Ph. D. Thesis, Univ. of Tokyo.

- Nakai, N. 1987, private communication.
- Nakai, N., Hayashi, M., Handa, T., Sofue, Y., Hasegawa, T., and Sasaki, M. 1986, PASJ, 38, 185.
- Nakai, N., Hayashi, M., Handa, T., Sofue, Y., Hasagawa, T., and Sasaki, M. 1987, PASJ, in press.
- Nakai, N., and Sofue, Y. 1984, PASJ, 36, 313.
- Noguchi, M. 1986, MNRAS, submitted.
- O'Connell, R.W., and Mangano, J.J. 1978, ApJ, 221, 62.
- Olofsson, H., and Rydbeck, G. 1984, A&A, 136, 17.
- Pence, W.D., 1981, ApJ, 247, 473.
- Prendergast, K.M. 1983, in Internal Kinematics and Dynamics of Galaxies, IAU Symp. No.100, ed. E. Athanassoula (D. Reidel Publ. Co., Dordrecht), p.215.
- Rickard, L.J., Palmer, P., Morris, M., Zuckerman, B., and Turner, B.E. 1975, ApJL, 199, L75.
- Rieke, G.H., Lebofsky, M.J., Thompson, R.I., Low, F.J., and Tokunaga, A.T. 1980, ApJ, 238, 24.
- Roberts, W.W., Jr. 1969, ApJ, 158, 123.
- Roberts, W.W., Jr., Huntley, J.M., and van Albada, G.D. 1979, ApJ, 233, 67.
- Sakashita, S. 1971, ApSS, 14, 431.
- Sandage, A. 1961, The Hubble Atlas of Galaxies (Carnegie Institution of Washington, Washington, D.C.), p.41.
- Schmidt, G.D., Angel, J.R.P., and Cromwell, R.H. 1976, ApJ, 206, 888.
- Schmidt, M. 1965, in Galactic Structure, eds. A. Blaauw and M. Schmidt (Univ. Chicago Press, Chicago), chap. 22, p.513.
- Scoville, N.Z., Soifer, B.T., Neugebauer, G., Young, J.S., Matthews, K., and Yerke, J. 1985, ApJ, 289, 129.
- Sofue, Y. 1977, A&A, 60, 327.
- Sofue, Y. 1984, PASJ, 36, 539.
- Sofue, Y. 1987, PASJ, 39, No.4, in press.

- Sofue, Y., and Fujimoto, M. 1987, PASJ, in press.
- Solomon, P.M., and de Zafra, R. 1975, ApJL, 199, L79.
- Sorensen, S.-A., Matsuda, T., and Fujimoto, M. 1976, APSS, 43, 491.
- Sutton, E.C., Masson, C.R., and Phillips, T.G. 1983, APJL, 275, L49.
- Tammann, G.A., and Sandage, A. 1968, ApJ, 151, 825.
- Telesco, C.M., and Harper, D.A. 1980, ApJ, 235, 392.
- Thronson, H.A., Jr., and Harper, D.A. 1979, ApJ, 230, 133.
- Tomisaka, K. 1987, in this volume.
- Tomisaka, K., and Ikeuchi, S. 1987, preprint.
- Tosa, M., and Hamajima, K. 1975, PASJ, 27, 501.
- Turner, J.L., and Ho, P.T.P. 1985, APJL, 299, L77.
- Uchida, Y., and Shibata, K. 1986, PASJ, 38, 631.
- Ulrich, M.-E. 1978, ApJ, 219, 424.
- Umemura, S., Iki, K., Shibata, K., Nakai, N., and Sofue, Y. 1987, PASJ, submitted.
- Visvanathan, N., and Sandage, A. 1972, ApJ, 176, 57.
- Watson, M.G., Stanger, V., and Griffiths, R.E. 1984, ApJ, 286, 144.
- Weliachew, L., Fomalont, E.B., and Greisen, E.W. 1984, A&A, 137, 335.
- Wheeler, J.C., Mazurek, T.J., and Sivaramakrishnan, A., 1980, ApJ, 237, 781.
- Willner, S.P., Soifer, B.T., and Russell, R.W. 1977, ApJL, 217, L121.
- Young, J.S. 1987, in *Star Formation in Galaxies*, NASA Conf. Pub. 2466, ed. C.J.L. Persson (NASA Office of Space Sci. Appl., Washington, D.C.), p197.
- Young, J.S., and Scoville, N.Z. 1984, ApJ, 287, 153.

